Diss. ETH N° 19367

High Temperature
Fast Response Aerodynamic Probe

DISSERTATION

Submitted to

ETH ZURICH

for the degree of

DOCTOR OF SCIENCES

presented by

CHRISTIAN LENHERR

Dipl.-Ing. ETH
born February 25, 1978
citizen of
Gams (SG)

accepted on the recommendation of

Prof. Dr. Reza S. Abhari, examiner
Prof. Dr. Hyung Gyu Park, co-examiner
Dr. Anestis I. Kalfas, co-examiner

Zurich 2010

Acknowledgements

I would like to thank Prof. Dr. Reza S. Abhari for having given me the possibility to carry out my multidisciplinary PhD thesis at the "Laboratory for Energy Conversion" (LEC) of the Swiss Federal Institute of Technology Zurich (ETH Zurich).

I am very grateful to Prof. Dr. Hyung Gyu Park and to Dr. Anestis I. Kalfas for accepting the role of co-examiners. I would like to especially express my profound gratitude to Anestis for supporting and encouraging me during the entire time of my project. Furthermore he provided me the opportunity to gain additional work experience by involving me in the project management team and the technical development team of "Limmat Scientific", a start-up company of ETH Zurich. I am very grateful to Anestis for all that as well as for the numerous enlightening discussions we had on all kind of topics.

Many thanks go to Dr. Ndaona Chokani for the helpful discussions, the editing of my manuscript and especially for his support during the pre-conference periods and at any critical situations during my project.

I don't want to miss to gratefully appreciate the support of Dr. Michel Mansour. Whenever needed he was there, providing the best support and the discussions with him therefore helped a lot to break some of the major barriers during my project. Next to the time in the Laboratory, I enjoyed the numerous hours I could spend with Michel and other colleagues outside of the Laboratory. A special thank therefore goes to Dr. Bob Mischo for his support in the last phase of my project.

I would like to thank all my colleagues at the LEC. It was a pleasure to work in such a friendly, multi-cultural working environment. I would like to specially acknowledge the support of Philipp Jenny and Armin Zemp in spending long days with me in the machine hall in order to conduct measurements in the various experimental facilities, but also in spending time to discuss the results. A special thank goes to Mrs. Marlene Hegner. She has always ensured that all the administrative hurdles were handled in time.

Ein herzliches Dankeschön geht auch an unser Werkstatt Team. Dank Ihrer hervorragenden Arbeit, stets verknüpft mit höchster Präzision, waren Sie massgeblich am Gelingen dieser Arbeit beteiligt. Ein Dank geht auch an Cornel Reshef, der bezüglich elektronischer Aspekte viel Unterstützung bot.

Ein riesiges Dankeschön geht an all meine Freunde, die immer für mich da sind und immer wieder helfen Ablenkung vom Arbeitsalltag zu schaffen.

Abstract

In the last decade, significant improvements have been achieved in the development of new materials and in cooling techniques in the field of turbomachinery. The main driver for the focus on such topics is due to the trend of higher turbine inlet temperatures. This leads to a larger amount of work per unit mass flow and an improved weight-to-power ratio of engines. However, under these severe flow conditions, it is of even more importance to be able to measure unsteady flow phenomena, in order to improve our understanding of loss generation mechanisms.

The objective of this work is therefore to design, build and evaluate a new Fast Response Aerodynamic Probe with a higher upper temperature limit (533K) compared to traditional unsteady pressure probe techniques, often limited to temperatures around 390K. Such a new probe, with a higher upper temperature limit therefore opens up a wide field of applications, such as measurements in centrifugal compressors at design point, or in the first compressor stages of axial machines. The development of the probe is therefore motivated by the need for unsteady measurement techniques that are capable of withstanding the harsh environment of turbomachines.

The new probe is comprised of a pair of piezoresistive pressure sensors that measure the unsteady pressure and the steady temperature, respectively. Special care is taken to account for effects related to the higher temperature levels. Furthermore, possible probe shaft vibrations when operating the probe at high temperatures are taken into account in order to achieve a robust probe design.

The thesis details the operating principle, the design and fabrication of the high temperature fast response aerodynamic probe (FRAP-HT), as well as the integration of additional sensors in order to thermally manage the probe and to monitor possible probe shaft vibrations.

Major challenges related to topics such as sensor technology, signal conditioning, material science, packaging technology as well as electrical connections are addressed in the thesis.

The calibration procedure, the dynamic response, the measurement system and the measurement uncertainty analysis for the new probe are described in detail. Furthermore, in order to be able to apply the probe in harsh flows of any kind, several subcomponent systems, such as a sensor calibration oven and a sensor characteristic test device working in the high temperature range are

required. Their design and evaluation is as well detailed in this thesis.

In order to demonstrate the measurement principle and to detail the unsteady flow in severe flow conditions, the new probe is applied in an axial research turbine equipped with a hot-streak generator. Furthermore measurements in a centrifugal compressor facility, in order to first time ever detail unsteady measurements at the design point of the facility are performed and discussed.

A comparison between measurements using the newly developed high temperature probe against various well-established steady and unsteady measurement techniques is performed. There is good agreement between all the techniques and therefore the new probe concept was proven to be applicable. The minor variations between the measurements of the different probe techniques might be related to combinations of different effects such as, wall proximity effects, blockage effects due to the difference in the probe diameter and relative sensor position, high total pressure gradients near the endwalls and a lower signal-to-noise ratio of the standard FRAP for elevated flow temperatures compared to the new FRAP-HT.

Based on the validation results of the new FRAP-HT probe and due to its higher degree of robustness it is concluded that the newly designed probe allows one to successfully conduct measurements in the harsh environment of real turbomachinery, such as at the exit of axial compressors as well as in a wide spectrum of centrifugal compressors. The probe therefore is a major contribution both to the turbomachinery community as well as for future developments of unsteady probe technology.

Résumé

Lors de la dernière décennie, d'importants progrès ont été réalisés dans le développement de nouveaux matériaux haute température ainsi que dans les techniques de refroidissement dédiées à la turbomachine. Ceci dans l'optique d'opérer à des températures d'entrée de turbine plus élevées. Les objectifs principaux étant de pouvoir générer un plus grand travail par unité de débit-masse, ainsi que d'améliorer le ratio poids/puissance des turboréacteurs. Néanmoins, il est d'autant plus important de pouvoir réaliser des mesures d'écoulements instationnaires. Afin d'améliorer notre compréhension des mécanismes de pertes aérodynamiques liées à ces conditions d'écoulements complexes.

L'objectif de cette thèse est de développer et d'évaluer une nouvelle sonde rapide de mesure aérodynamique, pouvant opérer à des températures d'écoulement plus élevées (533K) que les sondes rapides traditionnelles se limitant à des températures maximales d'utilisation de 390K. Cette nouvelle sonde haute température permet d'étendre les prises de mesures au point nominal de fonctionnement de compresseurs radiaux, ainsi que dans les premiers étages de compressions de machines axiales. De manière générale, la motivation principale est le besoin de technique de mesure en temps réels applicables aux écoulements rigoureux des turbomachines.

La nouvelle sonde est équipée d'une paire de capteurs de pression piézorésistif, permettant la mesure de pression instationnaire, ainsi que la mesure de température stationnaire. Un soin particulier a été apporté aux effets thermiques liés à l'utilisation à haute température. De plus, les effets vibratoires induits par la fréquence propre de la sonde sur la mesure de pression ont été considérés de manière à obtenir un design robuste de la sonde.

La thèse fournit une explication détaillée du principe de fonctionnement de la sonde. Incluant la conception et la fabrication de la sonde rapide aérodynamique haute température (FRAP-HT); ainsi que l'intégration de capteurs additionnels nécessaires à la gestion thermique et au monitoring des vibrations induites.

Les défis principaux liés aux thèmes aussi divers que la technologie des capteurs, le conditionnement du signal, la science des matériaux et les micros assemblages sont abordés dans la thèse.

La procédure de calibration, l'étalonnage dynamique, le système de mesure et le calcul d'incertitude sont décris en détail. De plus, la thèse inclut une

description exhaustive des stands de calibrations nécessaires à l'étalonnage de la sonde, et permettant de procédé à des mesures instationnaires dans des écoulements extrêmes et de caractéristiques très diverses.

La nouvelle technique de mesure a été validée dans une turbine axiale de recherche équipée d'un générateur de flux chaud. De plus les mesures d'écoulement instationnaire réalisé pour la première fois au point nominal de fonctionnement d'un compresseur radial sont présentées et analysées.

Les mesures réalisées avec la sonde haute température ont été comparées avec des techniques de mesure traditionnelles. Le haut niveau de concordance des résultats permet de conclure à la validité de la nouvelle technique au niveau stationnaire et instationnaire. Les faibles divergences observées entre les diverses techniques de mesure appliquées, peuvent être attribuées à la combinaison des facteurs suivants: effets de proximité de surface, différence de taille de sondes et de placement relatif des capteurs, gradients de pression prononcés proche de la paroi et niveau de bruit de mesure réduit de la FRAP-HT à haute température comparé aux sondes aérodynamique traditionnelles FRAP.

Sur la base des résultats de validation de la sonde FRAP-HT et sur sa capacité démontrée à mesurer dans divers écoulement éprouvant de turbomachines. Il peut être conclut que la sonde FRAP-HT offre une opportunité unique d'accomplir des prises de mesures instationnaires dans une large gamme de compresseur radiaux et axiaux, ainsi que dans un grand nombre des stands de recherche d'aérodynamique à températures élevées. De manière générale le développement de la FRAP-HT peut être considérer comme une contribution majeure pour la communauté des turbomachinistes et pour le développement future de nouvelles sondes aérodynamiques rapides.

List of Contents

1 Introduction

One of the key challenges related to globalization in the modern world of the 21st century is linked to the rising energy demand and questions about the future of energy supplies, particularly in developing economies. These questions arise for different reasons, such as concerns about global warming and climate change due to emissions from use of fossil fuels, concerns about the balance between the availability of energy resources and rapidly growing demand for energy, for power, heat and transport, and concerns about the rising price of fuels, particularly oil and gas.

Although gas turbines do produce combustion pollution, the levels of pollution are very low compared to other prime movers such as Diesel and reciprocating automobile engines. One of the main advantages for the use of gas turbines in the aerospace sector is their great power-to-weight ratio. In the electric power generation sector, the main advantage in the use of gas turbines is their ability to be turned on and off within minutes, thereby supplying power during periods of peak demand.

In the history of energy conversion, the gas turbine is relatively new. The first practical gas turbine used to generate electricity ran at Neuchatel, Switzerland in 1939, and was developed by the Brown Boveri Company. The first gas turbine powered airplane flight also took place in 1939 in Germany, using the gas turbine developed by Hans P. von Ohain. In England, the 1930s' invention and development of the aircraft gas turbine by Frank Whittle resulted in a similar British flight in 1941.

1.1 Principle of Gas Turbine

A gas turbine is a rotary engine that extracts energy from a flow of combustion gas. Energy is extracted in the form of shaft power, compressed air and thrust, in any combination, and used to power aircraft (Fig. 1-1), trains, ships and electrical generators from mobile small scale, to big scale powerplant generators. An example of the dimensions of such a gas turbine used in an electric energy power station is given in Fig. 1-2.
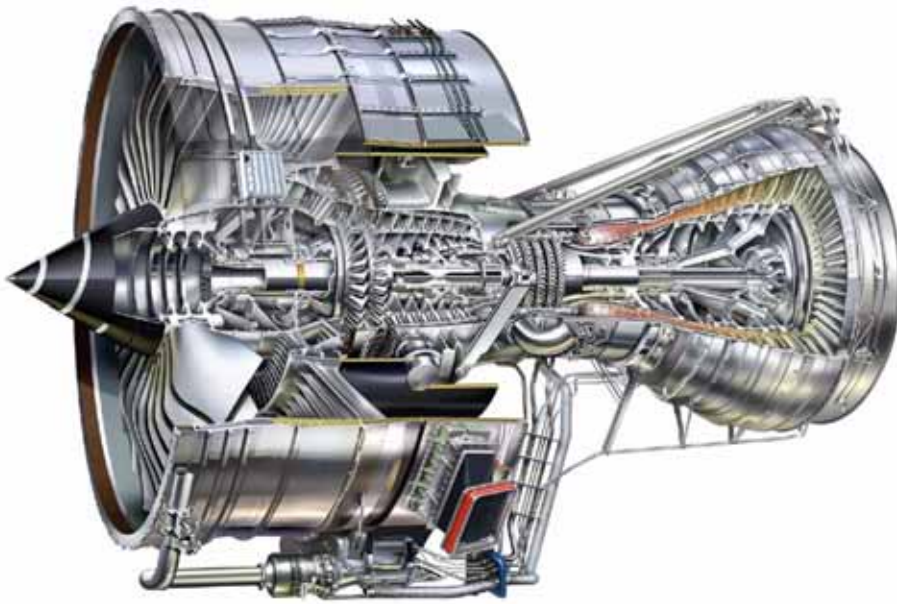
Fig. 1-1   Cutaway View of Rolls Royce Trent 900 turbofan engine, max. thrust 360kN.

.

Fig. 1-2   Core part of Siemens 340 MW Gas Turbine SGT5-8000H (courtesy of Siemens).

The simplest gas turbine, a turbojet (Fig. 1-3, top), is essentially a tube, open at both ends, with air continuously passing through it. The basic components of such a turbine are as follows. It has an upstream compressor coupled to a downstream turbine and a combustion chamber in between. Energy is released when air is mixed with fuel and ignited in the combustor.

The resulting gases are directed over the turbine's blades, spinning the turbine, and, cyclically, powering the compressor. Finally, the gases are passed through a nozzle, generating additional thrust by accelerating the hot exhaust gases through an expansion back to atmospheric pressure. This cycle of continuous combustion is known as the Brayton cycle. It defines a varying volume sequence with four distinct stages: compression combustion, expansion and exhaust. The Brayton cycle though is very similar to the Otto cycle (Fig. 1-3, bottom). There as well the working gas is compressed and burned and work is produced by the expansion of the hot gas. A temperature - entropy diagram of a Brayton cycle for a turbojet engine is shown in Fig. 1-4.
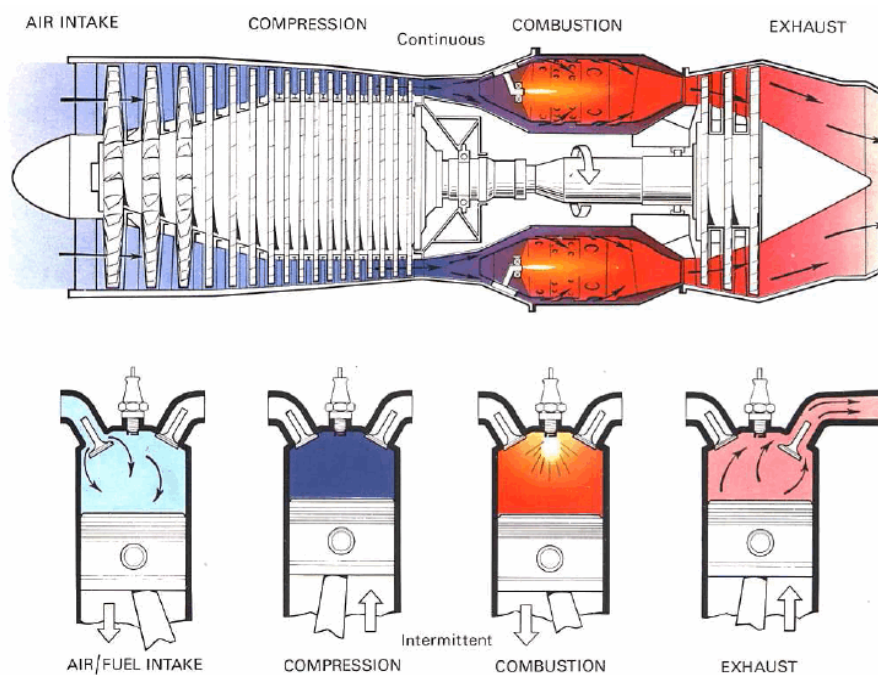
Fig. 1-3   *Comparison between the working principle of a TurboJet and a Piston Engine [1].*

The different stages of the cycle are:

- 0-1: Inlet: Incoming air is brought to stagnation conditions.

- 1-2: Compressor: Air is compressed over a given pressure ratio.

- 2-3: Combustor: Burning fuel raises the air temperature, with some pressure loss.

- 3-4: Turbine: Air is expanded until the work output is sufficient to power the compressor.

- 4-5: Outlet: Air is expanded to atmospheric pressure, increasing the velocity and providing thrust.
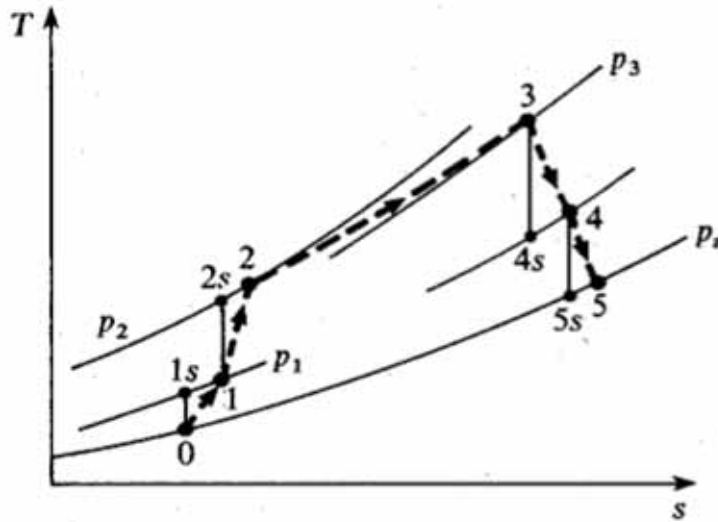
Fig. 1-4   Temperature- Entropy (T-S) diagram of Brayton cycle for an aero-engine.

1.2   Trends in Modern Turbomachinery

For both, aircraft engine manufacturers, as well for manufacturers in the power generation sector, decreasing energy sources, pricing pressure and matter of environmental compatibility are some of the main reasons why an increase in of the turbomachines' efficiency has become a major research topic in recent years. Therefore substantial efforts have been devoted to the following two topics:

  • The optimization of flow field influenced processes;

  • The further development of compressors and turbines.

Optimizing flow field influenced processes appearing in turbomachines means nothing else than in a first step "understanding" a turbomachines flow field and then detecting different sources of loss [2] and their relative importance compared to the overall losses in a turbine stage and in a second step modifying the detected sources of loss by means of constructive aspects.

In the last decades, empirical, theoretical and experimental approaches have been attempted to improve and optimize the overall efficiency. Most of these investigations were based on time-averaged data, but it is well known that the flow in turbines and compressors is inherently unsteady and predominantly three-dimensional. Between 25% and 100% additional losses are caused by unsteady aerodynamics in turbines compared to the steady state case [3]. As a

consequence from the highly fluctuating flow properties different time-dependent physical phenomena contribute significantly to loss production, undesired airfoil vibrations, heat transfer variations and noise. The most important source of unsteady flow in turbomachines, responsible for the above listed effects, is the relative motion of adjacent rows of airfoils, namely the alternately stationary and rotating annular blade rows that lead to strong flow fluctuations over a wide frequency spectrum [4].

Due to the importance of the unsteady flow effects and their association to turbomachinery performance, in recent years of research great interest was the investigation of time-varying flow fields and their impact on the overall blade performance. To achieve these, Computational Fluid Dynamics (CFD) has been used as well as time-averaged experimental methods. More recently traditional experiments using time-averaged methods have been supplemented more and more by numerical calculations for financial reasons. Today CFD-codes are limited by available computing power and by the their accuracy to appropriately model complex flow physics, for instance three-dimensional turbulent mixing processes in flows with strong thermal gradients at the exit of the combustion chamber of gas turbines. Furthermore computing unsteady flow features needs even more computing power than computing in a time accurate manner. Due to the general interest in the development of CFD tools that predict the unsteady flow behavior even more accurately, progressive measurement methods still remain very important for a great number of problems.

In terms of further development of compressors and turbines, some of the highest increases in overall efficiency can be accomplished by improving the high temperature sections of the engine, namely the combustor and the turbine. Thermodynamic cycle analysis shows, that higher cycle temperatures produce larger amount of work per unit mass flow and improves the weight-to-power ratio of gas turbines. Thus the trend to higher temperatures is strongly linked to the availability of materials that are able to withstand such high temperatures and the combined stresses due to temperature, rotation and aerodynamic loading.

Over the last decades, a lot of progress has been achieved in material science and in the development of more effective cooling techniques in order to protect the material that is exposed to these harsh conditions. The historical evolution in these topics is therefore directly linked to the evolution of the turbine inlet temperatures as shown in Fig. 1-5.
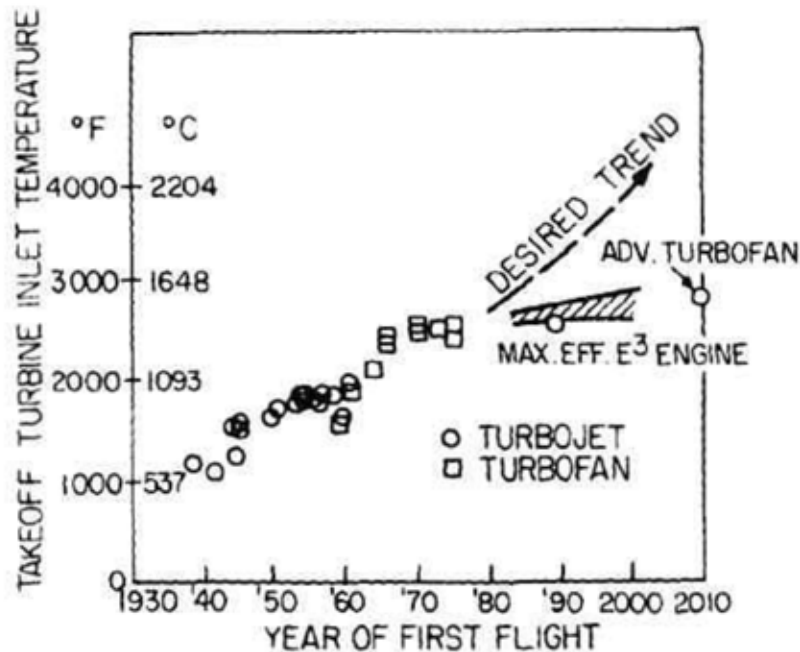
Fig. 1-5   Historical evolution of turbine inlet temperature (reproduced from Lakshminarayana [5]).

1.3   Motivation

Measurement systems to investigate the operation of gas turbines, as well as control and diagnostics are of major importance in the development of modern turbomachinery. Therefore, the drive in recent years has been toward the accurate measurement of time dependent flow properties, such as pressure, to gain more insight into phenomena which vary over time; the improved knowledge is fed back into new design processes [6-8]. But it is not only the design process that has been improved in recent decades. As predicted by several authors [9-13], significant progress has been made in areas such as the development of new materials and the improvement of cooling techniques, as well as in computational tools for the analysis and design of more powerful and efficient turbines. One of the main drivers for these improvements is related to the trend in higher inlet temperatures that lead to a larger work per unit mass flow and improvements in the weight-to-power ratio of gas turbines. Due to severe flow conditions at higher temperature levels, time resolved measurements of flow properties such as pressure or temperature are still a major challenge.

Fast Response Aerodynamic Probe (FRAP) technology has been developed

at ETH Zurich. This technology has been used extensively in the past for unsteady measurements of turbomachinery flow fields in a wide range of turbomachinery applications. Fast response pressure probes allow measurements of the flow angles, the Mach number, the velocity and unlike complementary techniques such as hot-wire anemometry or laser techniques, can also measure time resolved static and total pressure. The FRAP technology is based on piezoresistive miniature silicon sensors. The working principle of such sensors has been discussed in detail by several authors [8, 14-19].

A historical review of the development of invasive measurement probes used in turbomachinery is given in the literature review section of this chapter. To date however, FRAP technology has been limited to flow temperatures not exceeding 393K [18, 20, 21]. The main limiting temperature factors are related to sensor limits, reduced signal-to-noise ratios, packaging issues, material issues and electrical connections to the sensor.

From the discussion in the above introduction section, it can be stated, that higher probe operating temperatures are clearly an objective for applications such as low-pressure turbine stages, or high-performance compressor stages. Nowadays, microtechnologies for miniature chips based on silicon-on-insulator (SOI) with temperature limits of 500K and more exist as prototypes (e.g. [22]), which in principle opens up the field for the further development of FRAP that are operable with a higher upper temperature limit.

1.4   Literature Review

Before giving a brief overview about common measurement techniques in turbomachinery in this subsection, some information of the requirements for such systems shall be given. It is furthermore a goal, to point out some of the respective advantages and disadvantages of the different measurement systems, when applied in the field of turbomachinery.

1.4.1   Aerodynamic Efficiency

The losses associated with the unsteady flowfield in a turbomachine determine the overall efficiency. Based on Denton's [2] famous review of the loss generating mechanisms in turbomachinery, there have been identified three principal sources of loss in turbomachines, which are: viscous effects in boundary layers and in mixing process, shock waves and heat transfer across temperature difference. In the current work, measurements performed in a high-speed radial compressor and in highly loaded unshrouded one-and-1/2

stage turbine equipped with a hot streak generator are presented. Centrifugal compressors in general are of a compact design and able to provide higher stage pressure ratios than an axial design. Due to these characteristics, they are often used in automotive, marine turbocharging and distributed power applications

At the exit of the centrifugal compressor's impeller the flow is unsteady, three-dimensional and turbulent. The structure of this complex flowfield is affected by the tip clearance, which in turn affects the compressor's efficiency and operating range.

Similar to turbochargers the flow in low-aspect ratio turbines is dominated by secondary flows, see Fig. 1-6, in addition to the presence of the blade wake. In that context, the efficiency is influenced by secondary flow interaction, periodic wake impingement on the downstream blade, strong potential field effects, periodic interaction between the vane potential field and rotor exit flowfield. Thus all of these sources of blade interactions have to be considered in designing a modern high-pressure turbine and therefore being able to accurately predict the stage performance.
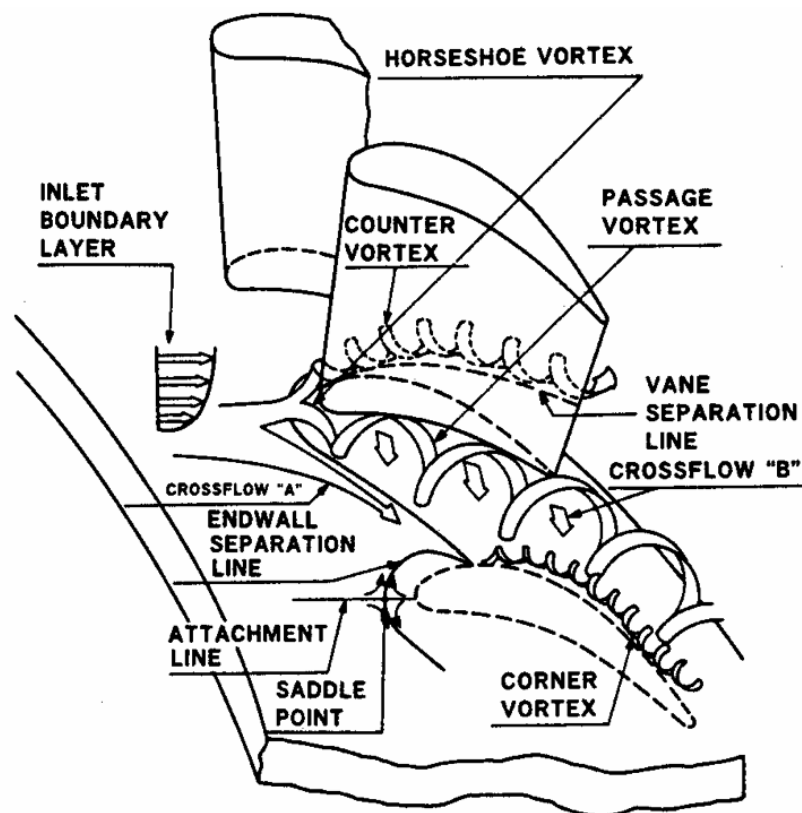
Fig. 1-6   Three-dimensional flow feature in an axial turbine rotor passage (source: Takeishi et al.[23]).

1.4.2   Overview about Measurement Techniques in Turbomachinery

As mentioned before, the knowledge of unsteady effects are of major importance in the development of modern turbomachinery. This subchapter therefore presents the various time resolved measurement techniques that are applicable in the field of turbomachinery.

Due to high flow velocities, considerable flow fluctuations (in amplitude as well as in frequency), and difficult spatial conditions fast measurements (highly time-resolved) in turbomachinery flows require very high standards for the measurement techniques employed. Therefore, only a small number of successful techniques exist. These techniques can be divided into two classes: invasive and non-invasive, contact-less methods. In invasive methods a probe is inserted into a flow field and the flow parameters are measured. Positioning the probe directly in the flow leads to a disturbance of the same. This disadvantage is avoided by using non-invasive methods. Non-invasive techniques mostly use optical methods to measure either some parameters of the whole flow field, so-called integral techniques (In.) or to measure some discrete flow field parameters, what then is called point techniques (Pn.). In Table 1-1 an overview of the most common measurement techniques used to measure unsteady flow parameters in turbomachinery is shown.

Invasive methods	In.	Pn.	Non-invasive methods	In.	Pn.
Hot wire Anemometry		x	Laser Doppler Anemometry (LDA)		x
Cold wire probes		x	Laser-Two-Focus Anemometry (L2F)		x
Aspiration probes		x	Holographic technique	x	
Fast aerodynamic probes		x	Schlieren technique	x	

Table 1-1   *Overview about the most common measurement techniques in turbomachinery for measuring unsteady flow parameters ("In." denotes integral techniques; "Pn." denotes point techniques).*

In the following, a short overview about the different techniques is given:

- **Hot wire anemometry**: A very thin wire is used (for example diameter $5\,\mu m$), that is heated by an electrical current. The heat transfer from the wire to the fluid can be calibrated. The time dependent velocity vector can be measured with three or four wire probes [24, 25].

- **Cold wire probes:** Cold wire probes differ from hot wire probes only by the fact that they have a low overheat ratio. They are used for

temperature measurements and not for velocity measurements as with the hot wire probes [26].

- **Aspiration probes:** Aspirating probes do not determine directly the concentration - or composition - of a binary mixture. The gas is sucked into a channel inside the probe where several properties of the flow are measured (pressure, temperature…), and by combining these data, it is possible to retrieve the concentration (Ng et al. [27]).

- **Fast aerodynamic probes:** A small and appropriately formed probe is immersed into a flow field. The flow around the probe head generates a pressure field on the probe surface. This pressure depends on the head geometry as well as on the velocity and the direction of the flow. At selected positions on the probe head, measurement holes are inserted to measure the corresponding pressures. This method needs at least one hole per flow value that has to be measured. Additional information about Fast Aerodynamic Probes is given later in chapter 1.4.3 and chapter 3.

- **Laser Doppler Anemometry (LDA):** The Laser Doppler Anemometer is a well-established technique that gives information about flow velocity [28]. Its non-intrusive characteristic and directional sensitivity make it very suitable for applications with reversing flow, chemically reacting or high-temperature media and rotating machinery, where physical sensors are difficult or impossible to use. It requires tracer particles in the flow.

- **Laser-Two-Focus Anemometry (L2F):** This Technique (L2F) is especially useful in measuring flow velocities and turbulence quantities in narrow blade channels or in high speed applications, whereas Laser Doppler Anemometry (LDA) is superior in flows with good accessibility and moderate spatial gradients and in flows with very high turbulence. The performance differences of these two types of velocimeters are caused by the geometry of the measurement volume [29, 30].

- **Holographic techniques:** In holographic techniques a flow is seeded with particles, and then multiple-exposure holograms are recorded. The holograms are reconstructed and scanned, and one obtains the 3D velocity distribution from the displacement of the particles. The technique is used to investigate both aerodynamic and mechanical behavior of a rotating unit. Holographic flow visualization provides clear, three-dimensional images of the transonic flow region between the

blades. Flow features such as shocks, shock/boundary layer interaction, and over-tip leakage vortices can be observed and measured [31, 32].

- **Schlieren techniques:** One of the experimental techniques that can be used to visualize shock and expansion waves is the so-called Schlieren technique, which is based on the density variations across shocks and expansion waves. The variation in the local density of the fluid produces a change in the refractive index of the medium, which in turn causes a change of direction of a light beam traveling in the medium measured by the Schlieren system [33].

The choice of which type of measurement technique is used depends primarily on the flow parameters one is interested in, even though the different techniques often allow the calculation of unmeasured parameters from the measured ones during post processing. A short overview of the primary focus of various fast measurement techniques can be seen in Table 1-2.

Primary focus of technique:	Preferred techniques:
Pressure	Fast aerodynamic pressure probes
Temperature	Cold wire probes, Aspiration probes
Density	Holographic and Schlieren technique
Velocity components	Hot wire, LDA, Fast aerodynamic pressure probes

Table 1-2   Primary focus of various fast measurement techniques.

As concluding remarks, it can be stated: The unsteady flow in a turbomachine can be measured by different techniques such as hot-wire anemometry, laser doppler anemometry (LDA) or pneumatic and fast response pressure probes. The latter two techniques have the advantage of measuring the local total and static pressures, in addition to the flow velocities, as opposed to the first two techniques. In the field of turbomachinery the pressure distribution is of particular interest to the designer. A measurement technique that provides the pressure quantities and the velocity is the ideal tool for understanding the complex physics of unsteady flows.

1.4.3   Aerodynamic Pressure Probes

In general, the total pressure distribution as well as three-dimensional flow-field in the flow path is of prime interest to the blade designer. From this perspective a broad variety of pneumatic pressure probes have been used (e.g. [34, 35]). Depending on the flow conditions and range of flow angles, different

probe head geometries have been designed. All these probes can determine one or more flow quantities such as total and static pressures, flow angles or Mach number by measurement of the pressures at different locations on the probe tip. However due the pneumatic damping between the pressure taps and the pressure transducers, these types of probes are limited to measurement of time averaged flow quantities.

The size and geometry of pressure probes have considerable variations, according to their particular use and the number of flow quantities that are required at the same time. Fundamentally, however, they all exploit a pressure distribution occurring over a body, when the body is immersed into a moving fluid. The variation of these pressures depends mainly on the speed of the moving fluid and on the detailed shape of the probe body. The relationship between the tap pressures and the wind speed can therefore be calibrated over a range of speed. In general, the design for a pressure probe varies depending on the measurement requirements. If only pressure needs to be monitored, one tap could be sufficient. However, a common additional requirement for pressure probes is the knowledge of the two flow angles together with total and static pressures. The degree of complexity of both, the probe and its method of operation will therefore depend on how many flow quantities are to be derived from one set of measurements, and if the quantities are derived in a steady or unsteady manner. Independent of the design complexity of such a probe, there are some general features which are desirable for all probes that are used in an intrusive manner to measure flow quantities at a point in a fluid. These features can be summarized as follows, where no significance is attached to the order in which the features are listed:

- Small size in order to minimize blockage effects (disturbance to the flow) and to maximize the spatial resolution in order track small-scale flow features

- Rapid time response

- Robust design

- Calibration unaffected by flow conditions

- All pressure taps are close to one point

The second point, is a general interest for any measurements in the turbomachinery sector due to the high unsteadiness related to interactions between stationary and rotating blade rows. Therefore the need for probes, capable of measuring flow properties in an unsteady manner has been known for decades, but the realization of this was for a long time impossible due to

technical constraints.

In the early 1970s, the progress in the miniaturization of piezo-resistive pressure sensors made possible probes that have the sensor installed closer to the pressure tap; thus the dynamic response was improved. Larguier and Ruyer [36] mounted a single piezo electric sensor into the probe tip of 8mm diameter, and made time-resolved measurements in air flows. To reduce the tip size, Senoo et al. [37] and Matsunaga et al. [38] used probes with several sensors in the probe stem. Two- and three-dimensional flows were measured with a bandwidth up of 1kHz. Kerrebrock [17] developed a 5-sensor cylindrical fast response probe. Epstein [15] was able to reduce the size of a fast-response probe to a head diameter of 3.3mm.

Since then, several research groups around the world have developed their own probes tailored to their applications. In general the design of fast-response aerodynamic probes was improved by further reducing the probe tip diameter down to less than 2mm. Gossweiler et al. [39] and Kupferschmied [40] introduced and developed the Fast-Response Aerodynamic Probe (FRAP) technology at the then Turbomachinery Laboratory (predecessor of the Laboratory for Energy Conversion) of ETH Zürich. Roduner [41] measured time-resolved flow quantities in a centrifugal compressor using a cylindrical shape 3-sensor probe of a diameter of 1.8mm. A reduction of the probe head diameter to 0.84mm was achieved by Pfau [42] in order to perform measurements of the cavity flow in labyrinth seals. In the recent work of Porecca et al. [43] a newly designed 2-sensor FRAP probe was used in a virtual 4-sensor mode to yield measurements of non-isotropic turbulence in a multi-stage axial turbine.

1.5   Research Objectives

First generation FRAP have been developed within the last two decades [7, 20, 21, 44, 45] in order to investigate unsteady flow phenomena such as secondary flows or rotor-stator interactions in turbomachinery [2-4, 6, 46, 47]. Fast response aerodynamic probes satisfy all required measurement criteria for turbomachinery, including having a high measurement bandwidth (of typically 5-12 kHz), a large Mach number range (typically between 0.1 up to transonic), high spatial resolution, as well as a high measurement accuracy and easy access to the test section. To date however, FRAP technology has been limited to flow temperatures not exceeding 393K [18, 20, 21]. A higher upper temperature limit of FRAP technology would significantly widen the range of

possible applications. The potential impact of FRAP technology that has a wider operational temperature range is evident when one considers turbomachinery applications of interest and their respective flow temperature ranges as summarized in Table 1-3.

Application:	Description:	Temperature range [K]
Turbochargers	Centrifugal compressors to turbocharge diesel- and gas engines (compression ratio: 5)	~523
Steam turbine research facilities	Some stages of low-pressure turbines (LPT) (operated by dry air in R&D centers)	>445
Gas turbines for electric energy power stations	Low pressure compressors (LPC) and first stages of high pressure compressors (HPC)	533 - 773 (HPC exit)
Aircraft turbofan engines	LPC, first stages of high pressure compressors (HPC)	~273 (LPC inlet) ~773 (HPC exit)

Table 1-3   Selected turbomachinery applications and respective temperature ranges.

It is evident from Table 1-3, and knowledge of the temperature limits of materials used in the probe, that the upper temperature limit of the new probe should be in the order of 533K. New FRAP technology with this higher upper temperature limit, furthermore enables the measurement of localized regions of high temperatures (hot streaks) that occur for example in gas turbine combustor exit flows; in this application, these non-uniformities in temperature are caused by the spatially discrete fuel and dilution air injection within the combustor. The resulting hot streaks interact with the different components within the turbine, and can locally cause increased blade heat transfer which potentially lead to reduced blade life."

Irrespective of the temperature range, a new Fast Response Aerodynamic Probe has to be miniature in size in order to minimize blockage effects and maximize the spatial resolution which leads to an improved tracking of small-scale flow features.

Particularly in terms of industrial rigs with large blade heights that are operated at high temperatures, the long probe immersion lengths in combination with strong temperature gradients could lead to possible conduction losses between the "hot" probe tip volume of the probe and the colder rear side. In order to correct for such possible conduction losses, additional temperature sensors shall be implemented into the probe.

An additional research objective related to higher flow temperatures and harsh industrial turbomachinery environment is the requirement of probe robustness. An integrated probe shaft vibration measurement system shall be developed, such that the probe is fully operative even in high dynamic head flows with sharp periodic fluctuations. This is of importance, since possible probe vibrations could have a significant impact on the accuracy of the pressure sensor output signal. Within the probe, vibrations could lead to erroneous pressure signals if vibration related mechanical stresses propagate through the structure of the probe onto the sensors' membranes. Furthermore could probe vibrations affect the local flow field around the probe and therefore lead to an adulterated sensed flow field pressure due to a vibration induced local parasitic pressure.

The current project therefore aims to: design, build and evaluate a new Fast Response Aerodynamic Probe with a higher upper temperature limit (533K). The principal requirements of the high temperature FRAP probe are:

- Significantly increase the upper temperature limit (up to 533K).
- Thermally manage the probe
- Monitor and eventually provide online control for possible probe shaft vibrations
- Large measurement range for multiple applications;
- Miniaturized design in the same range as existing FRAP (spatial resolution 1.8mm);
- Large frequency bandwidth (up to 40kHz);
- Robust construction for use in harsh turbomachinery environments.

1.6   Thesis Outline

The chapters of this thesis are structured as follows:

- **Chapter 1** outlines the motivation and the research objectives of this study. A comprehensive overview of the trends in modern turbomachinery is presented, as well as information about common measurement techniques applied in turbomachinery applications are given.

- **Chapter 2** presents the challenges related to the development of a high temperature fast response aerodynamic probe. A comprehensive overview of piezoresistive pressure transducers is provided as well as

the most important parameters used for selecting a possible pressure transducer. Furthermore the selected pressure transducer for the high temperature FRAP probe is introduced and its characteristics are presented.

- **Chapter 3** introduces details about the operating principle and the design and fabrication of the high temperature fast response aerodynamic probe (FRAP-HT). Furthermore, the integration of the secondary sensors such as the strain gauge in order to monitor probe shaft vibrations and the shaft PT100 sensor in order to monitor possible heat flux through the probe shaft is presented. Further this chapter details the calibration procedure and the dynamic response of the primary sensors. Last but not least characteristics related to the secondary sensors, such as probe thermal issues and probe shaft eigenfrequencies are presented in chapter 3.

- **Chapter 4** provides a comprehensive overview of the measurement system needed in order to facilitate measurements with the new developed FRAP-HT probe. Next the hardware equipment, an overview of the data reduction methodology for unsteady probe techniques, as well as for steady pneumatic probe measurement techniques, is presented. Finally, a novel flow adaptive traversing algorithm is presented in this chapter. The aim of the adaptive algorithm is to reduce the required time for turbomachinery tests. The algorithm therefore allows a turbomachinery manufacturer to reduce development costs and to maintain competitiveness in the marketplace.

- **Chapter 5** deals with further aerodynamic probe instrumentation used during this research work in order to validate the proof-the-concept of the newly developed high temperature fast response aerodynamic probe. The chapter provides some background about well known probes, such as different pneumatic probes, as well as the first generation FRAP. Finally, a newly developed steady temperature probe is introduced in chapter 5. The probe is able to withstand harsh conditions similar to the FRAP-HT and is used to evaluate the steady temperature output of the FRAP-HT pressure transducer.

- **Chapter 6** addresses the measurement uncertainty analysis of the newly developed FRAP-HT. Based on a standardized method which first converts all uncertainty information into probability distributions, the expanded uncertainties for FRAP-HT flow angle measurements and flow pressure measurements, as well as for FRAP-HT steady

temperature measurements are derived and discussed in detail.

- **Chapter 7** details measurements performed in a one-and-1/2-stage axial turbine facility equipped with a hot streak generator. The turbine configuration is representative of a high work aero-engine; details are given on the test facility as well as on the measurement setup. The probe's capability to provide measurements under real engine conditions is thus verified. Furthermore the interactions between the hot streak and the secondary flow are analyzed in detail within this chapter.

- **Chapter 8** presents and discusses results of measurements at the impeller exit of a high speed radial compressor, equipped with a vaneless diffuser. Due to the increased temperature range of the newly developed FRAP-HT probe, the first ever, time-resolved measurements at the design point of the facility are presented in this chapter. Furthermore details of the test facility as well as of the measurement setup are provided. Additionally, a combined calibration methodology is introduced and discussed in detail in order to increase the spanwise measurement range of the FRAP-HT measurements. The steady as well as unsteady FRAP-HT results are validated with respect to measurements with other probe technologies. The chapter furthermore discusses the structure of the impeller exit flow and details the unsteady loss mechanisms associated with the outlet flow of the high-speed centrifugal compressor equipped with a vaneless diffuser. Subsequently the aerodynamic stage efficiencies resulting from the FRAP-HT measurements are presented together with an efficiency related uncertainty analysis.

- **Chapter 9** summarizes and concludes the outcome of this research work and gives some suggestions for future work in order to further improve the high temperature fast response aerodynamic probe measurement technique.

2   High Temperature Instrumentation and related Challenges

As stated in chapter 1.4, intrusive aerodynamic pressure probes have the advantage of measuring the local total and static pressures, in addition to the flow velocities. Since the pressure distribution is of particular interest to the turbomachinery designer, aerodynamic pressure probes are the ideal tool for understanding the complex physics of unsteady flows. Most of the available fast response pressure probes are based on piezoresistive pressure transducers of miniature size, embedded in the tip of the probe shaft, in order in order to have as much reduced pneumatic damping of the cavity between the pressure tap and the pressure transducer. Locating the pressure transducer close to the tip of the probe, results in exposing the transducer to the flow conditions closer to the measurement point of interest. This limits the temperature application range of such a probe due to constraints related to issues, as:

- the pressure transducer max operating temperature,
- signal conditioning and electronic connectivity in a high temperature environment,
- and available packaging technologies in order to reduce thermally driven stresses onto the transducer,

This chapter therefore gives an overview of some of the high temperature related challenges in the development of a new high temperature FRAP probe.

2.1   Piezoresistive Sensor Technology

2.1.1   Historical Review

Soon after the discovery of the piezoresistive effect in silicon and germanium around 5 decades ago [48], the use of diffusion techniques for the fabrication of piezoresistive sensors for stress, strain and pressure was proposed by Pfann and Thurston in 1961 [49]. The first use of the proposed technique on a thin single-crystal silicon membrane was by Tufte et al. [50]. Thanks to the better performance of silicon resistors compared to classical strain gauges, the idea was rapidly adopted by others and a fast growing market came into existence.

The very first semiconductor strain gauges used a homogeneously doped silicon strip attached to a membrane of other material. In this case, the only advantage was taken of the higher gauge factor of silicon. Later, a whole wafer

was used as membrane being bent, and resistors were diffused in order to measure the maximum stress at the surface. Further refinement was introduced by etching away part of the silicon under the resistor until a thin membrane was left, so that higher stresses were created and therefore the sensitivity increased. This configuration is generally still in use today.

2.1.2   Working Principle

Piezoresistive silicon pressure sensors are well established and often used for fast response pressure applications (Fig. 2-1). Their ability to measure the average component of pressure is one main advantage compared to piezoelectric sensors, which measure only the fluctuating component.
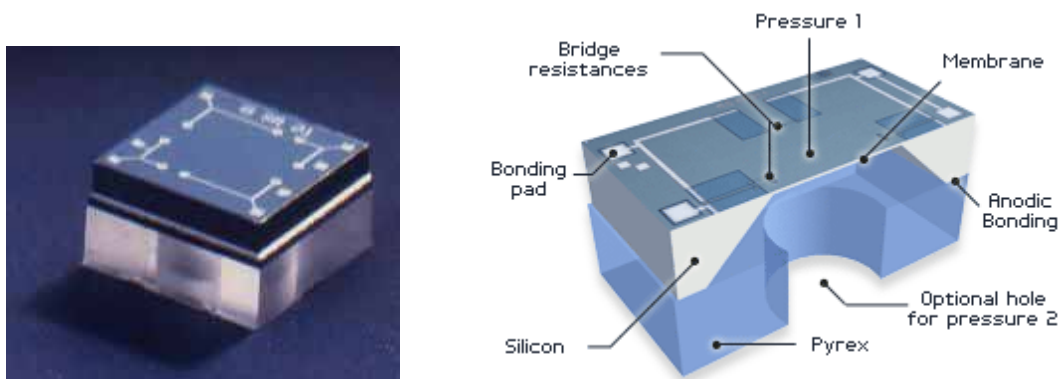
Fig. 2-1   Typical piezoresistive sensor (left) and cutaway view of such a sensor (right).

The sensing material in a piezoresistive pressure sensor is a diaphragm formed on a silicon substrate, which bends with applied pressure. A deformation occurs in the crystal lattice of the diaphragm because of this bending. This deformation causes a change in the band structure of the piezoresistors that are placed on the diaphragm, leading to a change in the resistivity of the material. This change can be an increase or a decrease depending to the orientation of the resistors.

The standard piezoresistive silicon sensors used for FRAP applications work as a Wheatstone bridge and are based on silicon strain gauge technology. In a Wheatstone bridge, four resistors are used as shown in Fig. 2-2. Two are placed parallel to opposite edges of the membrane, and the other two perpendicular to the other two edges. The two perpendicular resistors sense stress in the direction of their current axes and undergo thus an increase in resistance for positive pressure (membrane bent downward, causing traction on the membrane surface at the edge). The parallel resistors are under lateral stress and show a resistance decrease under the same condition. For negative

pressure (membrane bent upward), the resistance changes are of opposite sign. If the resistors are correctly positioned with respect to the stress field over the membrane, the absolute value of the four resistance changes can be made equal (overall bridge resistance). The connection scheme in order to build a Wheatstone bridge is given on the right of Fig. 2-2. Equally positioned resistors form opposite arms of the bridge so that, under an applied pressure, the left and right output nodes of the bridge deviate from zero with opposite sign.
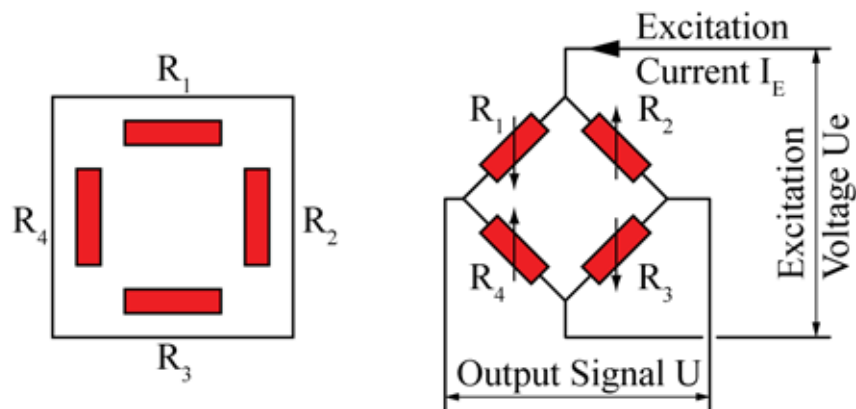
Fig. 2-2   Schematic view of the basic position of the piezoresistors on the membrane (left) and connection in a Wheatstone bridge (right). The arrows indicate resistance changes when the membrane is bent downward.

The advantage of a Wheatstone bridge configuration is that it converts the resistance change directly to a voltage signal. Power can be supplied to the bridge by applying either a constant voltage, or a constant current.

The differential output voltage (ΔU) of an ideally balanced bridge with assumed identical (but opposite in sign) resistance changes ΔR, in response to a differential pressure change Δp and is given by:

$$\Delta U = \frac{\Delta R}{R} \cdot Ue \qquad (2.1)$$

, where R is the zero-stress resistance and Ue the voltage over the bridge.

$$R = \frac{Ue}{I_E} = \frac{(R_1 + R_4) \cdot (R_2 + R_3)}{R_1 + R_2 + R_3 + R_4} \qquad (2.2)$$

An important advantage of the Wheatstone bridge configuration can be seen in Eqn. 2.1. The output voltage is, in first order, independent of the absolute value of the piezoresistors, but appears to be determined by the relative

resistance change and the bridge voltage.

By applying a constant excitation current I_E, the pressure sensitivity S is defined as the change of differential output voltage per unit pressure and per unit excitation current (expressed in e.g. mV/mA bar):

$$S = \frac{\Delta U}{\Delta p} \cdot \frac{1}{I_E} = \frac{\Delta R}{\Delta p} \qquad (2.3)$$

In the ideal case, the total resistance of each half-bridge and thus also of the total bridge is independent of pressure since the resistance changes cancel each another. At the same time, particular temperature influences are not detected at the differential bridge output, since a temperature rise increases the resistance of all piezoresistors equally, so that the output of the bridge remains zero. However, it has to be mentioned, that this is only the case for a perfectly balanced bridge. It is also interesting to note that for a constant bridge feeding current supply I_E, the total bridge voltage Ue will vary, so that a built-in temperature sensor is available for further compensation of temperature effects.

2.1.3   Types of Piezoresistive Pressure Transducers

Pressure sensors can be classified in terms of the pressure ranges that can be measured, temperature ranges of operation, and most importantly the type of pressure that are measured. In terms of pressure type, pressure sensors can be divided into five categories:

- Absolute pressure sensor: This sensor measures the pressure relative to absolute vacuum pressure (0 PSI or no pressure). Atmospheric pressure, is 101.325kPa (14.7 PSI) at sea level with reference to vacuum.

- Gauge pressure sensor: This sensor is used in different applications because it can be calibrated to measure the pressure relative to a given atmospheric pressure at a given location. A tire pressure gauge is an example of gauge pressure indication. When the tire pressure gauge reads 0 PSI, there is actually 14.7 PSI (atmospheric pressure) in the tire.

- Vacuum pressure sensor: This sensor is used to measure pressure below the atmospheric pressure at a given location. This has the potential to cause some confusion as in industry it is common to refer to a vacuum sensor as one which is referenced to either atmospheric pressure (i.e. measure negative gauge pressure) or relative to absolute vacuum.

- Differential pressure sensor: This sensor measures the difference between two or more pressures introduced as inputs to the sensing unit.

This is the type of sensor, which in general is used for fast response aerodynamic probes. Due to the fact, that a certain back pressure can be set, it allows measurement in devices of different absolute pressure. The limiting factor for such a sensor is determined by the level of unsteady pressure fluctuations, which must be smaller, then the linear range of the sensor itself.

- Sealed pressure sensor: This sensor is the same as the gauge pressure sensor except that it is previously calibrated by manufacturers to measure pressure relative to sea level pressure.

2.1.4 Fabrication of Piezoresistive Pressure Transducers

Microelectromechanical system (MEMS) fabrication incorporates numerous materials within an enormous variety of different process flows. Prior to around 1996, almost all MEMS process flows could be divided into two primary types: bulk (also called substrate) micromachining and surface micromachining. Bulk micromachining encompasses process flows that exploit preferential etching of silicon, glass or other substrates to form micromechanical structures. It is most widely known commercially in production of membranes for pressure sensors and nozzles for inkjet printing. Surface micromachining flows create microstructures out of thin films on the substrate surface. Commercial examples of components made from surface micromachining include airbag accelerometers and micromirror projection arrays.

Several books cover the area of micromachining in MEMS technologies as for instance [51-55]. However in order to let the reader gain some insight into the conventional process flow, an overview of such a process for bulk micromachined devices is given here (the chosen coating compounds can strongly vary, depending on the application):

- In general the manufacturing process is done on wafers. Such a wafer is out of a thin layer of silicon. The wafer is then passivated on both sides with insulating SiO_2 (Fig. 2-3a).

- On the passive surface, windows are opened by the photolithographic mask (Fig. 2-3b).

- The cleared area is doped in order to generate a p-doped substrate piezo resistor (Fig. 2-3c).

- The windows are then closed again, by applying a new insulation layer of SiO_2 (Fig. 2-3d).

- A second mask is attached by means of photolithography (e), and again new windows are generated within the insulating SiO_2.

- Aluminum is deposited and structured through the window in order to generate the electric connectivity to the top layer (Fig. 2-3f). The bonding pads generated in that step are later used, in order to connect the sensor.

- The active side of the sensor is ready. The chip is now machined on the backside, in order to generate a membrane. The passive layer is therefore removed on these spots, where chemical etching has to be applied in order to remove as much silicon substrate as needed, to generate a membrane of a certain thickness (Fig. 2-3g & Fig. 2-3h).

- As a last step, the wafer is superposed onto a thin backing film and the sensors are cut to their final size by means of a diamond saw.
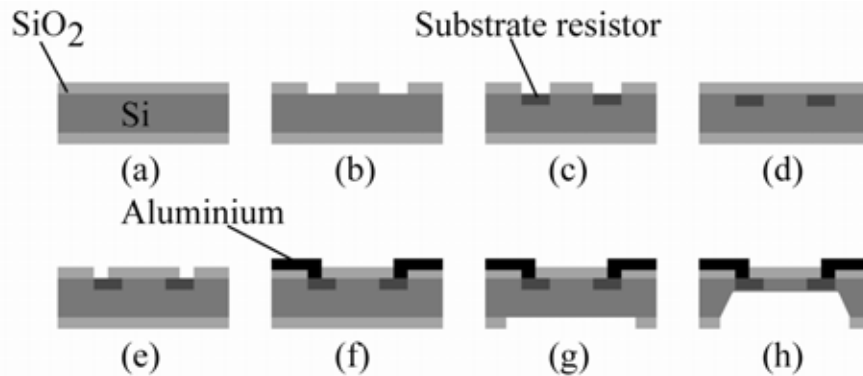
Fig. 2-3   Micromachining process flow for a piezoresistive pressure transducer (cross-sectional view).

2.1.5   Limits and Workaround

Traditional monocrystalline piezoresistive pressure transducers are limited in their temperature range (up to 393K) due to the nature of their construction. Above this temperature, the output signal is corrupted and therefore of no use. Reasons for the rapid decay of the signal-to-noise ratio are mainly related to thermal effects within the sensor and due to leakage current flowing from p-type silicon elements into the n-type diaphragm material [56-60].

Nowadays, microtechnologies for miniature chips based on silicon-on-insulator (SOI) with temperature limits of 500K and more exist as prototypes (e.g. [22]), which in principle opens up the field for the further development of FRAP to higher upper temperature limits.

Another type of sensor, able to withstand higher operating conditions would be based on silicon carbide (SiC). The advantages of SiC as a potential

material for MEMS devices were realized by several research groups in the mid-1990s [61, 62]. The excellent mechanical properties of SiC coupled to the high temperature stability of the material offered new possibilities for developing MEMS devices for more challenging applications than those possible with Si devices. Excellent examples of pressure sensors based on ultra-violet activated wet-etching have been demonstrated at temperatures up to 770K [63-65].

In generally it can be stated, that the research trends in the development of MEMS mainly focus on the base substrates and on the further scaling down of the devices. In terms of piezoresistive pressure transducers, there is an ongoing trend towards silicon on sapphire sensors (SOS) [66-69]. The SOS sensors are even more temperature robust than SOI Sensors. However, in the current state of art, SOS sensors are still bigger in terms of size, due to the critical machinability of sapphire.

Unfortunately, one of the major issues is the commercial availability of raw high temperature pressure sensor dies of miniature size. The availability of such dies is in general very limited, independent on the technology (SOI, SiC or SOS) that is used. One could argue, that today the technology for micromachining high temperature sensors is available and it should therefore be possible to design and manufacture a custom-tailored high temperature piezoresistive sensor, which fulfills all the design criteria for a high temperature fast response aerodynamic probe. However, this argument does not hold due to cost issues. Unfortunately there exists a so called "unwritten law in MEMS", which states, that, designing and manufacturing a new sensor costs roughly one million euro, independent of the amount of sensors produced. The MEMS manufacturer legitimizes his/her price level with the high initial costs that are incurred in the design of the product. Machining on the other hand has no influence on the price, as there is no price variation depending on the amount of ordered sensors.

Finding a sensor which fulfills all the probe design criteria is therefore one of the main issues.

2.1.6 Transducer Selection Criteria

Due to the standardized planar bulk machining processes nowadays used to microfabricated integrated circuit devices, the sensors are fabricated in large quantities as wafers and therefore show very small variations in properties, both in size, as well as in behavior. Nevertheless, the sensors have to be tested and characterized. On the one hand this is done to figure out, if a transducer

meet's the arrangement to be used as high-temperature fast response aerodynamic probe sensor. On the other hand the characterization is done after selection of a suitable sensor type and during the assembly process of a specific probe. Every sensor used for a probe is characterized and tested before assembling it in the probe. There are therefore a certain type of criteria, which are applied in order to figure out, if a sensor fits the agreement of a high temperature fast response aerodynamic probe application. These criteria are listed here as follows, whereas the respective characteristics for the finally used sensors will be listed in chapter 2.1.7.

2.1.6.1   Geometry and Size

The pressure transducer's geometry as well as size must fit to the design of a miniature probe. Furthermore the form and position of the sensor membrane relative to the sensor frame is of major importance. Due to packaging and thermal issues, the sensor needs to be embedded into the probe such, that no thermal stresses are induced on the sensor membrane. Due to the fact, that the probe body material needs to be mechanically manufactured, the body material will not be of the same type as the silicon sensor. In order to reduce mechanical stresses due to different thermal coefficients of expansions of the different components, the sensor has to be installed in a decoupled manner. This can be achieved by the use of silicone adhesives. However, embedding the sensor into an aerodynamic probe shaft by using silicone adhesives needs a minimum size contact surface such that the permanence of the bonding is ensured.

An additional bottle neck related to the sensor geometry is associated with the alignment of the bonding pads on the pressure transducer surface. The electric contact of the sensor has to be done on the side of the sensor dye and along the direction of the probe shaft, in order to reduce the overall dimension of the probe.

As a matter of fact, the requirements of designing a high temperature fast response aerodynamic probe of miniature size drastically limits the pool of possible transducers simply due to their geometry and size.

2.1.6.2   Limitation of Use

The operational limits of the sensors are given by the maximum differential pressure over the membrane, as well as by the maximum temperature of operation.

2.1.6.3   Pressure Sensitivity

The pressure sensitivity S quantifies the relation between a pressure

difference over the membrane (Δp) and the electric output signal U. For a sensor reference temperature T_{Ref}, the sensitivity is defined as:

$$S = \frac{U(\Delta p, T_{Ref}) - U(0, T_{Ref})}{\Delta p \cdot Ue(T_{Ref})}; \quad \left[\frac{mV}{bar\ V}\right] \qquad (2.4)$$

Often the sensitivity is normed with the feeding Current I_E in mA:

$$S = \frac{U(\Delta p, T_{Ref}) - U(0, T_{Ref})}{\Delta p \cdot I_E}; \quad \left[\frac{mV}{bar\ mA}\right] \qquad (2.5)$$

In order to compare the sensitivity of different types of sensors, a standard dissipated power ($P_D = U_E \cdot I_E = 5mV$) is defined for the measurement resistors. The standardized sensitivity is therefore defined as:

$$S_{5mW} = \frac{U(\Delta p, T_{Ref}) - U(0, T_{Ref})}{\Delta p}(P_{5mW}); \quad \left[\frac{mV}{bar}\right] \qquad (2.6)$$

2.1.6.4 Temperature Coefficient of Resistivity

The temperature sensitivity is defined by the change of the total bridge resistance R_E and defines the resolution in measurement of the temperature. The temperature dependency of the total bridge resistance R_E is described by the temperature coefficient TCR_E. The coefficient is determined in discrete steps for different ranges in temperature T_i to T_{i+1} and $\Delta p = 0$.

$$TCR_e(T_m) = \frac{1}{R_E(T_m)} \cdot \frac{R_E(T_{i+1}) - R_E(T_i)}{T_{i+1} - T_i}; \quad \left[\frac{1}{K}\right] \qquad (2.7)$$

with

$$T_m = \frac{T_i + T_{i+1}}{2}$$

The distribution of the TCR_E can only be given by some discrete points within the tested range. However, a continuous curve can be defined if the measurement points in the curve for $R_E(T)$ can be modeled by a continuous function. The resulting function for the temperature coefficient TCR_E is then defined as:

$$TCR_e(T) = \frac{1}{R_E(T)} \cdot \frac{dR_E(T)}{dT}; \quad \left[\frac{1}{K}\right] \qquad (2.8)$$

Often the defined function for $R_E(T)$ can be approximated accurately by a second order polynomial. The TCR_E coefficient can therefore be modeled as:

$$TCR_e(T) = \frac{2 \cdot a \cdot T + b}{a \cdot T^2 + b \cdot T + c}; \quad \left[\frac{1}{K}\right] \qquad (2.9)$$

2.1.6.5   Temperature Coefficient of Offset Voltage

The zero pressure output $U(0,T)$ is also temperature dependent, and needs to be specified, in order to determine, if the pressure related sensor output voltage is independent or shows only a weak dependency on the temperature that can be calibrated. The coefficient is defined as:

$$TCO_I(T) = \frac{U(0, T_2) - U(0, T_1)}{\Delta T \cdot I_E}; \quad \left[\frac{mV}{mA \cdot K}\right] \qquad (2.10)$$

2.1.6.6   Long Term Stability and Repeatability

The performance of a possible sensor should be stable and showing repeatability, even when cycled through loops of different temperatures and pressures. However, a constant drift with time can be calibrated out during measurements with a high fast response aerodynamic probe, by applying an offset- and gain correction either after a certain amount of measurement time, or after concluding a certain measurement task, such as a radial traverse.

2.1.6.7   Bridge Resistance

The overall bridge resistance and the pressure sensitivity define the secondary signal conditioning devices, such as the signal output amplifier and the power supply source. Due to the complexity and time constraints in the design of a new amplifier for the development of a new high temperature probe, it is the goal to find a new high temperature sensor, that works with the existing fast response aerodynamic probe amplifier system.

Furthermore it is known, that sensors with a very high bridge resistance R_E are limited in their analog bandwidth.

2.1.6.8   Physical Integrity of the Sensor Dies

The physical integrity of a sensor dye is checked by an optical quality control of a sensor, before considering its use for assembling within a probe. This step is required, since miniature sensors, which are produced on a wafer are in a last production step sawn into their outer shape. It sometimes happens during the sawing process, that some of the sensor edges are damaged. In order to avoid a subsequent crack propagation that often starts at these damaged

positions, these sensors are sorted out and not considered for probe installation.

2.1.7 Selected Piezoresistive Pressure Transducer

Based on the previously discussed selection criteria, a new differential pressure transducer showing a higher maximum temperature range is used in the present work. The new transducer, PRPT-HT (Fig. 2-4), is extensively tested in order to check the criteria as presented in chapter 2.1.6. Some of the characteristics are compared in Table 2-1 to the traditional low temperature sensor as used for first generation FRAP.
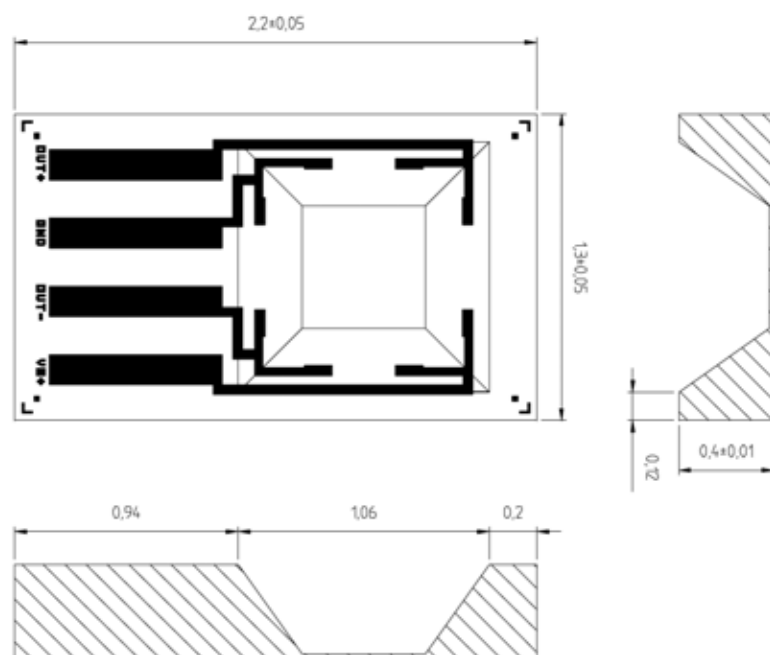
Fig. 2-4   High temperature piezoresistive pressure transducer PRPT-HT.

The sensor is based on monocrystalline silicon and intentionally is not designed for high temperature applications. However, the manufacturer used the newest microfabrication techniques, which in principle support an application at higher temperatures. In order to assess, if the sensor works for increased temperatures, initial characterization tests up to 463K (limited by the manufacturers equipment) have been conducted at the manufacturers site and are presented in Fig. 2-5 and Fig. 2-6.

	P788	PRPT-HT
Dimension (L x W x H) [mm]	1.7 x 0.6x 0.15	2.2 x 1.3 x 0.4
Technology (monocrystalline Si)	Yes	Yes
max. operation Temp.	393K	473-533K
Operation mode	differential	differential
No. of resistors on membrane	4	4
Bridge resistance R_E	$\approx 5.2 k\Omega$	$\approx 3.4 k\Omega$
Pressure Sensitivity S_I for I_E= 1mA [mV/mA bar]	≈ 70	≈ 39
Pressure Sensitivity S_{5mW} for P_D= 5mW [mV/bar]	≈ 67	≈ 84
Specific linear pressure range [mbar]	400	400
Excitation Voltage Ue_{5mW} for P_D= 5mW	$\approx 5.1V$	$\approx 3.4V$
Mean TCO_I [mV/mA K]	0.002	0.025

Table 2-1   Characteristics of traditional FRAP sensors (P788) versus new high temperature sensor PRPT-HT.

In terms of standardized pressure sensitivity S_{5mW}, the new pressure transducer exhibits advantageous behavior compared to the traditional sensor. Furthermore, due to the lower bridge resistance, the dissipated power within the probe will be reduced. This provides an advantage in measuring the gas temperature accurately since the erroneous influence due to sensor self-heating is of minor strength.

The TCR_e coefficient distribution (Fig. 2-5) for the new transducer is slightly higher than for the previously used P788 pressure transducer (mean value of 2300 ppm/K). The sensitivity in measurement of the temperature is therefore slightly higher for the new pressure transducer, which theoretically improves the resolution in measurement of the temperature. However, there are additional effects, such as coupling effects during packaging, which play a role due to the higher temperatures the probe is exposed to. The final capability in accurately measuring flow temperatures will be further discussed in chapter 3 of this thesis.

The mean TCO_I coefficient is calculated from the zero pressure distribution

in Fig. 2-6. The coefficient is an order of magnitude higher, which is related to the sensor behavior at higher temperatures. The PRPT-HT sensor therefore has a slightly stronger coupling between the temperature and pressure. This is mainly related to the behavior at the upper temperature limits, where coupling effects are stronger. However, since the behavior is fully repeatable and shows no evidence of hysteresis, these effects are taken into account during a combined pressure-temperature calibration (steady sensor calibration).
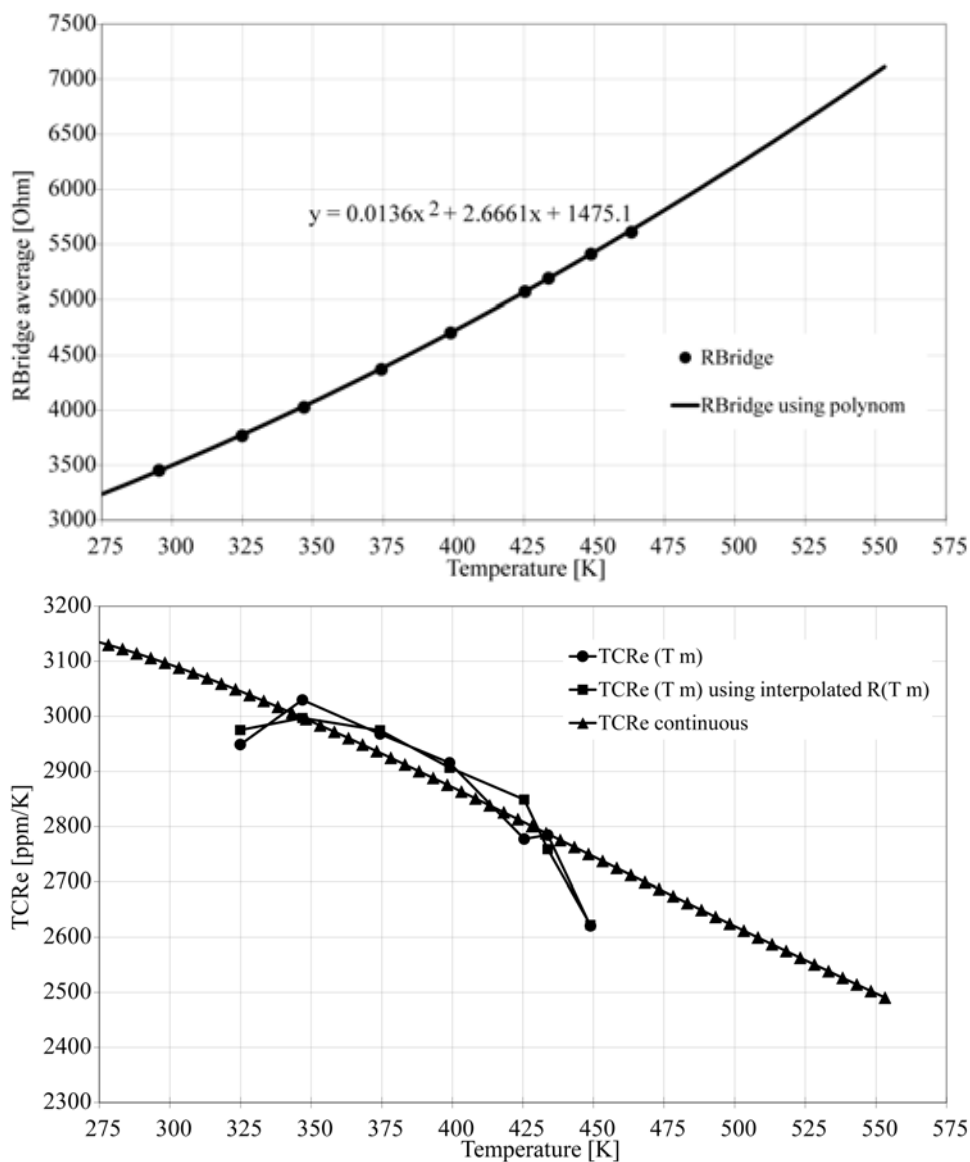
Fig. 2-5   *Distribution of the bridge resistance R_e (top) and TCR_e (bottom) for a PRPT-HT pressure transducer.*
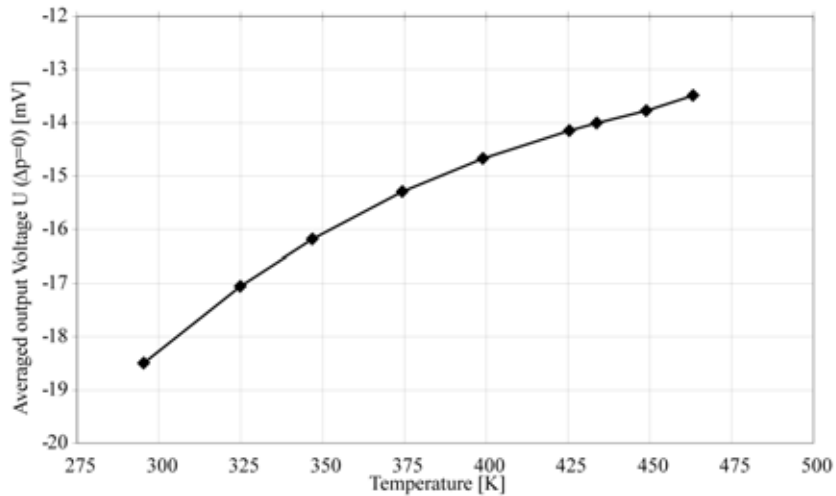
Fig. 2-6   Averaged output voltage U(Δp=0) for a PRPT-HT sample.

2.1.7.1   Pressure Sensor Characteristic

After the preliminary sensor characteristic test, the characteristic of the sensor when packaged under "real" conditions needs to be addressed. Therefore, samples of the PRPT-HT test dies are mounted on transducer outliners (TO). The TO's are built with a reference pressure opening at the bottom. The transducers are installed on the TO on top of this through-hole. Furthermore, sealing to the TO surface is accomplished with a silicone adhesive (red) (more details see chapter 2.3). By that, a differential pressure can now be applied over the transducer membrane.

The signal transmission from the sensor is done through aluminum wedge bonds between the sensor pads and the TO connectors. Some details about wire bonding techniques are discussed in chapter 2.2.1.
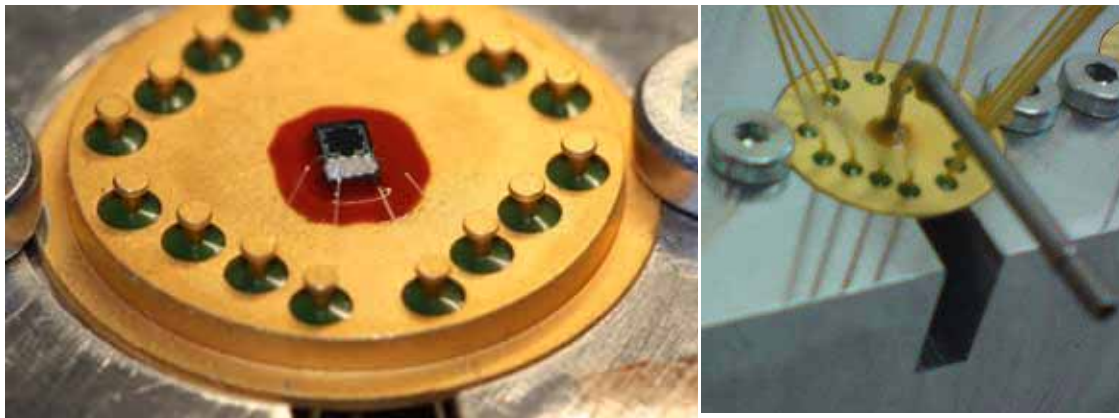
*Fig. 2-7   High temperature piezoresistive pressure transducer PRPT-HT
mounted on a transistor outliner (TO); rear view of a TO (right).*

The TO's then are installed in an inhouse developed pressure chamber (Fig. 2-8, left), which is placed in our Laboratory sensor calibration oven facility (Fig. 2-8, right).

Fig. 2-8   *High temperature sustainable pressure chamber (left), to be positioned within our laboratories sensor oven facility (right).*

Due to space limitations, specially designed high temperature feedthroughs are used for signal transmission (output signal as well as sensor power supply). The feedthroughs guide the signal out of the pressure chamber, and in a next step out of the oven facility. From there, these signals are fed into the data acquisition system (DAQ). For statistical evaluation, up to nine transducers can be installed and tested in parallel within the pressure chamber.

The signals are acquired using a 24-bit acquisition board that provides a resolution of 1.19×10^{-6}V of the measured sensor signals. The pressure is delivered to the chamber by a pressure controller (type: Druck DPI 520) that has a relative uncertainty of 0.05% over full scale. The calibration facility is pre-programmable and the data acquisition is fully automated.

The applied pressure and the temperature can be continuously varied in a range between 0 to 1bar and 298 to 533K, respectively, with temperature fluctuations of less than ±0.02K. A thermocouple (type: PT100), is installed in close proximity to the sensors within the pressure chamber and is used to measure the temperature within the chamber. The maximum measurement uncertainty is ±0.01K. The waiting time between two temperature steps is based on the measured transient behavior of the temperature within the chamber. The pressure cycling starts when the temperature variations are smaller or equal to ±0.02K around the target temperature. The temperature settling time is strongly dependent on the thermal inertia of the pressure chamber. Fig. 2-9 shows a fraction of the temperature history of a typical sensor characteristic cycle. The temperature's settling time is about 110

minutes for temperature steps of 15K.
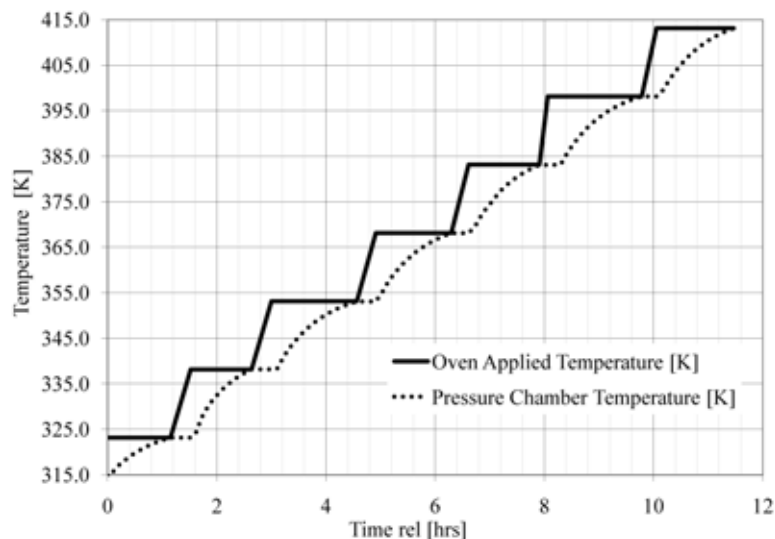
Fig. 2-9   *Typical temperature history of an automated transducer character-*
            istic test.

For all characteristic and performance investigations, the test dies are powered by a constant feeding current of 1mA. This specified feeding current corresponds to the feeding current in the final probe application. Fig. 2-10 shows the resulting characteristic for one of the purchased PRPT-HT transducers. The left hand part of Fig. 2-10, presents the output voltage *U* and the right hand part of Fig. 2-10 presents the output voltage *Ue*. Both voltage are presented as a function of applied temperature and pressure respectively.

The first tests are performed in a temperature range from 313K to 473K. The final probe characteristic, ranging even up to 533K, will be presented and discussed in chapter 3.

The temperature related excitation output voltage *Ue* shows no coupling to the pressure over the ranges of investigation. In terms of the output voltage *U*, which is mainly a function of the pressure and in the ideal case is decoupled from the temperature, a slight coupling is observed starting at around 340K and is more pronounced for differential membrane pressures above 300mbar. This is mostly related to packaging of the sensor. In order to differentially pressurize the transducer membrane, the sensors are packaged onto the TO using a silicone adhesive. Although the low viscosity of the silicone should minimize any kind of mechanical induced stresses on the sensor membrane, the stresses can not be completely avoided.

Another change in the trend of curvature is observed in the pressure related output voltage at temperatures around 460K. Since the available transducer is

not based out of polycrystalline silicon, nor based on the SOI transducers characteristic SiO_2 insulator layer, a leakage current flow from p-type silicon elements into the n-type diaphragm material is expected above a certain temperature. However, the behavior of the sensor when packaged within the high temperature fast response aerodynamic probe, can slightly differ from the first characteristic tests. The applied steady sensor calibration procedures for the assembled probe and the way to deal the non-linear effects, will therefore be addressed in chapter 3.3.1.
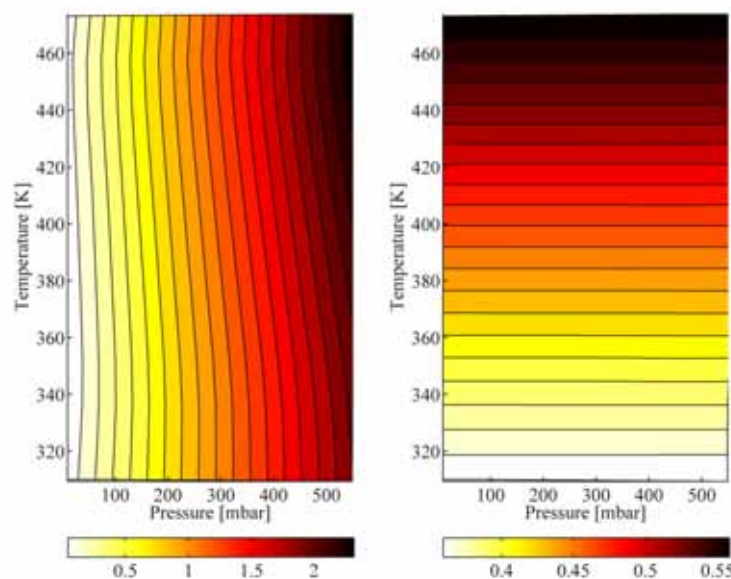
Fig. 2-10   Resulting characteristic of PRPT-HT transducer. U (left) and Ue (right) in Voltage [V] as a function of temperature and pressure.

During the sensor characteristic tests, a total of nine sensors have been tested in parallel. All nine sensors show the same and repeatable characteristics. These are presented in Fig. 2-11 for two transducer samples, each cycled three times between 308K and 473K. The change of the sensor pressure sensitivity is presented in percentage relative to the sensitivity at 308K. The difference in sensitivity at ambient conditions between the different samples was less then 0.3mV/bar·mA. The mean sensitivity of the new transducers, resulting out of the characteristic tests is 38.96mV/bar·mA with a standard deviation of 3.20mV/bar·mA. This measured sensitivity is as expected from the specification sheet presented in Table 2-1. In terms of standard deviation between different cycles, as well as between different test samples, the new sensor is much more stable (both in terms of repeatability, as well as between different samples) compared to the previous transducer (P788, standard deviation of 11.4mV/bar·mA).

The consistency between the PRPT-HT transducers is related to the fact,

that state of the art and therefore most accurate microfabrication techniques have been used in the process flow chain. Another reason for this consistency in the characteristic can be explained by the way, the sensors have been purchased. Since the sensors have been purchased in small quantities as single dies and not on a wafer, the manufacturer conducts quality control of every single die, before delivery.
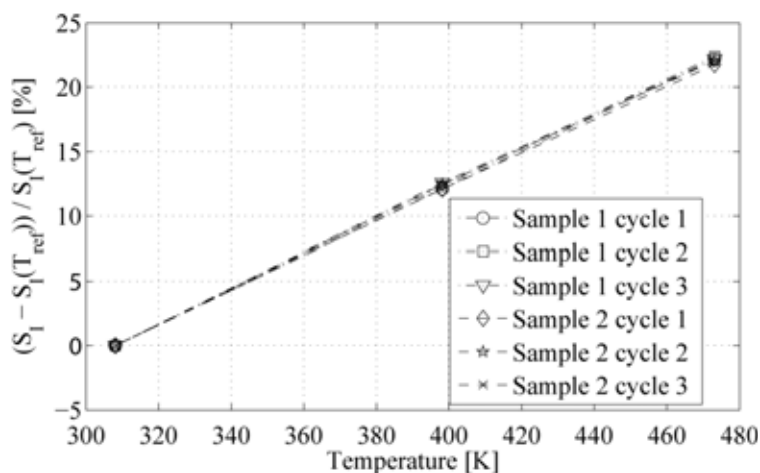
Fig. 2-11   Sensor pressure sensitivity S_I in percentage relative to the sensitivity at the start point at 308K for two of the test samples, each cycled 3 times.

2.2   Signal Transmission

Signal transmission summarizes the connections between the pressure transducer and the external power supply and amplifier respectively. Since the signal between the transducers is not amplified until it reaches the rear side of the probe where the amplifier is installed, the requirements for these connections is very high. The connections must survive high temperatures and high levels of vibrations, should show a neutral electromagnetic behavior and should be simple to handle.

The high temperature related challenges in terms of signal transmission can be split into two parts of the probe. One part which is exposed to the high temperatures since immersed into the hot gas flow, and the other part which is not directly in contact with the hot gases and outside the casing of the turbomachine, but still needs to be handled in order to figure out if thermal issues emerge.

- The first identified part is basically the probe tip and deals with the signal transmission of all the components within that part.

- The second identified part is the back-end of the probe, where the electronic amplifier is positioned. The amplifier and its electronic subcomponents have a maximum temperature of operation of around 353K. This topic will be further addressed in the design and assembly of the high temperature FRAP probe in chapter 3.

In this sub-chapter main focus is set on the first part of the probe. All the signal transmission related components within the probe tip are exposed to high temperatures and special care needs to be taken in order to ensure the operability and a long life-time of these components.

2.2.1   Wire Bonding

Wire bonding is the primary method of making interconnections between an integrated circuit (IC) and a printed circuit board (PCB) during semiconductor device fabrication. Wire bonding is generally considered the most cost-effective and flexible interconnect technology, and is used to assemble the vast majority of semiconductor packages. Bond wires usually consist of either aluminum, gold or copper. Depending on the wire material, there are different bonding techniques available. The most common one, ball bonding [70] usually is restricted to gold and copper wire and usually requires heat. Wedge bonding [71] can use either gold or aluminum wire, with only the gold wire requiring heat. In either type of wire bonding, the wire is attached at both ends using some combination of heat, pressure, and ultrasonic energy to make a weld. In terms of low lot sizes or prototyping, ball bonding is the most widespread, since it allows a lot of flexibility.

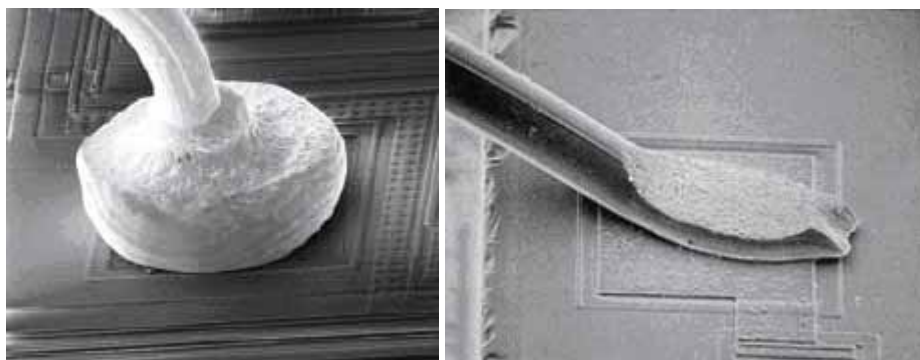*Fig. 2-12   Gold ball bonding connection (left), versus aluminum wedge bonding connection (courtesy of WestBond Inc.).*

The main advantage in using gold ball bonding is the flexibility in re-orienting the second bond stamp in any direction after positioning the first bond on the device (due to ball symmetry). This is not the case for the wedge bonding process, where the direction of the second bond must already be taken

into account when making the first bond (see examples of the bonding schemes for the two techniques in Fig. 2-12).

More than 90% of existing piezoresistive pressure transducers have AlSi alloy bonding pads embedded. These pads are used as the interface for the electronic connection to any power supply and signal-conditioning device. The use of the classical gold wire bonding to the aluminum sensor pads is known to be critical for high temperature applications due to the formation of gold-aluminum intermetallic compounds and associated Kirkendall voids [72, 73]. The compounds are typically referred to as "purple plague" [72-76]. This term comes from the characteristic color of the $AuAl_2$ intermetallic compound that often occurs around the perimeter of Au bonded on an Al pad [77-79]. In general, such compounds occur if the time-temperature product is large enough (typically 448K for 5 to 6 hours) and grow at any time when high temperatures are encountered during the life of the device. The temporal change of the interface area due to an evolving formation of the intermetallic compounds makes the connection more brittle, but also influences the local resistance. In the worst case this leads to a loss of connection. In order to avoid the formation of intermetallic compounds, a new method to electrically connect the sensors has to be developed.

High temperature long-running tests are performed within the oven facility at 533K. In order to simulate the later application, the electronic measurement chain of a fast response aerodynamic probe was built and installed in the oven facility.

The measurement chain consists out of a AlSi alloy sensor bonding pad, the wire bonding connection to a flexible circuit board (flexprint) and the high temperature soldering connection between the flexprint rear side and the cable, including around 55cm of high temperature cable (see chapter 2.2.2 for information about the flexprint device and the high temperature cable). The front area of the test arrangement is shown in Fig. 2-13.

Fig. 2-13   Specimen of dummy sensors, connected via wire-bond (black lines) to the flexprint pads for bonding characteristic tests.

In total nine samples are prepared and divided into three groups. Every

group therefore contains samples of exactly the same type. The differences between the three groups are only related to the wire bonding in the front area between the sensor samples and the flexprint pads. One group of samples is built by using traditional gold wire bonding (Fig. 2-12, left). A second group is used by connecting the sensor by aluminum wedge bonding to the flexprint (Fig. 2-12, right). The third group is again based on Al wedge bonding, but additionally, the pads of the flexprint are polished to reduce the gold layer on the flexprint pads and therefore avoid any intermetallic compounds between gold and aluminum.

In the short term thermal cycling tests, no difference has been observed between the nine samples. However, that changed during the long-term tests at 533K. All the samples within a given group showed the same behavior. The mean value per group is therefore taken and presented in Fig. 2-14. The plot shows the change in resistance with time for the three groups. It can be seen, that all the six samples, connected by aluminum wedge bonding, show a slight increase in resistance with time (around 0.4 Ohm in 70 hours). In relation with the overall piezoresistive transducer bridge resistance of around 3.4 kOhm, this change of resistance is of minor influence to a later application. However all the samples within the group based on gold ball bonding connections, showed a stronger and nonlinear increase in circuit resistance after being exposed to the high temperatures for around 40 hours.
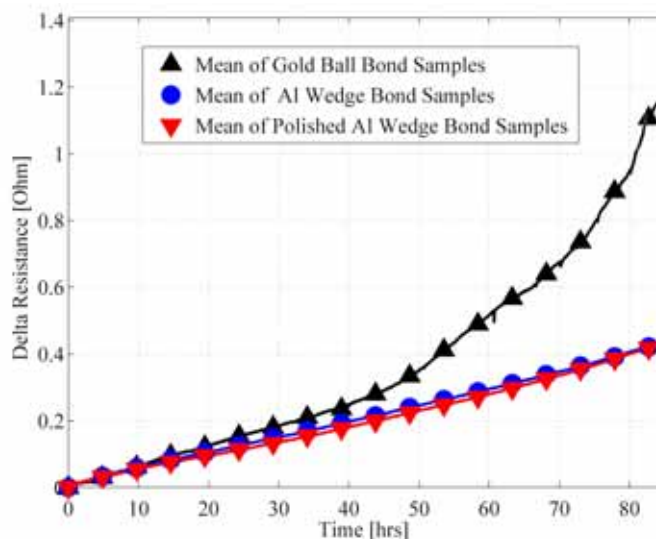

Fig. 2-14   Long-term results of combined wire bonding tests, connected to the DAQ board by a flexprint and the high temperature cable.

The more pronounced increase in resistance could be a sign of an evolution in formation of intermetallic compounds (purple plague, $AuAl_2$). If the

samples would be further expose to such high temperatures, the internal resistance would further increase in a nonlinear manner and at a certain point result in a loss in connection. The use of traditional gold wire bonding to connect the transducers with the flexprint is therefore avoided in a new high temperature fast response aerodynamic probe. Although more complex to apply and of less widespread use in industry, aluminum wedge bonding between the sensors and the polished flexprint pads is used. The complexity in applying wedge bonding is mainly related to the limitations in flexibility of directing the bonds after positioning the first stamp in the wedge bonding technology. This has an influence on the handling of the sensors during the later steps of probe installation and therefore requires TO's with connection points aligned to the direction of the final installation of the wires (more or less parallel to the transducer length axis).

2.2.2   Flexible Circuit Board (Flexprint) and Electric Signal Cable

Due to the small dimensions of the pressure transducers, a direct soldering to contact the sensor pads with the power supply and the signal output connection is not possible. Since the probe head needs to be of miniature size, the use of bonding pads right next to the transducers is not possible, due to space limitations. However, the contact can be done further away from the probe tip towards the probe rear side. In order to provide a high quality signal transmission, a flexprint, based on two identical, but mirrored parts is designed. Its dimensions are 90mm in length, 0.5mm in width and 0.11mm in thickness. The front end of the flexprint contain pads to provide for wirebond contact the sensors (see CAD view in Fig. 2-15). On its rear side, soldering pads are embedded (1.2mm x 0.4mm) such that signal cables can be used to make contact from the transducer on the electronic devices in the probe rear side. The base material of the flexprint is kapton, with signal lines embedded in it. The maximum working temperature of such a print is about 533K. The signal lines, based on copper, are finished with a gold layer on the pads, to prevent oxidation of them.

In order to prevent possible gold - aluminum interfaces, right before wedge bonding from having contact with the transducer pads on the flexprint pads, the flexprint pads are chemically treated and mechanically polished. This provides a reduction of the gold layer (down to the copper layer) on the flexprint pads and therefore prevents a loss of connection. However, special care is needed in doing this micro processing due to the small sizes involved in the process. Furthermore, the polishing should not be done much before applying the wedge bonding, since copper reacts with moisture in the humid

air to form a non-bondable oxide layer.
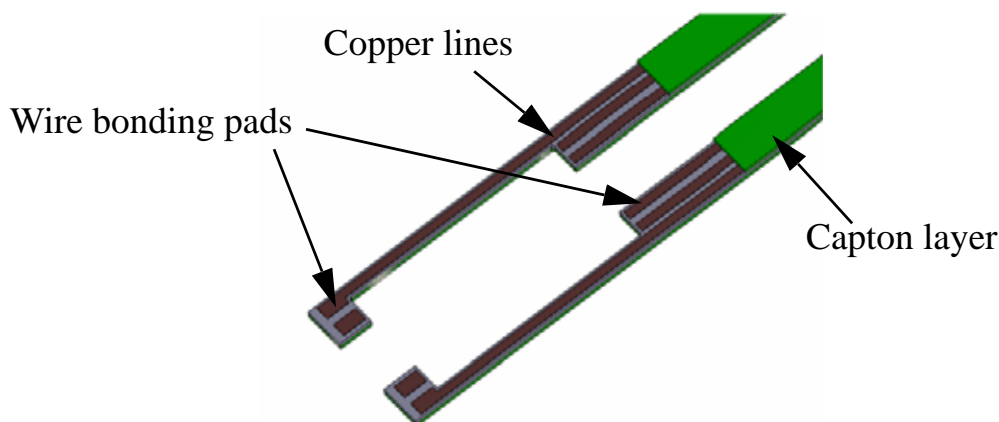
Fig. 2-15   3D CAD front area view of Flexprint (Flexible circuit board).

The electric cable used to connect between the back end soldering pads of the flexprint and the rear-side of the probe needs to withstand 533K in the worst case scenario. At the same time the maximum outer diameter of the cable must be in the range of 1mm, containing four stranded conductors and must be shielded to electromagnetically protect the raw and unamplified sensor signal. The number of available cables on the market that fulfill all these requirements is very limited. Thus we finally ended up with only one possible high temperature teflon cable, that met our needs.

Since the electrical resistance of a conductor such as a copper wire is dependent upon collisional processes within the wire, the resistance is expected to increase with temperature since there will be more collisions. Expressed in terms of the resistance at some standard temperature from a reference table, the equation is:

$$R(T) = R(T_0) \cdot (1 + \alpha \cdot \Delta T) \qquad (2.11)$$

Thermal cycle tests have been performed to characterize the flexprint behavior in combination with the solder cable of the length as used for a standard aerodynamic. At ambient temperatures, the measured and calculated resistance was around 6 Ohm. The observed and measured change in resistance between 293K and 533K is again around 6 Ohm, resulting in a total resistance of 12 Ohm at 533K. This value is in good agreement with the results of an analytical approach (using for copper $\alpha = 43 \cdot 10^{-4}$ 1/K and a ΔT of 513K).

2.3   Material Science

In terms of packaging, the piezoresistive miniature silicon pressure sensors are directly embedded into the probe shaft. For a high temperature range of application it is very important to mechanically decouple the sensor from the base substrate in order to reduce mechanical stresses on the sensor membrane caused by the different thermal coefficients of expansions of the materials.

Bolger et al. [80] found an analytical expression for the maximum induced tensile stresses in the transducer edges, based on how they are packaged. It shows, that several factors can significantly influence the thermally induced stresses. The most important of these parameters that contribute to reduce the stresses are as follows:

- Increasing the thickness of the adhesive layer between the sensor and the substrate (probe wall)

- Reducing the contact lengths between the sensor and the substrate. This is given by the sensor dimension and can not be reduced, since the complete transducer bottom area needs to be in contact with the adhesive in order to ensure a sealed packaging.

- Use of procedures and materials with low Young's moduli.

- Use of substrate material with similar thermal coefficients of expansion as the silicon transducers.

However, there is no standard product that is on the market, which fulfills all the criteria mentioned above and at the same time is able to withstand the high temperatures. Therefore, an alternative way to pack the sensors is developed. Extensive material research and survival tests have been performed. Furthermore, a broad variety of possible packaging components have been applied to transducer test specimen in order to investigate the variation in viscosity with temperature and time. The resulting output signal for varying temperatures can be linked to the strength of the thermally induced mechanical stresses and therefore allows one to draw some conclusions on the feasibility to use the specific product for packaging in our application.

A dual component RTV (room-temperature cross-linking) silicone elastomer able to withstand temperatures up to 533K showed the best performance and is used as a soft bonding agent. This silicone elastomer showed the best performance in terms of temperature resistance, long term stability, sealing and adhesivity properties, as well as in terms of a constant low viscosity that minimizes the thermally induced mechanical stresses on the

transducer membrane.

But not only packaging the sensor with a silicone adhesive is an issue for high temperature material. Due to the fact, that the pressure sensor die works as a differential sensor, after assembling and when closing the probe cover, hermetic sealing must be ensured, such that no pressure loss occurs over the membrane. Hermetically sealing the probe is achieved by a dual component epoxy, that is able to withstand temperatures up to 573K.

3   High Temperature Fast Response Aerodynamic Probe (FRAP-HT)

As discussed before and in chapter 5.2, the application of FRAP technology has been limited to flow temperatures not exceeding 393K [18, 20, 21]. The main limiting factors in terms of temperature are related to sensor limits, reduced signal-to-noise ratios, packaging issues, material issues and electrical connections to the sensor as discussed in chapter 2. This chapter now presents the design, assembly and extensive calibration of the newly developed miniature high temperature fast response aerodynamic probe (FRAP-HT) which can be applied in flows with temperatures up to 533K (500°F). Furthermore probe thermal issues as well as probe vibration issues are detailed.

3.1   Design

The focus in the design of the new probe was set on the probe tip, since it contains the primary element of the probe and must fulfill the need of measuring flow properties such as angles, total and static pressures, as well as Mach number in an unsteady manner. A close up view of the probe tip of the new developed FRAP-HT probe is presented in Fig. 3-1.

Fig. 3-1   Close -up view of FRAP-HT probe tip compared to a match for scale comparison.

Further, the probe contains an additional two sensors located 100m behind the tip of the probe. These two sensors, including their use and installation are discussed in more detail in chapter 3.2.2. Furthermore some electronic components are embedded in the probe box located at the back-end of the probe for signal conditioning and supplying power to the different sensor devices. In Fig. 3-2 an overview of the complete probe is given, including some of the dimensions and the three parts of interest: tip (detail A), secondary sensor area (detail B) and electronic signal conditioning unit (detail C).
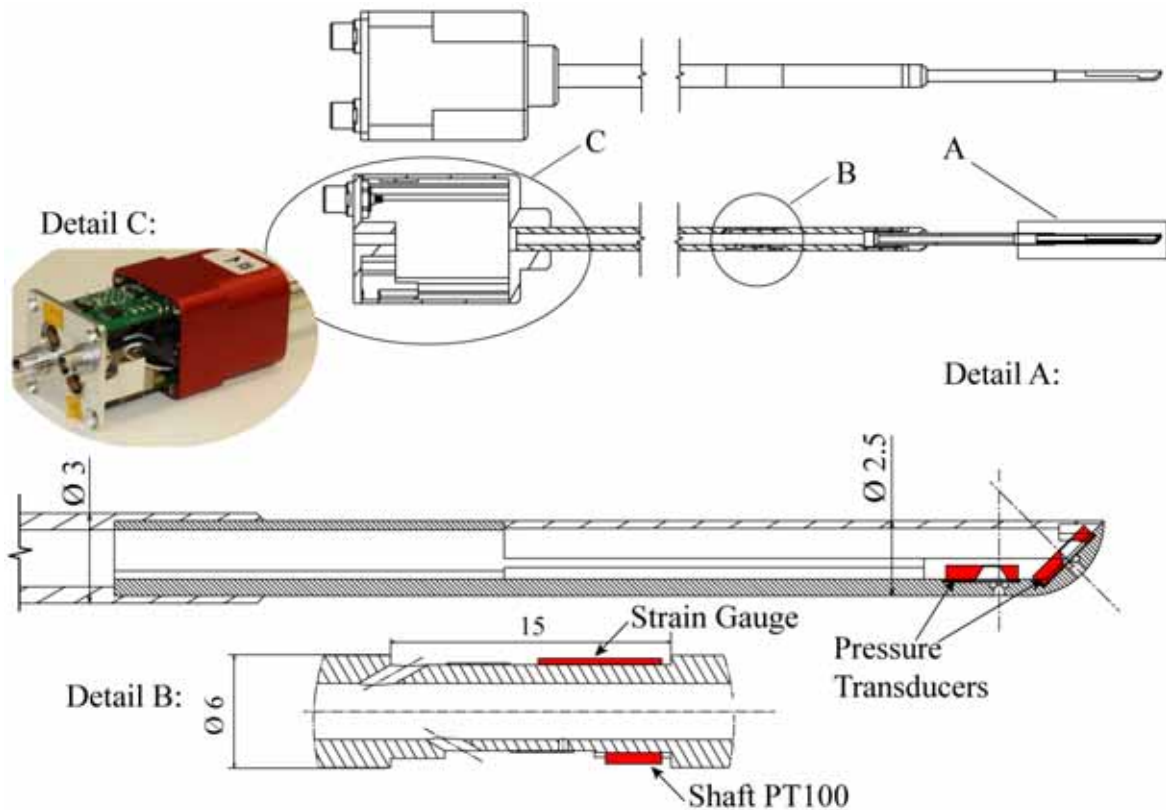
Fig. 3-2 Sketch of complete probe, including local zoom on tip area, area of the secondary sensors, 100mm behind the probe tip, as well as probe box for electronic signal conditioning devices.

In order to avoid blockage effects and therefore reduce induced measurement errors in an unknown flow field, it is necessary that the probe tip be miniature in size and therefore the probe size is the driving design parameter. On the other hand, the achievable probe tip diameter is influenced by other factors, such as mechanical producibility, dimensions of involved sub-components and structural mechanical stability. In terms of involved sub-components, the limiting factor for a further reduction of the probe tip diameter is related to the dimensions of the high temperature piezo-resistive pressure transducers used for the FRAP-HT probe as discussed in detail in chapter 2.1.7.

An optimization procedure has therefore been performed to iterate on these constraints. The procedure starts from the concept of designing the probe in a first step by means of computer aided design (CAD) software. The focus in this step is to set the minimum probe diameter by taking into account the dimensional boundaries of the associated sub-components. Moreover, this step involves also an assessment of the mechanical producibility for the different probe components, as well as a study of the feasibility of assembly. In a second step, a structural mechanical analysis is performed using finite element methods (FEM). The results from the FEM analysis are then used to optimize the involved mechanical parts, in order to reduce the mechanical stresses that are induced due to the applied thermal and mechanical loads occurring in a high temperature, high dynamic head flow field. The complete procedure has been performed twice, resulting in the final design of the FRAP-HT probe as presented in Fig. 3-2.

The resulting probe tip has a diameter of 2.5mm. The two miniature silicon piezo-resistive pressure transducers (see red parts in detail "A" of Fig. 3-2), located in the probe tip, are glued above their respective pressure taps. The pressure tap related to the yaw angle is 3.5mm from the probe tip at an angle of 0°. The pitch sensitive tap is located 0.73mm from the probe tip and at an angle of 45° from the probe axis on a shaped probe head.

In order to protect the sensors within the probe even in particle-laden flows, the pressure taps below the transducers are not designed as simple through-holes, but as a multi cavity system. This prevents any damage to the probe tip and the sensors due to particle impact. Nevertheless, on the outer surface of the probe tip, the taps have a circular shape with a diameter of 350μm.

The pressure tap and the probe tip body are electro-eroded in order to realize their small size and to provide high accuracy ($\pm$0.1μm) in the machining. This aspect of the probe design has a significant impact on the probe aerodynamics and measurement bandwidth. The reduction of the pressure tap volume is a key parameter to yield a high frequency measurement bandwidth as the eigenfrequency of the pneumatic cavity will affect the pressure sensor dynamic response. This issue will be discussed and quantified in the dynamic response section (chapter 3.3.5) of this thesis.

Detail "B" of Fig. 3-2 presents the part of the 6mm diameter probe shaft, located 100mm behind the probe tip, where the secondary sensors are installed. The sensors are embedded in a slot around the circumference of the probe shaft. The slot depth is 0.5mm and the circumference is separated into two parts in order to embed a strain gauge sensor on one of the semi-

cylindrical planes, and a PT100 temperature sensor on the other semi-cylindrical plane. The strain gauge sensor is used to monitor probe shaft vibration. The temperature sensor in the shaft is used to monitor the heat flux through the probe shaft.

The probe has two interfaces, where the probe shaft diameter changes. The first interface is located 28mm behind the tip, where the probe diameter changes from 2.5mm to 3mm. Further back from the first interface (34mm) is the second interface located, where the probe diameter changes from 3mm to 6mm. The different interfaces are designed such that the shafts are decoupled electrically, as well as thermally. This is done by using epoxy and macor interfaces. Both materials are electrically non-conductive and have a very low thermal conductivity (0.3 and 1.46 W/m K respectively).

Detail "C" of Fig. 3-2 shows the amplifier box, located at the rear side of the probe. The amplifier box provides for the signal conditioning electronics of the pressure transducers. Furthermore it provides four connector sockets to connect the probe sensors (2x pressure, 1x strain gauge and 1x shaft PT100) to the measurement system as presented in chapter 4.

3.1.1   Effect of Thermal Loading

Some of the components used in the FRAP-HT probe have a reduced temperature range of operability. The main limiting component is the amplifier and its electronic subcomponents, located in the probe box at the back-end of the probe. The maximum temperature of operation of these components is around 353K.

A conjugate heat transfer analysis is performed in order to investigate if active cooling of the electronic components is required in case of measurements in high temperature flows of up to 533K. The setup of the simulation has been done for measurements in LISA, as sketched on the bottom-right of Fig. 3-3. The left hand side of Fig. 3-3 presents a sketch of the front area of the FRAP-HT probe and identifies the components that are included in the conjugate heat transfer analysis.

For the simulation, the complete probe was meshed from the tip, to the end, including the amplifier box. The resulting mesh density for the probe is given in Table 3-1. Furthermore, bounding boxes around the probe proximity are defined and included into the meshing procedure of the simulation. Three main domains are defined for this purpose. The first domain within the turbine channel, where the flow parameters are defined by harsh flow conditions such as 533K and high Mach number flows (*Ma=0.7*). The second domain is

defined by the turbine casing, and the sealed probe tower, as presented in Fig. 3-3. Adiabatic walls are defined as boundary conditions for this domain. Finally, as a last domain, the volume around the 6mm diameter probe shaft outside of the casing including the amplifier box is defined. Ambient pressure and temperature has been set as dominant boundary conditions for this domain. The resulting mesh densities for the three domains around the probe are also listed in Table 3-1.
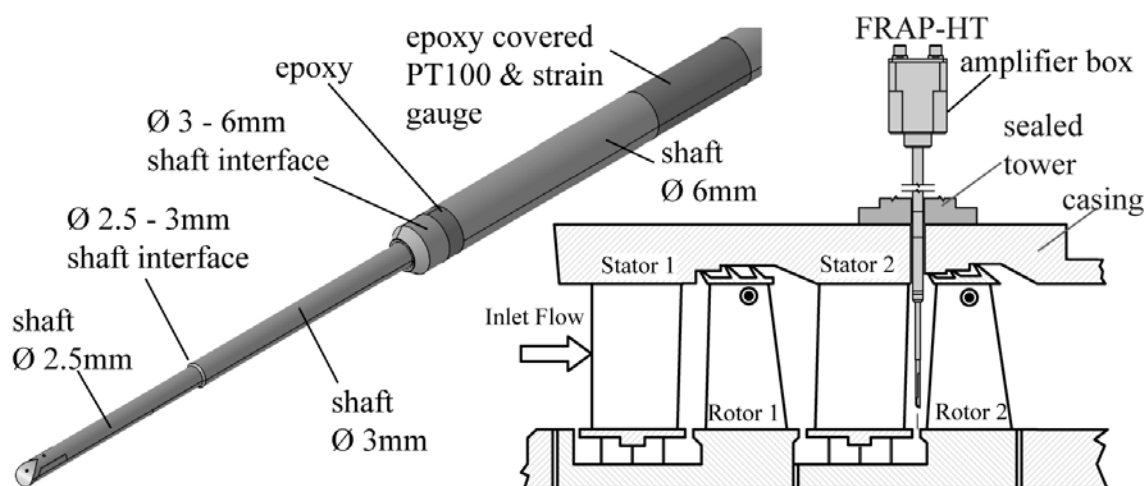
Fig. 3-3   Details on simulated FRAP-HT probe parts (left) and general probe setup for measurements.

What:	Node Number	Element Number
2.5mm probe tip, including all components within the tip (sensors, flexprint,..)	1'386'627	5'138'601
3mm shaft	174'263	618'353
3mm to 6mm shaft interface	165'228	561'769
Epoxy interfaces	129'936	465'609
6mm shaft	709'924	2'706'191
Amplifier box	1'343'951	5'456'699
turbine flow bounding box	428'717	1'773'408
casing bounding box	382'935	1'601'278
ambient domain bounding box	847'621	3'963'390
TOTAL	5'569'202	22'285'298

Table 3-1   Mesh details for FRAP-HT conjugate heat transfer analysis.

An additional boundary condition related to heat dissipation due to Joulean

heating is defined on the membrane surface of both piezo-resistive pressure transducers. Each of the sensors emit heat due to the electric feeding current that passes through the bridge resistance. In terms of the used sensors, the dissipated power of every sensor is 3.4mW.

Due to the complexity of the geometry as well as due to the large differences in length scale for the different components to be meshed, a wholly tetrahedral mesh did not show good results, especially near the boundary areas of the different domains. Even though it required a lot of effort, and an increased number of elements for the model, the quality of the meshing as well as of the results were improved by defining a triple layer of prism elements at all the surfaces of the model.

The results showed, that the maximum temperature in the amplifier box always is below a safety included critical temperature for the electronic components of 343.15K. Therefore no special cooling is needed for the electronic components.

3.2   Sensor Packaging

The sensor packaging and bonding techniques are related to MEMS technology and ensure an optimal spatial resolution, measurement bandwidth and protection of the sensors in the harsh environment of turbomachines. Moreover the gluing and bonding techniques must provide high degree of reliability and low disturbance to the sensors as the probe can experience large temperature and pressure fluctuations. The challenges as well as the resulting concepts and materials involved in embedding the selected piezo-resistive pressure transducers into the FRAP-HT probe have been addressed in chapter 2.

This sub-chapter will now focus on a few aspects directly linked to the assembly procedure of the different sensor devices into the FRAP-HT probe.

3.2.1   Pressure Sensors Installation

Before installing any sensor into a FRAP-HT probe tip, the characteristics of the respective sensors are checked. This requires that the sensors be connected such that their general properties can be evaluated. Transducer outliners (TOs) are used to perform the sensor selection. Therefore the different transducers are temporary mounted on the TOs and then connected to four of the TO connectors by the wedge bonding procedure. In the later installation, the bond wires are resolved on the TO pad side, but kept installed

on the side of the sensors.

As discussed in chapter 2.2.1, the wedge bonding process provides no flexibility to re-orient the second bond stamp after positioning the first bond on the device. The direction of the second bond must therefore already be taken into account when making the first bond. The required orientation of the different bonding wires for the later installation of the two pressure transducers is investigated by means of a 3D CAD model and resulted in specifications for the temporary installation of the sensors on the TO's (see Fig. 3-4).
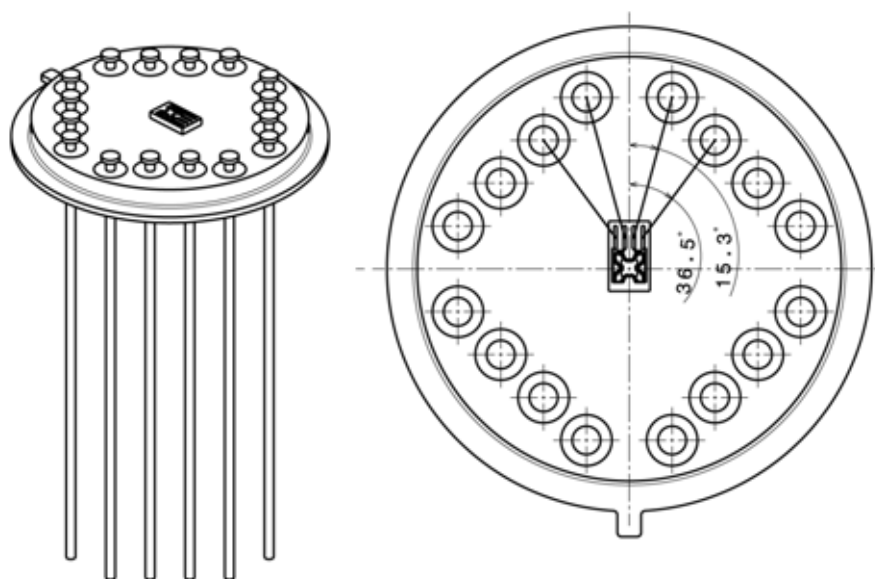
Fig. 3-4   TO, including wire bonding orientation specification for later probe installation.

As shown in Fig. 3-2, the miniature silicon piezo-resistive pressure transducers are then encapsulated into the probe shaft above the respective pressure tap. In order to reduce thermally induced stresses on the sensor membrane, the transducers are installed using a dual component RTV silicone elastomer.

The free end of the transducer bonding wires are in a next step grabbed and connected to the flexible printed circuit (flex print) that leads the signals to the amplifier.

The pressure sensor die operates as a differential sensor. After installing all the components into the probe (Fig. 3-5), hermetic sealing of the tip must be ensured, such that no pressure loss occurs over the membrane. Hermetically sealing of the probe is achieved by closing the probe tip with the respective tip cover by means of a dual component epoxy, that is able to withstand

temperatures up to 573K.

Fig. 3-5   Probe Tip pressure sensor installation view.

3.2.2   Probe Shaft Temperature and Strain Gauge Sensor Installation

3.2.2.1   Strain Gauge Installation

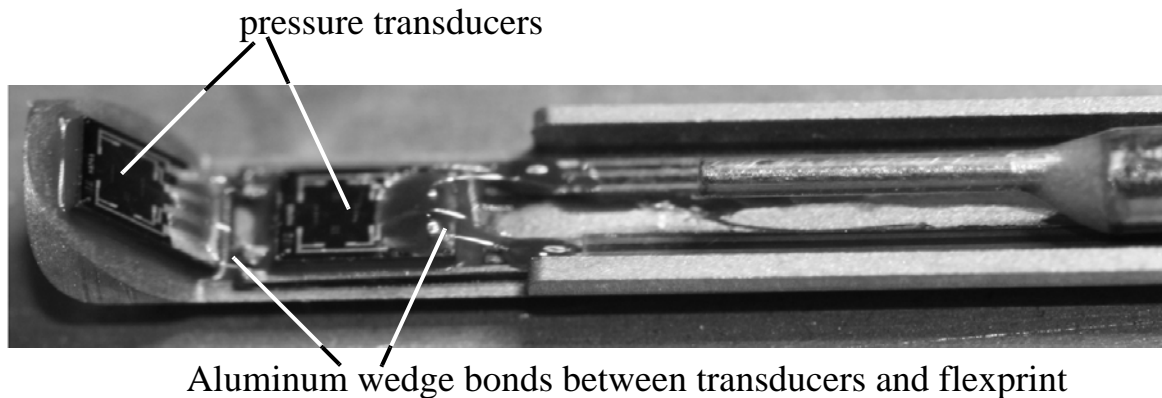An additional research objective related to higher flow temperatures and harsh industrial turbomachinery environment is set to the probe robustness. An integrated probe shaft vibration measurement system is developed, such that the probe is fully operative even in high dynamic head flows with strong periodic fluctuations.

The sensor used to detect any probe vibration is a standard fully encapsulated single strain gauge with polyimide encapsulated ribbon copper leadwires and is self-temperature-compensating. The strain gauge overall dimensions are 6.6mm x 4.1mm with a thickness of 0.05mm. The lead wires are 2cm and small terminals are used as an interface between the gauge device and the extension to the bridge circuit by twisted miniature copper wires.

The bondable terminals are produced from 0.036mm thick copper foil, laminated on a 0.08mm thick polyimide film backing material. The backing is readily bondable with strain gauge adhesives. Both, strain gauge as well as bondable terminals are suitable for long-term use up to 563K and 533K respectively.

The gauge is embedded in a slot around the circumference of the 6mm probe shaft (detail "C" in Fig. 3-2). The slot depth is 0.5mm and the circumference is separated into two areas. The high temperature resistant strain gauge matrix material is brittle when twisted too much at ambient temperatures. Therefore the sensor is preformed by adding heat at 533K. This is performed by means of a soldering iron with a cylindrical insert of 5mm in

diameter (Fig. 3-6).
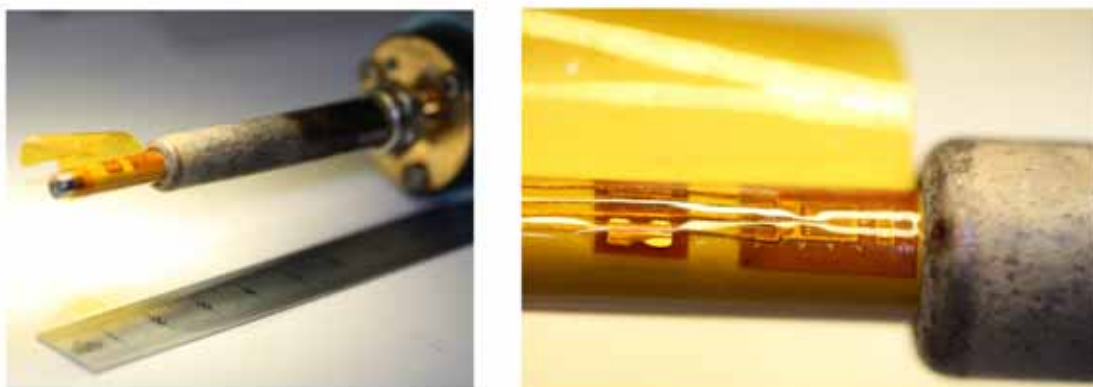
Fig. 3-6   Probe shaft strain gauge installation preparation (preforming).

After preforming the sensor, it is installed on the probe shaft by means of a high temperature epoxy and the sensor electrical connection is done by soldering the lead wires as well as the copper cables to the bondable terminals (Fig. 3-7). The soldering procedure itself is performed using a high-temperature soldering tin. The copper cables are inserted into the probe shaft and guided to the amplifier box. From there, the signal is transmitted to the measurement system as described in chapter 4.4.

Fig. 3-7   Probe shaft strain gauge installation on 6mm shaft, compared to a match for scale comparison.

3.2.2.2   Probe Shaft Temperature Sensor Installation

A PT100 temperature sensor is installed on the other semi-cylindrical plane of the slot on the 6mm shaft in order to monitor potential heat flux through the probe shaft.

The PT100 sensor is used in 4-wire-configuration. Again, bondable terminals are used to provide contact to the two PT100 leadwires to the pair-wise twisted copper cables (Fig. 3-8). The cables guide the signal to the inside of the probe shaft and feed the signal to the measurement system (chapter 4.4) by means of signal connectors at the amplifier box.

*Fig. 3-8   Probe shaft temperature sensor installation on 6mm shaft, com-
pared to a match for scale comparison.*

After the installation of both secondary sensors, the slot on the 6mm shaft is covered by an epoxy glue in order to further protect the two devices from mechanical failure due to collisional contact (Fig. 3-9).

*Fig. 3-9   Final view of covered slot on 6mm shaft, containing the strain
gauge device and a PT100 temperature sensor.*

3.2.3 Concluding Remarks regarding the FRAP-HT Probe Assembly

Altogether, an estimated 40 different mechanical and micro-mechanical steps of several hours each are necessary to build one probe. Each step is followed by a hardening time of at least 6 hours. This totals to 500 hours of elapsed time per probe. Due to the multiple steps required in assembling the probe, some support devices that provide for the accurate and repeatable positioning and handling of the different components have been specially engineered for the assembly of the FRAP-HT probe Fig. 3-10.
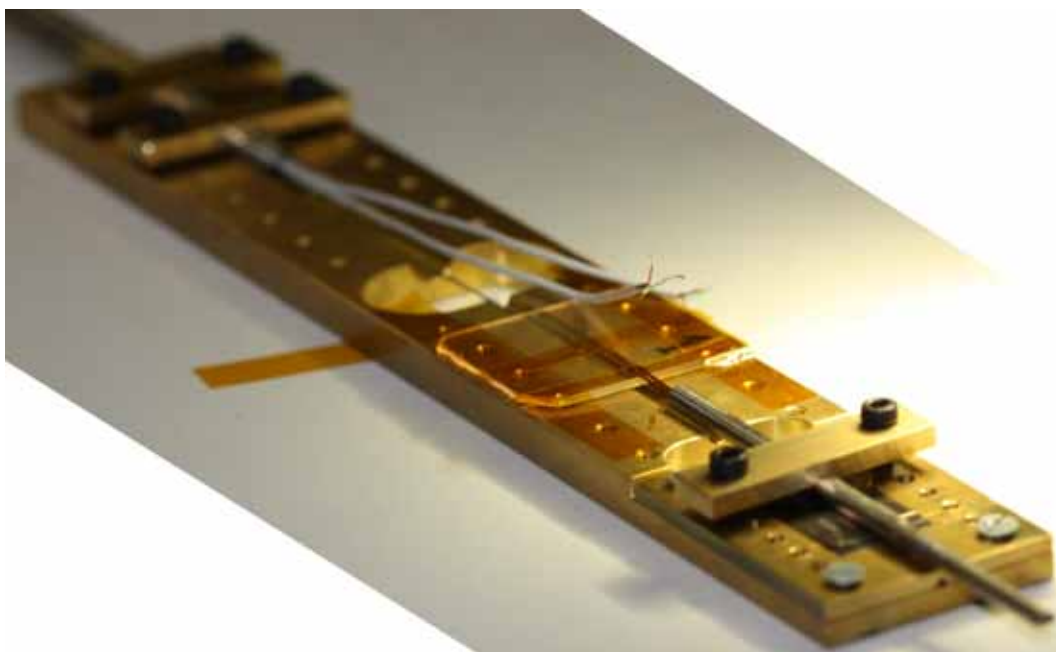
Fig. 3-10   FRAP-HT assembly device.

3.3 Probe Calibration

In this section, the concepts and results for the different calibrations performed for the FRAP-HT probe are presented.

The FRAP-HT probe requires two types of calibration: a static calibration and an aerodynamic calibration. In the static calibration, the piezo-resistive pressure sensor signals are calibrated over well defined pressure and temperature ranges. At the same time, the shaft PT100 is calibrated for various temperatures to derive a temperature-to-resistance curve of the shaft temperature sensor.

In a second step the probe is aerodynamically calibrated over a range of Mach number and relative flow angles.

3.3.1   Steady Pressure Sensor Calibration

3.3.1.1   Sensor Calibration Facility

Every sensor of the FRAP-HT probe is calibrated individually in an oven calibration within a predefined calibration range (pressure and temperature). The applied pressure and the temperature can be varied in a range between 0 to 1bar and 298K to 533K, respectively, with temperature fluctuations of less than ±0.02K. Fig. 3-11 shows a picture of the oven facility used for the sensor calibration.

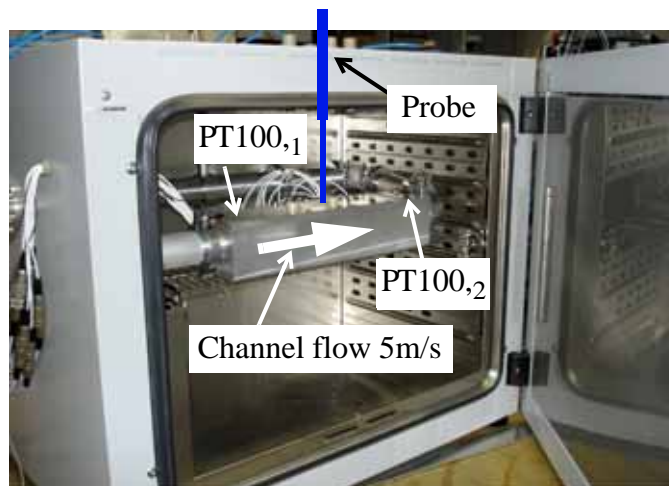*Fig. 3-11   Static pressure and temperature sensor calibration facility.*

The probe is inserted from the top through openings into the oven. During the calibration, the probe is exposed to a low speed (5m/s), isothermal air stream within a channel. The air stream minimizes the self-heating of the sensors and ensures a homogeneous temperature field within the channel. Two thermocouples (type: PT100), placed in close proximity to the probe, are used to measure the temperature of the air stream. The maximum measurement uncertainty is ±0.01K. The wait time between two temperature steps is based on the measured transient temperature behavior. The calibration of the pressure and temperature sensors starts when the temperature variations are smaller or equal to ±0.02K around the target temperature. The temperature settling time is strongly dependent on the thermal inertia of the calibration channel as well as dependent of the absolute level of the target temperature (around 110 minutes for temperature steps of 15K, above an absolute temperature level of 433K).

The pressure sensors are fed by a constant current source of 1mA. The excitation voltage, Ue is mainly a measure of the membrane temperature and the signal voltage, U is strongly proportional to the differential pressure across the membrane. The raw signals are amplified in the probe box at the back end

of the probe shaft by a factor of 100. The calibration procedure described in Kupferschmied [40] is applied to derive a sensor calibration model.

The signals are acquired using a 24-bit acquisition board that provides a resolution of 1.19×10^{-6}V of the measured sensor signals. The pressure is delivered to the probe by a pressure controller (type: Druck DPI 520) that has a relative uncertainty of ±0.05% over the full scale range (1bar). The calibration facility is pre-programmable and the data acquisition is fully automated.

3.3.1.2   Results

The static sensor calibration is performed in a range between 313K and 533K in temperature steps of 5K. The corresponding pressure range is varied between 10mbar and 550mbar, in steps of 40mbar.

In the temperature range between 313K and 473K, the results of the probe sensor calibration agree quantitatively to the characteristic tests performed on single sensor dies mounted on TO's as presented in chapter 2.1.7. Above around 490K, effects due to a leakage current flowing from p-type silicon elements into the n-type diaphragm material of the transducers results in strongly non-linear output voltages. This is further indicated by the *Ue* signal, that shows a maxima at this temperature and decreases above this temperature instead of further increasing (Fig. 3-13).

The sensor calibration is therefore divided into two temperature range windows. One window, that shows a dominantly decoupled *U* versus *Ue* behavior ranges from 313K up to 473K and a second temperature window, that shows the coupled region above 473K up to 533K. The upper limit of the lower range window is chosen at 473K, since the measurements conducted with the FRAP-HT probe and presented in the chapters 7 and 8 respectively, are expected to not exceed a temperature level of 473K.

For both temperature windows, a fifth-order bivariable polynomial interpolation, Eqn. 3.1 and Eqn. 3.2, is used to determine the pressure and temperature from the measured sensor signals.

$$\Delta p(U, Ue) = \sum_{i=0}^{n} \sum_{j=0}^{m} k_{p,ij} \cdot U^i \cdot Ue^j \qquad (3.1)$$

$$T(U, Ue) = \sum_{i=0}^{n} \sum_{j=0}^{m} k_{T,ij} \cdot U^i \cdot Ue^j \qquad (3.2)$$

Fig. 3-12 and Fig. 3-13 show the resulting 2D interpolation surfaces for the

U and *Ue* signals over the respective temperature ranges.

Fig. 3-12   *Typical output signals, U (left) and Ue (right) in voltage [V] as a function of temperature and pressure, resulting from the lower range probe sensor calibration.*
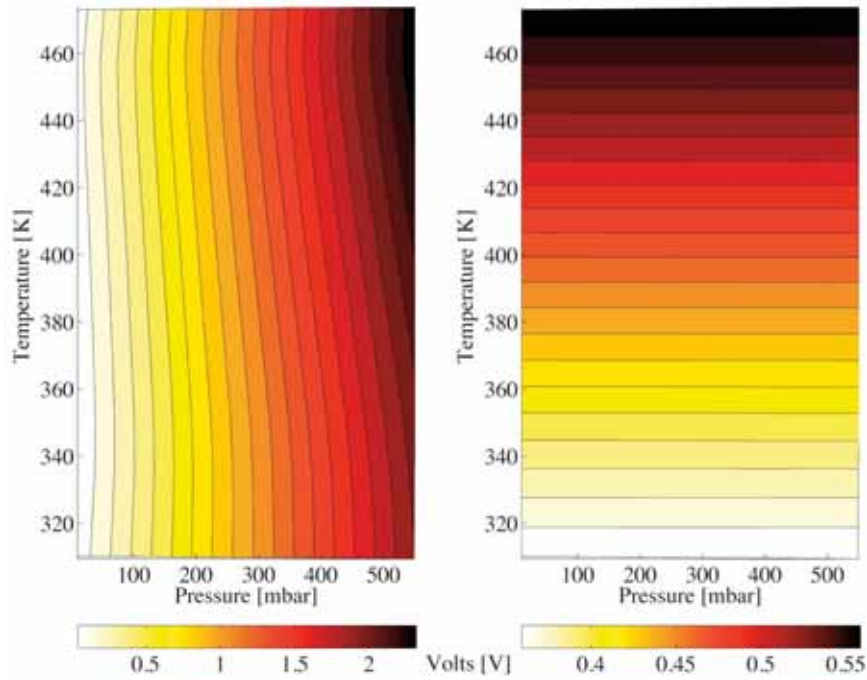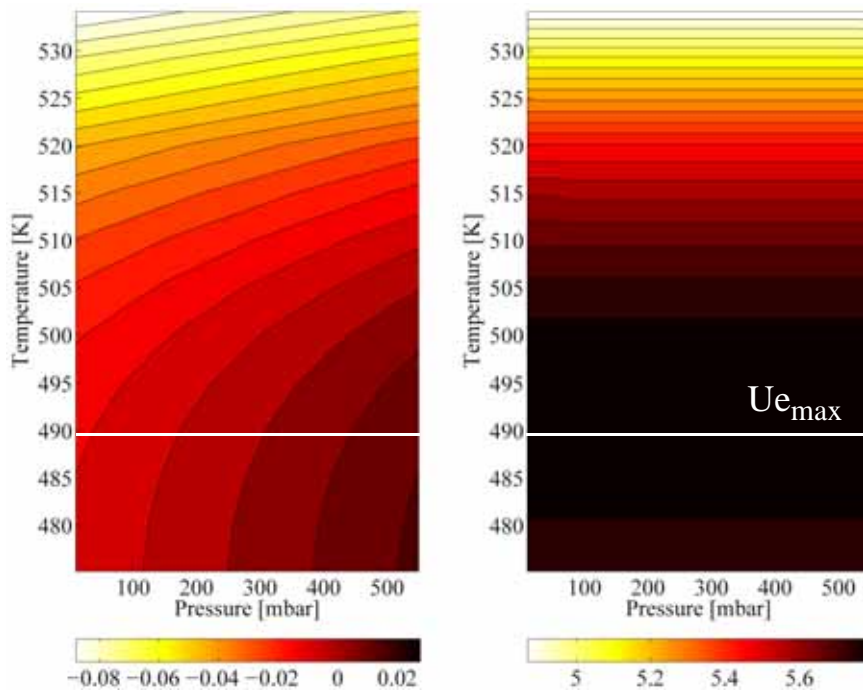

Fig. 3-13   *Typical output signals, U (left) and Ue (right) in voltage [V] as a function of temperature and pressure, resulting from the upper range probe sensor calibration.*

For the lower temperature window, the results show a mean pressure sensitivity of 4.35mV/(mbar·mA) for both sensors and a mean temperature sensitivity of 0.38 mV/K for both sensors. However, due to the strong coupling and the leakage currents, the pressure sensitivity for both sensors is reduced in the case of flow temperatures above 473K. The resulting sensitivities in pressure and temperature for both sensors in the upper temperature window are 0.14 mV/(mbar·mA) and 1.078 mV/K respectively.

The reduced sensitivity in the upper temperature range will induce additional measurement uncertainties in the pressure measurements.

The lower range calibration model exhibits an average standard deviation of 52.6 Pa and 0.13K, which corresponds to an error of less than 0.098% and 0.082% over the full calibration range of the probe. The model fit accuracy of the calibration model for the upper range shows reduced values for both sensors, due to the strong non-linear behavior of the pressure signal related surface (U). They are in the order of 1.5% of the full scale for both, pressure and temperature.

Although the accuracy for the upper range is reduced, the long term and repeatability tests showed good results. No significant drift was detected during the long term tests and the repeatability tests performed at 533K showed variations in the pressure and temperature related signal U and Ue of less than ±1.5mV.

The resulting two sets of pairs of calibration coefficients k_p and k_T are used in the data processing procedure of FRAP-HT measurements. A selection criterion based on multiple inputs is used to evaluate the respective flow conditions and therefore allows a determination of which of the two sets of coefficients need to be used at a respective measurement point. The selection criterion compares the log file data of the measured U and Ue and therefore takes trends in the temperature into account. Optionally the temperature of the shaft PT100 sensor could be used for a further weighting of the expected temperatures in the flow. Last but not least, user defined parameters, such as the expected flow temperatures are used to further define the selection process of the respective criterion. However, in order to minimize potential errors due to an application of the wrong set of coefficients, it is recommended to perform foregoing temperature measurements at the specific facility operating point and measurement plane. The steady temperature probe as introduced in chapter 5.3 can be used for this purpose. A further advantage of foregoing steady temperature measurements in case of expected high temperatures is related to probe safety issues, since exceeding 533K could harm the operation

of the probe.

3.3.1.3   Measurement Resolution due to Signal Noise

As an additional test, the maximum pressure resolution due to white noise influence is investigated in the oven facility. For this, the reference pressure of the probe is kept at a constant value and the oven temperature was set to 303K. The signal of the FRAP-HT probe is then directly acquired by means of the measurement system as detailed in chapter 4. The signal is acquired with a sampling frequency of 200kHz and monitored online. The resulting instantaneous noise amplitude is in the order of ±1mV. This yields a maximum pressure resolution of ±0.43mbar. Compared to the traditional FRAP probe, which has a maximum pressure resolution of around ±1.44mbar, the susceptibility to noise is reduced by a factor of more than 3.

However, in case of measurements in a periodically rotating machine, ensemble averaging procedures as discussed in chapter 4.7.1 are applied to the acquired data. The averaging procedure significantly reduces the impact of instantaneous white noise uncertainties on the overall results. Nevertheless, the test that has been performed shows that the new FRAP-HT probe is influenced less by white noise. Reasons for this could be the use of state-of-the-art components and materials in the new probe.

3.3.2   Shaft PT100 Sensor Calibration

In a second step, the probe shaft PT100 sensor is temperature calibrated in the oven calibration facility. The applied range is 313K up to 513K. The output signals of the complete measurement chain (output of the commercial temperature measuring transducer) are acquired for the shaft PT100. The measured mean sensitivity of the temperature sensor after amplification (chapter 4.4.1) is 32.9 mV/K.

Both, the short term drift as well as the aging effect on the long-term validity of the probe sensor have been investigated after more than 100 hours of operation. The resulting output signal showed no identifiable drift and in the long term investigation, the change in output voltage is in the order of ±2mV which expressed in terms of the sensed temperature error is approximately ±0.06K.

In order to implement the calculation of the resulting temperature for the shaft PT100 sensors into the complete measurement procedure in an automated manner, calibration coefficients are defined from the resulting oven facility calibration.

1st, 2nd and 3rd order polynomial curve fits have been applied to the resulting calibration data. An estimate of the absolute error, containing 50% of the predictions has been investigated for all three polynomial orders. The estimate with the first order fit has mean values of absolute errors in the order of ±0.321K, whereas the second and third order polynomial curve fits result in mean values in the absolute error in the order of ±0.099K and ±0.085K respectively. The third order polynomial curve fit has only a minor reduction in the estimated absolute error compared to the second order curve fit. The shaft PT100 sensor calibration coefficients are therefore based on a second order polynomial curve fit,

$$T_{shaft, PT100} = a \cdot (U_{PT100})^2 + b \cdot U_{PT100} + c \qquad (3.3)$$

where $T_{shaft,PT100}$ equals the sensed temperature of the sensor in the shaft. U_{PT100} equals the output voltage of the sensor and a, b and c are the respective polynomial coefficients

The resulting calibration curve for the second order polynomial curve fit is presented in Fig. 3-14. The resulting correlation coefficient R^2 is 0.9999978. The 2nd order polynomial curve fit is thus suitable for measurements.
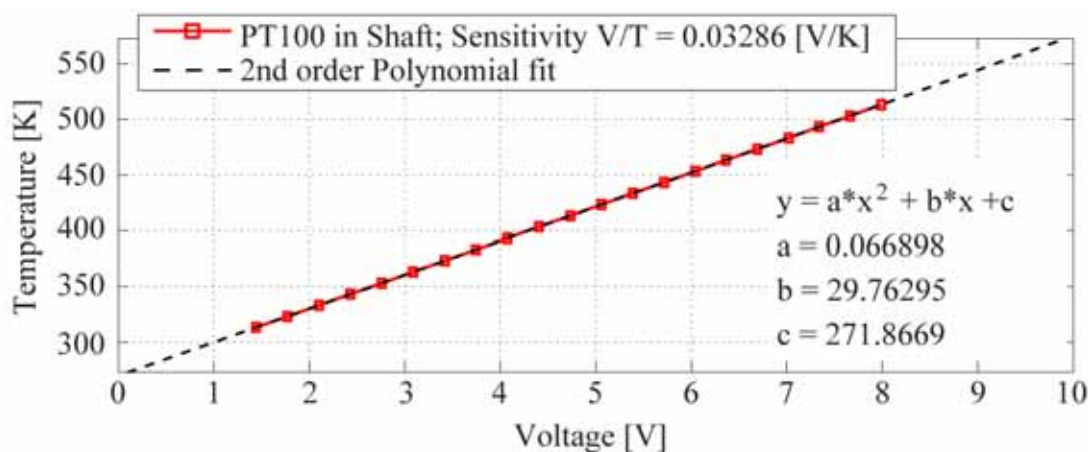
Fig. 3-14   Calibration polynomial for FRAP-HT shaft PT100 sensor.

3.3.3   Virtual 4 Sensor Mode

On themselves, two sensors on the FRAP-HT probe are insufficient to measure a 3D flow field. However, the need for a 3D flow measurement capability using two-hole probes that have minimal probe design complexity leads to the concept of the virtual probe measurement technique.

The reduced number of holes for FRAP-HT probes keeps the complexity of

the probe design and manufacturing low and furthermore removes the drawback of the missing pitch angle information for flow field measurements. By adding a second pressure tap at the tip of a shaped probe head, the probe can be used in virtual 4-hole technique in order to detail 3D flow fields. The concept of two-hole probes is adapted for fast response FRAP probes with two built-in piezo resistive pressure sensors within the probe head. The following schematic illustrates the measurement concept of the virtual 4 sensor mode using a two-sensor probe (Fig. 3-15).

Fig. 3-15 Measurement concept in virtual 4 sensor mode with a two-sensor probe.

The first sensor is used to measure in three consecutive steps the actual tap pressures (*P1*, *P2*, *P3*) at the three different probe setup angles (0°,-42°,+42° relative to the probe stem). The ideal setup angle for cylindrical probes is normally ±42° for the *P2* and *P3* pressures and relative to the middle position at 0° for *P1* [81]. The second sensor is only used for the fourth pressure (*P4*) in the first step. From this procedure a set of 4 independent pressures (*P1...P4*) is obtained. These pressures are then used for the definition of the different flow coefficients for flow yaw and pitch angles, static and total pressure as well as Mach number.

The local velocity vectors of the unknown flow field are derived from the actual probe measurement data (pressures *P1*, *P2*, etc.) using the aerodynamic calibration model and the sensor calibration model for FRAP probes with built-in sensors. When measuring the flow field with a probe the resulting velocity vector is always relative to the probe itself and therefore in the probe

relative coordinate system. Generally, the coordinate system of the probe is not identical to the rig or traversing unit coordinate system.

When making flow measurements with the probe, the X-axis (probe setup angle) is always oriented in opposite direction to the average expected velocity vector. Normally this setup angle is obtained from the intended design of the blade rows. This is required in order to keep the probe within the predefined calibration range, that is typically ±30° in yaw as well as pitch angle for the 2-sensor FRAP-HT probe (Fig. 3-16).
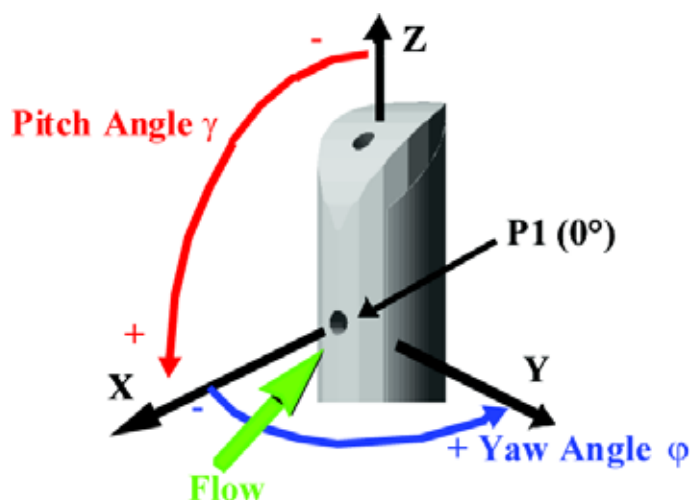
Fig. 3-16   Coordinate system of 2-Sensor FRAP probe (freejet facility).

This first guess of the unknown flow field direction and the large calibration range (48° in yaw and 40° in pitch) of the probe are normally sufficient for preventing an "out-of-calibration" error during the measurement.

As previously mentioned, the derived flow velocity vector is always related to the local probe coordinate system. The probe setup angle (in traversing unit coordinate system or global coordinate system) for the *P1* measurement is aligned to the expected flow angle by positioning the probe tip in the measurement grid at specified *R/θ/X* location using a traversing system. A schematic of this procedure is shown in Fig. 3-17.

After the *P1* (and *P4*) measurement is taken, the probe is turned at the fixed grid point by -42° relative to the initial probe setup angle in order to get the *P2* pressure and finally to +42° (84°) for *P3* in virtual 4 sensor mode. The flow data are derived in the local probe coordinate system and finally converted into the global coordinate system (rig) using a series of logged probe setup angles.
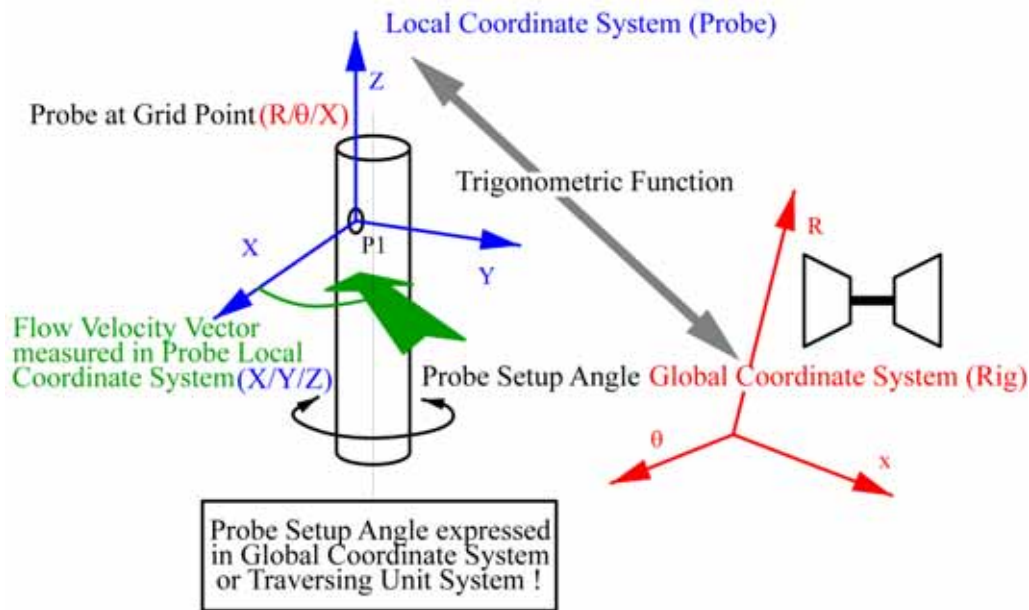
Fig. 3-17   Schematic of flow measurement for probes in virtual mode.

3.3.3.1   Trigger

The flow field within a rotating rig is always unsteady with periodic fluctuations of the flow field. The rotor blade passing frequency is the dominant term in the periodic fluctuations of the flow within the blade rows. This fact is important when using probes in virtual 4-sensor mode. The different pressures *P1* to *P4* that are measured during a run are not taken simultaneously but serially. This means, that the there is a time-lag between the different measurements that has to be compensated for in the postprocessing of the FRAP data.

All periodic flow variations that correlate with the rotor or blade passing frequencies are captured by this technique. Stochastic flow fluctuations can not be directly captured with this virtual mode technique. For a direct measurement of the full turbulence intensity *Tu* a real 4-sensor FRAP probes would be required. In order to resolve smallest possible turbulent length scales for such a 4-sensor probe, the miniaturization of the design is of even more importance and therefore the bottle neck in the design and assembly of such a probe. Based on the 2-sensor FRAP probes, two concepts have been introduced in recent years in order to still be able to capture stochastic fluctuations based on the virtual 4-sensor technique. In the first concept, the non-deterministic fluctuations aligned to the main flow direction are derived from the variation of the pressure *P1* on the probe center hole [82]. In the

second concept, the determination of the remaining two components of the 3D turbulence intensity vector are derived from the yaw and pitch angle information of the probe [43].

In virtual 4-sensor mode, the rotor or blade passing trigger is used for the correction of the temporal phase shift between the different signals. The trigger accuracy is therefore a key element for an application of this technique and requires special attention. The minimum trigger characteristics that are necessary for FRAP probe measurements in rotating facilities are summarized as follows:

Min. Number of Samples per Blade Passing: s_{min}=20 Samples

Example: Rotor Speed n=6000 rpm, b=80 Blades.

Min. Sampling Rate: fmin=n/60*b*smin=6000/60*80*20= 160'000Hz

Trigger Accuracy: Δs_{max}=±3-5% of s_{min}

(equal to ±1 sample for 20 samples per blade passage)

Standard Sampling Rate in FRAP System: *200kHz*

The trigger accuracy strongly depends on the signal quality and the trigger speed of the electronic device that is used for creating the trigger signal. The FRAP-HT measurement system uses a high frequency optical (glass-fibre) Schmitt-Trigger that has very short response times (within the MHz range) and is detailed in chapter 4.3.3. The resulting trigger accuracy is therefore sufficient for all applications using FRAP probes.

3.3.4   Steady Aerodynamic Calibration

The probe is aerodynamically calibrated in the free jet calibration facility of LEC as shown in Fig. 3-18. A detailed description of the calibration facility is found in [40]. The probe is installed on a three axis traversing system (yaw angle, pitch angle, and lateral motion) in order to rotate the probe relative to the fixed free jet. The automatic calibration procedure follows a defined measurement grid for different probe yaw and pitch angles. The flow angle convention is defined in Fig. 3-16.

The jet temperature is stable at 303K (within ±0.3K). The calibration range for the FRAP-HT probe is defined by a grid that is homogenous in yaw and pitch angles and covers ±24° in yaw (φ) and ±20° in pitch (γ) for different
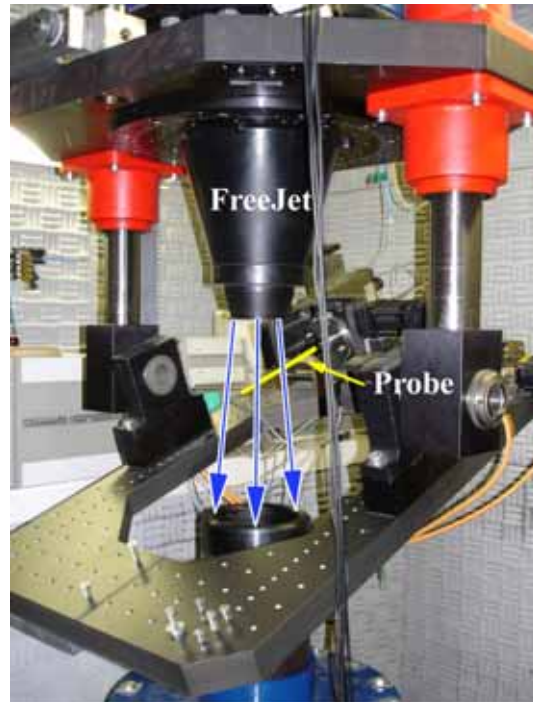
Mach numbers (*Ma = 0.15, 0.3, 0.5 and 0.7*).

Fig. 3-18   Inhouse freejet facility.

In order to derive a yaw range of ±24°, and due to use of the virtual 4 sensor mode technique, the probe needs to be rotated step-wise within a range of ±68°. The non-dimensional total pressure coefficients (*Cpt*) are detailed in Fig. 3-19. These data must in a second step be post-processed to form calibration coefficients related to the virtual 4 sensor mode.
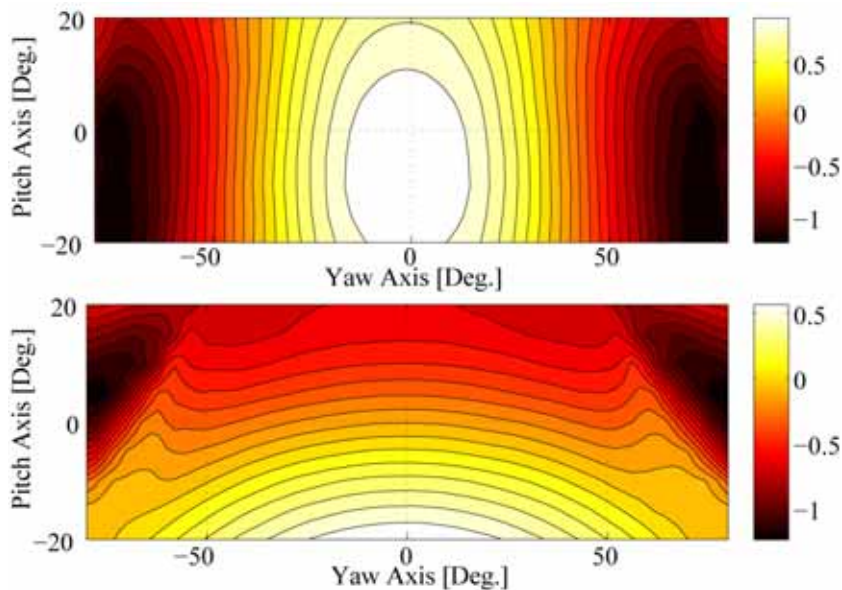

Fig. 3-19   Non-dimensional pressure contours of the two FRAP-HT pressure taps (top: center hole, bottom: tip hole).

The steady aerodynamic calibration is based on traditional methods [20, 83]. The approach uses a set of four calibration coefficients K_φ, K_γ, K_t and K_s for the flow yaw angle, flow pitch angle, total and static pressure. The flow angle coefficients depend on the different pressures *P1* to *P4* as given in Eqn. 3.4 and Eqn. 3.5. The surface pressure distribution around the cylindrical probe head depends on the relative flow yaw angle and the two pressure taps *P2* and *P3* sense a different portion of the dynamic head. The difference of *P2-P3* is non-dimensionalized with an average dynamic head, that results from *P1-(P2+P3)/2*. The same approach is followed for the flow pitch angle but the centre pressure *P1* and the top pressure *P4* are used in order to define the pitch angle coefficient K_γ. The difference is again divided by the average dynamic head for a given flow field around the probe's head.

$$K_\varphi = \frac{P_2 - P_3}{P_1 - \dfrac{P_2 + P_3}{2}} \qquad (3.4)$$

$$K_\gamma = \frac{P_1 - P_4}{P_1 - \dfrac{P_2 + P_3}{2}} \qquad (3.5)$$

The flow yaw and pitch angles φ and γ are now derived from K_φ and K_γ by an inverse calculation as suggested in [84]. The corresponding equations are given in Eqn. 3.6 and Eqn. 3.7 for the two flow angles.

$$\varphi = \sum_{i=0}^{n} \sum_{j=0}^{m} k_{ij\varphi} K_\varphi^i K_\gamma^j \qquad (3.6)$$

$$\gamma = \sum_{i=0}^{n} \sum_{j=0}^{m} k_{ij\gamma} K_\varphi^i K_\gamma^j \qquad (3.7)$$

In the calibration process, the flow yaw and pitch angles are defined in the calibration task, whereas the four pressures *P1* to *P4* result from the pressure measurement with the probe. The pressures are used to compute the calibration coefficient K_φ and K_γ. For every measurement point of the calibration task a combination of yaw and pitch angles φ and γ and *P1* to *P4* is obtained, which represents one equation of the total set of linear equations. The polynomial calibration coefficients $k_{ij\varphi}$ and $k_{ij\gamma}$ result from the solution of this set of linear equations using a least square approximation.

The calibration coefficients for the total and static pressures are defined according to the flow angle coefficients as a function of the acquired pressures

from the probe and the free jet setup with the total P_{tot} and static pressure P_{stat} within the jet and given in Eqn. 3.8. and Eqn. 3.9.

$$K_t = \frac{P_{tot} - P_1}{P_1 - \dfrac{P_2 + P_3}{2}} \qquad (3.8)$$

$$K_s = \frac{P_{tot} - P_{stat}}{P_1 - \dfrac{P_2 + P_3}{2}} \qquad (3.9)$$

The similar procedure as for the flow angles is applied to the pressure measurements in order to derive the polynomial calibration coefficients for the total and static pressures. The relations Eqn. 3.10 and Eqn. 3.11 for the total and static pressures are now a function of the computed flow yaw and pitch angles. In order to improve the interpolation quality in the next steps, the flow angles are converted into radians instead of degrees. The change of units into radians turned out to be more beneficial for the calibration model's accuracy since the interpolation of the calibration curves of up to 6th order for parameters m and n lead to a higher error bandwidth in particular at the limits of the defined calibration range.

$$K_t = \sum_{i=0}^{n} \sum_{j=0}^{m} k_{ijt} \varphi^i \gamma^j \qquad (3.10)$$

$$K_s = \sum_{i=0}^{n} \sum_{j=0}^{m} k_{ijs} \varphi^i \gamma^j \qquad (3.11)$$

The polynomial calibration coefficient vectors $k_{ij\varphi}$, $k_{ij\gamma}$, k_{ijt} and k_{ijs} are finally used for the evaluation of the unknown flow quantities from the measured set of 4 pressures *P1* to *P4* at a given grid point in an unknown flow field.

The calibration curves at *Ma=0.5* for the FRAP-HT probe are shown in Fig. 3-20 for a calibration range of $\pm 24^o$ in yaw (φ) and $\pm 20^o$ in pitch (γ) angle. The characteristic of the calibration surface for yaw angle coefficient K_φ is only a function of the yaw angle φ and is thus decoupled from a change of pitch angle γ. The same is valid for the pitch angle coefficient K_γ that is a bit more affected by a change of flow yaw angle φ. This indicates, that the pitch sensitivity of the probe is less pronounced than the yaw sensitivity, which is also found from the range of the coefficients (K_φ: -2.5/2, K_γ: 0.2/.2.2). The three dimensional flow field at the tip of the probe strongly affects the characteristics of the

surface pressure at the tip and thus the coupling term between the flow yaw and pitch angles with respect to the pitch angle calibration coefficient. The yaw angle coefficient, however is more defined by a two-dimensional flow field, since the pressure taps *P1* to *P3* that are used in order to define the yaw angle coefficient are further away from the probe tip.
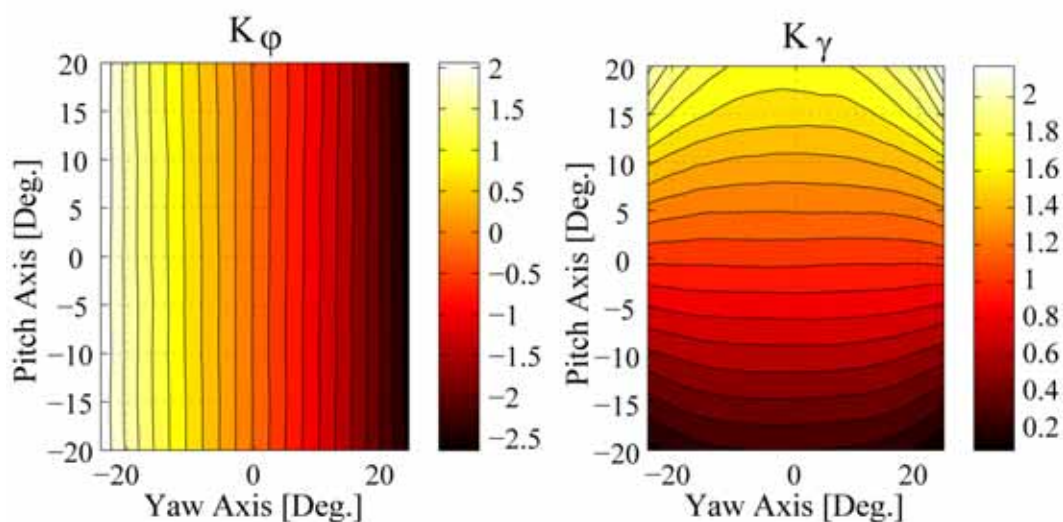

Fig. 3-20 Aerodynamic calibration coefficient curves for flow angles, K_φ and K_γ and for total and static pressures, K_t and K_s; calibration range: yaw ±24° and pitch ±20°.

The FRAP-HT calibration curves at *Ma=0.5* for the total and static pressures K_t and K_s are shown in Fig. 3-21. The surfaces are ideally symmetric with respect to the zero flow yaw angle. The symmetry is strongly dependent on the machined accuracy of the probe. Both surfaces show an excellent symmetry, which underlines the high quality, precision of the manufactured probes. The value of the curves increase with a higher flow pitch angle γ. Pitching the probe relative to a horizontal flow vector obviously reduces the maximum pressure that a pressure tap, e.g. the centre pressure *P1*, would register. The pressure tap sees less of the dynamic head, which is then corrected using the calibration curves in order to recompute the effective total pressure within the flow.

At 0° yaw angle and -8° in pitch angle both calibration curve surfaces flatten. At the negative pitch angle of -8° the probe is facing the maximum dynamic head and the correction factor for total and static pressures is minimum. The pressure measurement of the centre pressure hole for *P1* is close to the overall stagnation pressure of the flow.
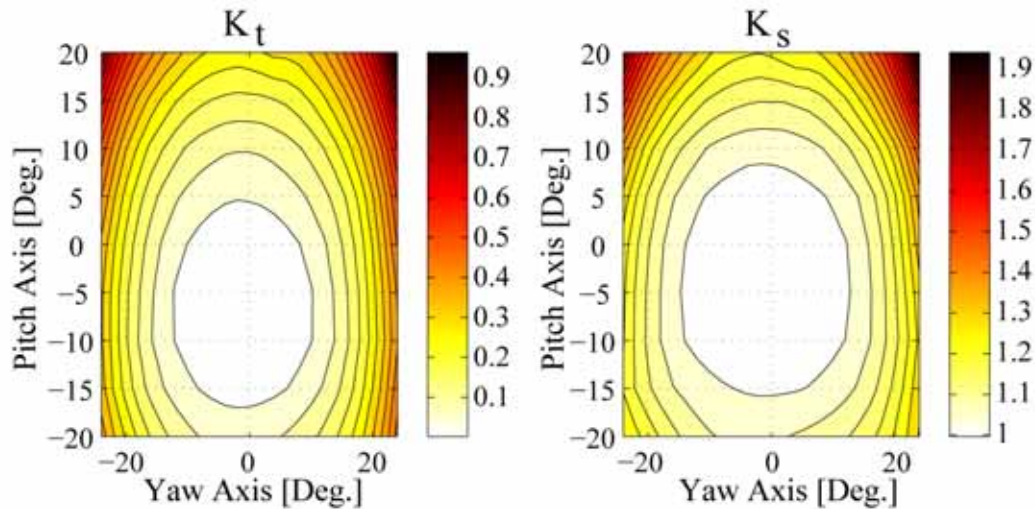
Fig. 3-21   Aerodynamic calibration coefficient curves for flow angles, K_φ and K_γ and for total and static pressures, K_t and K_s; calibration range: yaw ±24° and pitch ±20°.

The derived calibration accuracy at a Mach number of *Ma=0.5* is given in Table 3-2 for a calibration range of ±24° in yaw and ±20° in pitch angle, respectively. The calibration uses a polynomial interpolation order of 6th degree for both parameters *m* and *n*. The model accuracy is given in absolute values for the flow angles, as well as for total and static pressures. The accuracy for the Mach number is given as a percentage of the freejet calibration Mach number. Additionally, for total and static pressures, the accuracy is presented as a percentage of the real dynamic head at the freejet Mach number of 0.5.

Parameter	FRAP-HT accuracy	in % of dynamic head
φ	± 0.06°	
γ	± 0.13°	
P_{tot}	± 41 Pa	0.25%
P_{stat}	± 39 Pa	0.25%
Ma	± 0.18%	

Table 3-2   FRAP-HT calibration model accuracy for Ma=0.5 and cali-bration range ±24° for yaw and ±20° for pitch.

3.3.4.1   Probe Pressure Distribution for varying Mach Numbers

In Fig. 3-22 the non-dimensional pressures *Cp* of both pressure taps for

varying yaw angle at a constant pitch angle of 0° are shown. The non dimensional pressure coefficient is defined as the difference between the sensed pressure on the probe tap and the static pressure, divided by the difference of freejet total and static pressure. The data are extracted from the aerodynamic calibration data for the three Mach numbers, 0.15, 0.3 and 0.5. The C_p of the yaw sensitive tap is 0 at a turning angle of around ±42°; these angles are therefore chosen as the positions 2 and 3 in the virtual 4-hole probe concept (see Fig. 3-15).

Fig. 3-22 furthermore shows, that changes in the pressure distribution due to Mach number variations are small. The largest variation for the pressure taps is observed at extreme angles between ±(60° to 70°) for the pitch sensitive tap. This is related to flow separations on the probe body. The separations occur at slightly different angles, depending on the flow Mach number.

The Reynolds-number based on the probe head diameter is $Re_d = 8250$ for the Mach number of 0.15 and $Re_d = 2.75 \times 10^4$ for the Mach number of 0.5. This is well within the subcritical range of 10^3 to 10^5 where the drag coefficient of the probe head stays constant. Therefore any viscosity effects on the probe head can be omitted for Mach numbers above 0.08.
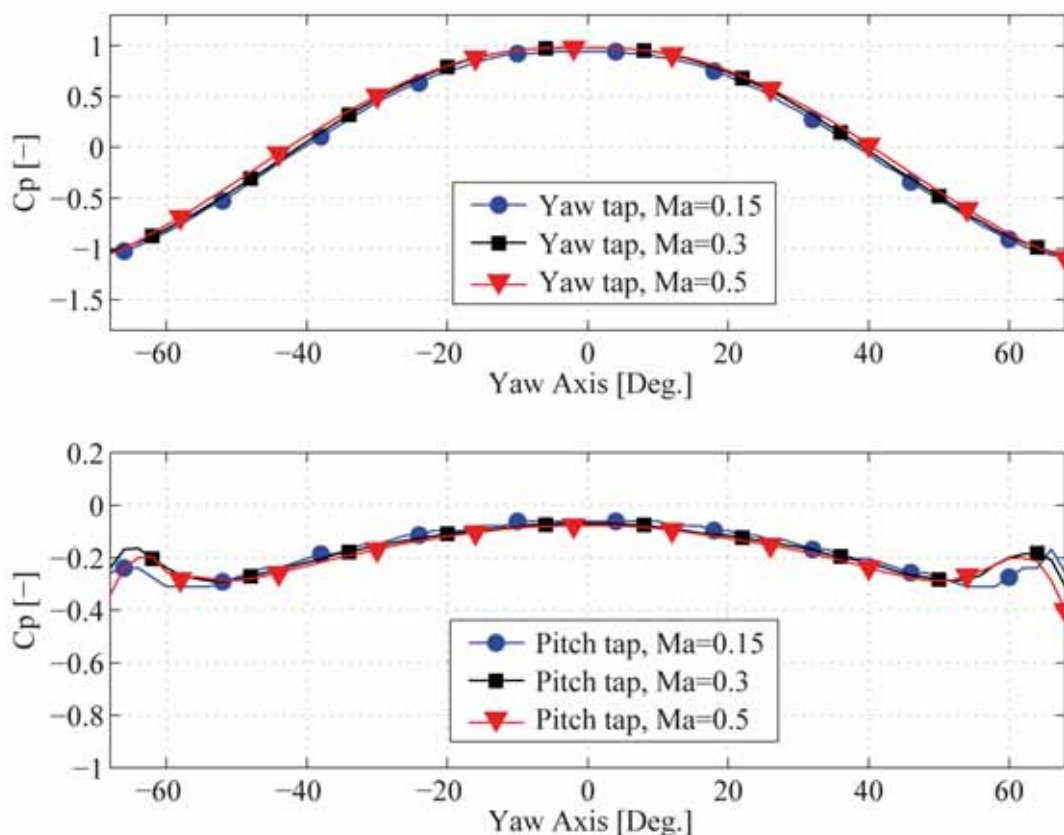

Fig. 3-22 Pressure reading of both sensors at 0° pitch angle and 3 Mach numbers, Ma=0.15, 0.3 and 0.5.

3.3.5   Probe Dynamic Response

The dynamic behavior of FRAP probes is investigated through the transfer characteristics of each different component of interest. The sensor diaphragm and the sensor's position relative to the pressure tap are the main components that influence the dynamic response of the probe. The investigations of the sensor membrane response are carried out analytically, whereas the investigations related to the pressure tap and cavity size are experimental.

3.3.5.1   Piezo resistive Miniature Silicon Chip

Due to design issues, the work of piezo resistive miniature silicon chips is almost lossless and typically shows very high natural frequencies (based on a 2nd order model of a spring-mass system). The natural frequency of the sensor membrane is calculated using the model of an all-round clamped rectangular plate (Harris [85], p.7.36). This results in a natural frequency of the sensor membrane of 710 kHz. This very high value is explained by the small membrane thickness and width, as well as by the high aspect ratio between the modulus of elasticity and the mass density for silicon.

3.3.5.2   Pneumatic Cavity

The frequency response of a sensor usually decreases when assembled inside a probe and can vary slightly for every probe, due to the complexity of the sensor assembly. The decrease of the frequency response is related to the pneumatic cavity that occurs if the membrane is not flush-mounted. Numerous analytical approaches, for example the organ pipe equation, have been applied in the past in order to calculate the frequency response of the pneumatic cavity [40]. These investigations showed that due to the complex cavity geometry, the simplified analytical models lead to deviations in the real eigenfrequencies of up to 30%.

Therefore, in order to validate the dynamic behavior of the probe, the sensor pressure signal of both sensors (yaw and pitch) has been measured in the freejet facility [40], equipped with a fine turbulent mesh grid. The resulting flow turbulence has constant amplitude over relatively low frequencies and then decays with a characteristic slope of 5/3 at higher frequencies. The normalized amplitude response $f^{5/3}PSD(f)$ versus frequency is shown in Figure 6. The normalization is achieved using the mean of the amplitude response $f_0^{5/3}PSD_0$ over a frequency range of 8-18 kHz.

Both yaw and pitch sensors show similar dynamic behavior. The peaks at 36 kHz correspond to the eigenfrequency of the pneumatic cavity of the yaw

and the pitch pressure tap respectively. For both sensors the amplitude is flat up to a frequency of 25 kHz, above which the amplitudes are in excess of 3 dB. Thus, the cut-off frequency of 25 kHz determines the measurement bandwidth of this probe.
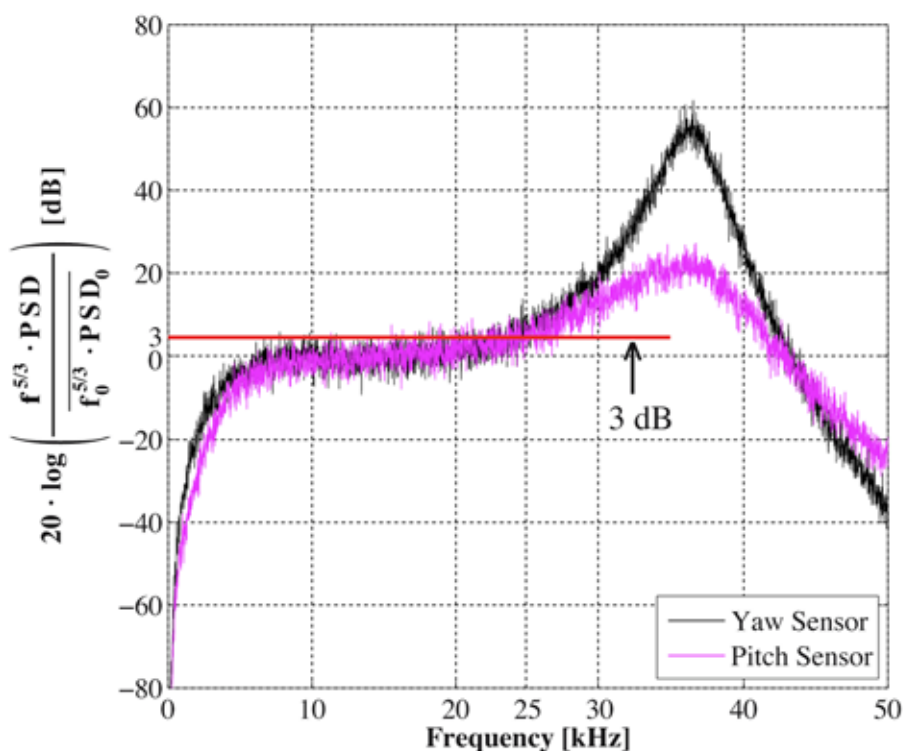

Fig. 3-23 Amplitude response of both sensors of the FRAP-HT probe. The measured response results from grid-generated turbulence.

3.3.5.3   Temperature Response

Piezo resistive sensors are sensitive to both pressure and temperature and the sensor calibration links both flow variables to voltage values. While the offset of each pressure signal can be readjusted during measurements by changing the reference pressure in the probe interior, a temperature offset cannot easily be detected while the probe remains inserted in the machine. Therefore, stability of the temperature reading is a requirement.

The behavior of the pressure and temperature signals under large temperature gradients, e.g. occurring during the run-up of a turbomachine or the sudden immersion in hot flows, is tested for the new probe. A typical response for a sudden temperature step of 60K showed similarities to a 1st order lag element.

Therefore an analytical approach based on Gossweiler's [39] work is used

and leads to following solution for the time-varying temperature as:

$$\hat{T}(t) = \Delta T \cdot \left(1 - e^{-\frac{t}{\tau}}\right); \quad \text{whereas} \quad \tau = \frac{m \cdot c_p}{h \cdot A} \qquad (3.12)$$

ΔT equals the temperature difference of the step of 60K and τ equals the time constant. The time constant itself is defined as product between the transducer mass and the specific heat of the sensor mass, divided by the product between the heat transfer coefficient and the sensor surface. When $t=\tau$, the solution of the above equation corresponds to the time required to increase the sensor temperature to 63% of the applied temperature step ΔT.

This results in time constant $\tau_{63\%}$ for the FRAP-HT in low air velocity (1.5 m/s) of 15.8s. For higher velocity flows, the time constant drops, e.g. 1.5s at $Ma=0.5$. The time constant therefore limits the probe to mean flow temperature measurements (order of 1Hz).

3.3.5.4   Effects of Probe Intrusion

The intrusion of a probe into the flow field always affects the flow within the measurement volume. When using the probe in vicinity of an endwall, the streamlines are curved within the gap between the probe tip and the wall, leading to minor measurement error results (in particular in the pitch angle). This issue is normally not problematic for measurements of main flow. For measurements within the cavity of i.e. labyrinth seals it is highly recommended to use large sized cavities or probes with very small tip diameters. The smaller the probe tip the less the flow disturbing effects.

$$\frac{D_{ProbeTip}}{L_{Geometry}} \leq \frac{1}{10} \qquad (3.13)$$

A typical aspect ratio between the probe tip diameter and the characteristic length of the flow geometry (i.e. height of labyrinth cavity or the blade length) is less than 1/10. In this case, the blockage effects of the probe on the flow field are minimized and reach acceptable levels.

3.3.5.5   Dynamic Effects at Probe Tip

The reduced frequency k is a non-dimensional measure for the probe's response to excitation frequencies. The excitation frequency f is given by the actual blade passing frequency, where D is the probe tip diameter (2.5mm) and c is the local free stream velocity within the main flow. In turbines there are typically two flow regimes, that are the rotor (low Mach number) and stator

exit flow field (high Mach number).

$$k_{krit} = \frac{f \cdot D}{c} \geq 0.1 \qquad (3.14)$$

For reduced frequencies of $k > 0.1$ the dynamic effects at the probe tip have to be corrected accordingly. However, the need for such corrections is very rare and generally not required. For lower Mach numbers i.e. *Ma=0.3* (at rotor exit) and a blade passing frequency of 3kHz the reduced frequency for the two sensor FRAP-HT is 0.07, which is well below the given critical number of *k=0.1* (that is, no correction is needed). At higher Mach numbers (stator exit) this value is even lower. The dynamic effects at the probe tip are only critical for high blade passing frequencies and low flow velocities.

3.4 Probe Thermal Issues

Probe thermal issues such as self heating of the probe due to Joulean heating is discussed in this subchapter. Furthermore, some issues related to accurately measure the stagnation temperatures are addressed within this section.

3.4.1 Self heating

Due to the excitation power dissipated in the sensor resistors, the sensor diaphragms are prone to overheat, whereby the measured absolute temperature level as well as the pressure signal stability are affected. One possible workaround for the self heating issues would be to cool the probe. However, cooling is not only problematic for the probe design (size and reference pressure supply), but also prevents the measurement of temperature.

The overheating ΔT of cylindrical probe tips was shown to be strongly dependent on the sensor excitation current and also the tip size [40]. It must be accounted for if the probe is used for flow temperature measurements as well. Therefore, a simplified self heating model is developed in order to quantify the influence of the self heating effects in terms of the FRAP-HT probe.

For the model, following assumptions are made:

- Steady flow, with negligible recovery temperature effects (low dynamic head).
- High thermal conductivity of the 2.5mm diameter probe tip.
- Low thermal conductivity through the 3mm and 6mm shaft, due to epoxy and macor interface layers (e.g. thermal conductivity of the epoxy

k_e= 0.3 W/(m·K), thermal conductivity of macor: k_m= 1.45 W/(m·K)).

- Convection therefore takes place only at the probe tip.
- Heat transfer due to radiation is negligible, due to small differences in temperature between the flow and the 2.5mm probe tip.

The parts considered for the thermal budget are sketched in Fig. 3-24:
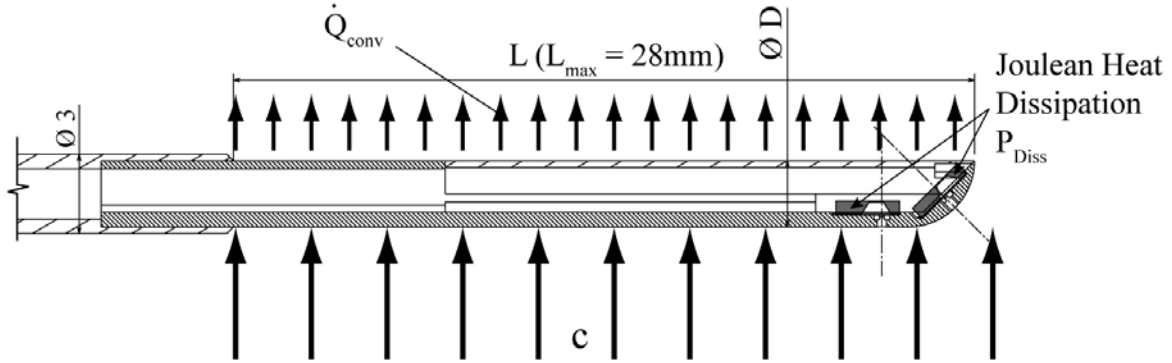

Fig. 3-24   FRAP-HT probe tip thermal budget for self heating estimation.

The resulting system equation is therefore:

$$- P_{Diss} + \dot{Q}_{conv} = -n \cdot R \cdot I_E^2 + \dot{Q}_{conv} = 0$$

The convective heat dissipation is defined as:

$$\dot{Q}_{conv} = h \cdot A \cdot (T_{sensor} - T_{Fluid}) = \frac{k_f}{D} \cdot \overline{Nu_D} \cdot \pi D L \cdot \Delta T$$

The Nusselt number $\overline{Nu_D}$ characteristic in air has been investigated by Hilpert, (e.g. presented by Incropera [86]) using following analytical approach for a Reynolds number range of *40<Re<4000*:

$$\overline{Nu_D} \cong 0.615 \cdot Re^{0.466}$$

After rearranging the system equation, the self heating effect in air results in an over-temperature defined as:

$$\Delta T = \frac{n \cdot R \cdot I_E^2}{k_f \cdot \pi} \cdot \frac{1}{0.615} \cdot \left(\frac{\upsilon}{D}\right)^{0.466} \cdot \frac{1}{L \cdot c^{0.466}}$$

where *n* equals to the number of sensors, *R* the transducer bridge resistance, I_E the sensor feeding current, k_f the thermal conductivity of air, υ the kinematic viscosity of air and *c* the velocity of the flow. The equation parameters *L* and *D*

are dimensional parameters of the probe head involved in the interaction.

Due to the lower bridge resistance of the sensors encapsulated in the new FRAP-HT probe compared to traditional FRAP probes, the resulting overheat between the fluid and the sensor is significantly reduced. Assuming for instance around 2/3 of the 2.5mm diameter shaft being involved in the heat interaction (*L=18mm*) and flow velocity of 20m/s around the probe, the resulting *ΔT* is in the order of 0.15K. The impact of the self-heating is even more reduced for higher velocities, e.g. *ΔT* tends to a constant value of 0.1K for flow speeds in the order of *Ma=0.1*.

The results obtained, imply that self-heating effects in regards to the newly developed FRAP-HT probe are of minor impact.

3.4.2   Recovery Temperature

As shown before, the self heating effects for the FRAP-HT probe are of negligible impact. However, the probe itself is capable of providing measurements of the membrane temperature. This temperature represents neither the static, nor the total gas temperature. This is due to an incomplete recovery of the airflow energy and the temperature rise may not be entirely due to an adiabatic process. Therefore a recovery factor *r* is introduced to compensate for this non-ideal behavior of the gas:

$$r = 1 - \frac{2 \cdot c_p}{c^2_{abs,freejet}} \cdot (T_{tot,freejet} - T_{sensed,yaw}) \qquad (3.15)$$

$T_{sensed,yaw}$ corresponds to the measured membrane temperature, whereas T_{tot} equals to the total temperature. The recovery factor *r* is therefore calibratable for a specific probe. The calibration of the recovery factor is performed in the freejet facility for Mach numbers in a range between 0.1 and 0.7. The velocity parameters c_{abs} and the stagnation temperature of the freejet flow are determined from facility instrumentation.

Furthermore it has been shown by Roduner [87] that the recovery factor has a strong dependency on the flow temperature. Therefore, a recovery factor calibration is performed for three different flow temperatures within freejet.

The recovery distribution at freejet temperatures of 343K represents the highest continuous and stable operating condition. Furthermore the Mach number dependent recovery factor distribution is calibrated at two additional freejet temperatures, namely at 323K and 303K respectively (Fig. 3-25). The results show that there is a significant Mach number dependency of the recovery factor. Furthermore, a non-negligible temperature dependency of the
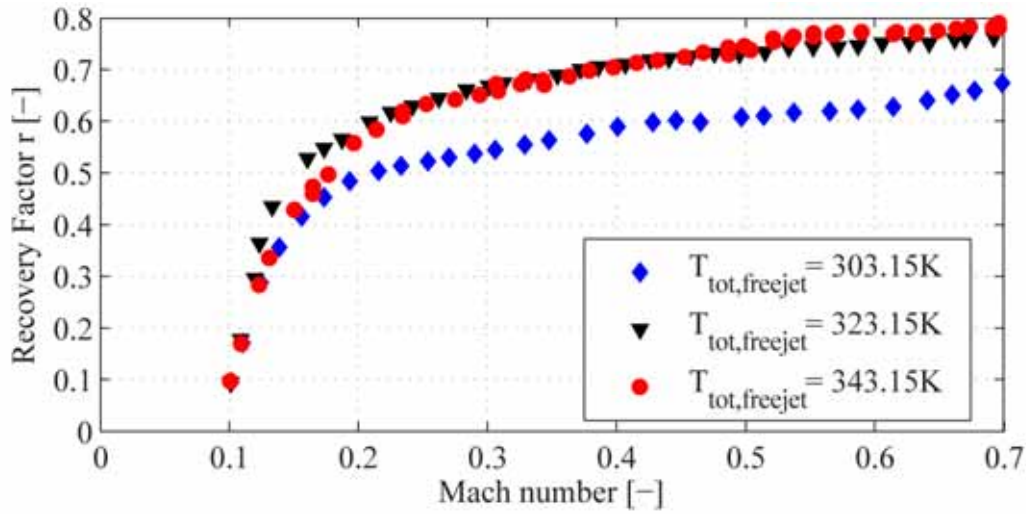
recovery factor can be seen.

Fig. 3-25 Mach number dependent recover factor distribution for three dif-
ferent freejet total temperature levels.

The calibrated recovery factor is used during measurements in an unknown flow field, to correct the sensed membrane temperatures and derive the total and static components of the flow temperature (Eqn. 3.16 and 3.17).

$$T_{stat} = T_{sensed, yaw} - r \cdot \frac{c_{abs}^2}{2 \cdot c_p} \tag{3.16}$$

$$T_{tot} = T_{stat} \cdot \left(1 + \frac{\kappa - 1}{2} \cdot Ma^2\right) \tag{3.17}$$

An iterative approach is required when the above equations are applied to an unknown flow field. The specific heat c_p of air is in a first iteration determined as a function of the sensed temperature T_{sensed} of the yaw sensitive transducer based on a 4th order polynomial fit [88]. The same idea underlies the calculation of the absolute velocity. In a first iteration the velocity is calculated from the resulting flow Mach number and the sensed temperature T_{sensed}. In a second iteration loop, the resulting static temperature is used to get the values for c_p and c_{abs} and from that again T_{stat}. In general, one iteration loop provides sufficient accuracy and the variation in static temperature occurs in the second decimal place. With the static temperature, the Mach number and the isentropic coefficient κ, the total temperature T_{tot} is calculated based on Eqn. 3.17.

As detailed in Fig. 3-25, the recovery factor is strongly dependent on the flow temperatures. In terms of the FRAP-HT probe it would therefore be of interest, to calibrate for the recovery factors at freejet operational points close

to the temperatures expected in later applications. However, due to limitations of the facility, 343K represents the highest temperature at which the freejet is operable in a stable manner. This therefore induces a certain uncertainty in the accuracy of the derived flow temperatures.

The yaw sensor tap is used to calculate the flow temperatures based on the recovery factor approach. If the yaw sensor is not aligned with the stagnation line of the mean flow, an additional uncertainty is induced, in the measurements of the respective flow temperatures.

It is concluded that the accuracy of the resulting temperatures measurements could be increased if the recovery factor calibration is performed at flow temperatures that match the temperatures in expected applications. A further improvement could be achieved by considering the yaw angle dependency of the recovery factor.

3.5   Control of Probe Shaft Vibrations

In order to control probe shaft vibrations in subsequent measurements, a strain gauge sensor is installed within the 6mm probe shaft. The sensor allows control of probe shaft vibration during measurements. Particularly during measurements in harsh environments of high temperature flows, vibrations of the probe in the eigenfrequency spectra of the probe have to be avoided in order to protect the probe from mechanical failure. This sub-chapter therefore discusses the probe eigenfrequencies for variations in the clamping position and suggests for possible damping devices in order to counteract possible probe excitations.

3.5.1   Probe Shaft Eigenfrequency

The installation of the FRAP-HT probe is strongly dependent on the respective facility. This is mainly related to accessibility issues and leads to large variations in the length between the probe clamping position and the tip. More details about the probe setup ahead of measurements are provided in chapter 4.

Due to the large variations in installation length, the FRAP-HT integrated strain gauge sensor is prior to any measurements used to derive the probe shaft eigenfrequencies for varying installation lengths. The operational capability of the strain gauge device is demonstrated by comparing the results to a performed FEM modal analysis. Fig. 3-26 details the FEM model and shows the FRAP-HT probe together with the assembly clamping module. Several

eigenfrequency modes are identified from the FEM modal analysis. However the mode most likely occurring with such an installation is the first mode.
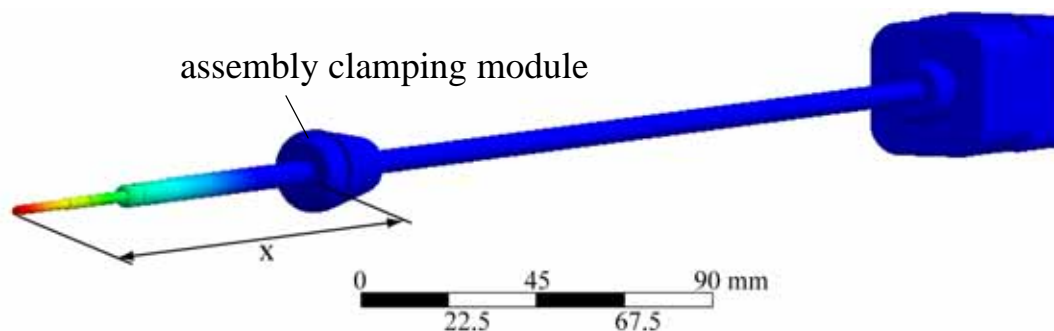

Fig. 3-26   Sketch of FEM model, including definition of probe tip to clamping distance x.

The focus in the experimental approach is therefore on the first mode. In the experimental test, the FRAP-HT is clamped for installation lengths *x* that are varied from 160mm to 400mm in steps of 40mm. For each length, the probe tip is excited with an impulse input force.

The instantaneous strain gauge output signal is acquired by means of the measurement system described in chapter 4. The sampling frequency is 200kHz and the signal is acquired in AC mode, in a range of ±0.1V around the expected DC mean of the signal (7.03V).

In a first approach, an impulse force hammer was used to excite the probe. However, the results were not satisfactory due to difficulties in synchronizing the pulse with the signal acquisition. Better results have been achieved by the following actions: bending the probe, starting the data acquisition and releasing the probe during acquisition. An example of an acquired raw signal is presented in Fig. 3-27.
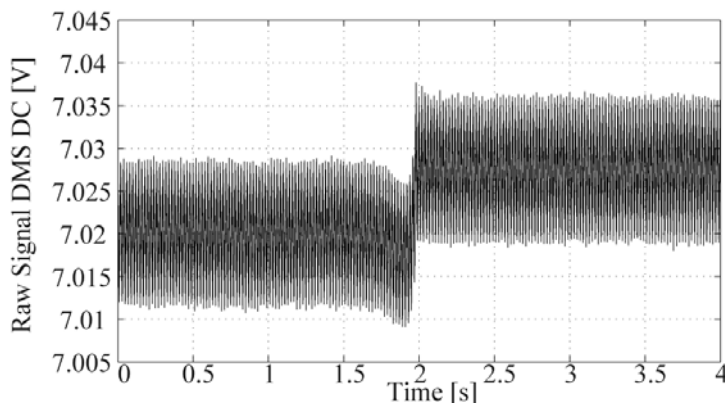
Fig. 3-27   Measured raw signal of strain gauge during eigenfrequency test.

Fig. 3-27 details the step in the DC signal after 2s in acquisition time due to releasing the bending moment on the probe shaft. Furthermore it details a

permanent and strong noise content. The frequency of that noise is 50Hz and most probably related to the power grid influencing the sensor signal.

In order to reduce the significance of the noise impact, the raw signals are filtered and a time-windowed frequency analysis is performed on the filtered signals. The results for one probe installation length are presented in Fig. 3-28.
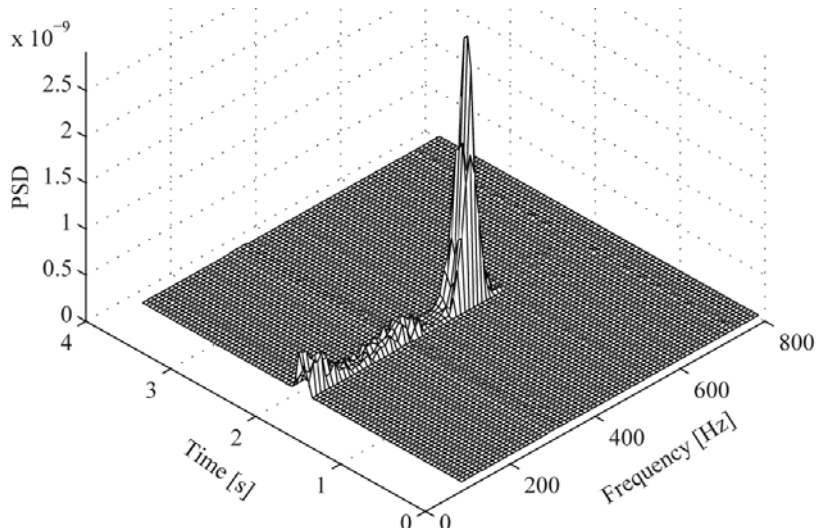

Fig. 3-28   1st Mode visualized by running window PSD for 120mm probe tip-to clamping distance.

Finally, the measured eigenfrequencies are summarized in Fig. 3-29 and compared to the results of the first mode eigenfrequencies obtained from the FEM modal analysis.

The results show a good overall agreement over the full range. Possible reasons for the small variations between the experiment and FEM analysis at 160mm, 200mm and 250mm length are due to some simplifications in the FEM model as well as due to some issues arising in the experiment at low clamping distances. These issues are related to difficulties in exciting the probe shaft due to reduced accessibility.

As an additional test, the fixed-end moment was varied for a constant installation length x. However, no clear trends in variations of the eigenfrequency were observed.

It can be concluded, that the strain gauge mounted on the 6mm shaft of the FRAP-HT probe can be used to monitor possible probe vibrations. In order to actively counteract such vibrations, an active damping device would be required. There are several ways to obtain such an active damping device. One possibility would be to use the principle of energy dissipation with shunted piezo-ceramics, which allows the conversion of mechanical energy into

electrical energy and vice versa. A second option would be to actively control and modify the stiffness of the probe shaft by a piezo-tube. Independent of the chosen solution, a control system is also required in order to allow a real-time control of possible probe shaft vibrations.
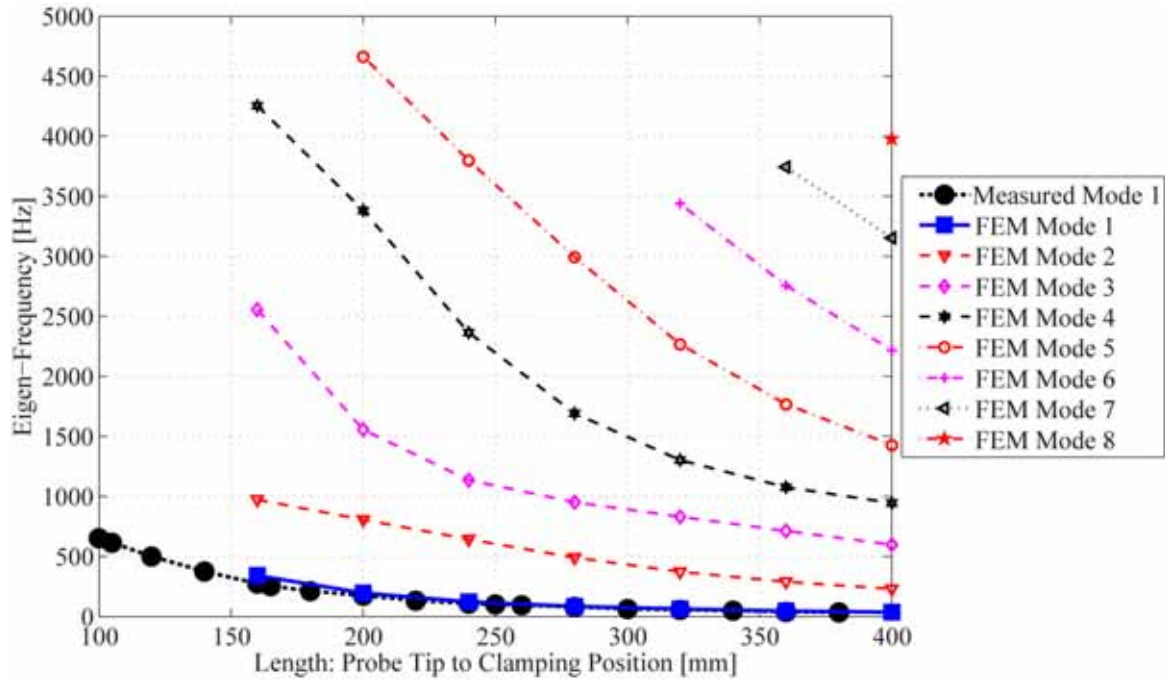

Fig. 3-29   Measured eigenfrequencies versus resulting eigenfrequencies out of ANSYS FEM modal analysis.

3.6   **Summary of Probe Characteristics**

The newly developed cylindrical FRAP-HT probe head has a diameter of 2.5mm. The pressure tap related to the yaw angle is 3.5mm from the probe tip at an angle of 0°. The pitch sensitive tap is located 0.73mm from the probe tip and at an angle of 45° from the probe axis on a shaped probe head. The pitch sensitive as well as the yaw sensitive pressure tap holes have a diameter of 0.35mm.

The primary elements of the probe are two piezo resistive pressure transducers that are used to measure the unsteady pressure and unsteady velocity field, as well as the steady temperature. A protection shield is designed in the cavity of the probe pressure taps in order to further increase the probe robustness in harsh turbomachinery environments. This is particularly important for industrial applications in order to prevent any damage to the probe tip and the sensors due to particle impacts. The two piezo resistive pressure transducers enable the measurement of the unsteady angles φ and γ,

as well as P_{tot}, P_{stat} and *Ma*, using the virtual four-sensor technique (chapter 3.3.3). Furthermore, the steady (1 Hz) flow temperature is measured.

Additional two sensors are installed on the 6mm probe shaft, 100mm behind the probe tip to allow a much higher degree of robustness in the use of this probe. The sensors are embedded in a slot around the circumference of the probe shaft. The slot depth is 0.5mm and the circumference is separated into two parts in order to embed a strain gauge sensor on one of the semi-cylindrical planes, and a PT100 temperature sensor on the other semi-cylindrical plane. The strain gauge sensor is used to monitor probe shaft vibration. The temperature sensor in the shaft is used to thermally manage the probe.

4   Measurement System and Data Reduction

The unsteady flow in a turbomachine can be measured with different techniques such as the hot-wire anemometry, laser doppler anemometry (LDA) or pneumatic and fast response pressure probes. The latter two techniques have the advantage of measuring the local total and static pressures, in addition to the flow velocities, as opposed to the first two techniques. In the field of turbomachinery the pressure distribution is of particular interest to the designer. A technique that provides measurement of the pressure quantities and the velocity is the ideal tool for understanding the complex physics of unsteady flows. Unsteady measurements require a high degree of accuracy in the complete measurement chain and all the procedures within this chain. Therefore, substantial efforts have been applied at the Laboratory for Energy Conversion to develop both the aerodynamic probes for measuring in turbomachinery in an unsteady manner, as well as to continuously develop the measurement system and the data reduction techniques that facilitate the application of the fast response measurement technology in a time and cost efficient manner.

The development efforts at the Laboratory have seen major steps and improvements of the FRAP technique for measuring time resolved flow fields in turbines or compressors. The FRAP system has reached a high degree of user-friendliness, which allows FRAP to be also used in an industrial environment. This chapter therefore gives an insight into the additional hardware measurement chain needed in order to allow both, steady pneumatic probe measurements, as well as high frequency fast response aerodynamic probe measurements in turbomachines.

Furthermore an overview of the data reduction methodology for both, pneumatic probe measurements, as well as FRAP-HT measurements is given. Finally chapter 4.8 presents the idea of an adaptive measurement algorithm that allows to further improve the time and cost efficiency in the performance of multiple traversing (area) measurements.

4.1   Measurement System Overview

The measurement system is designed as a stand-alone system that consists of a set of different 2-sensor FRAP probes, various multi-hole pneumatic probes and a dummy probe shaft, together with the measurement equipment that is the FRAP measurement tower. The tower includes a PPU (power

pressure unit) that supplies the required pressure for operating the FRAP as well as the electronic connections to the FRAP sensor. The system also includes a fast PC for the data acquisition of the signals, the power unit for the probe traversing system, a DRUCK pressure supply unit and a LCD monitor. The system also includes a 2-axis probe traversing system for the radial immersion of the probe into the facility as well as for yawing the probe to different flow angles during the measurements. An additional measurement rack is part of the overall rack and contains KELLER pressure transducers, in order to connect pneumatic multi hole probes (up to 5-hole probes). Furthermore the system includes an additional measurement rack, needed in case of FRAP-HT measurements in order to connect and condition the shaft strain gauge and the shaft PT100 sensors.

The FRAP system is fully automated and allows area-wise flow measurements of several thousand grid points within a one day-long measurement campaign. The data reduction time for typically 40-70GB of FRAP data lasts less than the measurement campaign itself, avoiding a bottleneck in the reduction of unsteady data.

An overview of the FRAP system as described in this chapter is shown in Fig. 4-1. As described above, the main parts of the FRAP system are the FRAP probe, the power pressure unit (PPU), the 2-axis probe traversing system with its power supply unit, the pressure supply DRUCK DPI520 and a fast pentium 4 PC for measuring and analyzing the FRAP data but also to control the FRAP system during the measurements. In terms of pneumatic probe measurements, the PPU is not used. Instead, the pneumatic measurement rack is used, to connect the ports of the pneumatic probe directly to the ports on the rack.

The key device of the FRAP system is obviously the FRAP probe itself which has two built-in miniature pressure sensors within the probe head. The probe sensors are all calibrated with respect to pressure and temperature. The probe heads are aerodynamically calibrated at different Mach numbers in order to relate the measured local probe pressures (with pressure tap) to the actual flow conditions such as total and static pressures, Mach numbers and flow angles. The probe sensor calibration mode is based on a direct parametric model (interpolation curves) for the calibration of the pressure sensor (Wheatstone bridge) voltage *U(pressure)* and *Ue(temperature)* to the actual pressures and temperatures. The aerodynamic model is also based on a direct parametric model using four pressure readings P1 to P4 and relating them to the calibration coefficients for flow angles and pressures. The four pressures are obtained from a virtual 4-sensor measurement mode with the 2-sensor

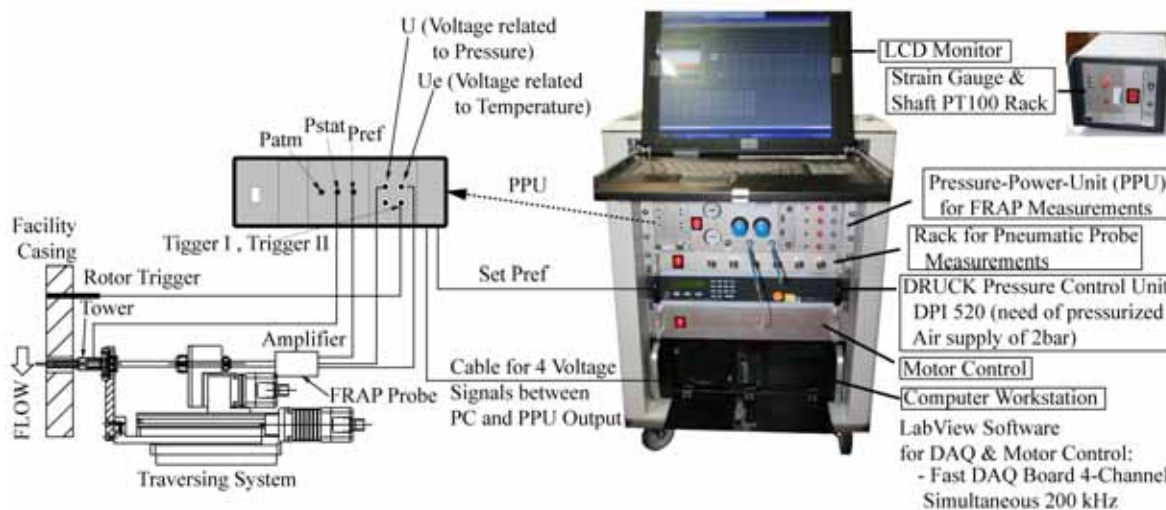probe. A description of the measurement concept is given in chapter 3.3.3.

Fig. 4-1   Overview of FRAP system.

The second key component of the FRAP system is the power-pressure-unit (PPU) that is used to supply the reference pressures for operating the FRAP probe as well as a signal port (connectors) for the FRAP probe. Furthermore it includes two optical Schmitt triggers that are used to generate the rotor trigger signal that is a key signal when measuring unsteady flows.

The FRAP system is numerically controlled with LabView VIs, that allow fully automated measurements and flexible control of the different units within the system. The main user interface (MUI) of the FRAP system provides an overview of all relevant steps and units of the FRAP system that are needed during the FRAP measurements (see Fig. 4-2). The MUI consists of 7 different sub-modules that are used to control the FRAP system. It is also used as a monitoring interface during the setup of the system ahead of the measurements. The measurement tasks are all started within the MUI environment. The data reduction which is conducted after the completion of the measurement run, is not done with the MUI but is based on MATLAB routines, that are included in the HERKULES data reduction package for the FRAP (see chapter 4.7).

The FRAP system is operated automatically during the traversing tasks in "batch-mode" style, which reduces the effort of user interaction and considerably reduces too the measurement time. Based on traversing task files, the probe is radially traversed within the flow field to different flow angles and radial grid points that are all predefined within the task-file.

After the completion of the FRAP measurement campaign, for example an

area traverse with 2000 grid points, a total amount of nearly 70GB raw data needs to be processed. For this task, the software package HERKULES (MAIN_HERKULES) that is written in MATLAB language is used to reduce the huge amount of data within some hours on the FRAP PC. The data reduction is controlled by a user-defined parameter file that includes all relevant information in order to allow a batch-mode data reduction without user interaction. The results of the FRAP measurements are finally visualized with the open-source routine Optic_Herkules (that is written in Matlab language) that can be used to produce space-time diagrams of a flow quantity and even animation movies of the flow field including also plots of secondary flow vectors.

4.2   FRAP User Control Interface (LabView)

The initialization and start of a FRAP measurement is always done with the master user interface panel (Virtual instruments in LabView). This interface consists of only one window, that includes all relevant control parameter and indicator for moving the probe within in the flow field, starting the traverse tasks and setting up the probe's signal acquisition and pressure supply system. The master user interface (MUI) is shown in Fig. 4-2.

The window of the MUI is split into different subparts, for the probe reference pressure supply, the signal acquisition boards, signal monitoring, traversing system controller as well as file management utilities and PPU calibration interfaces in order to pre-calibrate the pressure supply system ahead of any FRAP measurement campaign. The different subparts are labeled with numbers and explained within this section of the thesis. The different parts are listed in the following with corresponding numbers (in parentheses) as:

- Pressure Control of DPI520 (I)
- Monitoring of Probe/Trigger Voltage Signals (II)
- Radial Traverse Interface (by Taskfile) (III)
- Monitoring of Probe Traversing (IV)
- Data Acquisition Panel Interface (V)
- File-Management Interface (VI)
- PPU Calibration Interface (VII)

Due to the single window MUI the FRAP measurements are easily

controlled and the FRAP user always has a good overview of the measurement progress during for example FRAP area field traverses, that can last up to 8 hours of runtime.
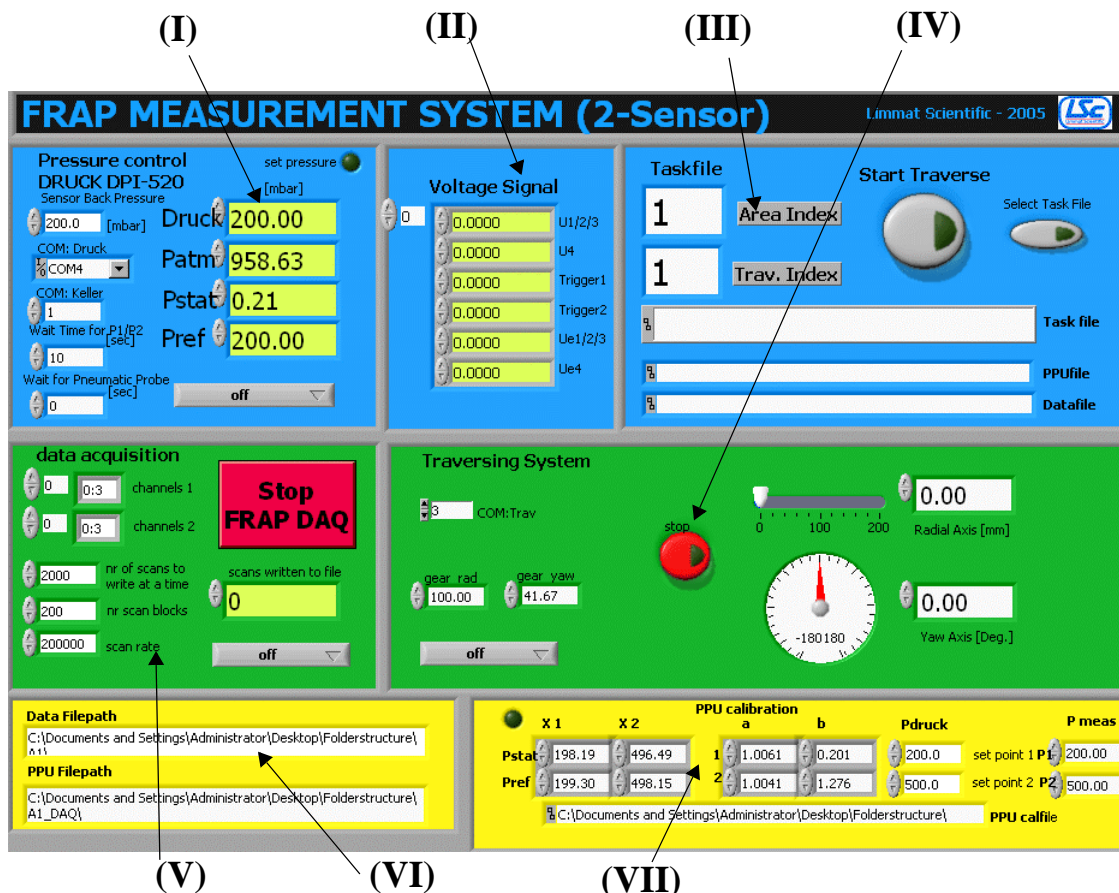
Fig. 4-2   FRAP (iTAP-2S v6.1) master control panel (LabView).

4.2.1   Probe Pressure Control - (I)

In the first module of the MUI the reference back pressure P_{ref} of the FRAP probe is controlled. The P_{ref} pressure is used to set a stationary relative back pressure in the cavity of the probe head behind the pressure sensor. This back pressure is always higher than the maximum expected total pressure within the flow field of the corresponding flow area. Typically an over-pressure of 200-300mbar is setup for P_{ref} when doing a FRAP traverse. The expected max. total pressure within the flow area is known from the rig operating point and the design intention for the turbine or compressor stage.

This sub-module monitors the back pressure of the probe P_{ref}, the pressure P_{stat} within the tower of the probe in the park-position and the local atmospheric pressure P_{atm} at the test rig. The P_{stat} pressure is equal to the static pressure within the tower-plenum of the probe when holding the probe at its park-position (idle state) and ahead of any radial traverse. Most test rigs

already monitor this pressure within their fixed instrumentation of the rig for this traversing plane and traversing hole. The fourth pressure (DRUCK) denotes the actual pressure of the DRUCK pressure supply controller DPI520, that is used to provide an accurate reference pressure to the probe.

4.2.2   Monitoring of Probe and Trigger Signal - (II)

The voltage signals for the 2-sensor FRAP probe for U, Ue and the trigger voltage of both triggers are monitored for every measurement run with the data acquisition system. The indicators for this submenu (II) of the MUI always show the time averaged value for a given measurement time of i.e. 2 seconds for all relevant channels (6 out of 8 used for FRAP 2-sensor probe with two triggers). The first four signals, that are the pressure sensitive voltage U of both sensors and the trigger voltage for trigger 1 and 2 are acquired by the first analog/digital board and displayed. The second DAQ-board gets the temperature sensitive signals of the FRAP probe that is Ue (quasi steady) for both sensors and displays their time averaged value in the 5th and 6th line.

Both DAQ cards are linked and used for simultaneous signal scanning of eight channels in total, out of which only 4 channels for the FRAP and two for the rotor and blade trigger are used (2 spare). The monitoring of the FRAP and trigger signal is very important as it provides the FRAP user the information of the state of the FRAP probe (any signal problems such as a loss of the signal due to a probe damage).

4.2.3   Start Radial Traverse Interface - (III)

The FRAP radial traverse is always started with interface tools as given in this submenu of the MUI. These tools are used for specifying the actual area and traverse indices x and y respectively for the annotation of the FRAP binary raw data files. The submenu also displays the actual selected taskfile, the filename of the generated PPU-file (P_{atm}, P_{stat}, P_{ref}, etc.) and the raw data binary file for every measurement point. The grid points for every new radial traverse are defined by selecting the corresponding taskfile.

4.2.4   Monitoring of Probe Traversing - (IV)

The FRAP traversing system can either be controller manually by hand or is automatically controlled by the FRAP system when doing radial traverses with a taskfile.

4.2.5   Data Acquisition Setup - (V)

This part of the MUI is used for the setup of the FRAP data acquisition of

the voltage signals using two high speed simultaneous analog/digital input boards at max. sampling rates of 200 kHz for all 8 eight channels (2x4).

4.2.6   Data File Management - (VI)

The FRAP DAQ system creates two different type of files during a radial traverse. The FRAP raw signals is stored in binary format. The constant pressures from the PPU are stored within the PPU file for every individual radial traverse.

4.2.7   PPU Calibration Interface -(VII)

The FRAP system uses a PPU for the control and pressure supply of the FRAP probe. This PPU includes 3 temperature compensated pressure transducers with quasi long term stability over one day. The FRAP tower experiences various influences from the local environment (heating up of the system due to the rig operation) during a measurement run. This could cause false pressure readings for the Keller transducers, which can reach as much as some [mbar] between two different days. Therefore ahead of any measurements, the Keller transducers are calibrated versus a unique pressure transducer. The current FRAP system uses the DRUCK built-in pressure transducer (not Keller) as the reference sensor for cross-calibrating the whole PPU system and its pressure transducers (Keller). These are the P_{ref} and P_{stat} transducers (both relative pressure transducers). When doing a PPU calibration these two sensors are automatically switched together and a common pressure is supplied to them by the DRUCK system (reference). The PPU is cross-calibrated by using this reference pressure and correcting the Keller pressure transducer signals (see also PPU section). The absolute pressure transducer is not calibrated during the PPU calibration but has a sufficient long term stability.

4.3   Power Pressure Unit (PPU)

The PPU is one of the key components of the FRAP measurement tower, that includes the pressure supply system for the FRAP probe, the connectors for the signals of the FRAP pressure sensor as well as the connections for the optical rotor or blade trigger (Fig. 4-3).

The PPU is used to supply the back reference pressure P_{ref} to the probe during the measurements. By a set of different pressure reducing valves and pressure switching valves the required P_{ref} is setup for the measurement run as well as during the offset-gain corrections at the beginning and end of every

radial traverse. The system is controlled using the LabView interface as explained in the previous section. Apart of the pressure valves the PPU also includes high accuracy Keller pressure transducers for measurement of the corrected pressures for P_{ref}, P_{stat} and P_{atm} (see Fig. 4-4). These pressures (steady) are measured in parallel to the FRAP probe and used for the correction of the offset-gain drift of the FRAP pressure sensor. The Keller pressure transducers are temperature compensated and show a long time stability that is essential for accurate FRAP measurements.
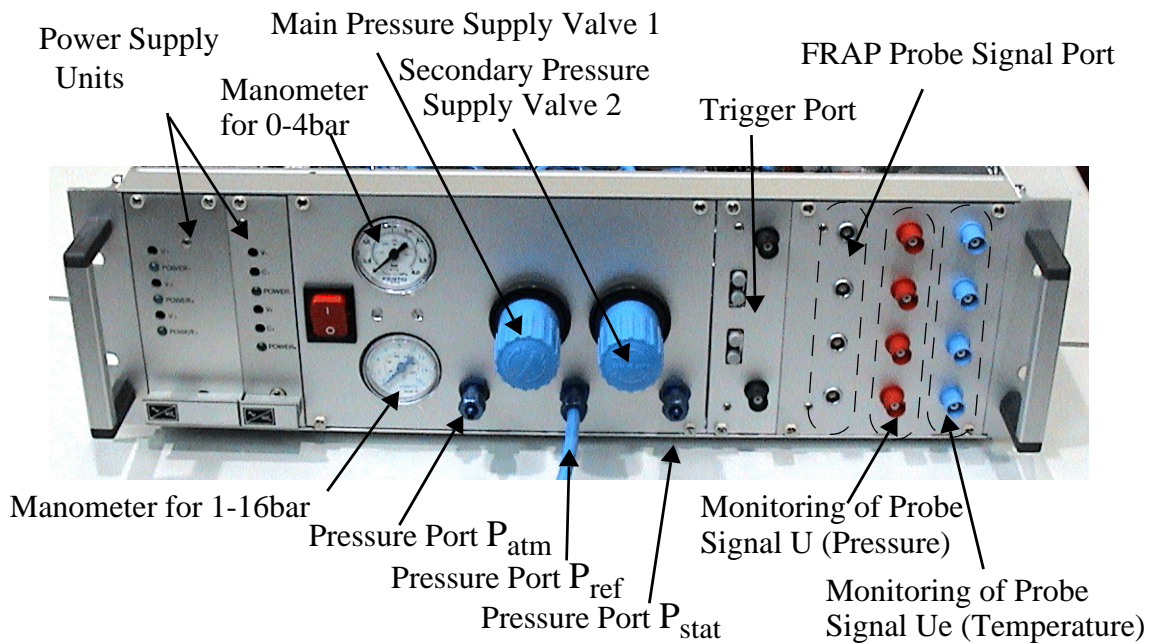
Fig. 4-3   FRAP system-Power-Pressure-Unit PPU, front side view.
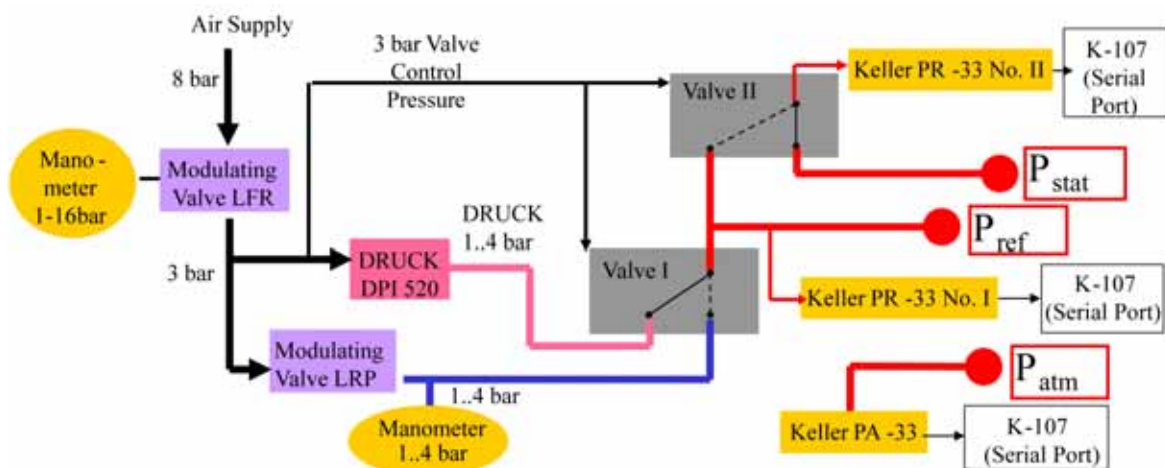
Fig. 4-4   PPU pressure supply schematic.

The PPU needs a main pressure supply of around 8bar. A first pressure

reduction valve is used to lower the pressure from 8bar down to 3bar (typically). The pressure valve is operated manually. A manometer shows the supplied pressure on the front side of the PPU. The reduced 3-bar pressure is supplied for a second pressure reducing valve (LRP in Fig. 4-4). The output of the pressure supply is displayed on an additional manometer and used for the second pressure level of the offset-gain measurement (see later section). The 3bar pressure is also used as a pressure supply for the DRUCK DPI520 pressure unit, that is numerically controllable by the LabView FRAP interface. The DPI520 reduces the pressure from 3bar down to the desired P_{ref} for the FRAP probe. The P_{ref} pressure must be adapted to the expected maximum total pressure within the measurement flow area P_{max} and adding typically 200mbar to this value, such that the pressure transducer is always preloaded from inside the probe and the chip remains attached to the probe tip inner wall.

The 3-bar pressure is also necessary for activating the two pressure valve switches (grey box in Fig. 4-4). These valves can also be operated at vacuum conditions when doing FRAP measurements in very low pressure field (under atmospheric). This feature is useful for measurements in closed loop facilities.

The first valve (VALVE I) is used to switch between the DPI520 pressure supply P_{ref} and the second P_{ref} of the manually controlled valve. The position of the valve is set automatically by the FRAP system when performing an offset-gain measurement. When doing offset-gain measurements, the FRAP system provides two different pressure levels P_{ref1} and P_{ref2} to the back side of the probe that are both at least 200 and 400mbar above the static pressure within the tower position of the probe. The actual tower pressure is given in the P_{stat} pressure reading when connecting the tower plenum to the pressure sensor for P_{stat} (Keller transducer) using the pneumatic connection at the PPU front panel.

4.3.1   Offset-Gain Correction of Probe Signal

In normal measurement mode, the valve II decouples the P_{stat} and P_{ref} connections from each other. The valve I is set to the position where the DPI520 pressure level is connected to the FRAP probe (default position). When doing an offset-gain measurement, the valve I is in default position. The FRAP system performs a single point measurement. The probe must be in park position and outside of the flow field. The measured FRAP probe pressure is compared to the measured pressures of the Keller transducers PR-33. Then the valve I is switched from the DPI520 (P_{ref1}) to the manually controlled pressure level P_{ref2} and supplies the second pressure on the back side of the FRAP

probe. Again, the Keller transducers measure in parallel to the FRAP probe the same pressures and compare the signals with each other. The P_{ref1} pressure is never the same as the P_{ref2} pressure (typically 200-300mbar difference) in order to avoid error of the offset-gain correction. From the first and second pressure measurements during the offset-gain cycle (two pressures from Keller and two pressures from the FRAP probe) a correction curve is defined between the non-drifting Keller signals and the drifted FRAP pressure signal (linear fit). The offset-gain correction parameters slope (gain) and offset between both curves are automatically used in the HERKULES FRAP data analysis routines to correct the measured FRAP signal for every individual radial traverse. In order to increase the measurement accuracy the offset-gain cycle is performed at the beginning and end of every radial traverse. The offset-gain correction parameter are then linearly interpolated between the starting and ending state of the traverse using a running index for the record numbers of every FRAP signal file.

4.3.2   PPU Calibration

Before a FRAP measurement is started, the PPU needs to be calibrated. For this purpose, the built-in pressure transducer of the DRUCK DPI520 is used as the reference value for the calibration of the Keller transducers (typically only offset correction). The gain drift of the Keller transducers is minimal. The PPU calibration is started within the FRAP user interface (LabView). The system will switch the valve II into PPU calibration mode and connect the P_{ref} and P_{stat} tubes together. Both Keller transducers PR-33 (Nr.1 and Nr.2) measure the same pressure, that is supplied by the DPI520 system. The DPI520 provides two different pressures to the Keller transducers and performs a linear correction between the DRUCK and Keller system for getting the offset-gain coefficients (analog to the FRAP offset-gain measurements).

4.3.3   Trigger Unit

The characteristics and accuracy of the trigger signal play a major role in the FRAP measurement system. Without an accurate trigger the FRAP measurement can not be done with any FRAP probe and in particular with 2-sensor probes in virtual 4-sensor mode. The function of the trigger is to relate accurately the different pressure signals for *P1* to *P4* measurements in virtual 4-sensor mode with respect to time and rotor-to-stator phase angle. Out of the superposition of these signals the unsteady flow field is reconstructed. When using a wrong or poor accurate trigger the signals will show a phase-lag between the serially acquired data sets and finally lead to a non-periodic flow

field, that does not correspond to the real flow in a rotating machine. In extreme cases, certain flow features (i.e. blade wake at exit of rotor blade rows) will not be detected by the probe.

The PPU system provides two optical Schmitt triggers. The optical trigger sensor consists simply of a pair of two optical glass fibres that are aligned at a given angle relative to each other in order to capture the light reflections coming from the first fibre (red light from LED diode) and ending in the second fibre. The light is reflected on the surface of the rotating shaft and is gathered by the second fibre, that redirects the reflection intensity to the light receiving diode.
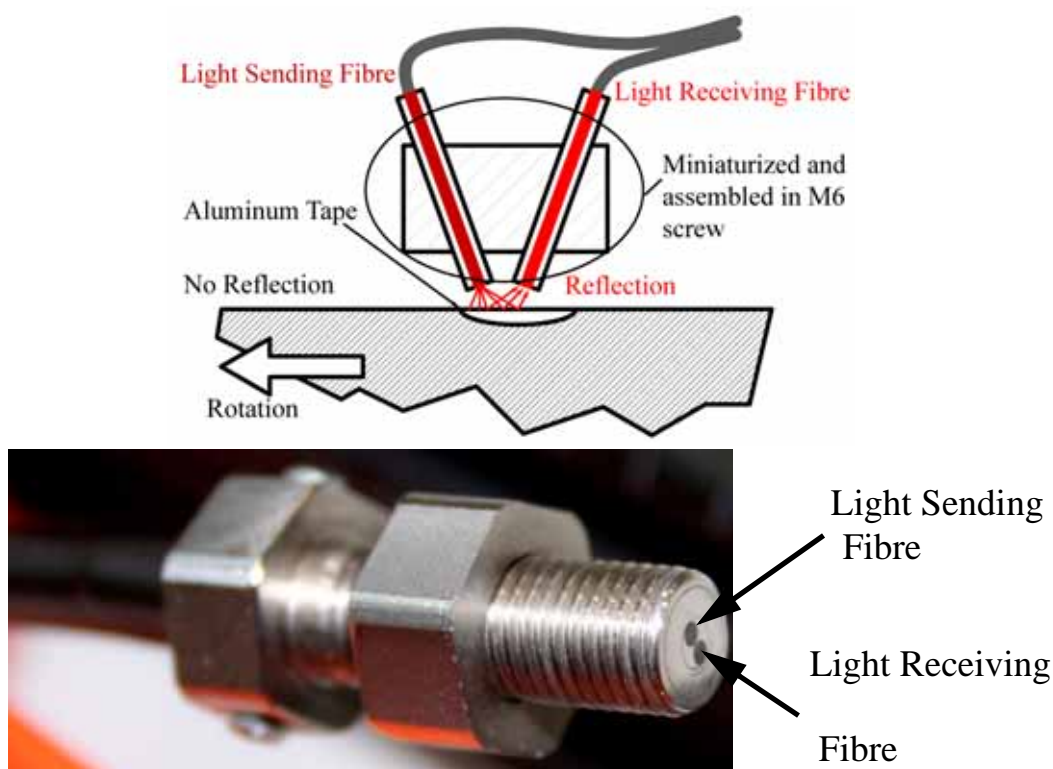
Fig. 4-5   *Working principle of optical trigger (top), and photograph, of assembled trigger mounted in an M6 screw (bottom).*

If the rotating shaft is of dark color and has a non-reflecting surface, then a white line of few centimeters in width is drawn axially on the shaft surface in order to create a variation of light reflection intensity when the shaft is rotating. This line will change the light reflection of the red LED coming from the first fibre cables, absorbed by the second fibre and registered by the light receiving diode. The system will change from 0V up to 5V until the white line has passed the trigger sensor and the dark surface prevents any reflection. It has been found, that aluminum tape is an ideal reflecting surface on a dark shaft. When facing a perfectly reflecting shaft for the trigger a dark line is

simply drawn and the trigger will operate accordingly but change its state from 5V down to 0V for any trigger event. This optical trigger is very fast and not a limiting factor for FRAP measurements.

4.4   Strain Gauge and Shaft PT100 Measurement Rack

The strain gauge and shaft PT100 measurement rack is used in terms of measurements by the new high temperature FRAP probe (Fig. 4-6). The rack works as power supply for the strain gauge and the shaft PT100 and at the same time is used to condition the output signals of the sensors. The conditioned signals are then fed by BNC connector cables to two channels of the fast DAQ cards (chapter 4.5) and sampled with 200kHz sampling frequency. In order to reduce possible electronic noise, the rack is shielded on its outside. Further shielding is installed in the inside of the rack to reduce possible noise from the power supply to the sensor signals within the rack.
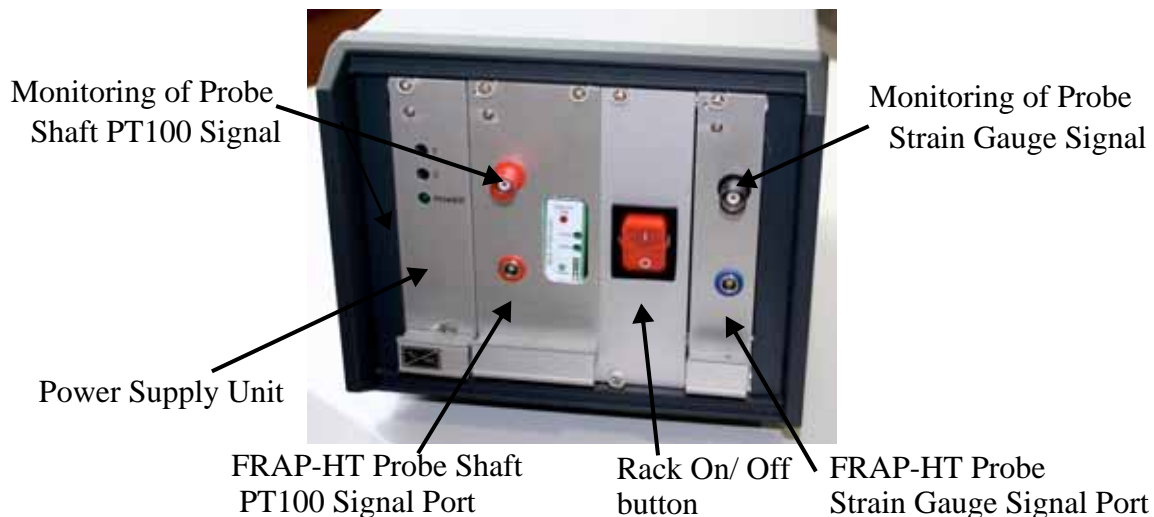
Fig. 4-6   FRAP-HT system-power unit for strain gauge and shaft PT100.

4.4.1   Signal Conditioning of Shaft PT100

For signal conditioning of the shaft PT100, a commercial temperature measuring transducer is used. The transducer converts the measured values of the PT100 sensor (IEC 751/EN 60 751) into electrically standardized analog signals. The sensor is supplied from the module with a low current. The resultant voltage drop is amplified in the module and converted into a signal, which is proportional to the temperature. To linearize the resistance characteristic, the measuring signal is fed back to the input. The output circuit provides the standardized analog signal. The device is used in a voltage output

mode and operated by an electrically isolated power supply. The setup of the device is adjusted to be used in 4-wire connection mode, working linear between 273K and 573K. The connections to the FRAP-HT probe are provided by shielded 4-wire cables. Adjustment potentiometers, which can be accessed on the front, offer the option of carrying out a measured distance adjustment (ZERO/SPAN). Some more details on the specification of the used transducer are given in Table 4-1.

Description	Value
INPUT:	
Supply current (PT 100)	1mA
Temperature range	273...573K
OUTPUT:	
Output signal	0...10 V
Maximum output signal	15 V
Load	$\geq 10 \, k\Omega$
Output signal at open circuit	> 11 V
GENERAL DATA:	
Supply voltage	20...30 V DC
Maximum current consumption	35 mA
Transmission error	$\leq 0.4\%$ of the final value
Temperature coefficient	$\leq 0.02\%/K$
ZERO and SPAN adjustment	$\pm 5\%$
Limit frequency	30 Hz
Step-response (10-90%)	11 ms
Test voltage: Supply/signal	750 V AC; 50 Hz, 1 minute
Transducer ambient temperature range	-253K to +338K

Table 4-1   Specifications of the shaft PT100 temperature measurement transducer.

4.4.2   Signal Conditioning of Strain Gauge

From an electronic perspective, the conventional Wheatstone bridge configuration for supplying power to the strain gauge installed in the FRAP-HT probe could not be employed. Instead, a constant current power supply was used with a step response time of 60kHz. The current was optimized for optimal noise to signal ratio, taking expected strain and heating into consideration. The connections to the FRAP-HT probe are provided by

shielded 2-wire cables. The strain was calculated using the following equation:

$$\varepsilon = \frac{U(t)}{U_0} \cdot \frac{1}{GF} \qquad\qquad (4.1)$$

where $U(t)$ is the measured voltage across a strain gauge and U_0 is the reference voltage due to strain gauge resistance of 350Ω and the constant current. The gauge factor GF represents the link between the strain a gauge experiences and the associated change in resistance. Given the above equation and the 24bit data acquisition system (+/-1V range) the strain resolution was $\Delta\varepsilon_{min} = 0.08\,\mu m/m$.

4.5   Fast Data Acquisition (DAQ) Boards

Two National Instruments Fast Data Acquisition boards (NI-4452) are used for the measurements of the FRAP probe and trigger signals at max. 200 kHz in a simultaneous manner.

4.6   Traversing System

When doing multiple area traverses with the FRAP probe measurement system a number of automated steps need to be performed. The FRAP probe is to be traversed to many different positions (along the span and the circumference) within the measurement volume in order to get the local probe pressures (*P1* to *P4*) for the evaluation of the unsteady flow field. In particular the positioning accuracy and positioning speed of a FRAP probe within the measurement area is to be kept high for any grid point and during the entire measurements of typically several hours for a 1000 grid point flow area. The required running rig hours for such measurements is an additional parameter that needs to be reduced as much as possible. Therefore, the FRAP probe has to be traversed at high traversing velocities within the measurement volumes in order to reduce rig cost and measurement time.

4.6.1   System Overview

The current FRAP probe traversing system is optimized for short duration area traverses with high precision and repeatable positioning accuracy of the probe. The system is controlled by the master FRAP unit (see section chapter 4.1) and positions the FRAP probe automatically to any grid points during one FRAP measurement run using a Task-File, that contains the relevant grid coordinates. The FRAP traversing system consists of the following units:

- Linear Traversing Unit   (radial position, blade span)
- Rotational Traversing Unit   (relative probe yaw angle)
- Gear Box   (transmission of rotating motion)
- Stepper Motors Power Units   (motion)
- Probe Clamp Unit   (holds probe shaft)
- Probe Task File   (grid points coordinates)

The 2-axes (radial immersion and roll angle) traverse system is implemented by the use of two Berger Lahr ICA-IFS stepper motors.

The probe is positioned in radial direction (for blade span) with the linear motion unit (stepper motor) as shown in Fig. 4-7. The probe shaft itself is clamped within a rotative traversing gear as marked by the dashed red line. The probe setup angle is set by the rotative motion drive (stepper motor) that transmits the rotative motion of the stepper motor through the connecting gear box onto the probe. Both stepper motors have a resolution of 20'000 steps for one full revolution.
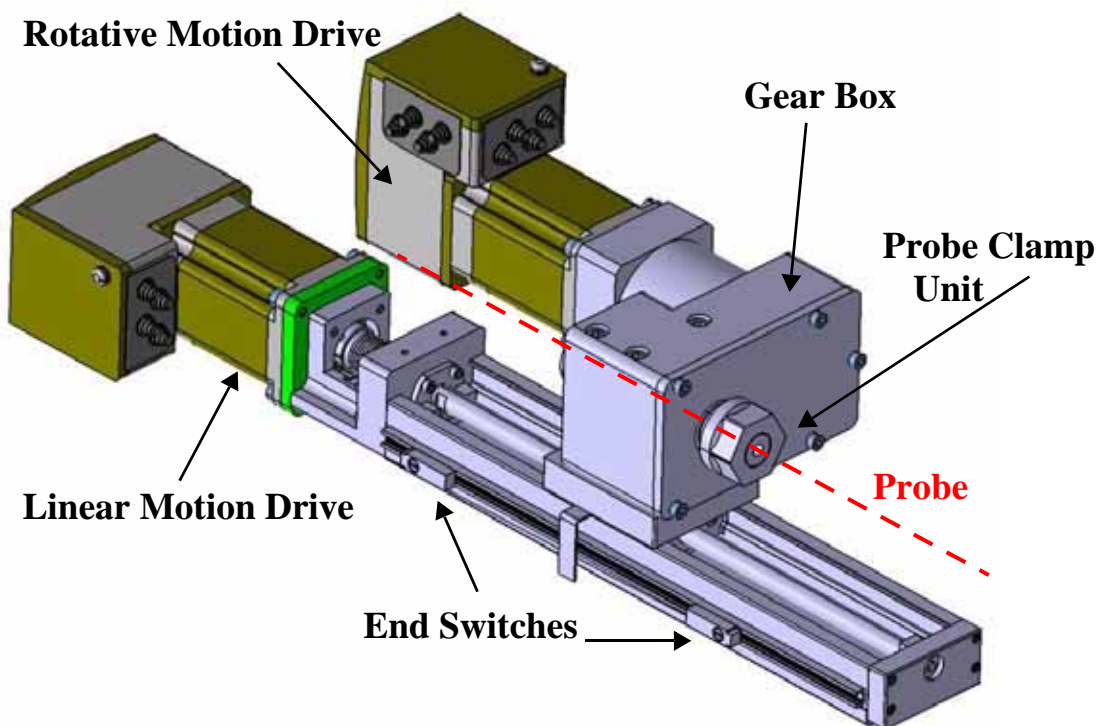
Fig. 4-7   FRAP traversing system.

The spindle of the linear axis uses a slope ratio of 10:1 (10mm radial motion for one full motor revolution).

The maximum and minimum positions of the linear motion drive (radial)

are limited by two end-switches on both sides of the traversing unit. The end-switches can be individually positioned according to the setup of the FRAP area traverse and the geometry of the rig. The entire traversing system is fixed to the test rig.

The probe is automatically positioned to different radial and circumferential grid points within the flow area during a FRAP area traverse. The coordinates and probe setup angles are defined within a Task-File. This file is individual for every area traverse, rig and operating point. The file contains the probe setup angle that is generally equal to the expected absolute flow yaw angle (design intention) for the blade row and operating condition. The probe has to be exposed to the main flow velocity vector within its calibration range of $\pm 24°$ in order to assure a reliable measurement of the unsteady flow field.

4.6.2   Motion Controller (LabView)

The probe traversing is controlled by a LabView based user interface panel. The virtual interface panel consists of two traversing axes, the linear motion (radial) and the probe yaw angle (rotation) as the second axis.

The linear motion is limited by two end-switches (movable) in order to prevent any damage of the probe. The rotational axis is not limited by any end-switches and therefore is covering the full 360° circle.

4.6.3   Probe Setup

4.6.3.1   Probe Alignment - Yaw AXIS

Of particular interest to the user is the correct and accurate alignment of the probe tip and probe relative coordinate system with respect to the traversing area and global research facility coordinate system. There are different ways to align a probe relative to the machine axis. Both, the pneumatic probes as well as the FRAP probes all use a squared box on the rear end of the probe. The upper surface of this red box defines the horizontal plane relative to the pressure tap of the probe tip. All probes are calibrated relatively to this plane using a water balance to zero the plane relative to the vertically aligned probe calibration freejet facility.

For vertically-oriented main flow test facilities the technique with the water balance can be easily adapted and used for zeroing the probe's reference plane relative to the ground (see Fig. 4-8). It is assumed, that the test rig is as well

perfectly aligned in vertical direction.
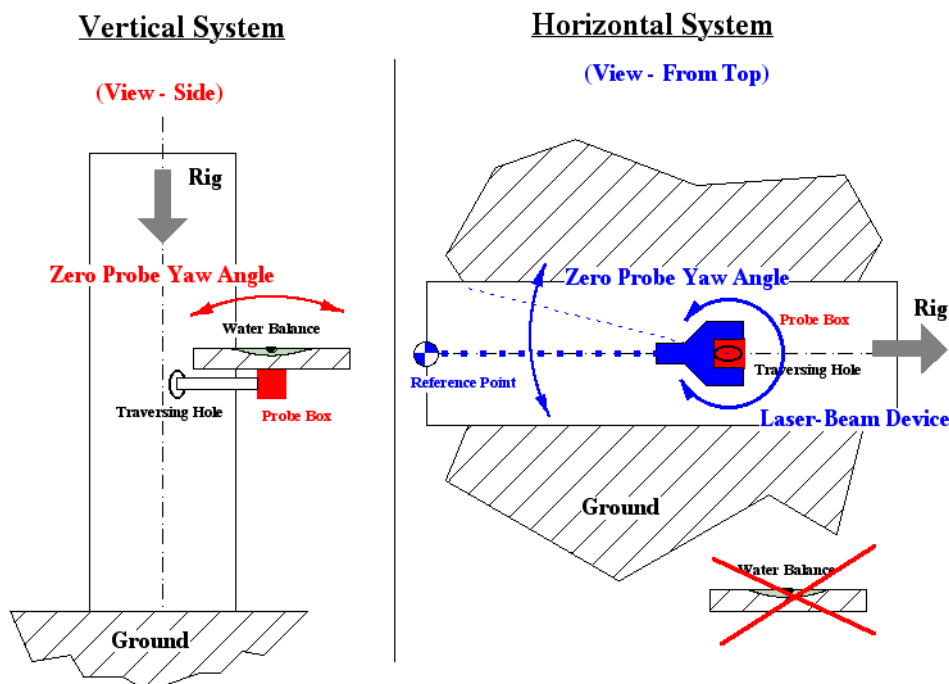
Fig. 4-8   Probe alignment concepts for vertical and horizontal test rigs.

For horizontally-oriented main flow facilities (which are those that are most often used), the water balance concept can not be used as seen in Fig. 4-8. The reference plane is perpendicular to the ground (not parallel) and therefore can not be used as a reference plane with the water balance concept. In this case a new probe setup system is used. The concept requires that the probe is on the maximum top position of the rig. The probe shaft is then defining the vertical axis and is seen as a single point when viewed from the top. The probe reference plane is pointed in the upstream direction of the flow. Then a C-shaped adapter with built-in laser beam device is attached to the red box. When yawing the probe with the traversing system to different angles, the laser beam will define a circle on the ground. The probe yaw angle is now simply yawed to the position, when this circle cuts the centre line of the test rig. In general, there is always a reference point on top of a facility (screw, bolts etc.).

There are cases, where the probe is neither in horizontal nor vertical position, but aligned in diagonal way. In this case, the water balance may be used in combination with the laser beam device. The device is only used as a support for defining a new reference plane and for positioning the water balance on the red box. The probe shaft is yawed until this new reference plane is aligned and parallel to the ground.

4.6.3.2   Probe Alignment - Radial Axis

The radial alignment steps for a probe relative to the test rig and traversing hole is much more complex, when compared with the setting up and zeroing of the probe yaw axis. Due to the radial penetration of the probe into the test rig a high risk of potential probe failure is present. An uncontrolled radial movement of the probe tip toward the hub section of an i.e. turbine endwall flow section can cause a damage of the probe and in extreme cases even a machine failure due to detached probe components within the blade rows. For this purpose, the traversing system uses two limit end-switches on both ends of the linear motion device (see Fig. 4-9). The radially moved probe holding platform carries a switch (sheet metal) that activates the end-switches when reaching the end positions on both sides. Both end switches can be positioned along the guidance metal at the relevant radial positions.
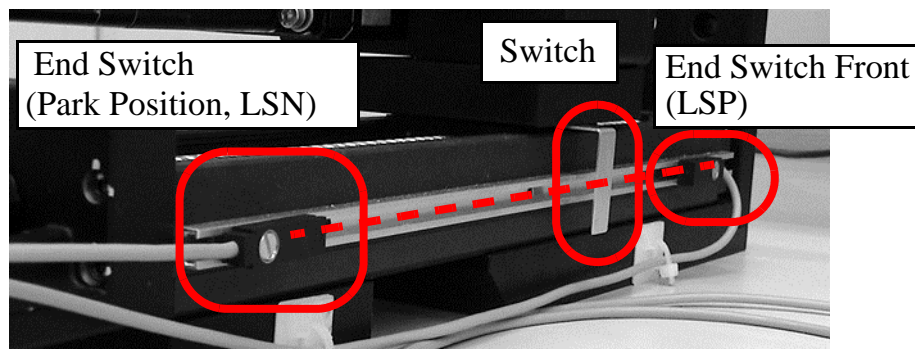
Fig. 4-9   End-switches on FRAP traversing system.

The maximum position of the front end-switch is normally defined as the distance between the probe holding nut (moving platform) and the connecting adapter plate of the traversing system. Ideally this distance should not be less than 30mm. The rear end-switch is normally put to its minimum position in order to have the probe tip out of the flow as far as possible. This position is called the "park-position" of the probe.

4.6.3.3   Use of Dummy Probe

The standard procedure for setting up a probe on the test rig is explained in this section of the thesis. Typically, the dummy probe (only probe shaft without probe tip) is first used to determine the real penetration length of the probe up to the hub endwall in the test rig (i.e. axial turbine). The concept with the dummy probe is shown in Fig. 4-10. Before mounting the dummy probe on the traversing system, the front end-switch (hub switch) is moved to the max. front position and the traversing gear is moved into this hub end-switch (over-shoot). The traversing system will show an error for the front end-switch and

immediately stops the traversing motion. This final position is equal to the maximum possible penetration depth of the traversing system when doing area traverses. When setting up a probe in this front position (with safety margin) the probe tip can never touch the hub endwall and therefore a damage by a misusage of the system is avoided.
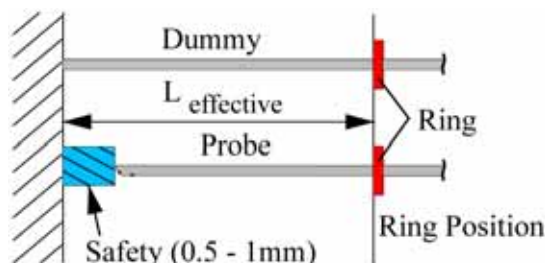
Fig. 4-10 Dummy probe concept and safety gap for FRAP probe.

4.6.3.4   Compensation of Probe Tip Diameter

The probe pressure center of the *P1* tap is never at the probe's tip but at some distance away from the tip (Fig. 4-11). This radial distance has to be taken into account when doing radial probe traverses with any kind of probes.
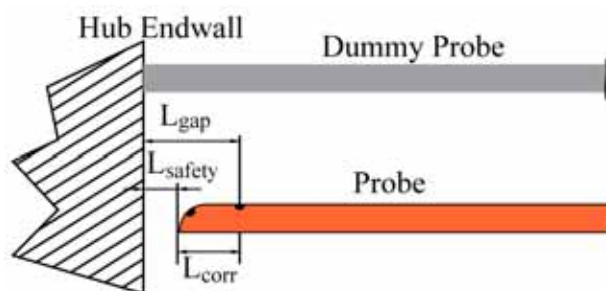
*Fig. 4-11   Radial correction of probe tip diameter (with over-shoot, dummy
        probe touches the hub endwall).*

For cobra shaped pneumatic probes this correction length is 0.45mm. For pneumatic 4-hole probes in FRAP style, the distance is significantly higher and therefore has to be taken into account for the definition of a respective measurement position. The radial coordinates have to be corrected by this gap and the added safety margin (see Fig. 4-11) of typically 1mm.

4.7   Data Reduction

This subchapter provides basic information on the data reduction procedures for both, FRAP-HT, as well as pneumatic probe data. Furthermore basic concepts about probe calibration modeling as well as on averaging procedures are provided.

4.7.1   Averaging Procedures

To compare time-resolved flow quantities such as velocity or flow angle history with time-mean data measured with pneumatic probes, data averaging is necessary. In general, probe data are taken on a structured grid of radial and circumferential points covering one pitch of a bladerow plus one circumferential position of the adjoining pitch. This is done for simplicity of postprocessing and for instance generating contour plots of measured data. An approach for using unstructured grids is presented in chapter 4.8.

If a structured grid is used, area measured data can be reduced to either pitchwise or radially averaged data, or over the entire pitch. The underlying discretization of the measured flow field is based on averaged values of the cell centers of the applied structured measurement grid. In general there are two averaging methods commonly used and applicable for both, steady pneumatic probe measurements, as well as unsteady FRAP-HT measurements. One method is based on an area average, whereas the other method is based on the mass flow-weighted-average. Depending on the flow parameter to be averaged, one of the two methods is chosen. Some details of the two methods are provided in chapter 4.7.1.1 and 4.7.1.2 respectively. A detailed analysis of appropriate averaging methods is given by Cumpsty and Horlock [89].

Additional methods applicable for unsteady measurements are phase-lock procedures and a simple time-averaging procedure. The phase-lock averaging (or ensemble averaging) procedure is widely used in the post-processing of unsteady data in order to resolve periodic flow structures [90]. By using this averaging technique the deterministic flow fluctuations are separated from stochastic and turbulent fluctuations. The method is therefore based on the facility's rotational frequency that is determined from optical trigger measurements (chapter 4.3.3). A time series of measured data is taken starting always at the same rotor relative trigger point $(x(t_1)...x(t_n)...x(t_N))$. By continuously measuring until the sampled data contain a sufficient number of rotations (m), the ensemble average for a certain spatial location and a certain relative blade position $(f(t_n))$ is derived from the $m \cdot N$ data samples by:

$$\tilde{x}(t_n) = \frac{1}{m} \cdot \sum_{i=1}^{m} x_i(t_n) \qquad (4.2)$$

In facilities with steady and therefore stable rotor speeds, the number of samples per averaging loop is constant, whereas in terms of unstable conditions, an additional time-base is required for each investigated flow

instability.

The time-averaging procedure is simple, but depending on the measurement set-up, its use must be considered very careful due to a lack in physical meaning (conservation-law). However, there are certain situations, for instance in vaneless centrifugal compressor applications, where a time-averaging procedure provides accurate results. This special case is discussed in chapter 8.6.1.

4.7.1.1   Area-Averaging

Non-convective flow quantities, such as static pressure or static temperature, are reduced by applying an area-weighted average. For this the local flow quantity x is weighted with the associated local area to calculate the averaged quantity $\bar{x}$. In terms of a structured and discrete measurement grid, the integral of Eqn. 4.3 can be expressed by a sum (Eqn. 4.5).

$$\bar{x} = \frac{1}{A} \cdot \int x dA \qquad (4.3)$$

$$dA = r \cdot dr \cdot d\theta \qquad (4.4)$$

$$\bar{x} = \frac{\sum x \cdot dA}{\sum dA} \qquad (4.5)$$

4.7.1.2   Mass flow-weighted Averaging

Convective flow quantities, such as total pressure, total temperature, are reduced by applying a mass flow-weighted average. For this the local flow quantity x is weighted with the associated local mass flow to calculate the averaged quantity $\bar{x}$. The mass flow of each cell is derived from the local values of the Mach number. Temperatures required for density and velocity are taken from the radial distribution of steady temperatures measured by FRAP-HT. In terms of a structured and discrete measurement grid, the integral of Eqn. 4.6 can be expressed by a sum (Eqn. 4.8).

$$\bar{x} = \frac{1}{\dot{m}} \cdot \int x d\dot{m} \qquad (4.6)$$

$$d\dot{m} = \rho \cdot c_x \cdot dA \qquad (4.7)$$

$$\bar{x} = \frac{\sum x \cdot d\dot{m}}{\sum d\dot{m}} \qquad (4.8)$$

4.7.2   Open Loop Correction

If measurements are performed in an open loop environment, the resulting flow pressures need to be corrected for changes in atmospheric conditions. This is usually done by calculating the non-dimensional pressure coefficient Cp. It usually incorporates pressure conditions at the facility inlet and outlet respectively, for example the total turbine inlet pressure $p_{tot,in}$ and static turbine exit pressure $p_{stat,exit}$.

$$Cp_t = \frac{p - p_{stat,exit}}{p_{tot,in} - p_{stat,exit}} \qquad (4.9)$$

4.7.3   Pneumatic Probe Data Reduction

Two consecutive steps are performed in order to reduce the acquired pneumatic probe data. In a first step, the data are processed and in a second step visualization of the data is performed. In order to correct for daily variations of atmospheric pressures (see chapter), rig operational data are logged with the same time stamp then the acquired pneumatic pressure files. The measured pressures of the pneumatic probe pressure taps are then used to form K_φ and K_γ. Together with the calibration coefficients (chapter 5) determined out of the aerodynamic calibration within freejet ($k_{ij\varphi}$ and $k_{ij\gamma}$) the flow yaw (φ) and pitch (γ) angles are calculated (Eqn. 4.10 and Eqn. 4.11) by solving the bivariable polynomial. Then the resulting flow angles in degree are converted into radians and in combination with the calibration coefficients k_{ijt} and k_{ijs} are used on the same manner to solve for the total pressure calibration coefficient K_t and static pressure calibration coefficient K_s respectively (Eqn. 4.12 and Eqn. 4.13). Finally the total pressure and static pressures respectively are calculated by rearranging the definition of K_t and K_s (Eqn. 4.14 and Eqn. 4.15 for a 4-hole probe; Eqn. 4.16 and Eqn. 4.17 for a 5-hole probe).

$$\varphi = \sum_{i=0}^{n} \sum_{j=0}^{m} k_{ij\varphi} K_\varphi^i K_\gamma^j \qquad (4.10)$$

$$\gamma = \sum_{i=0}^{n} \sum_{j=0}^{m} k_{ij\gamma} K_\varphi^i K_\gamma^j \qquad (4.11)$$

$$K_t = \sum_{i=0}^{n} \sum_{j=0}^{m} k_{ijt} \varphi^i \gamma^j \qquad (4.12)$$

$$K_s = \sum_{i=0}^{n} \sum_{j=0}^{m} k_{ijs}\,\varphi^i \gamma^j \qquad (4.13)$$

$$K_t = \frac{P_{tot} - P_1}{P_1 - \dfrac{P_2 + P_3}{2}}; \qquad P_{tot} = K_t \cdot \left(P_1 - \frac{P_2 + P_3}{2}\right) + P_1; \qquad (4.14)$$

$$K_s = \frac{P_{tot} - P_{stat}}{P_1 - \dfrac{P_2 + P_3}{2}}; \qquad P_{stat} = P_{tot} - K_s \cdot \left(P_1 - \frac{P_2 + P_3}{2}\right); \qquad (4.15)$$

$$K_t = \frac{P_{tot} - P_1}{P_1 - \dfrac{\sum_{i=2}^{5} P_i}{4}}; \qquad P_{tot} = K_t \cdot \left(P_1 - \frac{\sum_{i=2}^{5} P_i}{4}\right) + P_1; \qquad (4.16)$$

$$K_s = \frac{P_{tot} - P_{stat}}{P_1 - \dfrac{\sum_{i=2}^{5} P_i}{4}}; \qquad P_{stat} = P_{tot} - K_s \cdot \left(P_1 - \frac{\sum_{i=2}^{5} P_i}{4}\right); \qquad (4.17)$$

As introduced in chapter 3.3.3, the probe angles are calculated in the probe relative frame of reference. In order to get the global and rig dependent angles, the traversing set angles, as well as the rig specific angle convention has to be applied. By use of the global angles, as well as the total and static pressures respectively, additional properties, such as the Mach number and if the mean static gas temperature is provided, for instance from the rig operational file, the 3D velocity vector can be derived. The underlying equations for these property calculations are presented in Table 4-2.

In the last step of the data processing section, mass- or data averaging procedures are applied to the data, as described in chapter 4.7.1.

Property:	Equation:
Mach Number	$$Ma = \sqrt{\frac{2}{\kappa - 1}\left[\left(\frac{P_{tot}}{P_{stat}}\right)^{\frac{\kappa - 1}{\kappa}} - 1\right]}$$
Absolute velocity	$c = Ma \cdot \sqrt{\kappa R T_{stat}}$
Axial velocity	$c_x = c \cdot \cos\varphi \cdot \cos\gamma$
Radial velocity	$c_r = c_x \cdot \tan\gamma$
Circumferential velocity	$c_\theta = c_x \cdot \tan\varphi$

Table 4-2   Summary of some properties, calculated during pneumatic probe data processing. For the velocity calculation, the static gas temperature must be known (not provided by pneumatic probe measurements).

4.7.4   FRAP-HT Data Reduction

The measurements of unsteady flow fields at high sampling rates (200kHz) require a high level of data management and clear file structures for the acquired data points. The huge amount of data (up to 70GB per area traverse) can not be processed manually and is ideally analyzed using automatic batch-style software routines. For this purpose of FRAP data reduction, the software package "HERKULES" has been developed [91]. The code is based on a simple user interface (User parameterfile) with minimal user-interaction during the processing steps.

According to the described sensor and aeromodel evaluation routines, there are a number of different steps that need to be done for the processing of the binary raw data of the measurements. The HERKULES code is organized into four steps.

In Herkules - step 0, the relevant data files for the processing routines are prepared. These are the PPU files, the rig files, the Geo files as well as the probe calibration files (sensor and aeromodel). The PPU file contains the static pressure in the tower plenum, the atmospheric pressure and the reference pressure applied to the probe for every measurement point within a traverse. The rig file contains the inlet total pressure and exit static pressure at the beginning and the end of each traverse in order to calculate non-dimensional pressure quantities. These files are used during the data reduction (Step 0 to

Step 3) of the HERKULES data reduction. The acquired unsteady FRAP data from the 2-sensor probe are stored in several binary files and do not need to be preprocessed.

In Herkules - step 1, the raw sensor signals are reduced by applying a phase-lock. The trigger signal is used to phase-lock the different pressure signals (measured in serial mode with virtual 4-sensor technique) according to the rotor or blade trigger. The data is not averaged at this point of the data processing. The preprocessed data is written into to several files (*.dat extension).

In Herkules - step 2 the phase-locked FRAP data files (voltage signals U, Ue) are read and using the sensor calibration model (normally by bivariable polynomial) converted into pressure and temperature. The basic relations for this procedure are given in Eqn. 4.18:

$$\Delta p = \sum_{i=0}^{n} \sum_{j=0}^{m} k_{p,ij} \cdot U^i \cdot Ue^j \quad \text{and} \quad T = \sum_{i=0}^{n} \sum_{j=0}^{m} k_{T,ij} \cdot U^i \cdot Ue^j \quad (4.18)$$

In order to remove the sensor drift effects and therefore improve the DC pressure signal quality, an in situ offset-gain calibration is executed before and after a radial traverse. The calibration is done by placing the sensors of the probe in a region with a known pressure. During the freejet calibration this position is outside of the jet flow, whereas the ambient pressure is taken as the reference pressure. In a turbine measurement the probe tip is withdrawn into the probe access hole where stagnation conditions can be assumed. In this case a KELLER sensor measures the pressure of the plenum of the probe access hole, which is equal to the time-averaged pressure at the casing of the turbine flow path at this axial position. For the calibration the back pressure of the sensors is adjusted by the DRUCK pressure supply to two pressure levels. In this way, two known differential pressures are imposed on the sensors, from which a linear offset and gain correction of the pressure calibration can be done. From the calibration two adjustment coefficients J_o and J_I are determined, which extend the model of the sensor calibration (Eqn. 4.19).

$$\Delta p = J_0 + J_I \cdot \sum_{i=0}^{n} \sum_{j=0}^{m} k_{p,ij} \cdot U^i \cdot Ue^j \quad (4.19)$$

For the evaluation of the measurement points of a radial traverse in the turbine, the change of the adjustment coefficients over the time of the traverse

is linearly interpolated. In this way each measurement point has an individual set of adjustment coefficients. The pressure transducer senses a differential pressure over the membrane. This corresponds to the delivered pressure value resulting out of the inverted sensor calibration coefficient calculation. In order to further proceed in applying the aerocalibration model and to calculate various flow properties, absolute sensor pressures need to be obtained. This is done by subtracting the differential pressure from the sum of the atmospheric pressure and the sensor reference back pressure for each probe sensor:

$$p = p_{atm} + p_{ref} - \Delta p \qquad (4.20)$$

An adjustment of the temperature signal is not required since it has been shown to have a good long-term stability.

As a next step, the *.dat files are read in order to compute the flow parameters from pressure and temperature signals by sixth order bivariable polynomial, using the aerocalibration model. The yaw angle φ and pitch angle γ are expressed as a function of the angular calibration coefficients K_φ and K_γ.

$$\varphi = \sum_{i=0}^{n} \sum_{j=0}^{m} k_{ij\varphi} K_\varphi^i K_\gamma^j \quad \text{and} \quad \gamma = \sum_{i=0}^{n} \sum_{j=0}^{m} k_{ij\gamma} K_\varphi^i K_\gamma^j \qquad (4.21)$$

The coefficients describing the total and static pressure are expressed as functions of the yaw and pitch angle (in radian).

$$K_t = \sum_{i=0}^{n} \sum_{j=0}^{m} k_{ijt} \varphi^i \gamma^j \quad \text{and} \quad K_s = \sum_{i=0}^{n} \sum_{j=0}^{m} k_{ijs} \varphi^i \gamma^j \qquad (4.22)$$

Further flow properties are next calculated and finally, the computed data is phase-lock averaged (after the aerocalibration model) and stored into several results files for each grid point (*.av file extension).

In Herkules - step 3, the actual post-processor (Optic HERKULES) is used for the visualization of the computed flow parameters using various types of diagrams, charts and contour plots, including vector plots and animation of the flow field in *AVI*-movie files.

4.7.4.1   Overall Structure

The different data reduction steps are detailed in Fig. 4-12. The schematic shows the data flow of the required input files and the generated output files (*.dat*, *.av* etc.). On top of the FRAP data reduction process is the user interface parameter file (left) that controls all steps within the data reduction.

The data reduction time for a 40GB area traverse (around 1000 grid points) for a 2-sensor FRAP probe measurements lasts with the current FRAP systems (3.2GHz processor speed Pentium 4, 1 GB RAM) around 4-5 hours). The most time intensive steps are Steps 1 and 2 for the stand alone executable. The pre-processing (step 0) and post-processing (step 3) are less time intensive and normally completed within a few minutes.
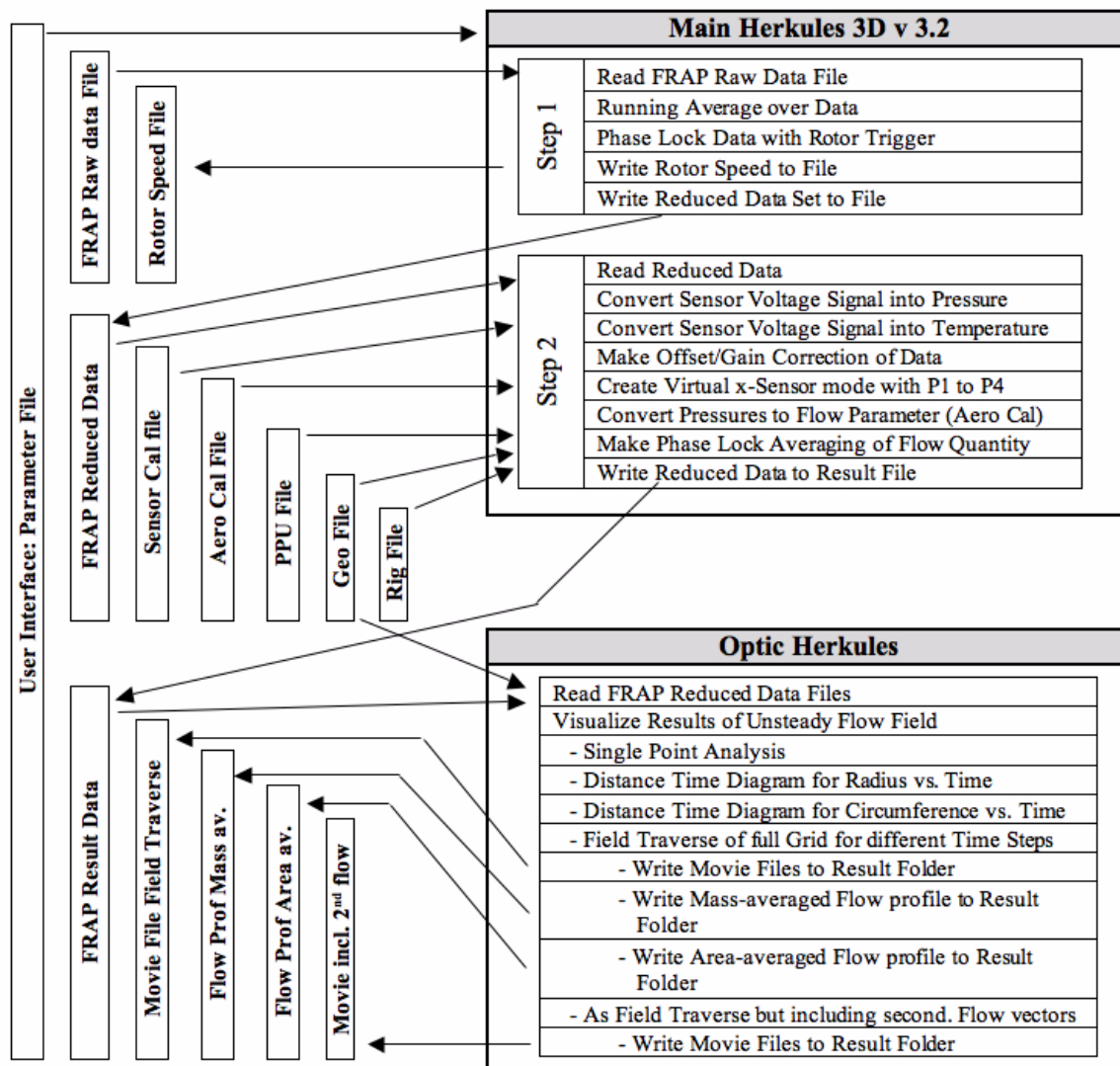
Fig. 4-12   Structure of FRAP data reduction routine (Herkules).

4.8   Intelligent Aerodynamic Probe Concept

Due to the harsh environment and limited accessibility of turbomachinery, point measurements derived from intrusive probes constitute the majority of techniques used in industrial applications. In the industrial setting, a

substantial amount of time, money and effort is expended in setting up, conducting, reducing and analyzing the large volumes of data that derive from point measurements. There is therefore great interest in the reduction of the required time for turbomachinery tests, as these reduce development costs and maintain competitiveness [92].

Therefore a novel flow adaptive traversing algorithm that has been used with both pneumatic and fast response probes [93] is presented. This algorithm requires minimal user input at the outset, thus reducing the set-up time for a measurement campaign. During the measurements, in an automated manner, the algorithm detects and measures flow features such as wakes and regions of secondary flows, such as vortical structures. This automated adaptation of flow measurements regions is important as regions in which measurements must be performed are not always intuitive. For example, in blade row clocking the flow phenomena of interest move with respect to the stationary frame of reference; this movement is not always proportional to the clocking angle [94]. In this case, the flow adaptive algorithm yields measurements at points related to the actual flow field, and thus the result with different clocking angles can be compared in an unbiased fashion. The number of measurement points on the flow adapted grid is substantially reduced compared to a uniform grid, without a loss of measurement accuracy. Thus the measurement time and the time for data reduction are reduced; also there are savings in the electronic space required to store the data.

The format of this sub-chapter is as follows. First, the flow adaptive traversing algorithm is described (chapter 4.8.1). In chapter 4.8.2 the instrumentation and axial turbine facility that are used to demonstrate the algorithm are presented. Measurements of the total pressure coefficient and yaw angle on uniform and flow adapted measurement grids at the second stator exit are discussed in chapter 4.8.2.4. Some concluding remarks with a summary of significant contributions of this new development are provided as a last in chapter 4.8.4.

4.8.1   Flow Adaptive Traversing Algorithm

The flow adaptive algorithm is designed to first detect points/areas of interest and then in an automated manner, add more measurement points. The adaptation is accomplished in both the radial and circumferential directions in

the measurement plane (Fig. 4-13).
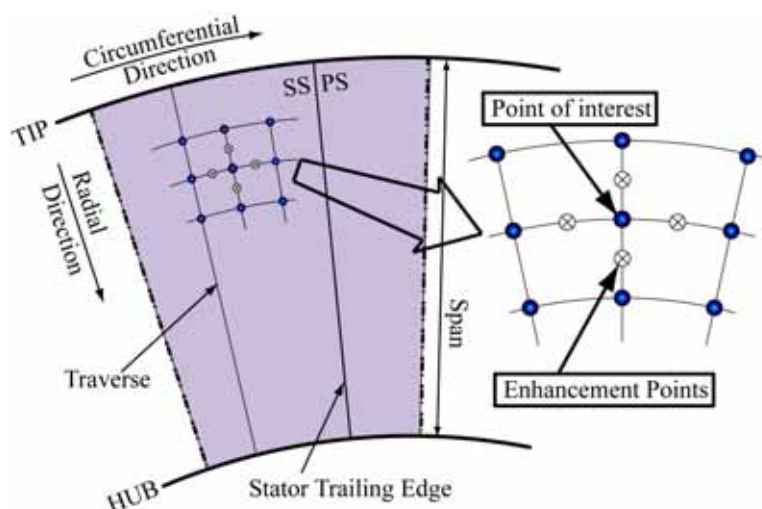
Fig. 4-13 Illustration of new enhancement points added around a point of interest.

Three sequential steps – pre-processing, main processing and post-processing – constitute the flow adaptive algorithm.

4.8.1.1   Pre-processing

The first step in the flow adaptive method is to define an initial uniform grid of measurement points. This initial uniform grid must cover the whole measurement domain with an optimum number of points such that the measurement time is short and no important flow details are missed. Subsequent flow adapted grids are based on this initial uniform grid. Algorithms that start from a uniform start grid to generate an adapted grid have been applied in adaptive mesh techniques for CFD [95]; thus in this regard the present approach is novel for measurement techniques but not new in fluid dynamics.

The optimum number of points to be used on the initial uniform grid was experimentally examined in the 2D axial measurement plane, Fig. 4-13, of the two-stage axial research turbine that is described below. This optimum number of points is a function of the geometrical parameters of the measurement plane, and thus will vary from one facility to another. For the present facility on the order of 10^2 (that is approximately 10×10 points in the circumferential and radial directions respectively) were found to be optimal.

Typical spanwise profiles of the mass averaged total pressure coefficient and yaw angle are shown in Fig. 4-14.

Spanwise distributions of circumferentially mass averaged total pressure coefficients and deviation between the results
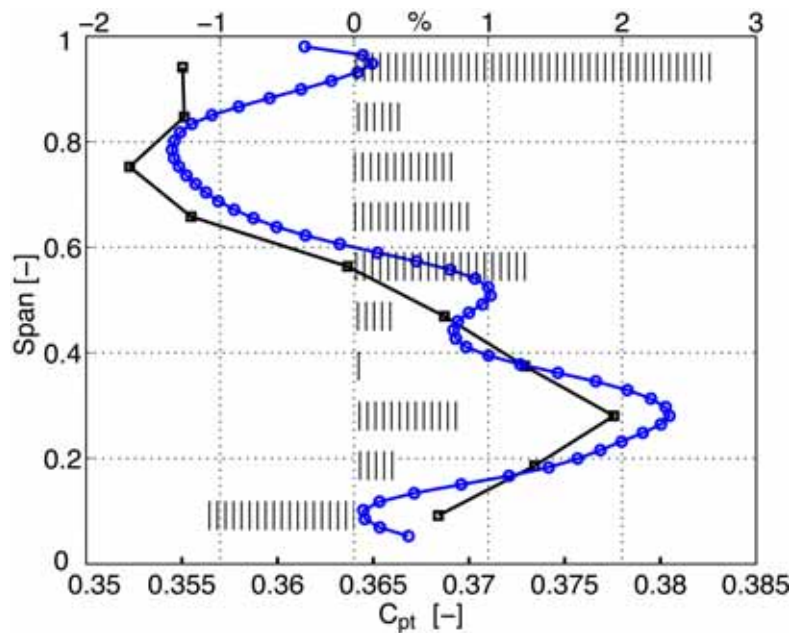
Spanwise distributions of circumferentially mass averaged yaw angles and deviation between the results
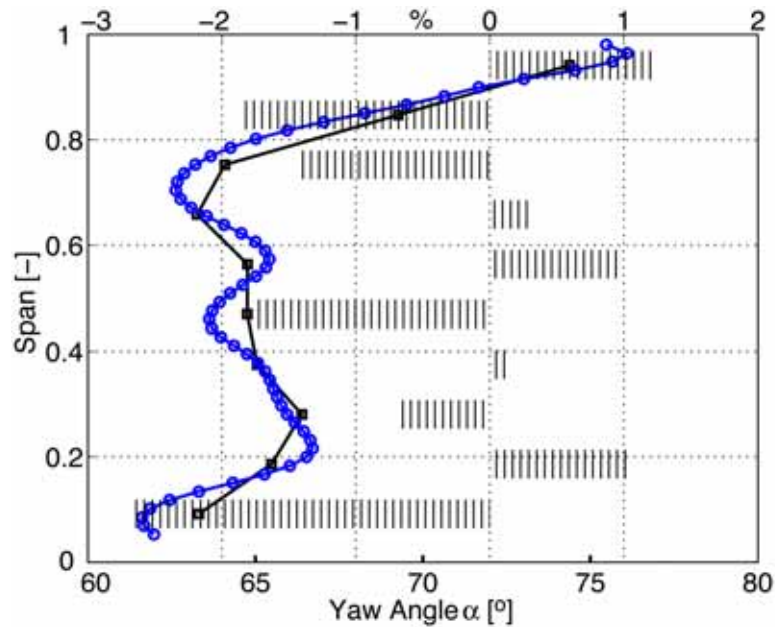
Legend: —o— Fine Uniform Grid 45 x 59
              —■— Initial Uniform Grid 8 x 11
              ||||||| Deviation in %

Fig. 4-14 Comparison of spanwise distributions of circumferentially mass averaged C_{pt} and yaw angles on fine uniform grid and initial uniform grid. Second x-axis shows the deviation between the two measurements.

The profiles are shown for two grids, an initial uniform grid and a fine uniform grid. The initial uniform grid has 8×11 points and the latter grid 45×59 points. This second grid is twice as dense in both radial and circumferential directions than a typical measurement grid that is used in the present facility without a flow adaptive measurement technique. In Fig. 4-14 the percent difference between the profiles on the two grids is shown along the second x-axis. Overall the agreement between the profiles is very good, with the exception of the measured total pressure at the tip. In this case, the relatively coarse initial uniform grid does not capture the tip leakage effects. However, when we consider that the initial uniform grid has 30 times fewer measurement points (88 compared to 2655) than the fine uniform grid, the 1% to 2.7% differences in the total pressure coefficient and 1.2% to -2.7% differences in yaw angle are very small.

After the initial uniform grid is specified, the pre-processing step is concluded with the definition of a finest uniform grid. Not all the points of this second grid are used; rather this second grid is used as the basis for an interpolated measurement grid when regions of interest are detected in the main processing step of the 2D adaptive algorithm. The desired measurement time and details of the probe geometry are amongst the parameters used, together with the initial uniform grid, to define this finest uniform grid.

4.8.1.2 Main processing

The refinement to a flow adapted grid and measurements on this adapted grid is done during the main processing step. The refinement is based on user-defined detection criteria that identify regions of interest in the measurement plane. In the present work detection criteria are specified, and thus the main processing step has three phases. In each phase a detection criterion is applied, the grid is refined and a series of measurements are made. In order to automate the main processing, the number of times to repeat a phase (termed here, loops), the number of points to be measured in each loop, and termination criteria are specified *a priori*.

The termination criteria are based on user-specified minimum and maximum distances and the distances between a measurement point of interest and its neighboring measured points. If the distance between the point of interest and a previously measured neighboring point is not less than the user-specified minimum distance, then a new measurement point is inserted midway between the point of interest and the previously measured points. If the distance exceeds a user-specified maximum distance, then the newly

inserted measurement point is placed at a specified distance from the point of interest. This procedure ensures that the new measurement points are within the area of interest; our experience shows that the overall quality of measurements on the flow-adapted grid is then better. The user-specified minimum and maximum distances are defined in terms of the positioning uncertainties of the probe traversing system and the diameter of the probe head.

The insertion of new measurement points results in an unstructured grid. However it is computationally more efficient to perform the data acquisition tasks on a structured grid using an object oriented programming language. Thus after each refinement, the resulting unstructured grid is interpolated onto a structured utility grid. This structured grid has the same grid point spacing as that of the finest uniform grid. A distance weighed mean averaging procedure is used for the interpolation.

As described above, the adaptation of the grid and measurements are done in a series of phases. In each phase, a detection criterion is used as the basis for the adaptation. In the present work, the axial turbine flow, that is examined, is characterized by wakes, which are shed from the rotor and stator blades, and vortices that are generated by the passage and leakage flows. Thus three detection functions, minimum pressure (PM), pressure gradient (PG) and yaw angle (YA), are employed. The pressure related functions provide for accurate measurements in the wake, since the total pressure in the wake is lower than that of its surrounding flow.

Kalfas et al. [96] and Binder et al. [46] have shown that the yaw angle is a reliable indicator to identify both wakes and vortices, especially in the passage downstream of a stator. Thus the sequence of detection, adaptation and measurement phases, Fig. 4-15, is PM, PG and finally YA.
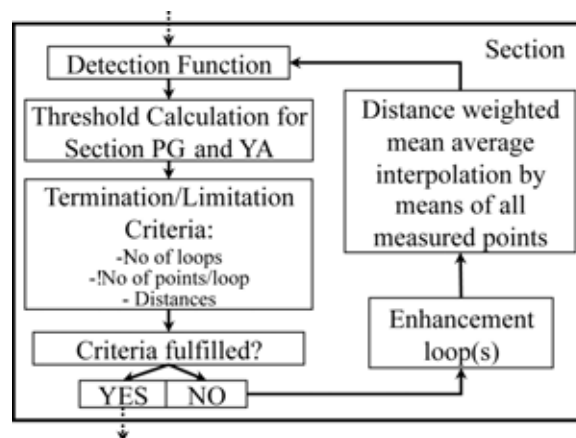
Fig. 4-15   Flow chart of an adaptation and measurement phase.

In the PM phase, the adaptation and measurements are performed if local minima of the measured total pressures are found. In the PG and YA phases, the adaptation and measurements are performed if the detection functions exceed a threshold value. The detection functions for the pressure gradients are:

$$DF_i(r) = \left(\frac{\partial P_{tot}}{\partial r}\right)_i^2 \qquad (4.23)$$

$$DF_i(\theta) = \left(\frac{\partial P_{tot}}{\partial \theta}\right)_i^2 \qquad (4.24)$$

And for the yaw angle:

$$DF_{1i} = \left(\frac{\partial \varphi}{\partial r}\right)_i^2 \cdot \left(\frac{\partial \varphi}{\partial \theta}\right)_i^2 \qquad (4.25)$$

$$DF_{2i} = \left(\frac{\partial^2 \varphi}{\partial r^2}\right)_i^2 \cdot \left(\frac{\partial^2 \varphi}{\partial \theta^2}\right)_i^2 \qquad (4.26)$$

The threshold value is given as

$$threshold = \frac{1}{m} \cdot \sum_{i=1}^{m} DF_i, \qquad (4.27)$$

where DF_i is a detection function given in Eqn. 4.23 - 4.26. It is pertinent to point out that the detection functions involve squares of the first and second derivatives. This results in smother distributions of the detection functions and an improved identification of the points of interest.

4.8.1.3   Post-processing

The adaptation algorithm is initiated on the initial uniform starting grid, and then is applied on successively refined grids as areas of interest are identified and measured. If a uniformly spaced grid were used for the measurements, then the measurement data would be stored in matrices that are easily post-processed. However as the 2D flow adaptive algorithm results in measurements that are clustered in areas of interest, the resultant measurement data are not amenable to efficient post-processing. Thus the measurements on the flow-adapted grid are interpolated back onto a uniform grid in order to facilitate the post-processing. This interpolation is done in two steps. First, a 1D cubic spline is used to uniformly space points along the boundary of the

measurement area. Then the flow parameters at each uniformly spaced point (x_0, y_0) are evaluated as a distance weighted average of the four closest measurement points. For example, for the yaw angle:

$$\varphi_{(x_0, y_0)} = \frac{\dfrac{\varphi_1}{d_1} + \dfrac{\varphi_2}{d_2} + \dfrac{\varphi_3}{d_3} + \dfrac{\varphi_4}{d_4}}{\sum\limits_{i=1}^{4} \dfrac{1}{d_i}} \qquad (4.28)$$

4.8.2   Experimental Validation of the Technique

4.8.2.1   Instrumentation

Two probes, a pneumatic cobra-shaped 5-hole probe [97], Fig. 4-16, and a first generation fast response aerodynamic probe (FRAP) [98], Fig. 4-17, are used to evaluate the flow adaptation algorithm. Gossweiler et al. [20] and Johansen et al. [83] discuss the calibration procedures for the aforementioned probes. Additional information on both, the used probes, as well as the calibration procedures are given in chapter 5. Traditional calibration techniques are limited to small flow angles [99], but a theoretical basis for extending the range of flow angles, beyond those used in the calibration, has been given by Pisasale et al. [100]. The pneumatic probe has a calibration range of $\pm12°$ in yaw angle and $\pm30°$ in pitch angle (Fig. 4-17). The diameter of the probe head is 0.9mm and the tip has a slanted pyramid shape (Fig. 4-16). The five-hole probe yields steady measurements of φ, γ, P_{tot}, P_{stat} and Ma.
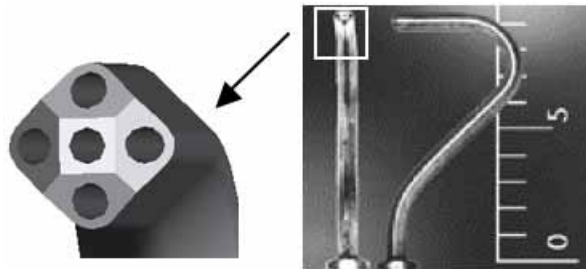
Fig. 4-16   Cobra-shaped 5-hole probe.

Unsteady measurements are derived from the first generation FRAP (Fig. 4-17(b), [7, 18, 20, 21, 44, 101]. This probe incorporates a single, temperature-compensated sensor that is operated using a Wheatstone bridge. The diameter of the cylindrical probe is 1.8mm. The pressure tap is located 1.8mm from the probe tip and has an angle of 0° with respect to the *x*-axis (Fig. 4-17(a)).

The sign convention is that a positive yaw angle is in the direction of the rotor sense of rotation (*y*-axis), and a positive pitch angle is directed toward the

blade tip (*z*-axis).

<p align="center">(a)   (b)</p>
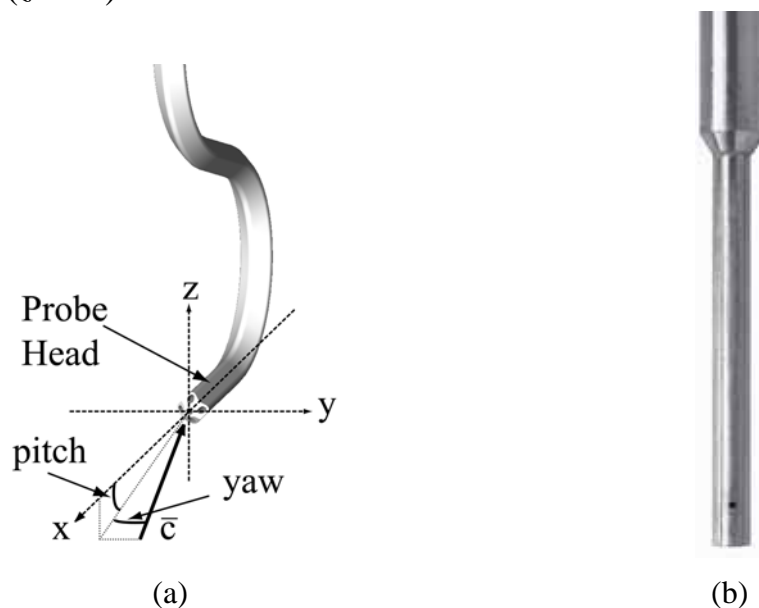
*Fig. 4-17   (a): Yaw and pitch angle convention; (b): Fast response aerody-
namic probe.*

4.8.2.2   Facility

The 2D adaptive flow concept was applied in the axial turbine research facility "LISA" [47]. This is a large (max. power 400 kW), low speed (Mach numbers 0.1-0.4) facility that can accommodate up to two axial turbine stages. Some more information about the axial turbine research facility is given in chapter 7, where measurements are presented in a one and a half stage configuration of this turbine facility. The primary characteristics of the turbine used in this study (two stage configuration with shrouded rotors) are given in Table 4-3.

Parameter	Value
Rotational Speed	2500 RPM
Pressure Ratio	1.34
Aspect Ratio (Span/Ax. Chord)	1.8
Blade Count (Rotor/Stator)	42 / 42
Outer Tip Diameter	0.8m
Mass flow	10.26 kg/s

Table 4-3   Characteristic turbine parameters.

The present measurements are made in a traversing plane that is located

downstream of the second stator row (Fig. 4-18).
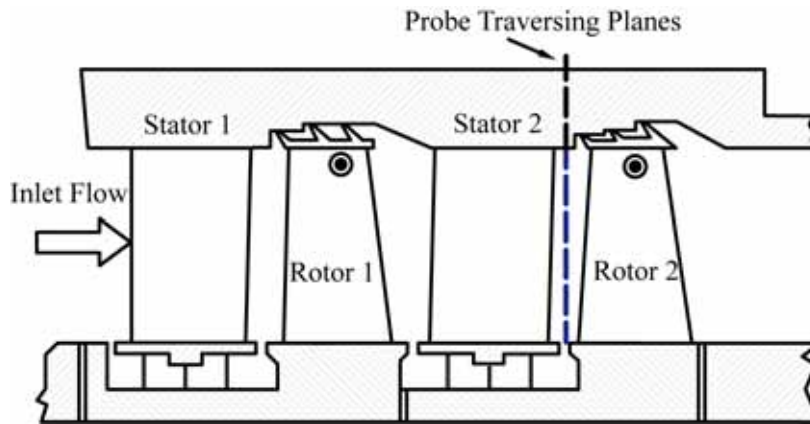
Fig. 4-18   Measurement position after 2nd stator.

4.8.2.3   Test Matrix

The baseline grid used to evaluate the 2D flow adaptive algorithm is a uniform grid with dimensions of 23×60 points in the circumferential and radial directions, respectively. Two test cases, TC1 and TC2, with flow adapted grids are examined. The salient features of these grids are summarized in Table 4-4 and Table 4-5. The primary differences in the two test cases are the number of loops in the PM, PG and YA phases of the main processing step, and the number of measurement points in each of these loops.

Phase	N_L	N_P	N_T	N_A
Initial Grid	1	88	88	88
PM	3	50	150	118
PG	2	40	80	64
YA	4	50	200	84

Table 4-4   Test case 1 (TC1).

Phase	N_L	N_P	N_T	N_A
Initial Grid	1	88	88	88
PM	4	50	200	145
PG	4	40	160	133
YA	4	40	160	147

Table 4-5   Test case 2 (TC2).

The total numbers of possible measurement points are 518 and 608 for the test cases TC1 and TC2 respectively. However, due to the termination criteria based on distances that are discussed above in section 2.2, the actual numbers of measurement points are 354 and 513, respectively, compared to 1380 points on the baseline uniform grid. In the subsequent section contour plots, as well as circumferentially mass averaged line plots of the measured total pressure coefficients and yaw angles are presented for the two test cases to show the application of the 2D flow adaptive algorithm. In the contour plots, circle symbols that show the location of the measurement points are superposed on the flowfield contours. Although other flow variables could be shown on the plots, the total pressure and yaw angle are presented since they are also used in the detection functions.

4.8.2.4   Discussion of Results

Fig. 4-19 and 4-20 show contours of the total pressure coefficients at the end of the measurement series for test cases TC1 and TC2, respectively. Since a five-hole probe and FRAP are used for the measurements, a safety clearance must be maintained close to the hub. Additionally near the rotor tip, there is a leakage flow that results in yaw angles that are outside the calibration range of the probe. Thus in Fig. 4-19 and 4-20, and in the subsequent contour plots, the regions in the range of 0 - 5% span and 99 - 100% span are shown as blanked out white zones.

A comparison of test case TC1, Fig. 4-19, to test case TC2, Fig. 4-20, shows that although the former has approximately 30% fewer measurement points, there are no significant differences between the two cases.

This is confirmed in Fig. 4-23 where the spanwise distributions of the circumferentially mass averaged total pressure coefficient and yaw angle are shown, and compared to those of the reference grid. It can be seen from the circle symbols in Fig. 4-19 and 4-20 that the 2D flow adaptive algorithm results in more finely resolved measurements in the regions of low total pressure that are associated with the wake. For test case TC2, Table 4-5, more loops involving the pressure related criteria are performed in comparison to the test case TC1, Table 4-4. Thus a comparison of Fig. 4-19 and 4-20 also show that test case TC2 has a higher density of measurement points in the wake and its surrounding flow. This higher density of measurement points is also evident when the yaw angles are compared in Fig. 4-21 and 4-22.
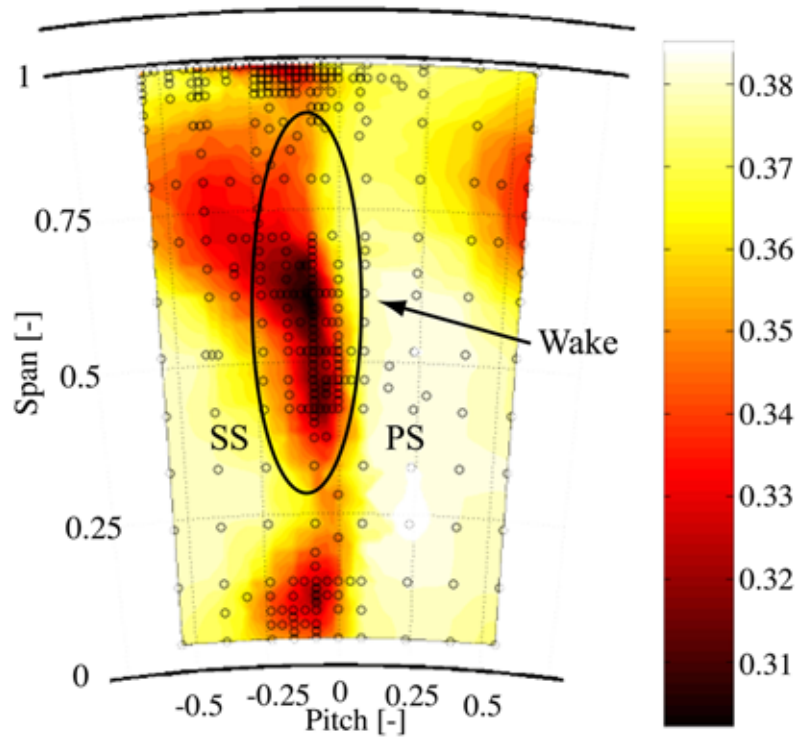
Fig. 4-19 C_{pt} [-] distribution for test case TC1.
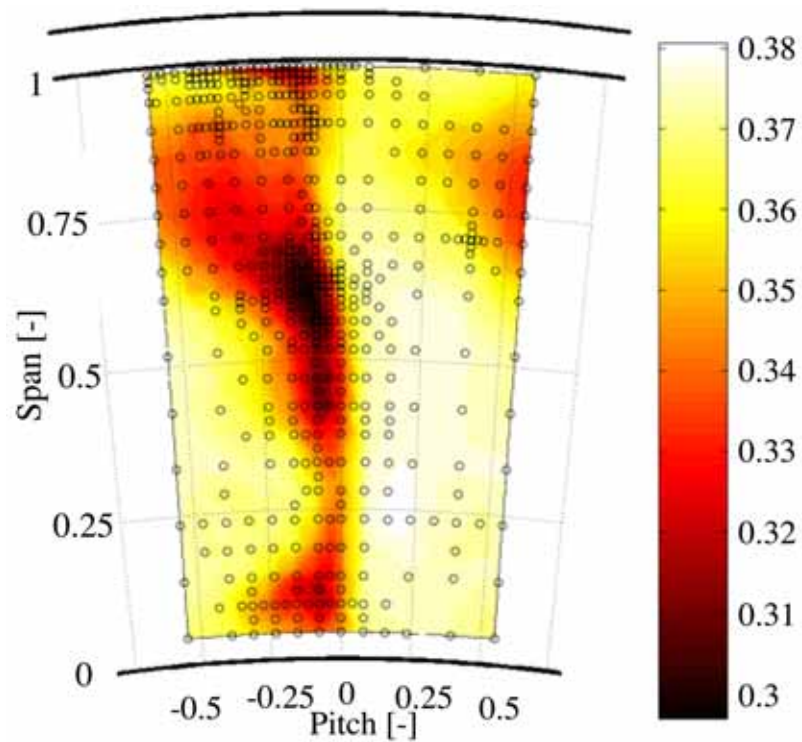
Fig. 4-20 C_{pt} [-] distribution for test case TC2.
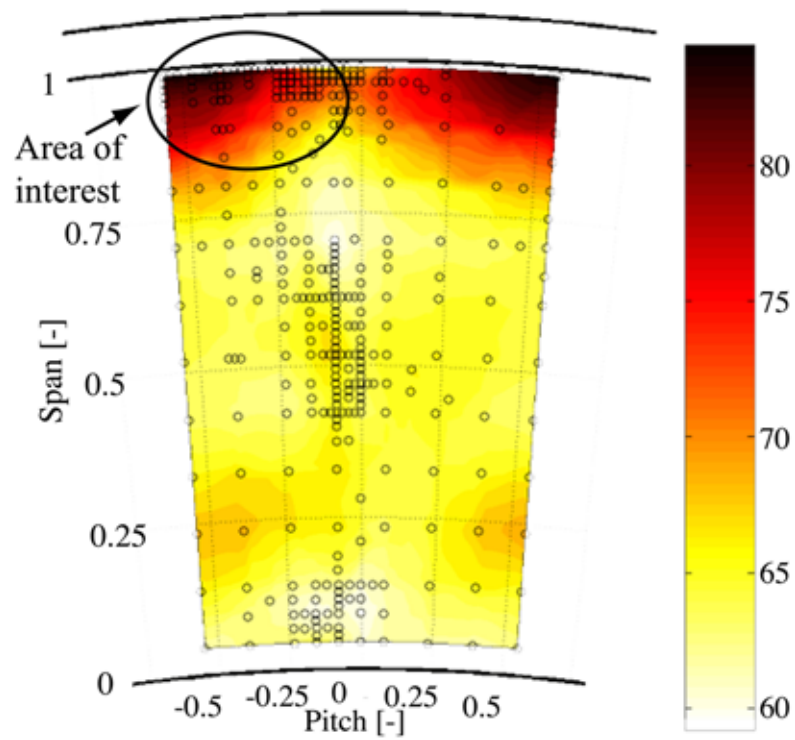
Fig. 4-21   Yaw angle φ [°] distribution for test case TC1.
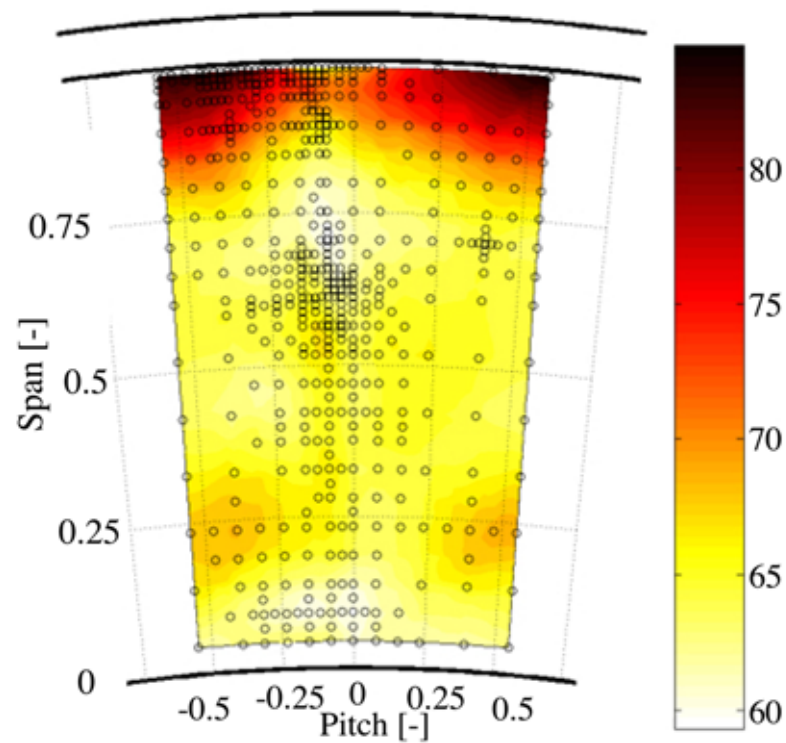
Fig. 4-22   Yaw angle φ [°] distribution for test case TC2.

Spanwise distributions of circumferentially mass averaged total pressure coefficients
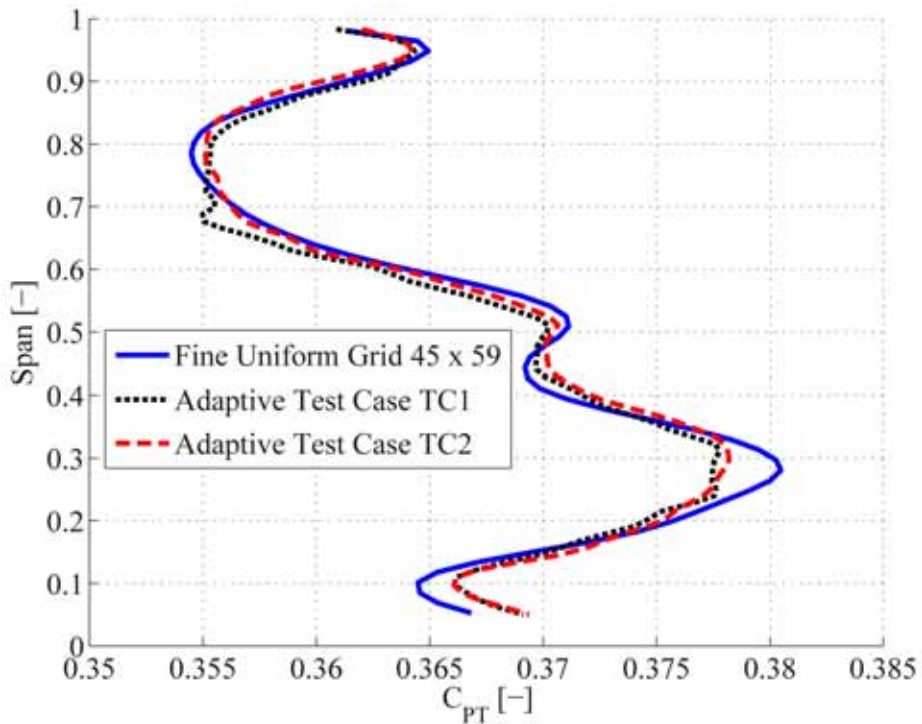
Spanwise distributions of circumferentially mass averaged yaw angles
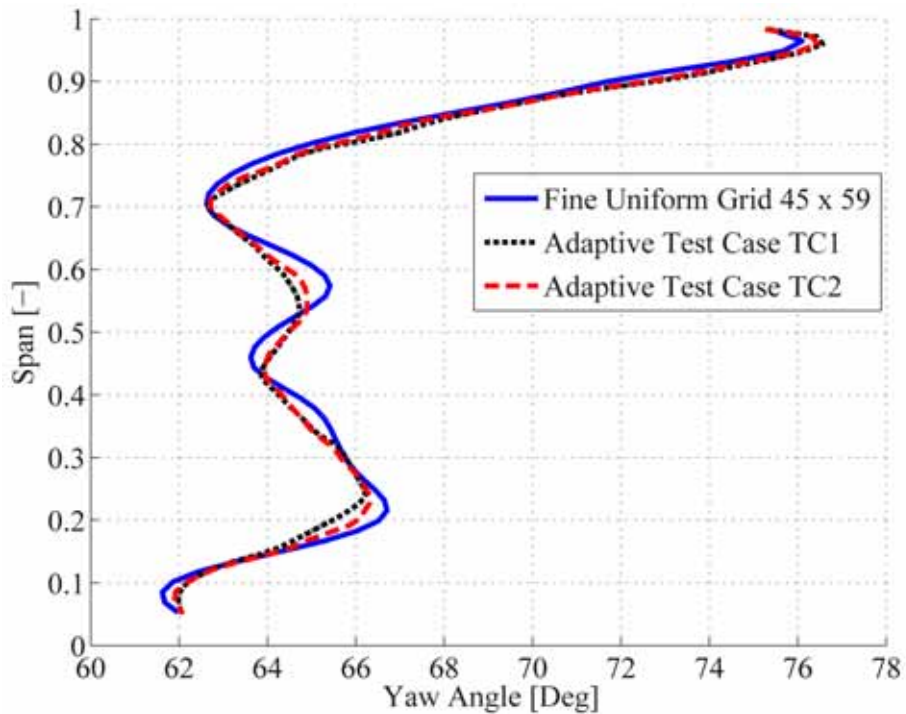
Fig. 4-23   Comparison of spanwise distributions of circumferentially mass averaged C_{pt} and yaw angles on fine uniform grid and grids of adaptive test case TC1 and adaptive test case TC2.

Fig. 4-21 and 4-22 also show that there is a relatively high density of measurement points in the outer 25% span of the measurement plane. In this region the tip leakage vortex results in relatively high gradients of the yaw angle.

A close-up view of the measured total pressure and yaw angles is shown in Fig. 4-24 to 4-29. In these contour plots only the outer 50% span is shown for the uniform grid and the two test cases, TC1 and TC2. The total pressure coefficients are shown in Fig. 4-24 to 4-26 and the yaw angles in Fig. 4-27 to 4-29. Overall it can be seen that there is very good qualitative agreement between the two flow adapted grid test cases and the reference case. As described above, more highly refined measurements are obtained at around 60% span in the vicinity of the wake, and around 90% span in the region of the tip leakage flow. Although there is a high density of measurement points in these two regions, a comparison of for example Fig. 4-28 (test case TC1) and Fig. 4-29 (test case TC2) shows that there is measurement points distributed over the whole measurement plane. The user-specified minimum spacing distance assures that additional points are not inserted in the regions of interest, even if the number of measurement loops is high. The small differences between the flow adapted results, Fig. 4-25, 4-26, 4-28 and 4-29, compared to the reference case, Fig. 4-24 and 4-27, are thought to be a result of the non-uniform grid in the flow adapted test cases and the uniform grid in the reference case. The measurements on the non-uniform grid have to be interpolated back onto a uniform grid during the data processing step described above. It is thought that the use of a higher order interpolation scheme would minimize these differences. Nevertheless, the spanwise distributions of the circumferentially mass averaged total pressure coefficients and yaw angles, shown in Fig. 4-23, show that the differences between the flow adapted grid and uniform grid are small.

The measurement time for each of the three cases is 8 hours for the uniform grid, 1.5 hours for test case TC1 and 3 hours for test case TC2, respectively. The difference in the measurement times on the flow adapted grids is a result of the difference in the number of measurement points, 354 points for test case TC1 compared to 513 points for test case TC2. Test case TC1 thus has a gain of 81% in measurement time compared to the uniform grid of the reference case.

Uniform grid 23 x 60
Total pressure coefficient C_{pt}

Uniform grid 23 x 60
Yaw angle φ
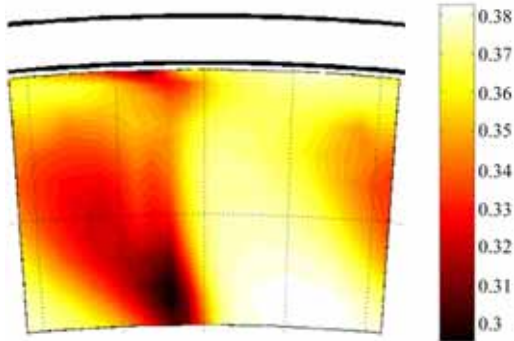
Fig. 4-24 Upper 50% span of C_{pt} [-] distri-
bution over one pitch measured on
uniform grid 23x60.
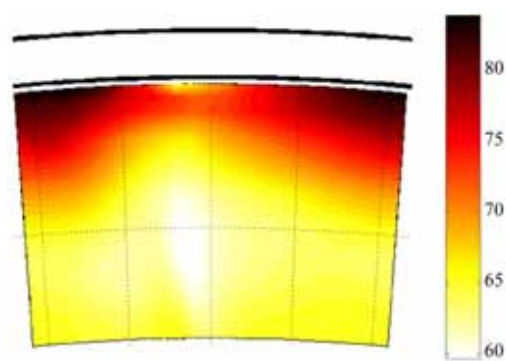
Fig. 4-27 Upper 50% span of φ [°] dis-
tribution over one pitch measured
on uniform grid 23x60.

Flow adaptive probe concept
Total pressure coefficient C_{pt}, TC1

Flow adaptive probe concept
Yaw angle φ, TC1
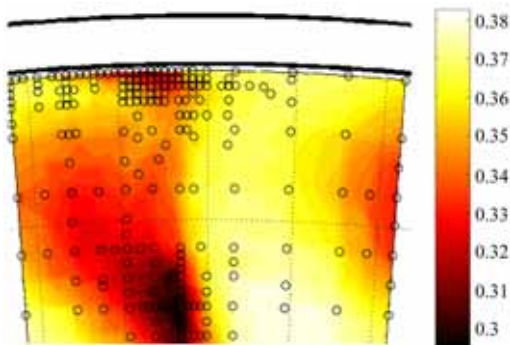
Fig. 4-25 Upper 50% span of C_{pt}
[-] distribution over one pitch mea-
sured on flow adapted grid, TC1.

Fig. 4-28 Upper 50% span of φ [°]
distribution over one pitch mea-
sured on flow adapted grid, TC1.

Flow adaptive probe concept
Total pressure coefficient C_{pt}, TC2

Flow adaptive probe concept
Yaw angle φ, TC2
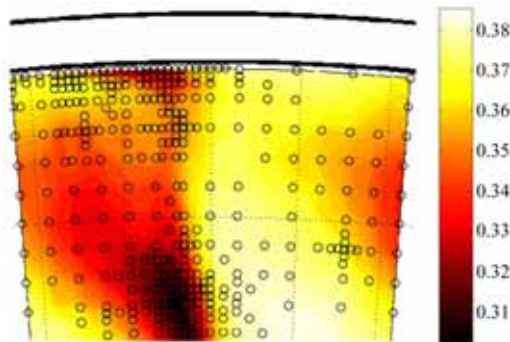
Fig. 4-26 Upper 50% span of C_{pt} [-] distri-
bution over one pitch measured on
flow adapted grid, TC1.
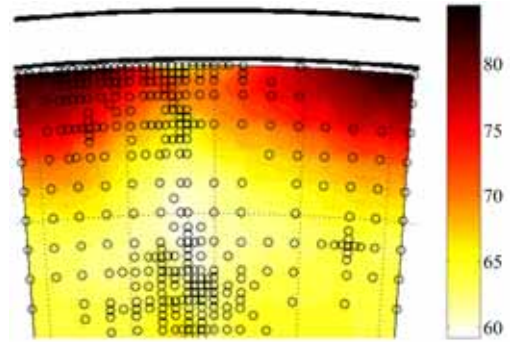
Fig. 4-29 Upper 50% span of φ [°] distri-
bution over one pitch measured on
flow adapted grid, TC2.
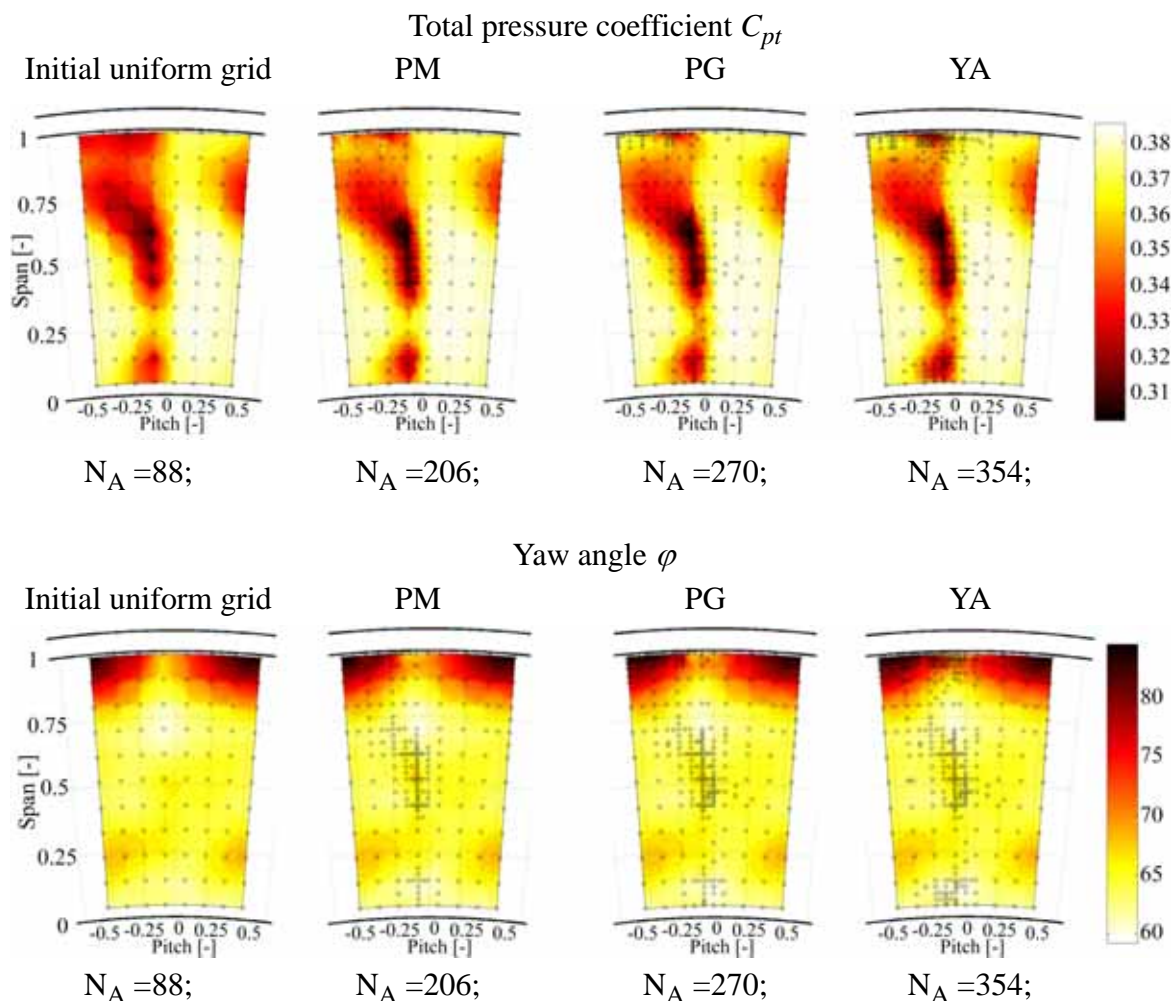
Fig. 4-30   Evolution of C_{pt} [-] and φ [°] distributions over one pitch during a run. Test case TC1.

The evolution of the grid adaptation during a series of measurements is shown in Fig. 4-30. Test case TC1 is shown as a representative example. In Fig. 4-30 the measured flowfield on the initial uniform grid, and then at the end of the three successive main processing phases, PM, PG and YA, are shown. The corresponding evolution of the mass averaged total pressure coefficient and yaw angle are shown in Fig. 4-31 and 4-32. An error bar shows the uncertainty in the five-hole probe measurements and the result from the uniform grid is shown as a horizontal dashed line that is denoted as the trend line. It can be seen that 300 measurement points on the flow adapted grid yield the same result (within the measurement uncertainty) as on the uniform grid that has 1380 points.

Trend for changes in mass averaged C_{pt}
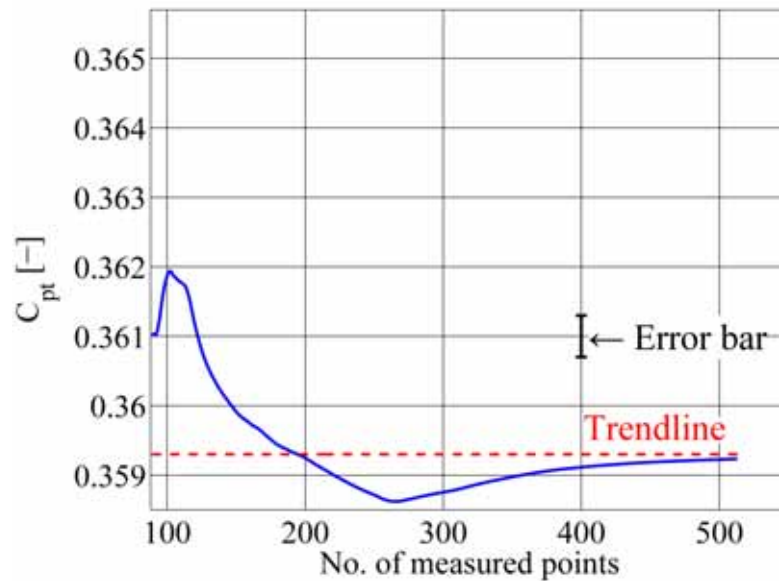
Fig. 4-31   Evolution of mass averaged total pressure coefficient C_{pt} [-].

Trend for changes in mass averaged yaw angle
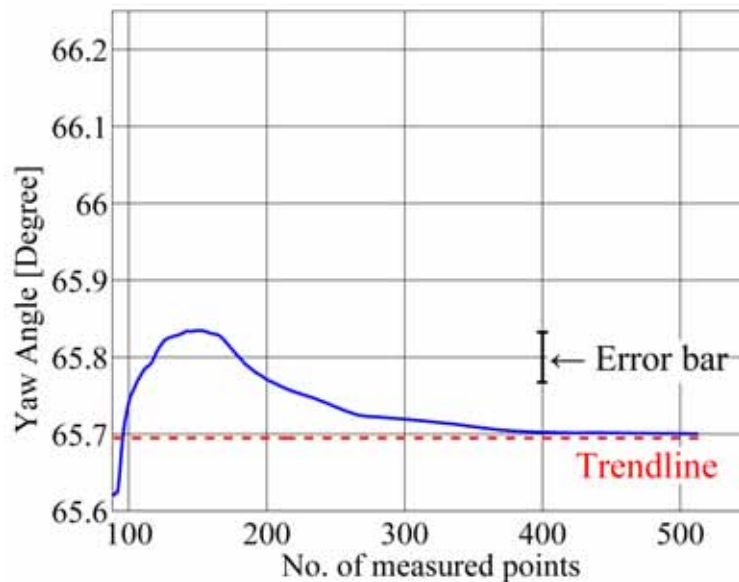
Fig. 4-32   Evolution of mass averaged yaw angle φ [°].

4.8.3   Further Application of the Method

The applications of the novel flow adaptive algorithm are not limited to the test case considered above. Below we briefly summarize two other related applications.

4.8.3.1   Fast Response Aerodynamic Probe (FRAP)

An accurate assessment of the losses in turbomachines requires the measurement of the unsteady flow field [2-4]. These measured flow properties can then be used to derive parameters such as the non-deterministic pressure coefficient and turbulence intensity that are used to quantify the losses. The initial development of the novel flow adaptive algorithm used the FRAP from which the aforementioned parameters can be determined. It is thus evident that the novel flow adaptive algorithm has the potential to facilitate the design and development of new turbomachines.

4.8.3.2   1D Flow Adaptive Traversing Algorithm

The novel flow adaptive algorithm has been applied to a 1D, radial traverse. In this case, the algorithm was used to automatically traverse a probe step-by-step from tip to hub. At each radial position, the previously acquired yaw angle is used as an input for the following traverse point. After a traverse, points of interest are determined, and arrays of locally refined radial positions are generated. The measurement and refinement steps are repeated until the algorithm terminates due to the limitation criteria. Compared to measurement on a standard uniform grid without refinement, the 1D algorithm is 30% faster. As a 1D traverse is made, the detection functions in the circumferential direction are not evaluated. Therefore, the flow adaptive algorithm can be applied in test facilities in which an automated traverse in the circumferential direction is not available, since each radial traverse can be independently made.

4.8.4   Summary

A novel flow adaptive 2D traversing algorithm has been developed. Measurements in a large axial turbine facility demonstrate the potential of the algorithm to substantially reduced measurement time, whilst maintaining measurement accuracy. This novel approach can be used for pneumatic probe measurements, as well as for unsteady measurements using a Fast Response Aerodynamic Probe.

The flow adaptive algorithm is comprised of three sequential steps – pre-processing, main processing and post-processing. In the first step an initial uniform grid of points are defined and the flow measured. Then in the next step, in an automated manner, the algorithm detects points/areas of interest, and adds additional measurement points as are required. The adaptation is accomplished in both the radial and circumferential directions in the measurement plane. The detection functions employed in the present work

identify the wakes, which are shed from the rotor and stator blades, and the vortices, that are generated by the passage and leakage flows. In the final step, the measurements on the flow-adapted grid are interpolated back onto a uniform grid in order to facilitate the post-processing.

The application of the flow adaptive 2D traversing algorithm shows that compared to a uniform measurement grid, a flow adapted grid with 75% fewer measurement points can be used to resolve the flow field. This reduction in measurement points has a significant impact on the measurement time; specifically measurement time using the flow adaptive algorithm is 81% quicker than on the uniform measurement grid.

5   Further Instrumentation

In order to validate the concept of the newly developed FRAP-HT, comparisons of measurements using the new probe and measurements with standard measurement equipment, such as traditional FRAP probes, and pneumatic 4-hole probes and 5-hole probes are made. A short overview shall therefore be given about the measurement technologies applied in order to make the comparisons.

All pneumatic multi-hole probes (4-hole, 5-hole etc.) as well as FRAP probes are individually calibrated in the freejet calibration facility (see chapter 3.3.4) within a given range of probe relative yaw and pitch angles as well as at different Mach numbers Ma. The probe is positioned with linear motion controllers within the freejet and by tilting and yawing the probe within the known flow conditions the relevant calibration coefficients of the aerodynamic calibration model is derived. The aerodynamic calibration model is based on a parametric approach. The model is defined by a set of four calibration coefficients K_{φ}, K_{γ}, K_t and K_s for the flow yaw angle (φ), flow pitch angle (γ) and total and static pressures (P_{tot} and P_{stat}).

The data reduction methodology in order to get the flow properties out of an unknown flow field for both, pneumatic probes, as well as FRAP probes, is described in detail in chapter 4.7 of this thesis. The focus in this chapter is therefore to present the shape of the further used probes, as well as to describe the definition of the aerodynamic calibration coefficients for the respective probes.

5.1   Pneumatic Probes

Pneumatic probes are used to verify the results of the fast-response aerodynamic probes (FRAP). The simplicity of the measurement chain enables this technique to provide reliable reference data of the steady pressure field. Differences between the results of fast-response probes and pneumatic probes occur due to the different size of the cavity between sensor membrane and flow field. The pressure tubes of the pneumatic probe connecting the probe tip to the pressure sensor causes frequency damping of the unsteady pressure signal. The pressure that is measured by the sensor is therefore referred to as a pneumatically averaged pressure. Due to the different ways of averaging and the effect of flow turbulence and flow angle variation the measured averaged pressure can differ from the time-averaged pressure of a FRAP probe.

According to Arts [102] turbulence intensities of 20% can cause a maximum change of total pressure of up to 2%. For interpretation and comparison of pneumatic probe results with FRAP results it is important to keep in mind the frequency characteristic and the source of the pressure signal measured with both techniques.

In general all the calibration models used for the pneumatic probes are based on a parametric model proposed in [103]. Within our Laboratory, a large range of pneumatic probes exist. The differences in shape are mainly related to access issues. For instance a cylindrical 4-hole probe requires a smaller measurement access than cobra shaped probes. On the other hand, cobra shaped 5-hole probes have the advantage of similar pressure sensitivity to angle variations, due to the symmetrical shape of the probe head and due to the reduced potential field influence of the probe body to the pressure taps related to the increased distance between the body and the measurement volume (of about 5 tip diameter).

5.1.1   Cylindrical 4-Hole Probe

The cylindrical 4-hole probe head shape is similar to the standard FRAP probes (chapter 5.2) and the diameter of the probe is 1.8mm (Fig. 5-1). This probe therefore provides a good reference to the results obtained by FRAP probes and the FRAP-HT probe since differences related to the probe geometry are absent.

Fig. 5-1   Cylindrical 4-hole probe (FRAP shape) compared to a match for scale comparison.

5.1.1.1 Calibration Coefficients

The steady flow properties, φ, γ, P_{tot}, P_{stat} and *Ma* are measured with the 4 hole probe. The definition of calibration coefficients is identical to the definition of the calibration coefficients for the FRAP-HT probe as presented in chapter 3.3. The numbering convention of probe holes is therefore identical to that of the FRAP-HT probe used in the virtual 4-sensor mode (Fig. 5-2). Due to the identical definition of the calibration coefficients K_{φ}, K_{γ}, K_t and K_s compared to FRAP-HT probes, the resulting angular dependent coefficients are neither presented nor further discussed.
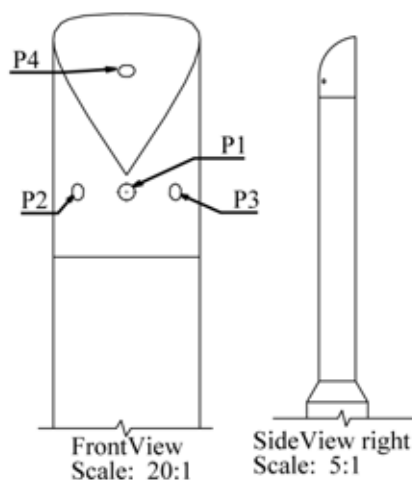
Fig. 5-2 Pressure tap numbering convention of cylindrical 4-hole probe (FRAP shape).

The cylindrical 4-hole probe used for the measurements in this thesis has a calibration range of ±24° in yaw and ±20° in pitch angles.

The derived aerodynamic calibration accuracy for the probe is given in Table 5-1 for a calibration range of ±24° in yaw and ±20° in pitch angle, respectively. The calibration uses a polynomial interpolation order of 6th degree for both parameters m and n. The model accuracy is given in absolute values for the flow angles, as well as for total and static pressures. The accuracy for the Mach number is given as a percentage of the freejet calibration Mach number. Additionally, for total and static pressures, the accuracy is presented as a percentage of the real dynamic head at the freejet Mach number of 0.5.

The given model accuracy is not the total measurement accuracy of the entire measurement system but only specifies the quality of the aerodynamic calibration. Information about measurement uncertainties of a standard 4 hole probe are provided in the chapter 6 of this thesis.

Parameter	4-hole probe accuracy	in % of dynamic head
φ	$\pm\,0.063°$	
γ	$\pm\,0.116°$	
P_{tot}	$\pm\,44.3$ Pa	0.245%
P_{stat}	$\pm\,45.1$ Pa	0.249%
Ma	$\pm\,0.19\%$	

Table 5-1   Calibration model accuracy for a cylindrical 4-hole probe for Ma=0.5 and calibration range ±24° in yaw angle and ±20° in pitch angle.

5.1.2   Cobra-Shaped 5-Hole Probe

The cobra-shaped 5-hole probes ([97]) consist of a soldered bundle of four tubes arranged around a center tube. Depending on the requirements in terms of robustness, there exist 5-hole probes of different tip diameter in our Lab. However, in order to reduce potential blockage effects, the probe with the most miniature tip diameter of 0.9mm is preferred. The tip of the probe is shaped as a quadratic pyramid with 45° inclined surfaces and a truncated tip. The center hole is placed on a surface which is orthogonal to the probe tip's axis.

Fig. 5-3   Cobra-shaped 5-hole probe compared to a match for scale comparison.

5.1.2.1   Calibration Coefficients

All flow quantities in the freejet facility are known and used for the relation

of the five pressures with the flow angles, pressures (static and total) and Mach number.

FrontView   SideView left
Scale: 20:1   Scale: 5:1
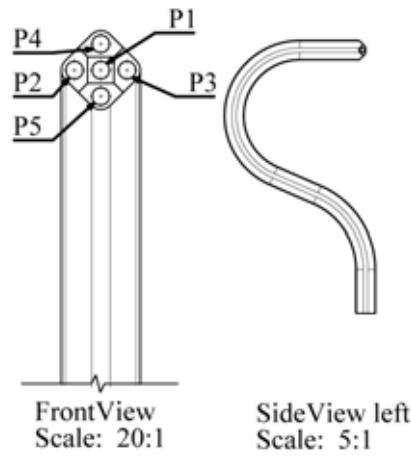
Fig. 5-4   Cobra shaped 5-hole probe; tap numbering convention.

The calibration coefficient for the yaw angle φ and pitch angle γ for the 5-hole probes are formed using the five pressures and non-dimensionalized as:

$$K_\varphi = \frac{P_2 - P_3}{P_1 - \dfrac{P_2 + P_3 + P_5 + P_5}{4}} \qquad (5.1)$$

$$K_\gamma = \frac{P_1 - P_4}{P_1 - \dfrac{P_2 + P_3 + P_4 + P_5}{4}} \qquad (5.2)$$

The calibration coefficients for yaw and pitch angles K_φ and K_γ are shown in Fig. 5-5 as a function of yaw and pitch angles and for a calibration Mach number of Ma=0.5.
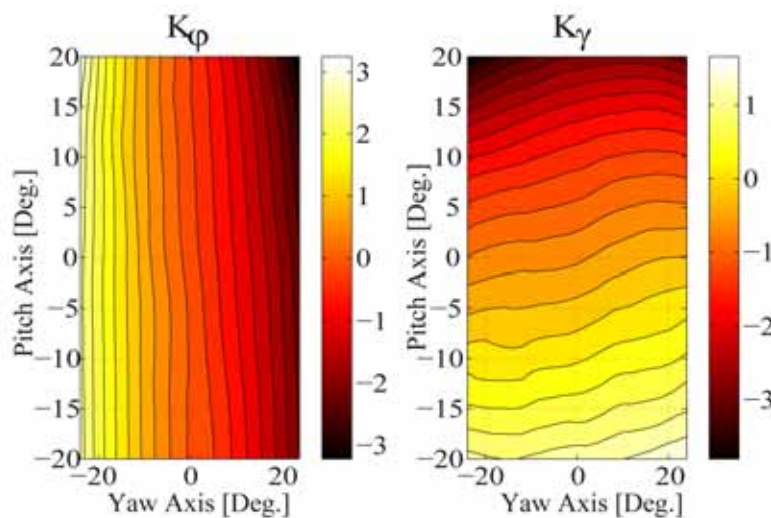
Fig. 5-5   Calibration coefficients K_φ and K_γ for a 5-hole probe as a function of yaw ±20° and pitch ±20° angle (Ma=0.5).

The coefficients K_φ and K_γ are dimensionless. The variation of flow yaw angle affects the subtraction of the *P2* and *P3* pressures and leaves the approximate expression of the dynamic head *(P1-(P2+P3+P4+P5)/4)* nearly constant (ideally). A similar effect is seen for pitch angle variation and *P4-P5*. Both parameters are used for the interpolation curves for the flow yaw and pitch angles based on pressure measurements only. The corresponding polynomial functions are given in chapter 4.7.3.

The calibration coefficients for the total and static pressures are obtained in a first step from the definition of total and static pressure coefficients as given in the following equations:

$$K_t = \frac{P_{tot} - P_1}{P_1 - \dfrac{P_2 + P_3 + P_5 + P_5}{4}} \qquad (5.3)$$

$$K_s = \frac{P_{tot} - P_{stat}}{P_1 - \dfrac{P_2 + P_3 + P_5 + P_5}{4}} \qquad (5.4)$$

The calibration coefficients for total and static pressures are shown in Fig. 5-6 as a function of yaw and pitch angles and for a calibration Mach number of 0.5.
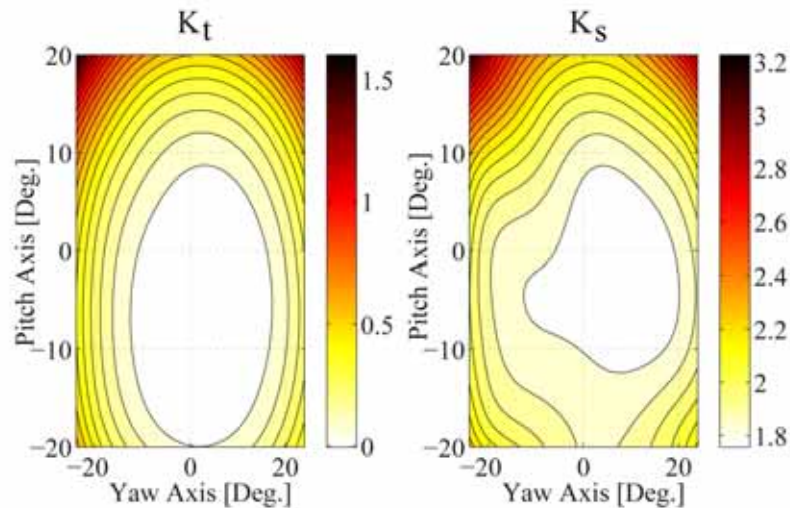
Fig. 5-6   Calibration coefficients K_t and K_s for a 5-hole probe as a function of yaw ±20° and pitch ±20° angle (Ma=0.5).

The total and static pressure coefficients are finally represented by the interpolation curves that use the flow yaw and pitch angles and the polynomial coefficients of the interpolation curves. The corresponding equations are again provided in chapter 4.7.3.

The derived aerodynamic calibration accuracy for the probe is given in Table 5-2 for a calibration range of $\pm 24^o$ in yaw and $\pm 20^o$ in pitch angle, respectively. The calibration uses a polynomial interpolation order of 6th degree for both parameters m and n. The model accuracy is given in absolute values for the flow angles, as well as for total and static pressures. The accuracy for the Mach number is given as a percentage of the freejet calibration Mach number. Additionally, for total and static pressures, the accuracy is presented as a percentage of the real dynamic head at the freejet Mach number of 0.5.

Parameter	5-hole probe accuracy	in % of dynamic head
φ	$\pm 0.076°$	
γ	$\pm 0.388°$	
P_{tot}	± 10.1 Pa	0.056%
P_{stat}	± 12.8 Pa	0.071%
Ma	$\pm 0.05\%$	

Table 5-2   Calibration model accuracy for a cobra-shaped 5-hole probe for Ma=0.5 and calibration range ±24° for yaw angle and ±20° for pitch angle.

Again the stated model accuracy is not the total measurement accuracy of the entire measurement system but only specifies the quality of the aerodynamic calibration. Information about measurement uncertainties of a standard 5 hole probe are provided in the chapter 6 of this thesis.

5.2   FRAP Probe

The standard two-sensor FRAP technology, even though limited to flow temperatures not exceeding 393K [18, 20, 21], has been used in recent years. A series of publications describe measurements conducted with this probe type (for instance, [94, 104-106]). The probe (Fig. 5-7) has a similar head shape compared to the newly developed FRAP-HT, but differs in its dimensions. The probe head has a diameter of 1.8mm. The pressure tap related to the yaw angle (*P1* and in virtual 4-sensor mode equally to the *P2* and *P3* tap) is 2.8mm from the probe tip at an angle of 0°. The pitch sensitive tap (*P4*) is located 0.6mm from the probe tip and at an angle of 45° from the probe axis on a shaped probe head.

The definition of calibration coefficients is identical to the definition of the calibration coefficients for the FRAP-HT probe as presented in chapter 3.3. Due to the identical definition of the calibration coefficients K_φ, K_γ, K_t and K_s compared to FRAP-HT probes, as above the resulting angular dependent coefficients are not presented.

Fig. 5-7   Picture of standard FRAP probe compared to a match for scale comparison.

All the standard FRAP probes used for the measurements in this thesis have the same calibration range as the FRAP-HT probe.

The derived aerodynamic calibration accuracy for the probe is given in Table 5-3 for a calibration range of ±24° in yaw and ±20° in pitch angle, respectively. The calibration uses a polynomial interpolation order of 6th degree for both parameters m and n. The model accuracy is given in absolute values for the flow angles, as well as for total and static pressures. The accuracy for the Mach number is given as a percentage of the freejet calibration Mach number. Additionally, for total and static pressures, the accuracy is presented as a percentage of the real dynamic head at the freejet Mach number of 0.5.

The given model accuracy is not the total measurement accuracy of the entire measurement system but only specifies the quality of the aerodynamic calibration. Information about measurement uncertainties of a standard 4 hole probe are provided in the chapter 6 of this thesis.

Parameter	standard FRAP accuracy	in % of dynamic head
φ	± 0.076°	
γ	± 0.119°	
P_{tot}	± 48.79 Pa	0.269%
P_{stat}	± 48.77 Pa	0.269%
Ma	± 0.20%	

Table 5-3   Calibration model accuracy for a standard FRAP probe for Ma=0.5 and calibration range ±24° in yaw angle and ±20° in pitch angle.

5.3   Steady High Temperature Probe

An additional probe has been designed and built in order to investigate possible conduction losses between the "hot" probe tip volume of the FRAP-HT probe and the cold back-end of the probe that is outside of the rig. The probe is a simple steady temperature probe (F0S-PT100-HT) of cylindrical shape with a diameter of 2.5mm.

PEEK with a very low thermal conductivity (0.2 W/(m·K)) compared to steel alloys (for instance steel 1.4301, thermal conductivity in the order of 15 W/(m·K) is used as the probe tip material in order to reduce possible conduction through the probe shaft (Fig. 5-8).
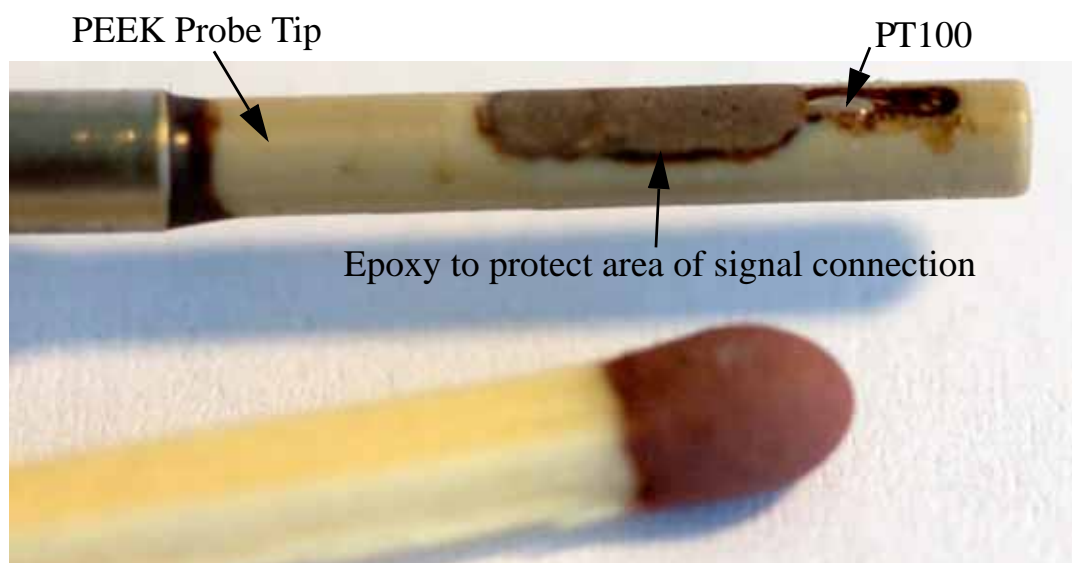
Fig. 5-8   Steady temperature probe based on a PT100 thermocouple compared to a match for scale comparison.

Two slots are incorporated in the PEEK probe tip. One of 1mm in width, close to the tip in which the PT100 is installed such that the PT100 top surface is aligned to the cylindrical outer surface of the 2.5mm tip. The other slot is 1.8mm in width and is used to connect the legs of the PT100 by means of soldering pads to high temperature cables. The cables are then fed to the probe inside and then issued to the probe back-end. After connecting the PT100 tip sensor to the soldering pads, the 1.8mm slot is filled up with a high temperature epoxy to thermally protect the contacts. Fig. 5-9 shows a 2D sketch of the probe design. The purple highlighted area represents the tip PT100 and the red area the position of the soldering contacts. The design of the probe has been done based on the know-how gained from the development of the FRAP-HT probe. The steady temperature probe therefore shows the same operating temperature limit of 533K as the FRAP-HT probe.
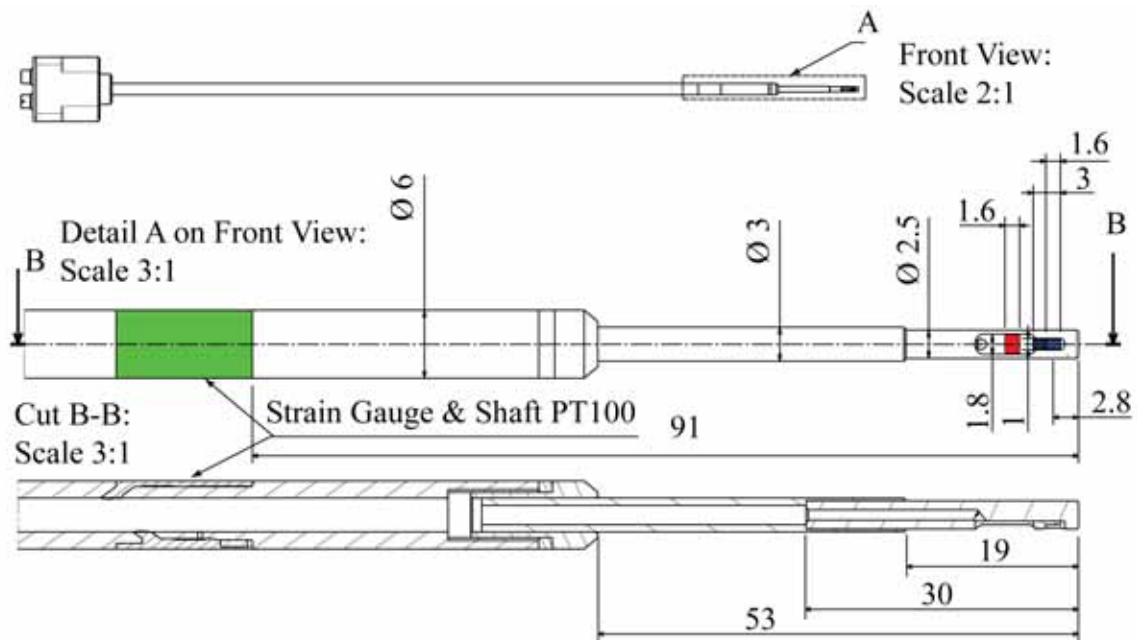
Fig. 5-9   *2D Sketch of PT100 temperature probe, including close-up view of probe tip (green: epoxy covered strain gauge and Shaft PT100; red: soldering contact; blue: Tip PT100.*

A goal in the design of the steady temperature probe was to have as close as possible mechanical design to that of the FRAP-HT probe. This was not achieved completely due to the mechanical properties of PEEK. An FEM structural mechanical analysis has been performed. In the analysis, the probe tip region is thermally loaded as well as a dynamic head as expected at high Ma number flows is applied. The resulting Von-Mises stresses were close to the yield strength. In order to not risk possible probe failure due to mechanical

fracture, the 2.5mm diameter probe tip overall length was made approximately 9mm shorter than the FRAP-HT.

Nevertheless in order to be as identical in design than the FRAP-HT and to allow investigation of difference in possible conduction within the probe shaft, the FRAP-HT contains a second pair of sensors, namely a shaft PT100 and a shaft strain gauge (green area in Fig. 5-9).

In terms of signal conditioning, both shaft sensors (strain gauge and PT100) are operated by the same power supply and DAQ rack then the FRAP-HT probe (see chapter 4.4). However, the primary tip PT100 sensor of the steady temperature probe varies from the FRAP-HT probe and therefore requires its own power supply and DAQ system to condition the signals. The same PT100 type of sensors are used in the tip and in the shaft (chapter 4.4.1). The tip PT100 sensor is wired to be used in 4-wire connection mode and therefore identical measurement principles underlay to the DAQ hardware of both PT100 sensors. An additional measurement rack is therefore designed and built in order to measure with the steady high temperature probe (Fig. 5-10, right). The rack operates as a power supply for the tip PT100 and at the same time is used to condition the output signals of the sensors. The conditioned signals are then fed by BNC connector cables to a channel of the fast DAQ cards (chapter 4.5) and sampled with 30kHz sampling frequency. In order to reduce possible electronic noise, the rack is shielded to the outside. Further shielding is installed in the inside of the rack to reduce possible noise from the power supply to the sensor signals within the rack.

FRAP-HT Probe Shaft PT100 Signal Port   Monitoring of Probe Shaft PT100 Signal
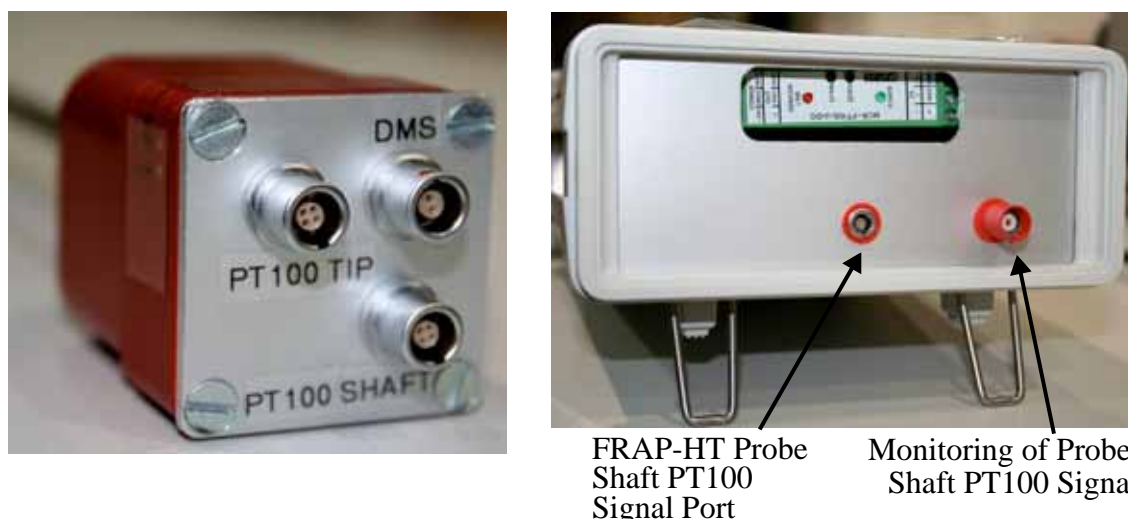
Fig. 5-10   Steady temperature probe, strain gauge and 2 x PT100 sensor connection at probe box at the back-end of the probe (left) and additional measurement DAQ rack for Tip PT100 acquisition (right).

The setup of the device is adjusted to be used in 4-wire connection mode, working linear between 273K and 573K. The connection to the tip PT100 sensor of the steady temperature probe is provided by an additional shielded 4-wire cable. The probe therefore shows 3 connectors, one for the tip PT100 sensor, one for the shaft PT100 sensor and one for the shaft strain gauge sensor (Fig. 5-10, left).

5.3.1   Calibration Coefficients

The probe is temperature calibrated in the oven calibration facility of LEC (chapter 3.3.1.1). The applied range is set from 313K up to 513K. The output signals of the complete measurement chain (output of the commercial temperature measuring transducer) are acquired for the tip PT100 and the shaft PT100 respectively. The resulting output voltages for both PT100 sensors is almost identical, as shown in Fig. 5-11. The measured mean sensitivities of the temperature sensors after amplification are 33.0 mV/K for the tip sensor and 32.8 mV/K for the shaft sensor respectively. These results are consistent with the characteristics of the commercial temperature measuring transducer that is used with 0 to 10V for the full scale temperature range of 273K to 573K
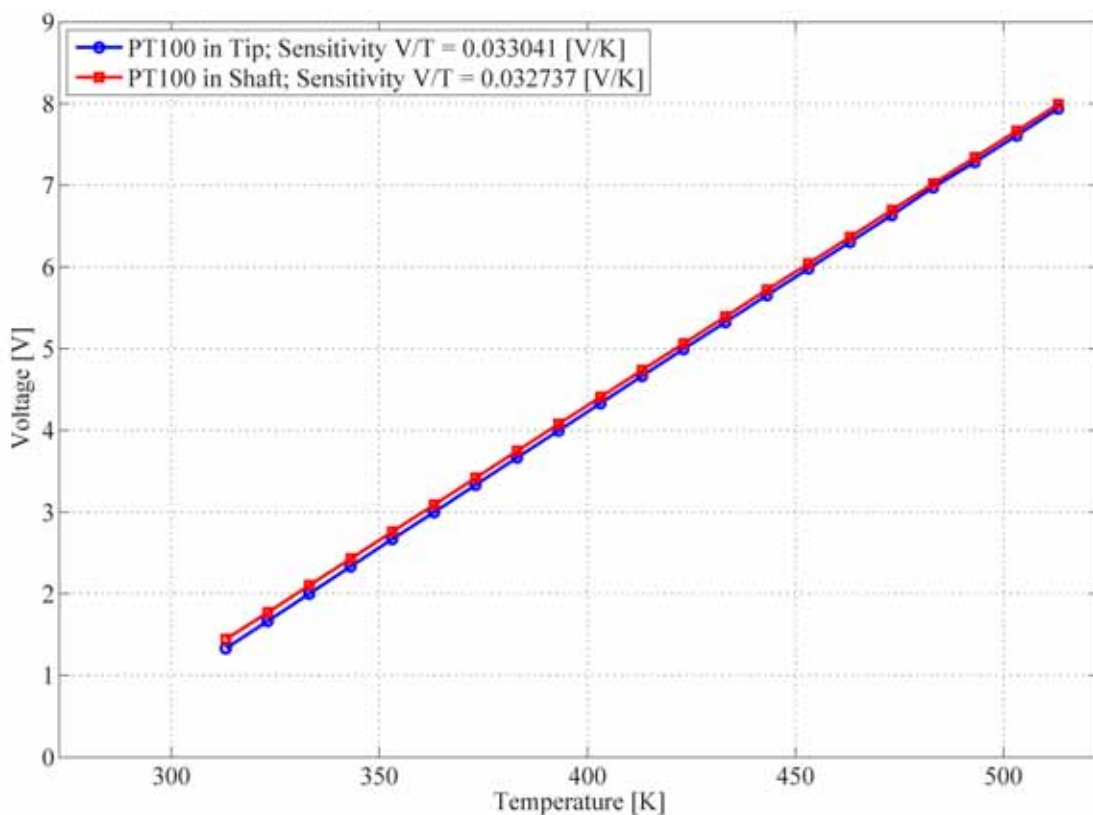
Fig. 5-11   Oven facility calibration output results for PT100 at tip and at shaft of the steady high temperature probe.

Both, the short term drift as well as the aging effect on the long-term validity of the probe sensors have been investigated after more than 100 hours of operation. The resulting output signals showed no specific drift and in the long term investigation, the change in output voltage is in the order of ±2mV which expressed in sensed temperature error equals a value around ±0.06K.

In order to implement the calculation of the resulting temperature for both PT100 sensors into the complete measurement procedure on an automated manner, calibration coefficients are defined out of the resulting oven facility calibration. 1st, 2nd and 3rd order polynomial curve fits have been applied to the resulting calibration data. An estimate of the absolute error, containing 50% of the predictions has been investigated for all three polynomial orders and for both sensors. The estimate with the first order fit has mean values of absolute errors in the order of ±0.321K for both PT100 sensors, whereas the second and third order polynomial curve fits result in mean values in the absolute error in the order of ±0.099K and ±0.085K respectively for both PT100 sensors. The third order polynomial curve fit has only a minor reduction in the estimated absolute error compared to the second order curve fit. For the shaft PT100 sensors as well as for the tip PT100 sensors, therefore calibration coefficients based on a second order polynomial curve fit are defined:

$$T_{sensed, PT100(i)} = a_i \cdot (U_{PT100(i)})^2 + b_i \cdot U_{PT100(i)} + c_i \qquad (5.5)$$

where $T_{sensed,PT100(i)}$ equals the sensed temperature of the respective sensor i (tip or shaft). $U_{PT100(i)}$ equals the output voltage of the respective sensor i and a_i, b_i and c_i are the respective polynomial coefficients

The resulting calibration curves for the second order polynomial curve fit are presented in Fig. 5-12 for both probe PT100 sensors. The resulting correlation coefficients, R^2, are 0.9999974 for the tip PT100 and 0.9999986 for the shaft PT100. The 2nd order polynomial curve fit is thus suitable for measurements.

As discussed in chapter 3.4.2, the direct measurement of total flow temperatures in an accurate manner is always approximated by because of the incomplete recovery of the kinetic energy of the air by the temperature probe. Furthermore parasitic heating or cooling of the temperature sensor due to the signal conditioning could lead to some additional errors.

The aim of the designed probe is to measure the steady temperature. In principle no aerodynamic calibration is required. But to reduce any erroneous

temperature measurement effects, it is necessary to position the probe in the average flow direction, such that the sensor is facing the stagnation line of the flow. The mean flow direction needed for that approach results from FRAP-HT measurements. The measured steady gas temperature is primarily used to develop feasible temperature correction models for the FRAP-HT probe. Therefore no extensive calibrations are performed in order to correct for the incomplete recovery of the kinetic energy.

In terms of self heating of the designed temperature probe, the model investigated in chapter 3.4.1 has been adapted for the current probe. Due to the low feeding current for both PT100 sensors (1mA) and a more than an order of magnitude reduced "bridge" resistance of a PT100 sensor compared to a FRAP-HT pressure transducer, PT100 self heating is of negligible influence to the accuracy of the measured flow temperatures. More specifically it adds an erroneous temperature of less than 0.03K to the measured temperature at flow speeds above 5m/s).
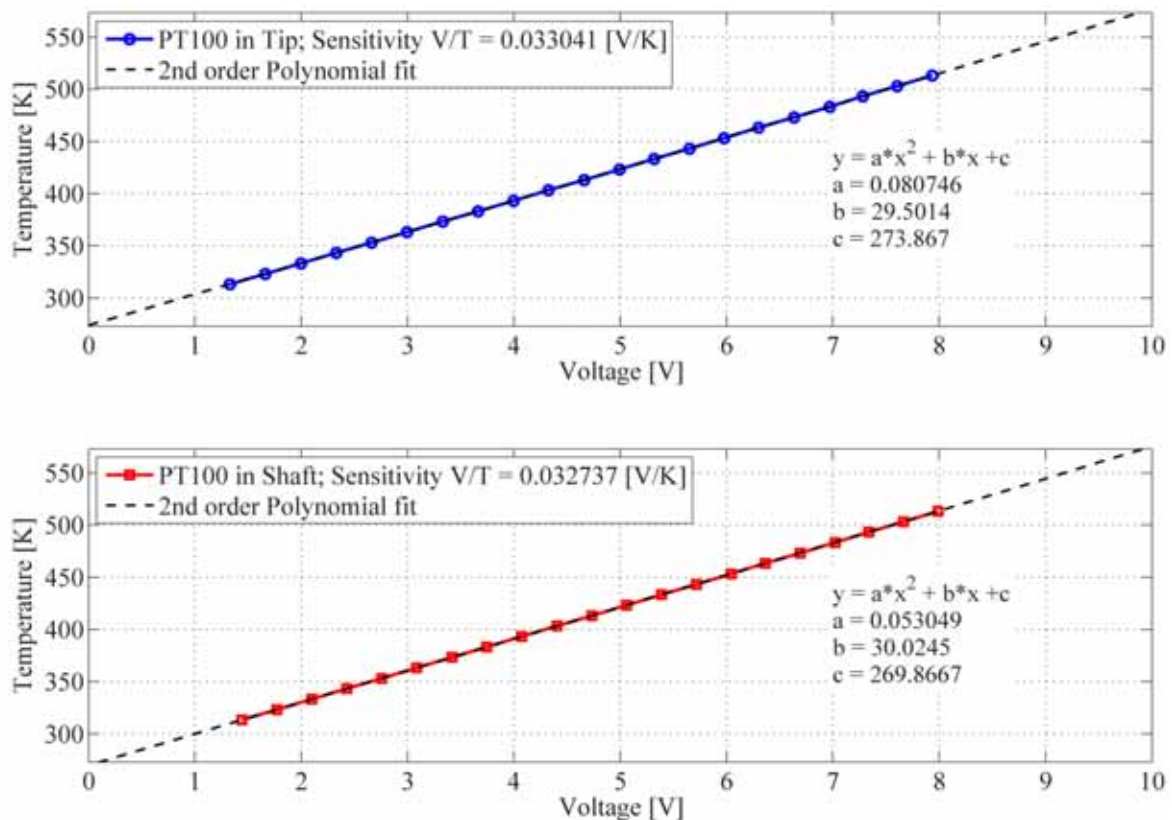
Fig. 5-12   2nd order calibration polynomial for both PT100 sensors (shaft and tip).

6   Probe Measurement Uncertainty

Experiments are an essential and integral tool for engineering and science in general. By definition, experimentation is a procedure for testing (and determination) of a truth, principle, or effect. However, the true values of measured variables are seldom (if ever) known and experiments inherently have errors, e.g., due to instrumentation, data acquisition and reduction limitations, and facility and environmental effects. For these reasons, determination of truth requires estimates for experimental errors, which are referred to as uncertainties.

Rigorous methodologies for experimental uncertainty assessment have been developed over the past 50 years. Standards and guidelines have been put forth by professional societies (ANSI/ASME, 1985 [107]) and international organizations (ISO, 1993 [108]).

The Guide to the Expression of Uncertainty in Measurement (GUM) [108] follows these standards and describes a standardized method which first converts all uncertainty information into probability distributions. Based on this, it is consistent to use only the Gaussian error propagation formula to derive the overall uncertainty of the result, which represents a 67% confidence level. In the case of correlated parameters, cross-correlation coefficients are used to evaluate their combined uncertainty contribution.

In DIN 1319-3, section 4.4, it is recommended to divide the evaluation process into four steps:

- 1 - Development of a mathematical model based on the definition of the measurand that describes the measurement problem.

- 2 - Gathering of uncertainty information (observations, data sheets, etc.) and converting them to probability distributions.

- 3 - Calculation of the result and the associated standard uncertainty by applying the model and propagating the uncertainties.

- 4 - Presentation of the result and its extended uncertainty.

Within step 2, the gathered knowledge of the input data is converted into probability distributions and therefore allows the use of the Gaussian uncertainty propagation method. In terms of types of input data, two different kinds of are used in the GUM method.

- Type A input data: Observed statistical data collected during a measurement.

- Type B input data: Non-statistical data, which are known prior to the measurement.

Two types of distribution can be applied: normal or rectangular distributions. If the uncertainty information is given in terms of a statistical data set then the normal distribution can be applied. If the uncertainty information is provided in terms of limits then the rectangular distribution can be applied. In the latter case the standard uncertainty u of a rectangular distribution with a known half-width a is calculated from:

$$u = \frac{a}{\sqrt{3}} \qquad (6.1)$$

In step 3 the partial derivatives of the model function y are calculated to obtain the sensitivity of every input quantity x_i:

$$g_i = \frac{\partial y}{\partial x_i} \qquad (6.2)$$

The uncertainty contribution $u_i(y)$ is calculated by a multiplication of the sensitivity coefficient g_i with the standard uncertainty of the input quantity $u(x_i)$.

$$u_i(y) = g_i \cdot u(x_i) \qquad (6.3)$$

The law of error propagation is given as follows:

$$u^2(y) = \sum_{i=1}^{n} u_i^2(y) + \left\{ 2 \cdot \sum_{i=1}^{n-1} \sum_{j=i+1}^{n} r(x_i, x_j) \cdot u_i(y) \cdot u_j(y) \right\} \qquad (6.4)$$

The right hand summand of Eqn. 6.4 equals to zero, if the input quantities x_i and x_j are not correlated. The correlation coefficient $r(x_i, x_j)$ is defined as:

$$r(x_i, x_j) = \frac{u(x_i, x_j)}{u(x_i) \cdot u(x_j)} \qquad (6.5)$$

whereas $u(x_i, x_j)$ is the covariance between the input quantities x_i and x_j. From Eqn. 6.4 is clear that the sign of the uncertainty contribution $u_i(y)$ is important to calculate the correct uncertainty in correlated cases.

The GUM method uses a special term called the expanded uncertainty. It essentially represents uncertainty limits and was introduced to allow a comparison to other kinds of uncertainty specifications. The expanded uncertainty U is computed from the standard uncertainty $u(y)$ multiplied by a coverage factor k.

$$U = k \cdot u(y) \qquad (6.6)$$

Consequently, the final statement of uncertainty of the measurement result contains the limits and the distribution of the expected values. Generally a coverage factor of *k=2* is used. This value represents a level of confidence of 95% if the result is normally distributed and is therefore rather conservative.

Behr [109] applied the concept for pneumatic 5-hole probes, as well as in a simplified way for standard FRAP probes. For both probes he reported the error propagation for two Mach numbers, representative for the range of dynamic head of the LEC axial turbine test stand (Table 6-1). The values for the yaw and pitch angles are given as relative uncertainties in the calibration range of ±24° in yaw and ±20° in pitch. The pressure uncertainties are presented relative to the dynamic head. The presented values represent expected uncertainties for real flow angles situated within the inner 85% of the angular pitch calibration range (0° to ±17°). At extreme pitch angle positions, the uncertainty shows increased values, due to flow separation around the probe stem. The influence on the overall uncertainty when measuring such high flow angles is discussed in more detail in the uncertainty analysis for the FRAP-HT probe.

Probe type	Parameter	Rotor exit (Ma = 0.25)	Stator Exit (Ma = 0.5)
5HP	φ	± 0.7%	± 0.5%
5HP	γ	± 1%	± 0.8%
5HP	P_{tot}	± 1.9%	± 0.7%
5HP	P_{stat}	± 2.2%	± 0.9%
FRAP	φ	± 1.3%	± 0.5%
FRAP	γ	± 1.6%	± 0.8%
FRAP	P_{tot}	± 2.8%	± 1%
FRAP	P_{stat}	± 3.7%	± 1.2%

Table 6-1   Typical range of expanded uncertainty (k=2) of flow parameters yaw angle φ, pitch angle γ, total pressure P_{tot}, static pressure P_{stat} for pneumatic 5-hole probes and standard FRAP probes.

Furthermore the concept of Behr has been adapted in order to investigate the expanded uncertainties of a pneumatic 4HP, as used in this thesis (chapter 5.1.1). The resulting expanded uncertainties are presented in Table 6-2 for Mach number ranges of 0.3, 0.5 and 0.7. Again, the values for the yaw and pitch angles are given as relative uncertainties to the calibration range of ±24°

in yaw and $\pm 20°$ in pitch. The pressure uncertainties are presented relative to the dynamic head. The presented values represent expected uncertainties for real flow angles which are within the inner 85% of the angular pitch calibration range ($0°$ to $\pm 17°$).

Probe type	Parameter	Ma = 0.3	Ma = 0.5	Ma = 0.7
4HP	φ	$\pm\,0.5\%$	$\pm\,0.3\%$	$\pm\,0.3\%$
4HP	γ	$\pm\,0.7\%$	$\pm\,0.5\%$	$\pm\,0.5\%$
4HP	P_{tot}	$\pm\,1.5\%$	$\pm\,0.8\%$	$\pm\,0.6\%$
4HP	P_{stat}	$\pm\,1.6\%$	$\pm\,1.1\%$	$\pm\,0.7\%$

Table 6-2   Typical range of expanded uncertainty (k=2) of flow parameters yaw angle φ, pitch angle γ, total pressure P_{tot}, static pressure P_{stat} for pneumatic 4-hole probe.

6.1   FRAP-HT

The proper evaluation of the uncertainty of the FRAP-HT technique is more difficult compared to the evaluation for the pneumatic probe technique. This is due to the more complex measurement chain and also due to the unsteady sources of uncertainty. However, the focus of this chapter is to present the uncertainty analysis of the FRAP-HT primary measurement device, which is used to measure the flow pressures and flow kinematics of an unknown flow field.

The measurement accuracy of the FRAP-HT system depends not only on the character of the measurements (type of test rig, high speed/ low speed etc.) that are performed with the system but also on other factors and uncertainties of the measurement setup. Some of the uncertainties are related to steady sources such as:

- Pressure transducer stability, repeatability and hysteresis
- Stability of oven calibration facility
- Sensor model accuracy
- Induced uncertainty due to Offset/ Gain modeling.
- Self heating effects within FRAP-HT probe
- Aerodynamic model accuracy

- Positioning accuracy of probe traversing system

- Stability of freejet aerodynamic calibration facility

- Reference flow accuracy in freejet (differences of real freejet flow angles and pressures compared to ideal freejet)

- Calibration accuracy of FRAP-HT system (DRUCK pressure supply)

- Setup accuracy (mounting of probe for calibration as well as on rig)

- Type of measurement facility (low speed or high speed rig)

- Overall data acquisition accuracy (DAQ board, range, resolution crosstalk and noise sensitivity).

In addition to uncertainties related to steady sources there are unsteady sources of uncertainties, which must be taken into account. A few of the possible unsteady sources of uncertainties are listed as follows:

- Blade passing frequencies and rig stability (facility related)

- Quality of rotor trigger

- White noise (thermal noise within resistors)

- Random noise (thermal noise within conductors)

- Systematic noise (line frequency, power supply ripple, etc.)

- Probe vibration induced errors on the probe stagnation pressure measurements as observed by Winternitz [110].

However, the calibration of the FRAP-HT probe is done in a steady environment of the freejet flow. It is therefore difficult to fully quantify and correct for effects related to the unsteady flow uncertainties, since there is no unsteady reference flow available. Therefore all known and in terms of probability distributions formable unsteady sources are integrated in the uncertainty analysis that is presented here.

6.1.1   Overview of Uncertainty Model

The uncertainty model is based on the standard processes involved in terms of FRAP-HT calibration and measurements. Fig. 6-1 shows the basic signal path involved in a FRAP-HT measurement process as a flow chart. Furthermore the chart presents the dominant uncertainties that propagate into the model and are assigned to the chart based on their location.
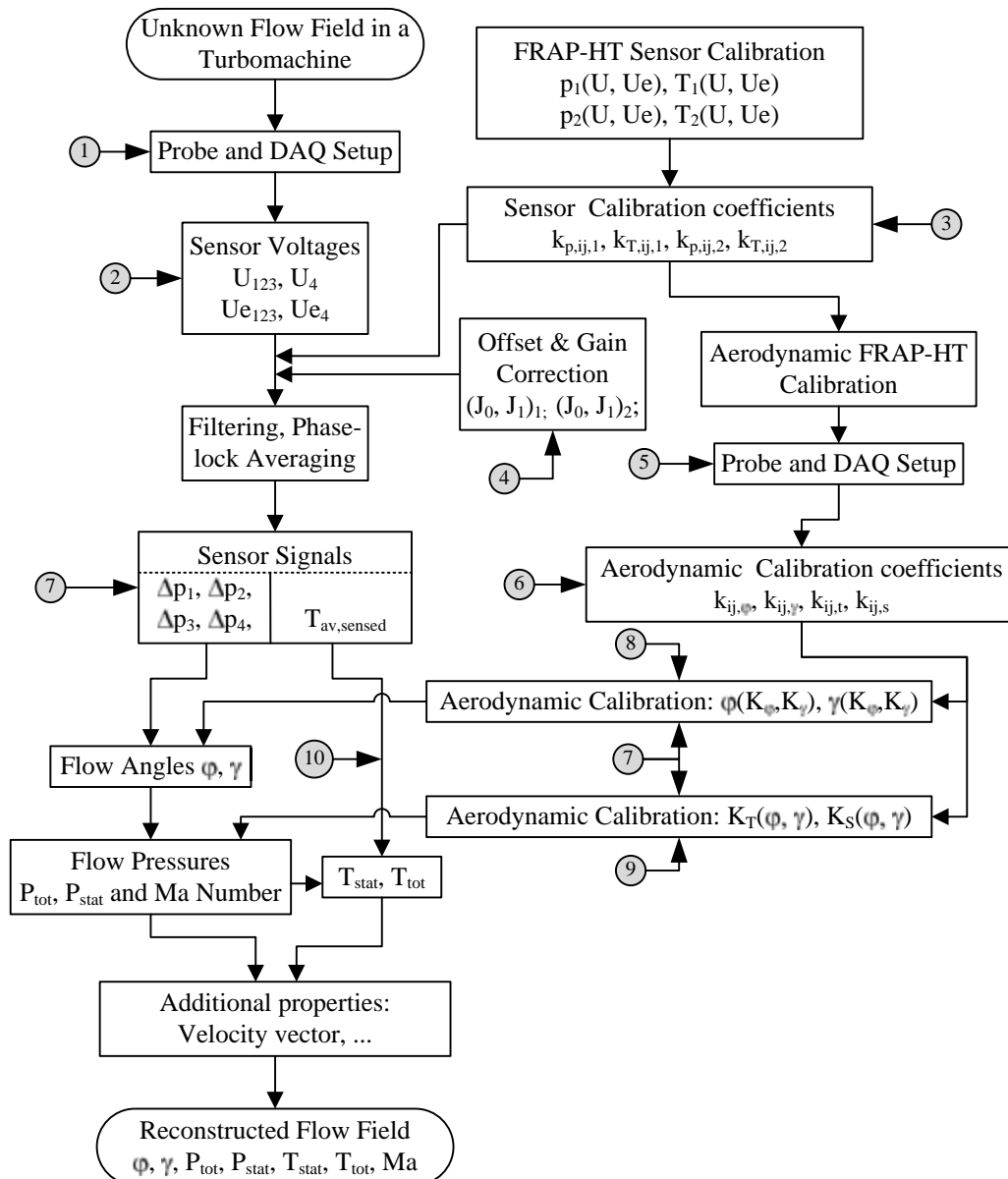
Fig. 6-1   Signal path from flow to measurement results, including main uncertainties propagating into the path.

As presented in Fig. 6-1, the starting point of the signal path is the unknown flowfield in a certain facility. The signal path goes through the different steps, as further described in the FRAP-HT data postprocessing (chapter 4.7.4) and ends with the reconstructed flow field at the bottom of Fig. 6-1. At several points of the flow path some uncertainty sources influence the accuracy of the measured local process and therefore propagate through the signal path from the point of their occurrence. The most significant sources of uncertainty are shown as circularly framed numbers and discussed in the following:

①: In the probe and DAQ setup, uncertainties related to the probe positioning are taken into account. These uncertainties cover the difference between the actual probe position and the intended position. Reasons for the differences are related to the probe handling and the traversing system accuracy. Furthermore the uncertainties related to the facility operating conditions and the resolution of the DAQ board that is used to acquire the operating conditions are taken into account at that step of the analysis. These facility operating conditions are in a later step used for further calculations of certain flow properties (e.g. turbine total inlet pressure and static exit pressure to nondimensionalize the measured total pressure by the FRAP-HT probe).

②: The error sources involved in acquiring the probe voltage signals are mainly related to the resolution of the DAQ board and the stability of the power supplies used to power the FRAP-HT measurement system.

③: All uncertainties related to the sensor calibration facility (stability in temperature, temperature gradients within oven, as well as stability of the pressure sources) are taken into account in this position. Furthermore the pressure transducer uncertainties are induced in this process step for the resulting differential pressure as well as for the sensed steady temperature. They are either related to a known physical behavior that is indicated in the transducer's specification sheet, such as temperature hysteresis, pressure hysteresis, or are obtained from the extensive performed sensor tests (e.g. repeatability and self heating effects). In order to assess the error in the repeatability of the temperature signal, three independent calibration cycles were compared. The standard deviation of the temperature calibration curves across a range from 313K to 463K was determined to be ±0.038K. Furthermore the uncertainty of the polynomial models obtained from the sensor calibration are taken into account at this point of the flow evaluation process. The calibration data model fit uncertainty is calculated as the root mean square of the difference between the measured parameter at each calibration point and the value reproduced by the calibration polynomial. All uncertainties incorporated at the process step further propagate through the measurements, as well as through the aerodynamic calibration path.

④: The process of evaluating the sensor voltages includes the offset and gain correction coefficients J_0 and J_1, as described in chapter 4.7.4. The correction procedure was found to be accurate to within ±25Pa against a first order accurate pressure measurement device which therefore influences the propagation of the overall uncertainties onwards from point ④.

⑤: This process step involves the same kind of uncertainties applied to the

freejet calibration facility as ① for an arbitrary rig. Furthermore it includes also the reference flow uncertainty which represents the difference of flow angle and flow pressures between an ideal freejet flow and the real flow in the freejet calibration facility as evaluated by Kupferschmied [40]. Additionally, the uncertainties due to the turbulence level of 0.3% in the freejet calibration facility are introduced at this point of the signal path. At the freejet nozzle with an exit diameter of 100mm this leads to a stochastic deviation between the aerodynamic and geometric flow angles in the range of ±0.015°.

⑥: The uncertainty of the polynomial models resulting from the aerodynamic calibration are taken into account at this point of the flow evaluation process. The calibration data model fit uncertainty is calculated as the root mean square of the difference between the measured parameter at each calibration point and the result from the calibration polynomial. The polynomial fit uncertainty is in a later step of the measurement again incorporated, when the aerodynamic calibration coefficients are built on an inverse manner during the measurements in an unknown flow field (points ⑧ and ⑨).

⑦: The uncertainty sources related to this point are due to the pressure data acquisition uncertainty. Applying the sensor calibration coefficients results in a differential pressure over the FRAP-HT transducer membrane (Eqn. 4.20 in chapter 4.7.4). In order to derive absolute pressures, uncertainties due to the atmospheric pressure sensor (p_{atm}), as well as the measured relative pressure sensor (p_{ref}) need to be taken into account. This uncertainty is taken into account twice in the complete signal path, since it appears during calibration and propagates into the overall uncertainty of the polynomial calibration coefficients ($k_{ij,s}$ and $k_{ij,t}$) as well as during measurements to form the aerodynamic coefficients (K_s and K_t). Since two additional sensors are needed to derive the absolute pressure, a slightly higher uncertainty is expected for the total and static pressure expression of FRAP-HT compared to pneumatic probes, where only one additional sensor is required.

⑧: At this point the combined uncertainties related to the modeling of the flow angles out of the calibration and the measurements are induced. For instance out of the pure aerodynamic calibration exists an angle model uncertainty which contains the traversing system uncertainty in deriving the coefficients. However, during measurements and additional source of angular uncertainty is added, since the probe is now installed at another rig.

⑨: The uncertainties induced at this process point are similar to those at point ⑧, but are related to the combined angular calibration and measurement

uncertainties and their influence in forming the aerodynamic coefficients K_s and K_t. The related uncertainties are obtained from the polynomial model for K_s and K_t by the partial derivatives for φ and γ and resolving for the variation in K_s and K_t due to angular uncertainties $\Delta\varphi$ and $\Delta\gamma$ (⑧).

⑩: Finally at point ten, uncertainties related to the calculation of the steady temperature from the sensed transducer temperatures are included. These uncertainties are mainly related to the recovery factor correction procedure and their limits for high flow temperatures. Furthermore the uncertainties resulting from the Mach number calculation are considered in this step. This is related to the fact that the recovery factor is modeled as a function of the Mach number (chapter 3.4.2).

Stochastic errors of the complete measurement chain are not included in the overall analysis, since they are in generally removed by phase-lock averaging in the post processing algorithm. Table 6-3 lists some of the dominant uncertainty sources involved in the model as presented in Fig. 6-1.

	System	Uncertainty (abs./rel.)	
Δp_{atm}	absolute KELLER sensor (PAA-33, 0.8-1.2bar)	± 20 Pa	0.05% FS
Δp_{ref}	relative KELLER sensor (PR-33X, 0.5bar)	± 25 Pa	0.05% FS
Δp_{cal}	DRUCK DPI-520 pressure controller (1bar)	± 50 Pa	0.05% FS
$\Delta p_{S,rep}$	Sensor pressure repeatability	± 20 Pa	-
$\Delta p_{S,hyst}$	Sensor pressure hysteresis	± 20 Pa	-
$\Delta p_{S,mod}$	Sensor pressure calibration model uncertainty	± 35 Pa	-
Δp_{OG}	Uncertainty of Offset/ Gain correction	±25 Pa	-
$\Delta T_{S,rep}$	Sensor temperature repeatability	±0.038 K	-
$\Delta T_{S,hyst}$	Sensor temperature hysteresis	±0.125 K	-
$\Delta T_{S,mod}$	Sensor temperature calibration model uncertainty	±0.06 K	-
$\Delta T_{S,SH}$	Sensor self heating uncertainty	±0.08 K	-
$\Delta T_{Oven,s}$	Temperature stability of sensor calibration facility	±0.1 K	-
$\Delta T_{Oven,G}$	Temperature gradients within sensor calibration facility	±0.05 K	-
$\Delta\varphi_{pos,c}$	Accuracy in probe positioning in freejet calibration	±0.01°	-
$\Delta\gamma_{pos,c}$	Accuracy in probe positioning in freejet calibration	±0.015°	-
$\Delta\varphi_{pos,m}$	Accuracy in probe positioning during measurements	±0.015°	-

Table 6-3   Dominant uncertainty sources, involved in the FRAP-HT uncertainty propagation model.

It is expected, that the expanded uncertainties for all properties of interest

depend on the Mach number, as well as on the angle of attack of the flow. Therefore for each Mach number, the uncertainty algorithm has been applied for different combined yaw and pitch angles, in order to investigate the angular dependency of the overall uncertainties. Fig. 6-2 presents the expanded uncertainty at *Ma=0.5* for both flow angles (top) and both measured pressures (bottom) for a set of six different yaw and pitch angle combinations.

The overall uncertainties are influenced by uncertainties related to the polynomial model, as well as by uncertainties related to the measurement of the differential sensor pressures. The elevated uncertainties are therefore influenced by flow separations that occur at extreme positions, such as at flow yaw and pitch angles of 20°/20° as can be seen for both, flow angles and measured pressures on the right hand side in Fig. 6-2. The figure further shows that the expanded uncertainties are not symmetric about the pitch axis, since they are lower for the yaw and pitch angle combination of -20°/-20° (left on Fig. 6-2). The reason for this behavior is related to the downwash effect that occurs at the tip area of the probe; this downwash deflects the flow towards the tip end of the probe. This shifts the stagnation point for the probe towards a more negative pitch angle of around -7° and therefore improves the overall uncertainty for negative pitch angles compared to their positive values. The downwash effect is also clearly identified by the pressure contour plot of the center hole in Fig. 3-19 and in the contours of K_t and K_s in Fig. 3-21.

In order to reduce the complexity of the uncertainty analysis presented here, the following subchapters present expanded uncertainties for varying Mach numbers, but not for varying angles of attack. Nevertheless, a set of different yaw and pitch angle combinations has been used to obtain the underlying uncertainties for each Mach number. Based on the results of the extensive analysis for each Mach number, a weighted mean has been formed based on the probe calibration range. The formation of this mean value equally weights the complete calibration range in yaw, but weights the calibration range in pitch based on a normal distribution around the 0° pitch axis. Since very high pitch angles above ±15° rarely occur during measurements in a turbomachine it is valid to introduce a weighted mean value concept as introduced above. Therefore all the expanded uncertainties presented for all Mach numbers in the following subchapters are weighted mean values derived from multiple uncertainty algorithm runs for varying angular flow combinations.
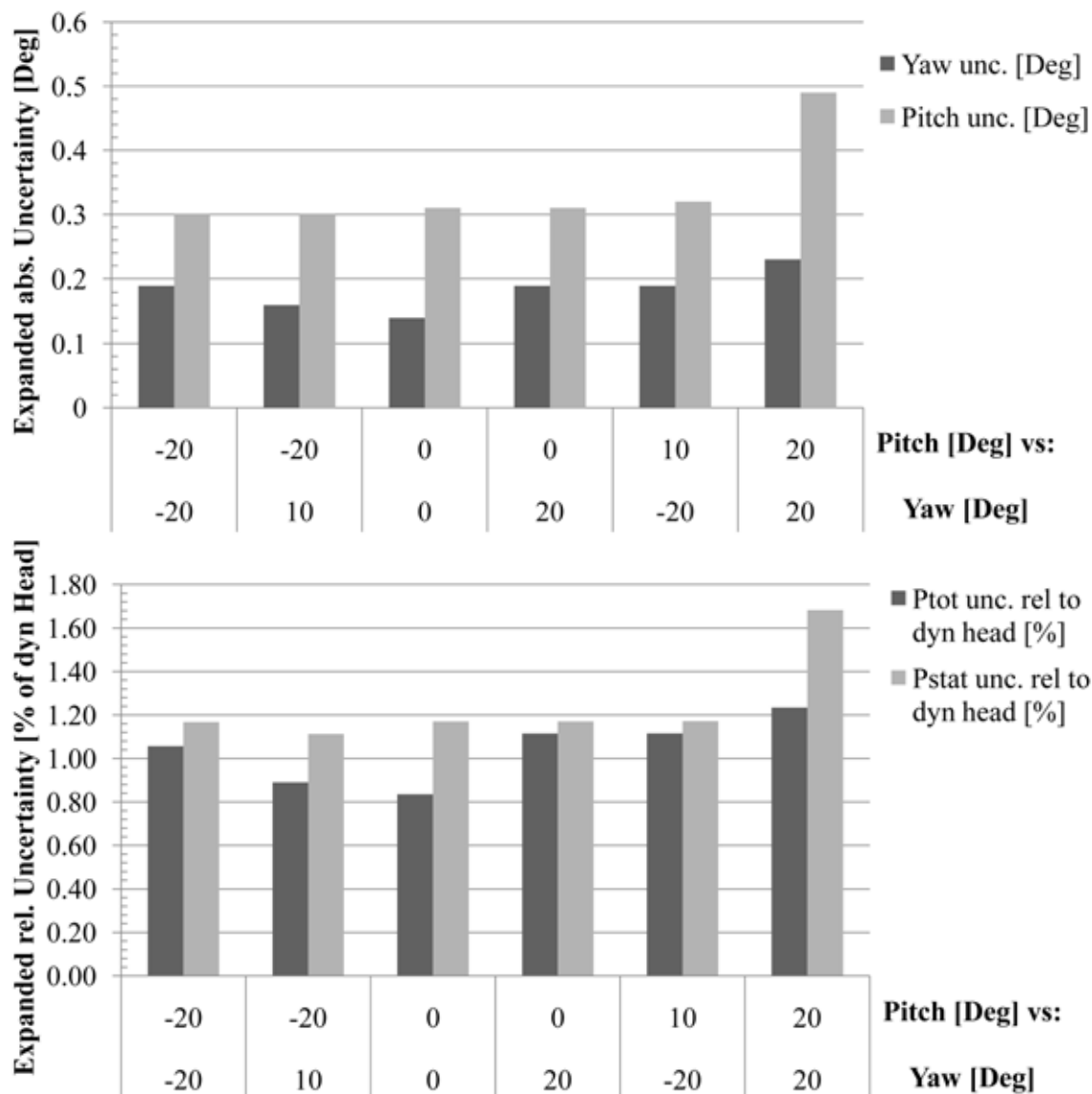
Fig. 6-2   Angular dependency of expanded uncertainty (k=2) of flow param-
eters yaw and pitch angle (top), as well as total and static pressure
(bottom) for FRAP-HT probe calibration at Ma=0.5.

6.1.2   Flow Angle Uncertainties

The uncertainty of the FRAP-HT flow angles are determined from the uncertainty algorithm as presented in Fig. 6-1. The incorporated uncertainties are based on the sensor calibration model, based on the probe positioning accuracies as well as based on the uncertainties related to the differential pressure sensed by the FRAP-HT sensor. The basic model equation incorporated for the uncertainty propagation into the differential sensor pressure is defined as follows. The pressure $p_{diff,model}$ equals the differential

pressure output based on the sensor calibration polynomial, and all the included $\Delta p_{x,y}$ pressures on the right hand side of the equation are the incorporated sources of uncertainty in order to express the uncertainty afflicted differential sensor pressure Δp:

$$\Delta p = p_{diff,model} + \Delta p_{S,mod} + \Delta p_{S,hyst} + \Delta p_{S,rep} + \Delta p_{cal} + \Delta p_{OG} \qquad (6.7)$$

The typical uncertainty bandwidth is presented in Fig. 6-3 and summarized in Table 6-4. At low Mach numbers around $Ma=0.15$ the uncertainty is mainly determined by the accuracy of the probe pressure data acquisition system. The expanded uncertainty ($k=2$) at this Mach number is around $\pm1.5°$ for the yaw angle and $\pm2.5°$ for the pitch angle. With increasing Mach numbers this value reduces due to the improved accuracy of the pressure DAQ system. The uncertainty at higher Mach numbers is mainly determined by the accuracy of the calibration models. At $Ma=0.5$ the angle uncertainty reduces with polynomial models to around $\pm0.2°$ and $\pm0.3°$ respectively. The variations between the accuracies of the yaw and pitch angles are due to the non-symmetric shape of the probe tip.
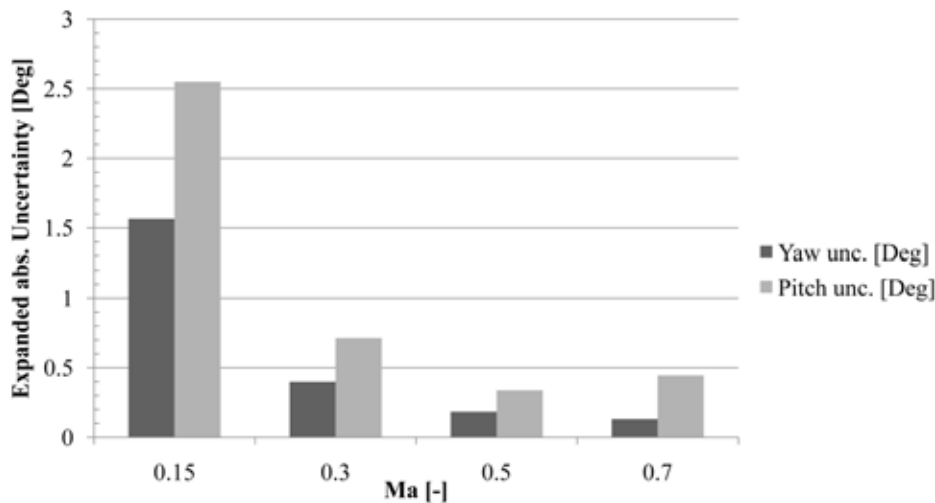
Fig. 6-3   FRAP-HT Mach number dependant expanded uncertainty (k=2) of flow parameters yaw angle φ [Deg] and pitch angle γ [Deg].

The incorporated uncertainty values for the FRAP-HT differential pressures are based on the rather conservative uncertainty information of the manufacturer which represent combined values of systematic and stochastic errors including long term effects. During the application in a short time measurement campaign, it can be assumed that not all sources of uncertainty considered in the manufacturer's value, are relevant. For this reason the expanded uncertainties in Table 6-4, presented relative to the calibration range of the respective flow angles, can be considered as a conservative

uncertainties.

Parameter	Ma = 0.15	Ma = 0.3	Ma = 0.5	Ma = 0.7
φ	± 3.2%	± 0.8%	± 0.4%	± 0.3%
γ	± 6.3%	± 1.8%	± 0.8%	± 1.1%

Table 6-4   Typical range of expanded uncertainty (k=2) of flow parameters yaw angle φ and pitch angle γ for FRAP-HT probe presented relative to the calibration range of the respective angle.

6.1.3   Flow Pressure Uncertainties

The uncertainty of the resulting FRAP-HT flow pressures incorporates the same uncertainties as the flow angles. Furthermore, the expanded uncertainties of the resulting yaw and pitch angles are accounted for. Finally, the uncertainties in determining absolute pressures from the differential sensor pressures are based on Eqn. 6.8. The expression for the absolute pressure p therefore incorporates the uncertainties for the sensor differential pressures (Δp based on Eqn. 6.7) as well as the uncertainties of the secondary pressure devices such as the KELLER relative (Δp_{ref}) and absolute (Δp_{atm}) pressure transducers:

$$p = p_{atm} + p_{ref} - \Delta p + \Delta p_{ref} + \Delta p_{atm} \qquad (6.8)$$

The extended uncertainty of the flow pressures at low Mach numbers around *Ma=0.15* amount to ±160Pa for the total pressure and ±188Pa for the static pressure. With increasing Mach numbers the uncertainty of the calibration model does not necessarily increase and in terms of relative uncertainty based on the dynamic head, the expanded uncertainties are therefore reduced at higher Mach numbers. However, the model uncertainty is multiplied with a term representing the partial derivative of the overall uncertainty equation. This term increases with higher Mach numbers due to higher absolute pressure levels. For this reason the model uncertainty contributes more to the overall uncertainty at higher Mach numbers. This effect can be seen in the results shown in Fig. 6-4.
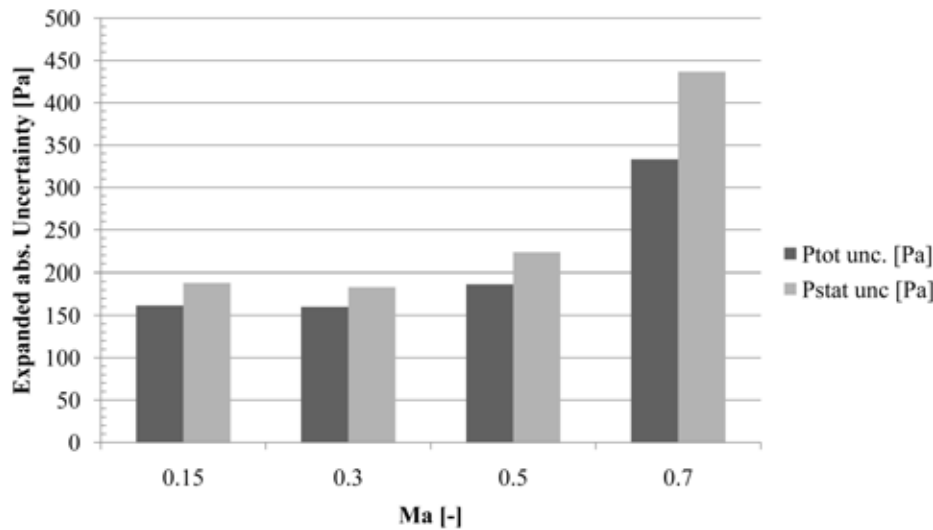
Fig. 6-4   Mach number dependant expanded uncertainty (k=2) of total pressure P_{tot} [Pa] and static pressure P_{stat} [Pa] for FRAP-HT probe.

As mentioned before, the incorporated uncertainties for the FRAP-HT differential pressures are based on the rather conservative uncertainty information of the manufacturer. During the application in a short time measurement campaign, it can be assumed that not all sources of uncertainty apply, that are considered in the manufacturer value. For this reason the expanded uncertainties in Table 6-5, presented relative to the dynamic head range of the respective flow angles, can be considered as a conservative uncertainty information.

Parameter	Ma = 0.15	Ma = 0.3	Ma = 0.5	Ma = 0.7
P_{tot}	± 10.5%	± 2.6%	± 1%	± 0.9%
P_{stat}	± 12.2%	± 2.9%	± 1.2%	± 1.2%

Table 6-5   FRAP-HT probe expanded uncertainty (k=2) of flow parameters total pressure P_{tot} and static pressure P_{stat} presented relative to the Mach number respective dynamic head.

6.1.4   Temperature Measurement Uncertainties

The quantification of the steady temperature resulting out FRAP-HT measurements allows the calculation of further rig conditions, such as the stage efficiency. In order to quantify the uncertainties related to the steady temperature measurement, different temperature related sources of uncertainties as listed in Table 6-3 are taken into account in the evaluation of the sensed temperature. The quantification of the uncertainty inputs is

achieved by the specification sheets of the different involved "sensors" and facilities, as well as based on results from extensive sensor and oven characteristic tests. The overall uncertainty for the sensed FRAP-HT steady flow temperature results from the following model equation:

$$T_{sensed} = T_{cal} + \Delta T_{S,mod} + \Delta T_{S,hyst} + \Delta T_{S,rep} + \qquad (6.9)$$

$$\Delta T_{S,SH} + \Delta T_{Oven,s} + \Delta T_{Oven,G}$$

The resulting expanded uncertainty for the sensed temperature T_{sensed} is in the order of ±0.25K. However, the final uncertainty for the total and static flow temperature respectively are higher. They result from the model equations based on chapter 3.4.2.

The resulting expanded uncertainties for the total temperature range from ±0.3K for a Ma number of 0.15, up to ±1.8K for a Mach number of 0.7. For the common Ma number range of around 0.5, the expanded uncertainty in measuring the total temperature equals ±0.9K. In terms of static temperature, the expanded uncertainty ranges from ±0.27K for a Mach number of 0.15, up to ±1.7K for Mach number of 0.7. For the common Ma number range of around 0.5, the expanded uncertainty in measuring the static temperature equals ±0.8K. The uncertainty analysis showed, that the errors due to modeling the recovery factor correction procedure accounts for most of the expanded uncertainty for T_{stat} (over 90%). Roduner [87] showed, that the recovery factor is not only dependent on the Mach number, but also on the temperature. The expanded uncertainty is mainly due to the limits in predicting the recovery factor distribution for high flow temperatures. Furthermore the uncertainties resulting from the Mach number calculation are considered in this step. This is related to the fact that the recovery factor is modeled as a function of the Mach number (chapter 3.4.2).

6.1.5   Concluding Remarks

The uncertainties derived from the model as described in the previous subchapters are related to the FRAP-HT for the temperature range up to ~473K. The range chosen for the investigation is in accordance to the range of all performed turbomachinery measurements and showed a satisfactory range of expanded uncertainties (see Table 6-4 for flow angles and Table 6-5 for pressures, as well as chapter 6.1.4 for the steady temperatures). For the range between 473K and 533K, the expanded uncertainties have been roughly estimated based on the polynomial uncertainties during sensor calibration. The uncertainties for the temperature measurements are expected to result in

expanded uncertainties up to 6 times higher, compared to the lower temperature range area, whereas the uncertainties in the angle and pressure measurements are expected to contribute respectively up to 4 and 8 times higher expanded uncertainties compared to the lower temperature range uncertainties.

7 Hot Streak Generator equipped One-and-1/2-Stage Axial Turbine Measurements

The newly developed high temperature FRAP probe is applied in the one–and-1/2-stage, unshrouded axial turbine at ETH Zurich; this turbine configuration is representative of a high work aero-engine. The flow conditioning stretch upstream of the first stator is equipped with a recently designed hot streak generator. Several parameters of the hot streak, including temperature, radial and circumferential position, and shape and size can be independently controlled. The interactions between the hot streak and the secondary flow present a perfect scenario to verify the probe's capability to measure under real engine conditions. Therefore, measurements with the novel probe have been made in order to validate the fidelity of the probe's measurements and to detail the interaction effects with blade row pressure gradients and secondary flows.

7.1 Hot Streaks

Experimental data taken from gas turbine combustor exit flows appear to have strong radial and circumferential temperature gradients, often referred to as hot streaks or hot spots. These pronounced temperature non-uniformities in the combustor exit flow field are caused by circumferentially discrete fuel and dilution air injection within the combustor. The hot streaks interact with the different turbine parts and can locally cause increased blade heat transfer leading to reduced blade life and significant risks. As a consequence turbine components are generally designed for higher temperatures than the mean turbine entry temperature. As the induced migration physics can not be quantitatively predicted with satisfying accuracy for the hot gases, turbine designers need to budget for the worst case temperature distortions. An improved understanding of hot streak thermally driven transport mechanisms and unsteady blade row interactions is required to set up an effective blade cooling strategy in order to minimize the usage of performance costing cooling flow in the turbine.

One of the earliest studies about inlet flow distortion effects on a stationary blade row has been performed by Munk and Prim in 1947 [111]. It has been shown for inviscid steady flow that the stream line pattern in a vane passage is theoretically not influenced by the presence of a variation in total temperature as long as the stagnation pressure distribution remains constant, more precisely

as long as the absolute momentum distribution remains unaltered. Hermanson and Thole [112] showed that the driving parameter for secondary flow generation in a turbine vane is the stagnation pressure distribution. Experimental studies on the transport mechanisms of combustor exit stagnation pressure and temperature profiles conducted in a high pressure turbine vane by Barringer et al. [113] show a significant effect of the near endwall stagnation pressure profile on the redistribution of the stagnation enthalpy on its way through the vane. The induced changes in heat transfer on high pressure vanes and endwalls have been experimentally and numerically analyzed by Povey et al. [114] and Barringer et al. [115]. Further the combined effect of high turbulence and film cooling on the mixing and dispersion of a hot spot in a nozzle guide vane was experimentally studied by Jenkins et al. [116]. It was shown that turbulence effects and film cooling considerably reduce the hot spot peak temperatures.

The thermally driven effects of an inlet temperature distortion on the rotor flow field are more complex. In the absolute frame the hot air travels at the same absolute momentum and flow angle as the free stream. In a rotor relative view the hot gases have a higher relative momentum and thus higher relative stagnation pressure. Whereas a variation of stagnation pressure generates secondary flows in a stationary blade row, the gradients in relative stagnation pressure induced by a hot spot are source of additional secondary flows. The preferential migration of hot gases toward the pressure side and cold gases toward the suction side as well as the migration of the hot gases toward the endwalls once arrived on the pressure side have first been experimentally observed by Butler et al. [117] and experimentally verified by Roback and Dring [118, 119]. Three dimensional unsteady computational investigations by Dorney et al. [120] and Rai et al. [121] have reported similar findings. The tendency for separation of hot and cold gases was first mentioned by Kerrebrock et al. [122] in their work about the effect of the high temperature compressor rotor wakes on downstream stator blades. Assuming a steady and incompressible flow and neglecting circumferential gradients Butler et al. [117] show that in a rotating blade row the generation of stream wise vorticity is a function of radial relative stagnation pressure and density gradients. Dunn et al. [123] analyses convective heat transfer on blade rows in the presence of hot streaks. The time resolved transport mechanisms in the rotor flow field have only been rarely addressed so far in the open literature, and mainly based on CFD results. The unsteady migration of injected coolant mass flow in a turbine rotor flow field has been investigated and analyzed by Ong et al. [124] and An et al. [125].

Next to the presented results within this chapter of the thesis generated by an inlet temperature distortion, based on the results of an experimental measurement campaign that was carried out in a real engine like test turbine environment, additional results are presented in the work of Jenny et al. [126]. The aim of his work is to analyze the unsteady transport mechanisms. The effect of the NGV and the rotor on the hot streak and the unsteady interaction between rotor and stator blade rows are analyzed in detail with particular attention on the unsteady thermally driven transport mechanisms. In addition to the experimental results presented here a numerical study carried out by Basol et al. [127] analyses the effect of the hot streak's position at the NGV inlet on the stage heat load, and particularly on the rotor blade tip.

7.2   Experimental Facility

7.2.1   LISA Axial Research Turbine Facility

The experiments for the current investigation have been conducted in the axial research turbine test rig (LISA) at the Laboratory for Energy Conversion of ETH Zurich. The facility is a continuously running, moderate-speed, generally low-temperature rig which initially was designed to investigate unsteady effects in axial turbines.

The facility extends over 3 floors (Fig. 7-1). The air-loop of the facility is quasi-closed opening to atmosphere at exit of the turbine. A 1 MW radial compressor providing a maximum pressure ratio of 1.5 and a maximum mass flow of 13 kg/s situated in the basement delivers the air flow. The operating point of the compressor and with it the turbine pressure ratio is controlled by adjustable inlet guide vanes. The main mass flow is measured upstream of the compressor by a calibrated venturi nozzle.

At the exit of the compressor the flow is guided through two water to air heat exchangers, which control the inlet total temperature to a constant and adjustable value in the range of 308K to 328K. The stability and the accuracy of the two exchangers in order to control the inlet total temperature $T_{tot,in}$ is in the order of 0.2K.

A homogenous flow field to the turbine is provided by a flow conditioning stretch of 3 meter in length, upstream of the turbine. Furthermore, the flow is accelerated ahead of the turbine section to reduce the significance of remaining flow non-uniformities from upstream.

An angular gear box located on the top floor halves the rotational speed. A

horizontal shaft connects the gearbox to a DC generator of 400kW maximum power, which absorbs the turbine power and controls the rotational speed with an indicated accuracy of 0.02% (0.5rpm). For control and performance issues, a torquemeter is installed and provides measurements of the torque on the rotor shaft.
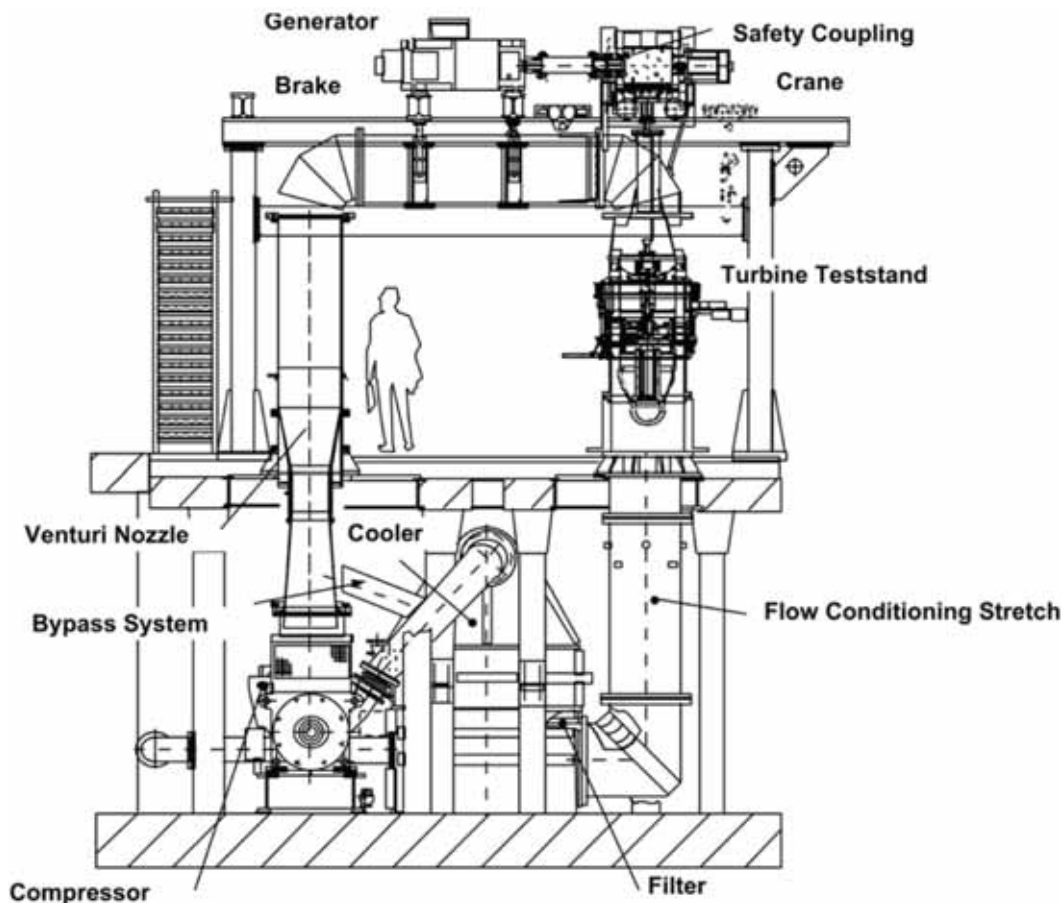
Fig. 7-1   Schematic view of "LISA" axial research turbine test facility.

The turbine test stand (Fig. 7-1) itself, is interchangeable. A detailed viewgraph of it is presented in Fig. 7-2. The primary 2-stage, shrouded turbine configuration (Sell et al. [128]) was redesigned by Behr [104] as a 1.5 stage turbine, following the design objectives of modeling unshrouded, high-pressure gas turbine stages with high stage loading and low aspect ratios with the aim to provide compressibility effects under realistic rotor exit flow field through a second stator. The redesigned turbine consists of one highly loaded stage and a second vane. This results in maximized Mach numbers, stage loading and pressure ratio for the first stage. The presence of the downstream second stator row results, through upstream potential effects, in a representative stage exit flow field. This adds in additional rotor stator interaction phenomena to be investigated.
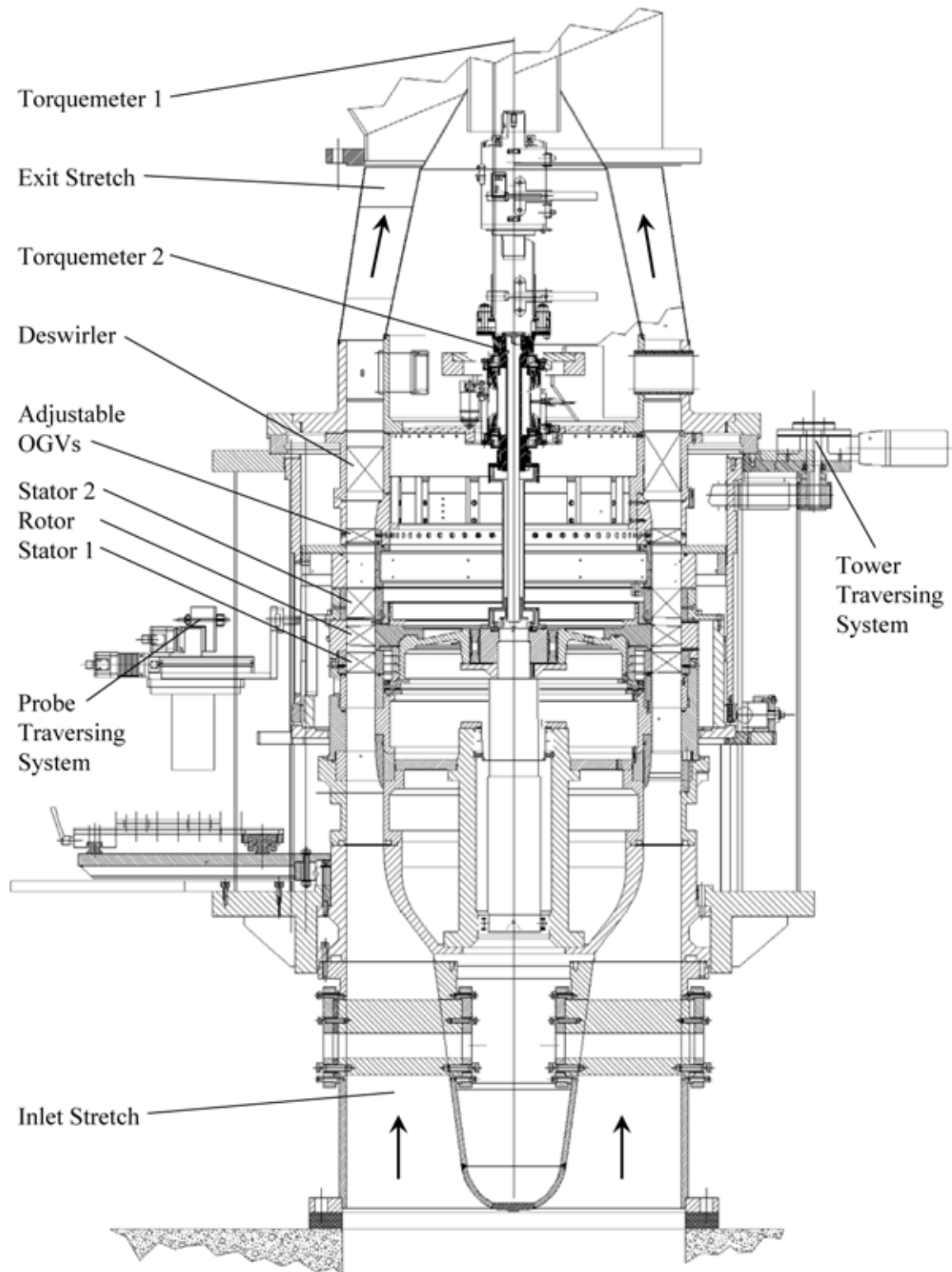
Fig. 7-2   "LISA" One-and-1/2-stages, unshrouded axial turbine facility.

A cross sectional view of the turbine module is presented in Fig. 7-2. A detailed description of the turbine design is given by Behr et al. [104]. Global

parameters of the turbine at the design operating point are shown in Table 7-1 and the characteristics of each blade row are presented in Table 7-2.

Turbine parameter	Value
Rotor speed [RPM]	2700
Pressure ratio (1.5-Stage, total-to-static)	1.65
Turbine entry temperature [K]	314
Total inlet pressure [bar abs norm]	1.4
Mass flow [kg/s]	11.8
Hub/tip diameter [mm]	660/800

Table 7-1   Main parameters of "LISA" 1.5-stage axial turbine research facility at design operating point (measured).

	Stator1	Rotor	Stator2
Number of blades	36	54	36
Inlet flow angle [°] (midspan)	0	54	-42
Exit flow angle [°] (midspan)	73	-67	64
Aspect ratio (span/chord)	0.87	1.17	0.82
Blade row relative exit Mach numbers [-] (average)	0.54	0.50	0.48
Reynolds number based on true chord and blade row relative exit velocity [-]	$7.1 \cdot 10^5$	$3.8 \cdot 10^5$	$5.1 \cdot 10^5$

Table 7-2   Characteristic geometry and performance parameters of the 1.5-stage turbine configuration (performance values derived from P5HP measurements at design operating point).

7.2.2   Hot Streak Generator

The test rig is equipped with an internally designed hot streak generator (Jenny et al. [126]). The temperature distortion generator is designed to introduce one single hot spot upstream of the first nozzle guide vane row allowing to mix ahead of the NGV1 inlet plane. The hot streak was generated by passing a bypass flow through an external flow heater and blower before reintroducing the heated flow through circular injector pipes with a diameter of 30% span (red part on Fig. 7-3).

The single passage hot streak generator has an inlet duct diameter of 22mm, with an exit wall thickness of 0.5mm and is operated in equal Ma number

mode (compared to the main flow). In order to reduce main flow disturbance, the conical outer shaped injection tube is installed on a vane-shaped support strut (blue part on Fig. 7-3). The injection plane is approximately 3.5 stator axial chords upstream of the first nozzle guide vane (Fig. 7-4).

Both the turbine and the hot streak generator are designed such that a variety of parameters can be adapted in order to investigate their influence on the flow field. The most interesting parameters are the hot streak temperature, the span-wise position of the hot streak (from about 20% to about 65% span), the shape and size of the hot streak (interface exchange), the pressure of the hot streak, the clocking angle of the stator and the temperature of the main flow.
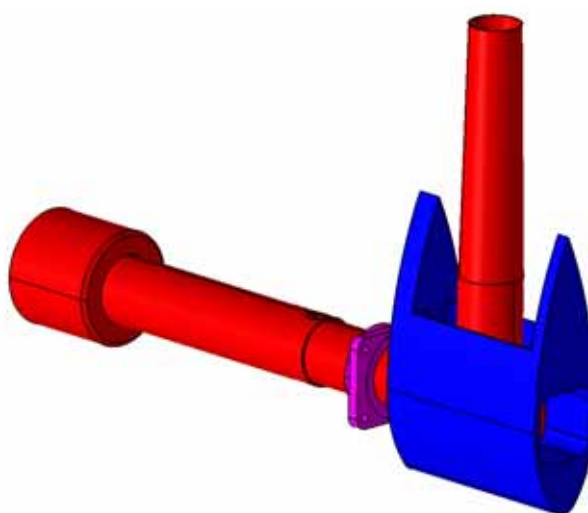
Fig. 7-3   Hot Streak generator, designed for LISA application.

Fig. 7-4 shows a cut through the turbine with the hot streak generator. In Fig. 7-4, the strut is represented in blue where the red part represents the injection pipes for the hot air.

In the present study the hot streak generator was located at 20% and at 50% span and circumferentially positioned at mid pitch so that the hot streak does not impinge onto the blades. The bypassed air can be heated to a maximum peak temperature over free stream ratio of 1.36 allowing different temperature profiles. The applied hot streak temperature ratios presented in this study, are presented in chapter 7.4.
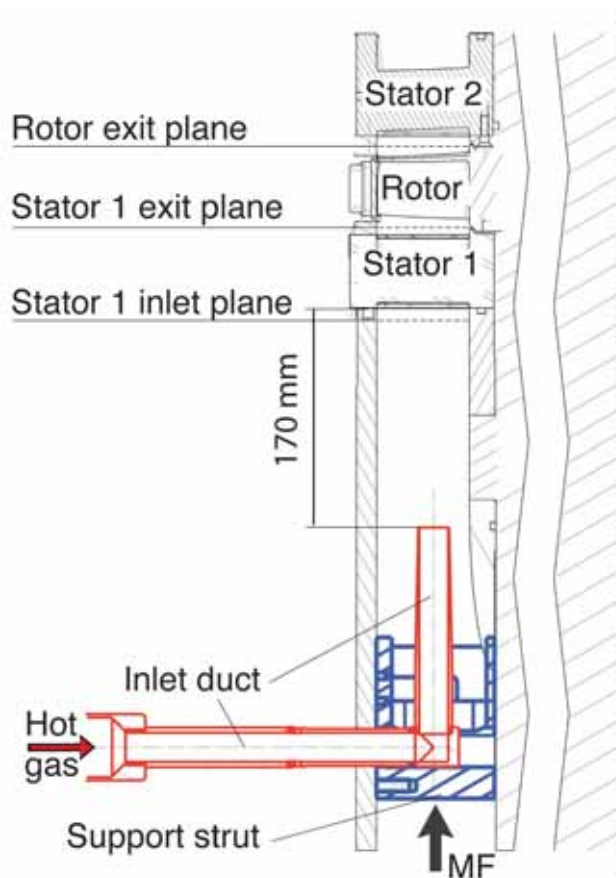
Fig. 7-4   Close-up view of the one-and-a-half stage unshrouded axial research turbine, equipped with a hot streak generator (inlet duct and vane-shaped support strut).

The turbine pressure ratio, as well as the main flow entry temperature and the hot streak temperature are kept constant during operation. Daily variations in ambient pressure are considered by non-dimensionalizing the measured pressures by the respective total inlet pressure and static outlet pressure. In order to represent real engine conditions, the hot streak mass flow is controlled, such that its stagnation pressure and Mach number are equal to the free stream level.

7.3   Facility Specific Probe Configuration

7.3.1   Expected Temperature Range

The expected maximum temperature to phase during the measurements does not exceed 473K. Therefore, the piezoresistive sensors behave dominantly linearly, and the temperature window of 303K up to 473K was used to define the sensor calibration coefficients (Fig. 7-5). This results in a

mean pressure sensitivity of 4.35mV/(mbar·mA) for both sensors and a mean temperature sensitivity of 0.38 mV/K for both sensors.
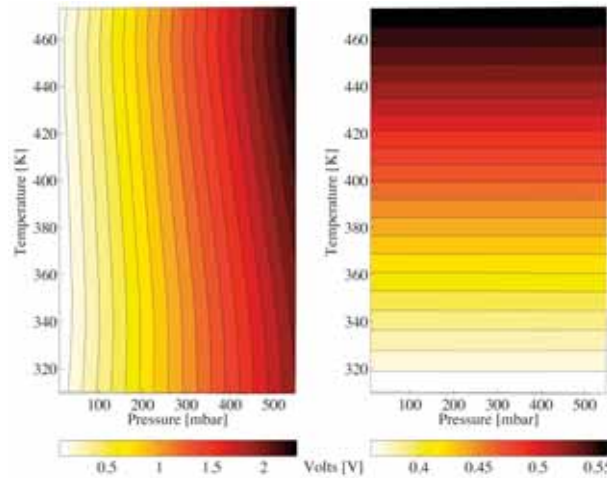
Fig. 7-5   Typical output signals, U (left) and Ue (right) in voltage [V] as a function of temperature and pressure, resulting from the probe sensor calibration.

7.3.2   Accuracy of applied Instrumentation

The GUM-based measurement uncertainties (chapter 6) for FRAP-HT, FRAP and 4HP are given in Table 7-3, evaluated for the specific "LISA" facility measurements.

The values for the yaw and pitch angles are given as relative uncertainties to the calibration range of $\pm 24°$ in yaw and $\pm 20°$ in pitch. The pressure uncertainties are presented relative to the dynamic head.

Flow property:	FRAP-HT	FRAP:	4HP:
φ	$\pm 0.4\%$	$\pm 0.5\%$	$\pm 0.3\%$
γ	$\pm 0.8\%$	$\pm 0.8\%$	$\pm 0.5\%$
P_{tot}	$\pm 1.0\%$	$\pm 1.0\%$	$\pm 0.8\%$
P_{stat}	$\pm 1.2\%$	$\pm 1.2\%$	$\pm 1.1\%$

Table 7-3   Typical error bandwidth of flow parameters for the three different probes with the same calibration range.

7.4   Measurement Configuration

The data are measured at three different traverse planes in the turbine test facility. Fig. 7-6 shows the geometry and the relative positions of stators one

and two, as well as the relative position of the three traverse planes stator 1 inlet, stator 1 exit and rotor exit.
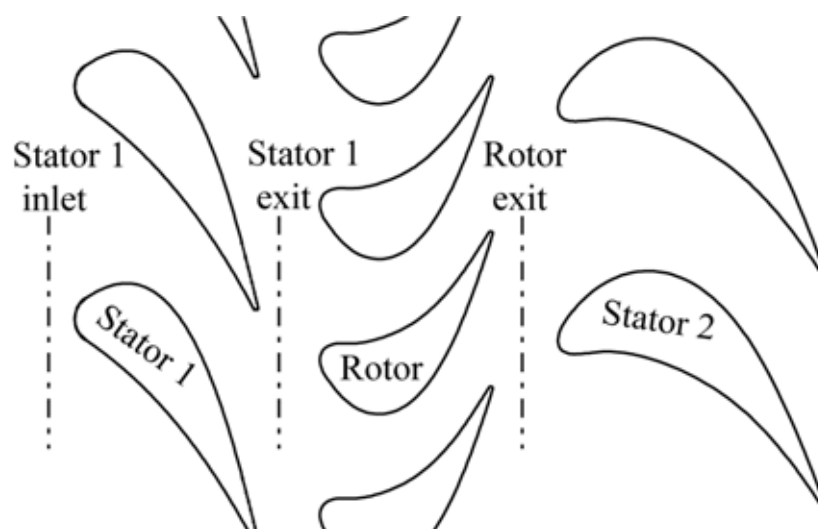
Fig. 7-6   Illustration of geometrical relations and measurement planes.

In order to prove the concept of the newly developed probe and to allow qualitative and quantitative comparisons to other well-established probes, measurements were performed using a uniform data point grid. One measurement plane consists of 41 traverses for the stator 1 exit plane and the rotor exit plane and due to access issues, 33 traverses for the stator 1 inlet plane. For all measurement planes one traverse contains 45 measurement points. In the case of the stator 1 exit and rotor exit plane, this leads to an overall measurement point density of 1845 points per stator pitch of 10 degrees. In the radial direction, the measurement locations range from 5.7% span to the near tip endwall region, located at 99.3% span. Based on the virtual four-sensor probe concept, one measurement point consists of three records, all sampled for two seconds with a data acquisition frequency of 200 kHz. Before and after each radial traverse an offset and gain measurement is performed in the tower position outside the flow by applying two different probe back pressure levels. One measurement plane therefore consists of 5699 records, which results in 71.3 Gbytes of raw data per measurement plane and lasts for approximately 10 hours.

In the first step of the data processing, the raw data are phase-locked based on one specific trigger position on the rotor circumference. Each resulting data set covers three consecutive passages, containing 82 samples per passage. The previously discussed sensor calibration procedures are applied to the reduced data set. The received pressure signals are then phase-lock-averaged and the aerodynamic calibration model is applied to derive the unsteady flow angles as

well as unsteady total and static pressures, Mach number and based on the steady temperature (1 Hz), the velocity components.

Measurements are conducted at the inlet of the first stator, the exit of stator one, as well as on the exit of the rotor (Fig. 7-4 and Fig. 7-6). Three different test configurations will be presented within this chapter (Table 7-4):

Configuration (Conf):	T_{MF}: [K]	T_{HS}: [K]	T_{HS}/T_{MF}:	HSG span position:
1	314	378	1.21	50%
2	314	429	1.36	50%
3	314	429	1.36	20%

Table 7-4   Investigated test cases, for different hot streak temperatures and different span-wise injection positions.

The hot streak generator was positioned at two different radial locations: at 50% span and at 20% span. Circumferentially, the HSG was positioned at mid-pitch, in order to avoid a direct impingement onto the blades of the first stator. The measured span-wise distribution of the pitch-wise mass-averaged stagnation to main flow temperature ratio $T_{tot,mav}/T_{MF}$ is presented in Fig. 7-7 for test configurations 2 and 3. The variation in the maxima for the two cases is related to the variation of the HS due to the wall proximity.
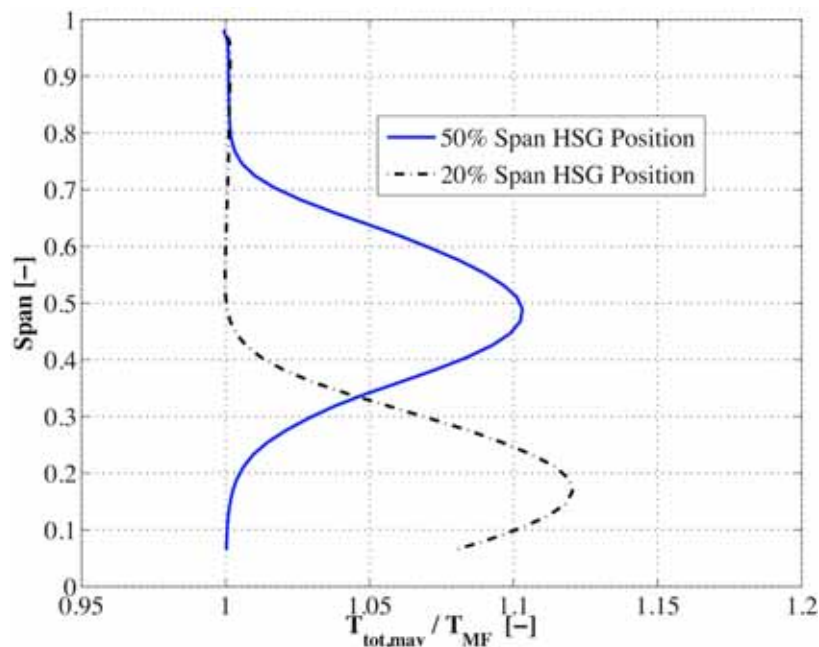
Fig. 7-7   Normalized total temperature $T_{tot,mav}/T_{MF}$ measured with FRAP-HT at the inlet of stator 1 (pitch-wise mass-averaged) for configurations 2 and 3.

7.5   Results and Discussion

7.5.1   Steady Hot Streak Inlet Conditions

At the inlet of the first stator, the focus of the FRAP-HT measurements is to demonstrate the capability to measure the steady temperature.

Fig. 7-8 represents the steady temperature normalized by the main flow temperature. Measurements performed at the stator inlet with the FRAP-HT probe for configurations 2 and 3 are compared to ideal case simulations at the HS injection plane further upstream. In the simulation of the ideal case, the HS was positioned mid-pitch of the first stator. However, the measured temperature profiles at the first stator inlet plane show a slight shift of the HS core (-0.05 stator pitch position) compared to the target position of zero pitch. The profiles are circularly shaped for configuration 2 and slightly squeezed in the measurement for configuration 3. The difference in shape is related to wall proximity effects. Another reason for the squeezed shape of the hot spot at 20% span could be related to a slight misalignment of the HS inlet duct compared to the main flow streamlines. The inlet duct is positioned from outside of the turbine casing. The vane-shaped support strut gives guidance for accurate positioning. However, the high thermal gradients could lead to some warping of the duct structure. Any misalignment of the duct compared to the free stream would then lead to a jet in cross-flow, resulting in a deflection of the jet in the direction of the crossflow.

For both configurations, the HS core to free stream stagnation temperature ratio is at the same level as at the injection plane (T_{tot}/T_{MF} =1.36). This, as well as the squeezed and therefore wider temperature profile of the 20% span HS position, is further illustrated in Fig. 7-9a, where a pitch-wise cut through the area plots of Fig. 7-8b and d is represented for T_{tot}/T_{MF} at the respective HS span position.
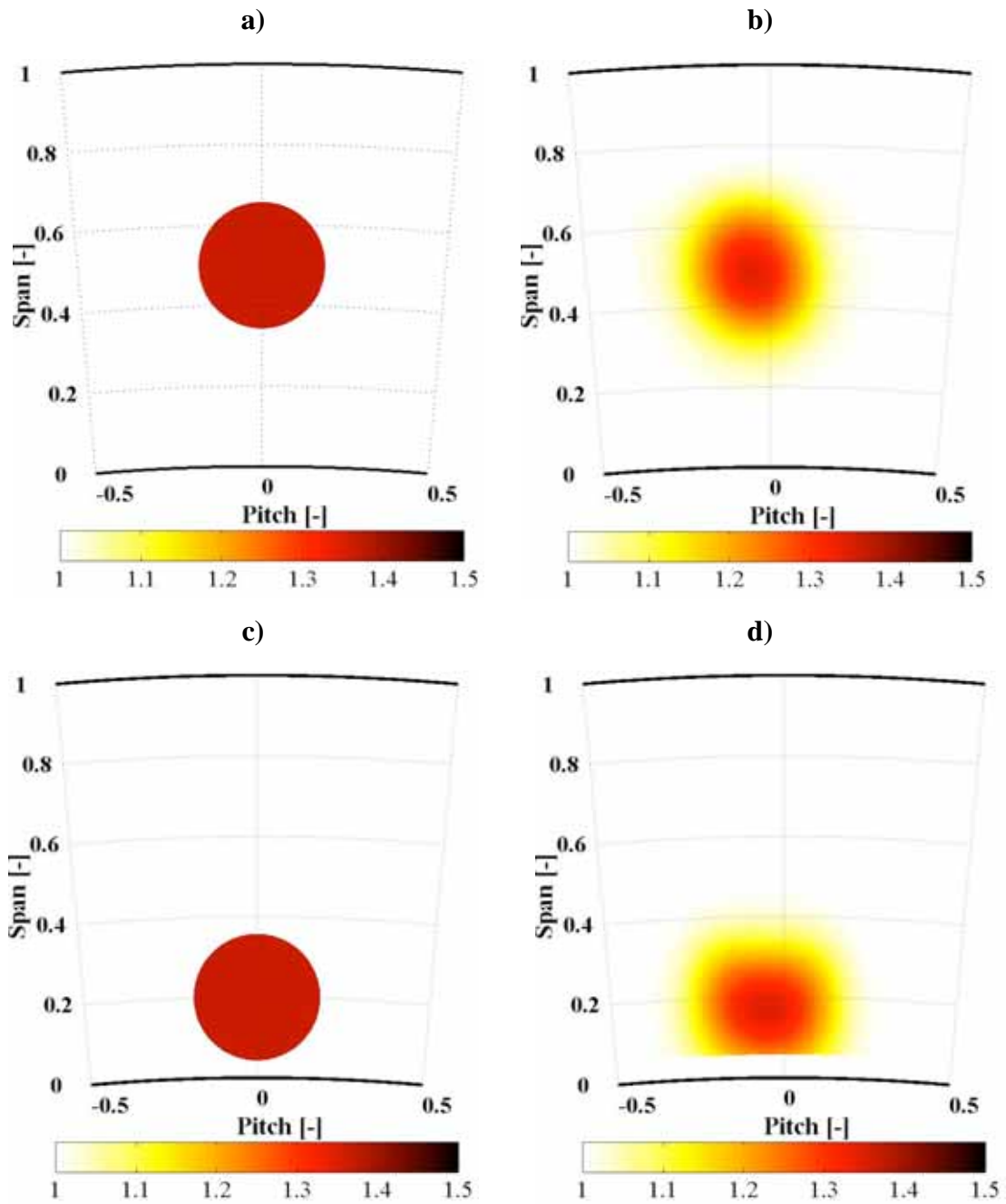
Fig. 7-8   *Steady normalized total temperature (T_{tot}/T_{MF} [-]) over one stator pitch. Ideal case simulation at the HS injection plane for configurations 2 (a) and 3 (c); FRAP-HT results at the inlet of stator 1 for configurations 2 (b) and 3 (d).*

a)

b)
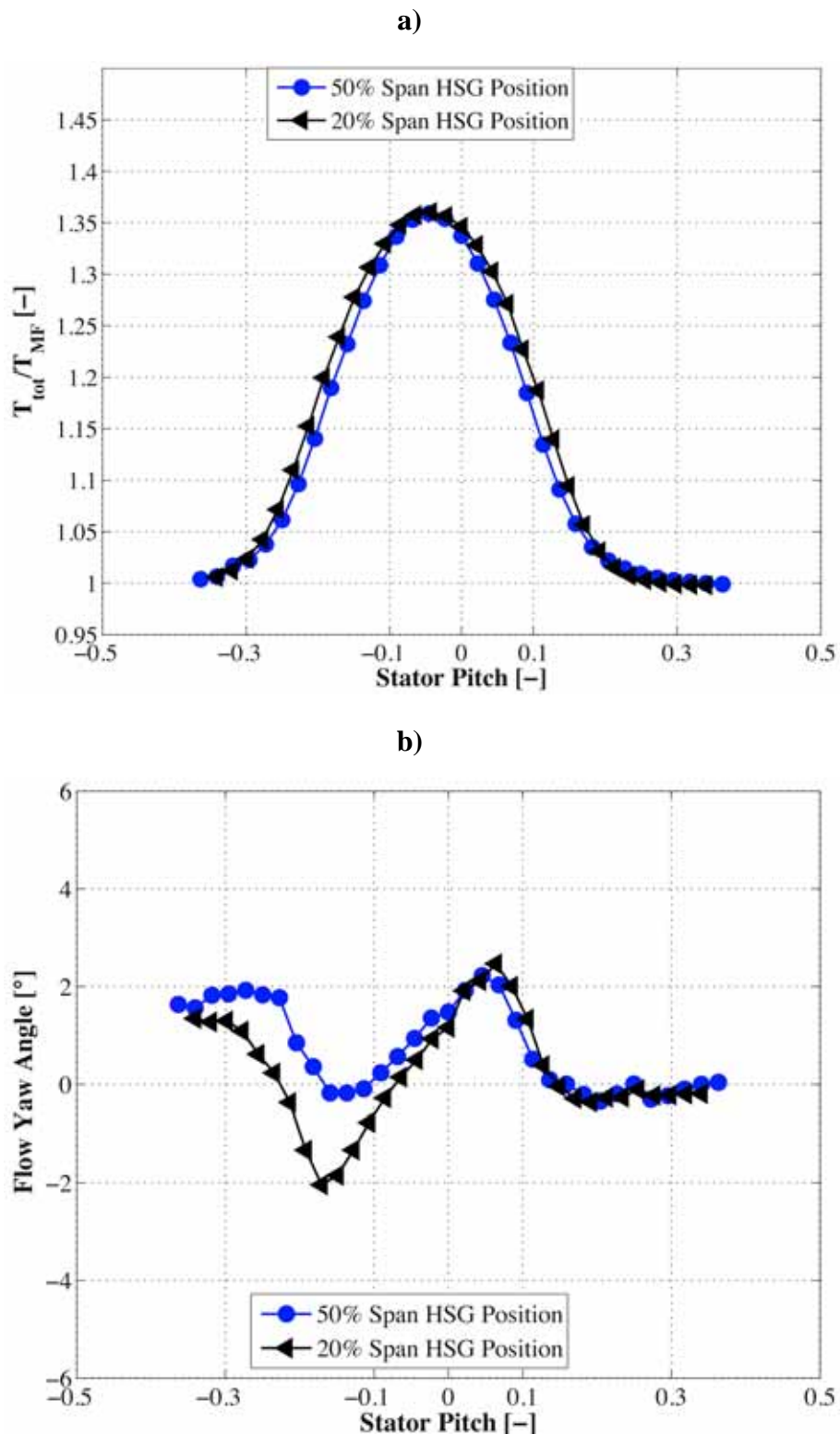
Fig. 7-9   FRAP-HT pitch-wise distribution of time-averaged T_{tot}/T_{MF} (a) and flow yaw angle φ (b) at the span positions of the respective HS core for configurations 2 and 3.

As shown in the measurements presented in Fig. 7-8, the temperature at the boundary regions of the HS is reduced. The dissipation of the hot jet is related to mixing effects in the shear layer and to the turbulent temperature profile in the injection pipe flow. An identification of the jet dissipation and the entrainment of the cold flow by the jet is done by a pitch-wise cut through the jet cores in Fig. 7-9b, showing the typical change of sign of the yaw angle in the core of the respective jet.

7.5.2   Comparison between various Probe Measurement Techniques

Four parameters define the flow: total and static pressures and the yaw and pitch flow angles. In Fig. 7-10 the pitch-wise averaged difference between the results measured with a 4HP, a standard FRAP and the FRAP-HT are brought together for test case configuration 1 at the exit of stator 1. The 4HP measurements are used as a baseline and for both fast response aerodynamic probe measurements the differences are defined with respect to the pneumatic baseline measurements. The combined error bandwidth for the respective properties are defined from the sum of the error bandwidth for the 4HP and the FRAP-HT.

All results for the flow angles are within the error bandwidth (Fig. 7-10a). Comparing P_{tot} and P_{stat}, except for a small region at around 10% span, the FRAP-HT results are within the error bandwidth (Fig. 7-10b). Fig. 7-10a shows differences of yaw angle for the FRAP ranging from -0.65° to 0.5° and for the FRAP-HT in the range of -0.55° to 0.4°. This is considered to be a good agreement. The pitch angle difference for the FRAP ranges from -1.2° to -0.25° and for the FRAP-HT from -0.8 to 0.25°. This is consistent with Table 7-3, which shows that errors in pitch angle are expected to be larger than those for the yaw angle. Focusing on the FRAP-HT measurements, both flow angles show a change in difference close to the tip radius, where the shear layer is located. A combination of endwall proximity effects, blockage effects due to the difference in the probe diameter and high total pressure gradients located near the endwalls might be reasons for this.

The difference in non-dimensional total and static pressure measurements is presented in Fig. 7-10b. All measurement technologies presented measure the pressures as being in good agreement. The level of deviation is small and ranges around 0.003 in P_{tot} and 0.007 in P_{stat} for most parts of the span. Concerning the average static pressure level, the FRAP-HT shows slightly higher span-wise variations compared to the standard FRAP.
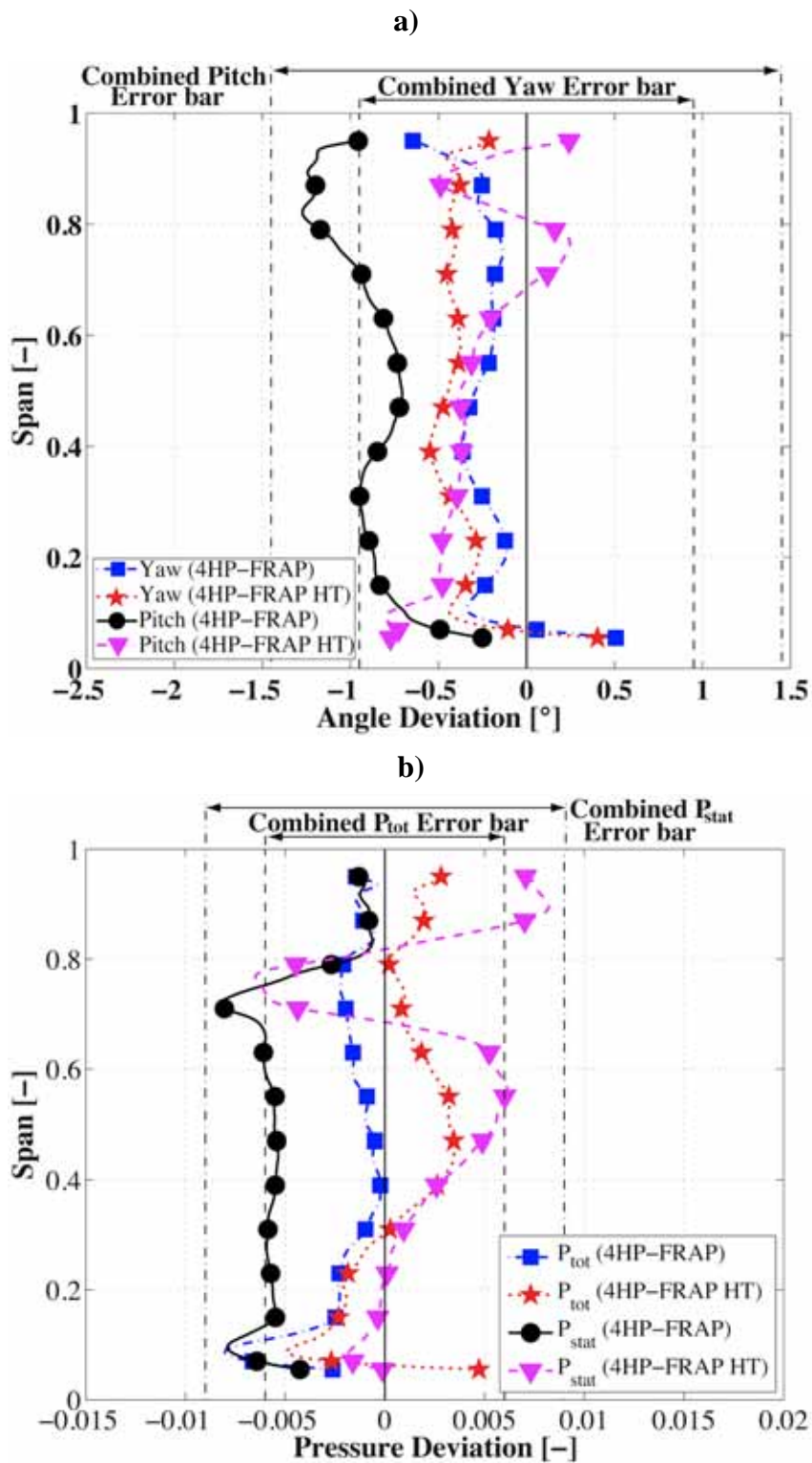
Fig. 7-10   Pitch-wise mass-averaged differences of FRAP, FRAP-HT and 4HP
(including error bars). a) Deviation in flow angles φ and γ respec-
tively; b) non-dimensional pressures. All measured for configura-
tion 1 at the exit of stator 1.

In order to show the capability to resolve unsteady flow structures, the unsteady results are compared between FRAP and FRAP-HT. A *Cpt* time snapshot at *t/T=0.41* over one stator pitch measured with FRAP-HT is presented in Fig. 7-11a for test configuration 1. It shows the interaction between the stator exit flow field and the potential field of the passing rotor (zones of increased *Cpt*), as well as the secondary flow features that leave the stator blade row (areas of reduced *Cpt*). The core of the stator hub passage vortex reaches from the hub casing wall up to 10% span. The stator passage vortex can be found at between 80% and 90% span. Both vortices are connected by the stator wake, which exhibits a straight shape and is almost perfectly aligned in the radial direction.

Generally, the flow field out of the stator shows a clear two-dimensional character over a range from 10% to 70% span. Fig. 7-11a further shows that the left-hand stator pitch secondary flows vanish almost completely due to the vicinity of a rotor leading edge, whereas the wake and both vortices are fully developed and approach the mid-pitch region of two rotor blades in an undisturbed manner on the right hand stator blade. In this case the total pressure in these areas reaches its minimum value. No direct impact off the HS can be found in the *Cpt* distribution around mid-span. As stated by Munk and Prim [111], the measurements obtained show that the secondary flows at the vane exit are not affected by the HS.

Fig. 7-11b shows the same area, but compares rms of the difference in *Cpt* between FRAP and FRAP-HT for the same sample time *t/T*. The average of the difference between the two probe technologies scales the result and allows a better comparison between them. Zones of complete agreement between the two measurements therefore have an rms of zero. Fig. 7-11b shows a dominant area of complete agreement. Some small deviations are identified near the tip endwall, in the wake between 60% and 75% span and within the passage vortex regions between 5% and 10% span, and 80% to 95% span respectively. As previously stated for the mass-averaged differences, a combination of endwall proximity effects, blockage effects due to the difference in the probe diameter and relative sensor position, as well as high total pressure gradients located near the endwalls might be reasons for these variations.

Another zone with slight differences is identified between 30% span and 60% span at mid-pitch. This is the location of the HS and a lower signal-to-noise ratio of the standard FRAP for elevated flow temperatures could therefore be an explanation for the appearance of the deviation zone.
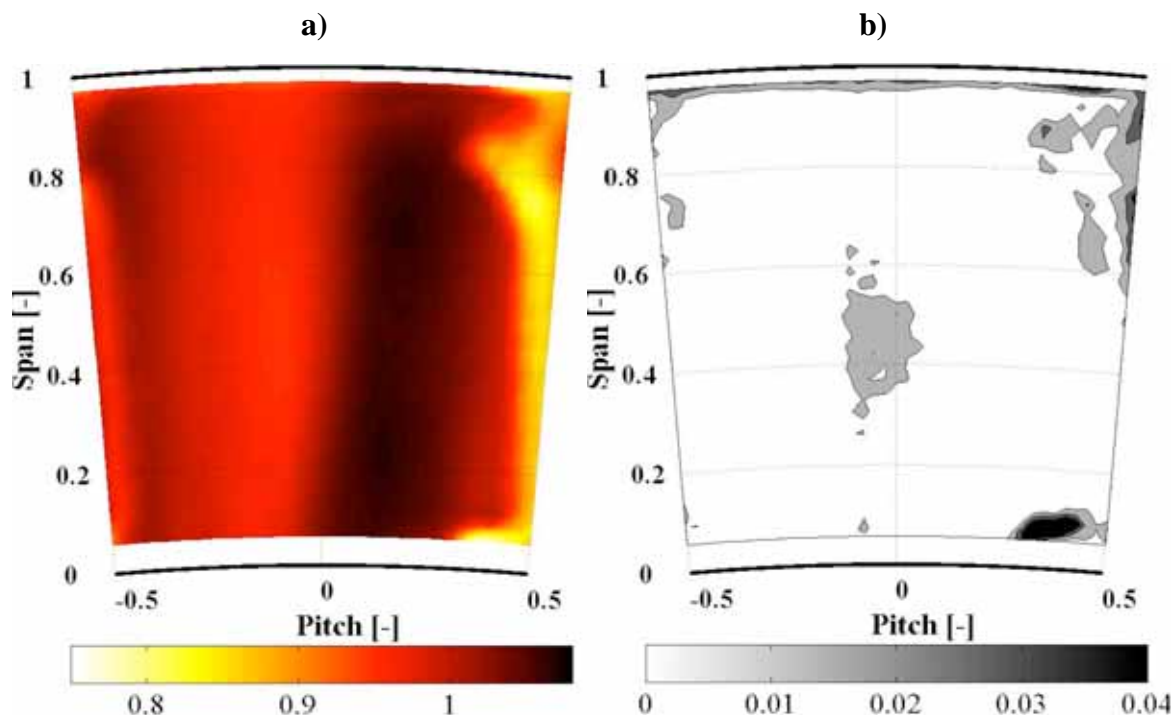
Fig. 7-11   Time resolved (t/T = 0.41) area plot at the exit of stator 1 measured for configuration 1 (absolute frame of reference); a) C_{pt} measured with FRAP-HT. b) Difference in C_{pt} FRAP and FRAP-HT, expressed by the rms at the same sample time.

7.5.3   Unsteady Flow Analysis

The HS-related thermally driven effects on the rotor flow are more complex. In a rotor-relative frame of reference, the HS has a higher relative momentum and thus a higher relative stagnation pressure. As has been shown by Kerrebrock et al. [122], this leads to additional sources of secondary flows, with the hot gases tending to migrate toward the pressure side and then the endwalls. Fig. 7-12 shows the steady T_{tot}/T_{MF} measured with FRAP-HT for the test case configurations 2 and 3 at the rotor exit. The data are presented over one stator pitch and help to identify the time-averaged main location of the HS for later time-resolved area plots at the rotor exit. The span position of the HS core can clearly be identified. Furthermore, the tendency toward an increasingly span-wise distribution of the hot gases on the right-hand side (direction of rotor PS) is identified. A strong shape difference between the steady temperature distributions for the two test cases is shown. The shape for the lower HS span position is much more distorted, which could be related the complex interactions of the hot gas particles with the hub passage vortex and be further influenced by wall proximity effects.
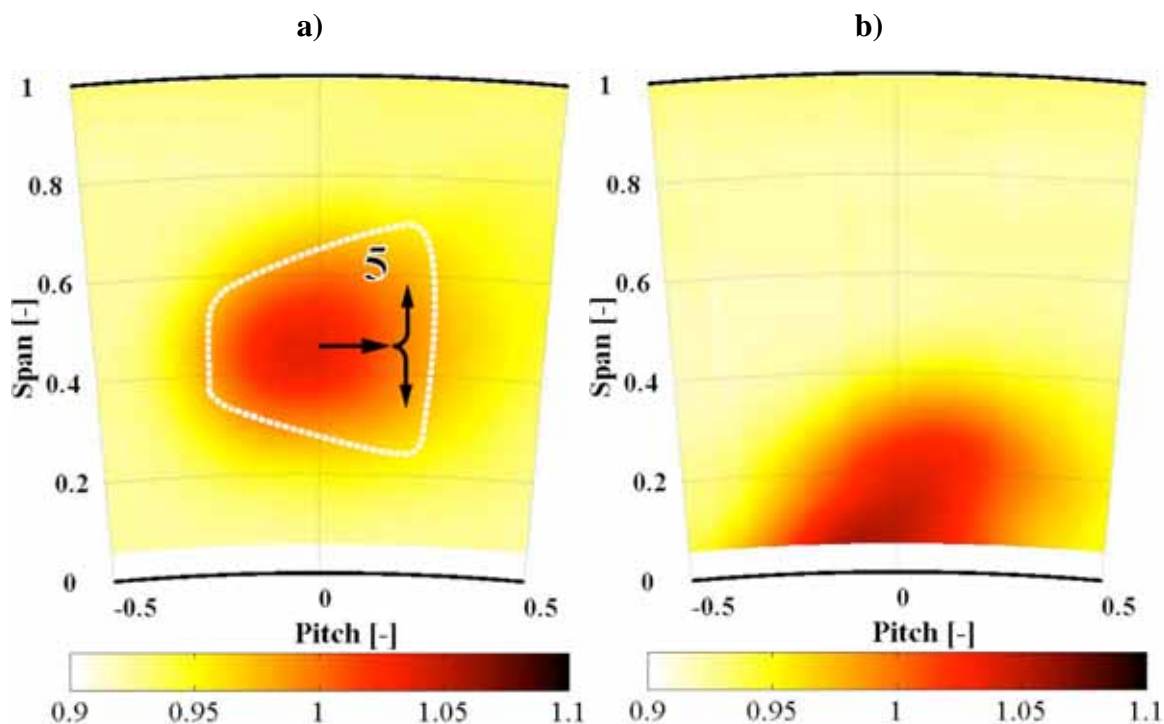
Fig. 7-12   Steady normalized total temperature (T_{tot}/T_{MF} [-]) over one stator pitch measured with FRAP-HT at the exit of the rotor for configurations 2 (a) and 3 (b).

In order to track both the hot streak effects, as well as flow-related unsteady effects such as the wake and vortical structures at the rotor exit, the root mean square value of the random part of the total pressure is presented in Fig. 7-13 for the HS cases 2 and 3 ($P'_{tot, rms}$). Regions of high $P'_{tot, rms}$ are indicative of eddy shedding or regions of high turbulence. Rotor exit flow measurements are presented over one complete stator pitch. Due to the stator to rotor blade count ratio of 2:3, two rotors and their dominating effects are presented within one stator pitch.

Similar $P'_{tot, rms}$ levels occur in the areas of the tip leakage vortex (1), in the area of the upper passage vortex (2) and the core of the rotor wake (4) for both test cases. The rms level for the hub passage vortex shows an increase in size and intensity for the second test case (3) (Fig. 7-13b). This is mainly related to the hot gas area (5) being located at around 20% span for measurement configuration 3, influencing the secondary flows and therefore the hub passage vortex located at the same span position. Furthermore, the migration of the HS toward the PS of the rotor and subsequently toward the endwalls is recognizable in zone 5 for both test cases.
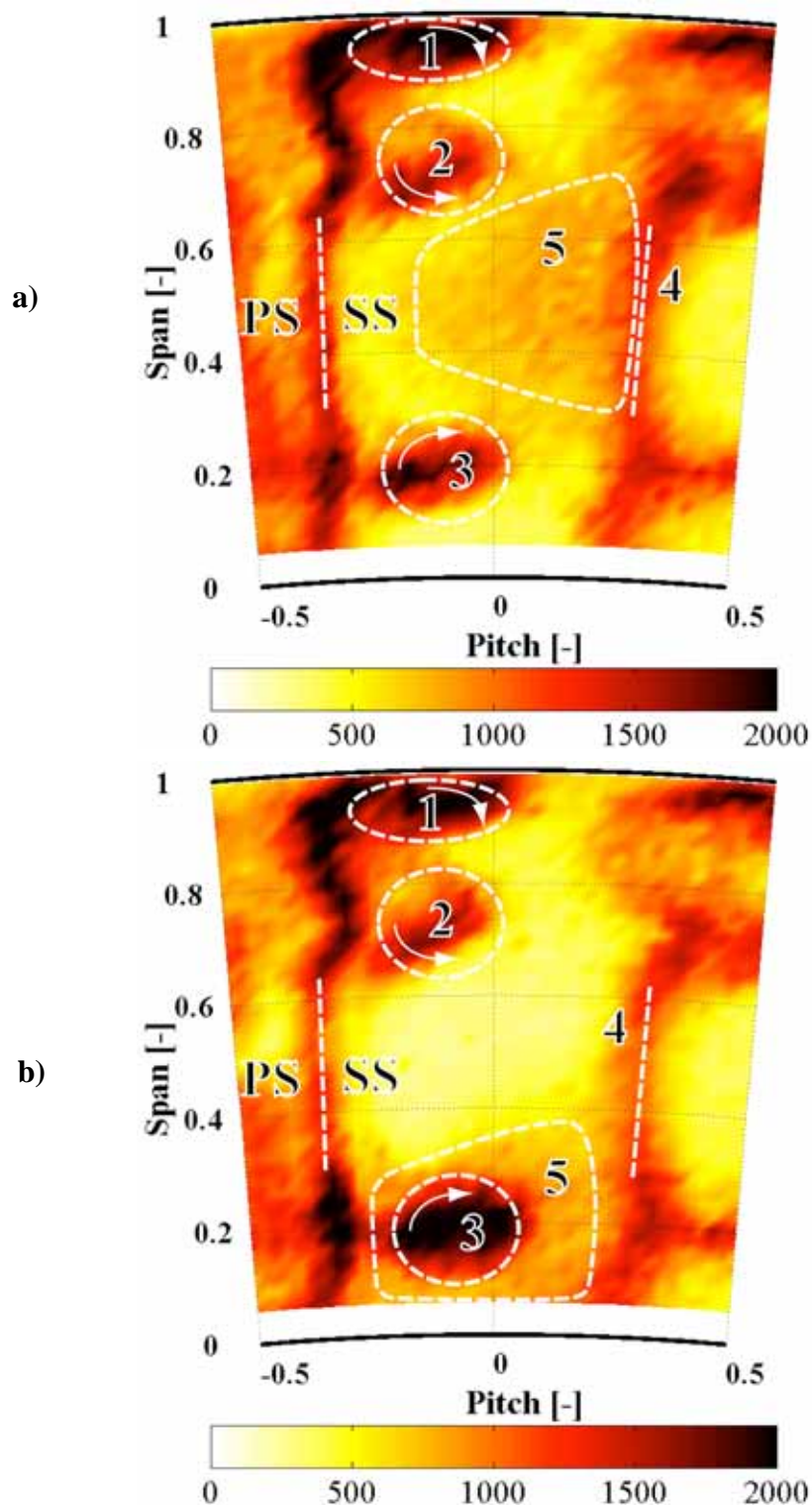
*Fig. 7-13   Time resolved (t/T = 0.85) area plot at the exit of the rotor mea-
           sured with FRAP-HT and presented over one stator pitch (absolute
           frame of reference). a) rms of the random part of P_{tot} for configura-
           tion 2, b) rms of the random part of P_{tot} for configuration 3.*

7.6   Summary and Concluding Remarks

A novel high temperature fast response aerodynamic probe has been developed, built and tested. The FRAP-HT probe is based on the virtual 4-sensor probe measurement concept. The probe can be applied in flows with temperatures up to 533K (500°F) and can measure three dimensional and unsteady flows up to the cut-off frequency of 25 kHz, covering flow angles of ±24° in yaw and ±20° in pitch direction. Furthermore, the probe is able to capture the steady flow temperature.

The probe robustness and capability to provide steady temperature and high frequency flow measurements in harsh environments is demonstrated within the hot streak generator equipped axial 1.5 stage turbine facility, LISA. The combination of that high work aero-engine and hot gas spots leads to sharp temperature gradients within the flow and to interactions with the blade row pressure gradients and secondary flows and therefore presents a perfect scenario to verify the probe's ability to measure under real conditions.

The steady hot streak inlet conditions show equal HS core temperatures compared to the temperatures at the injection plane. The trends of the hot jet dissipation and the entrainment of the cold flow by the jet are shown by the reduced gradients at the HS boundary area upstream of the first stator.

A comparison between measurements using the newly developed high temperature probe against various well-established steady and unsteady measurement techniques is performed. Agreement between all the techniques has been found and therefore the new probe concept was proven to be applicable. The minor variations between the results for the different probe techniques might be related to combinations of different effects such as, wall proximity effects, blockage effects due to the difference in the probe diameter and relative sensor position, high total pressure gradients near the endwalls and a lower signal-to-noise ratio of the standard FRAP for elevated flow temperatures compared to the new FRAP-HT. In terms of the unsteady flow analysis, the Munk and Prim principle [111], stating that the HS does not affect the secondary flows at the vane exit, is verified for the measurements performed. The flow analysis at the rotor exit further shows the interactions between the HS-related thermally driven effects and the unsteady flow. Kerrebrock and Mikolajc [122] observed the migration of the hot gases toward the rotor pressure side and subsequently toward the endwalls. These effects are identified and visualized in the FRAP-HT measurements by time resolved area plots of the turbulent fluctuating part of the total pressure.

8   Measurements in a high Speed radial Compressor

The focus of the present chapter is the structure of the impeller exit flow in a centrifugal compressor. Centrifugal compressors are in use since more than a century. They still play a major role in the turbomachinery market [129] and are used in fields such as aero engines for small aircrafts, automotive, marine turbocharging and distributed power because of their compact design and high stage pressure ratio. As reported by several authors (e.g. [130, 132]) the flow at the outlet of a centrifugal impeller is very complex and highly fluctuating. The structure of this complex flowfield is affected by the tip clearance, which in turn affects the compressor efficiency.

Hot-wire techniques became the standard tool used to investigate on time dependent phenomena (e.g. [130, 133-135]) but their use was mostly limited to low speed compressors. Optical methods, such as Laser Doppler Velocimetry (LDV) or Laser-two-Focus Velocimetry (L2F) proved to be very fruitful in investigating the rotating impeller channels as well as the diffusers ([136-140]) but did not allow direct pressure measurements. Pressure fluctuations were measured by wall transducers (e.g. [133, 134, 141]). Later on, focus was set on steady and unsteady pressure and velocity field measurements using both, pneumatic and fast-response aerodynamic probes (e.g. [142]). All these measurement techniques have their respective advantages and disadvantages, and thus are complementary.

Due to the increased temperature range of the newly developed FRAP-HT probe, first time ever, resolved measurements at the design point of our centrifugal compressor facility could be conducted. The present chapter therefore demonstrates the use of the newly designed unsteady high temperature FRAP probe in the harsh environment of a centrifugal compressor. The measurements made with this new probe provide new insight into the structure of the impeller exit flow and detail the unsteady loss mechanisms associated with the outlet flow of the high-speed centrifugal compressor equipped with a vaneless diffuser.

In the next two subchapters, the test facility as well as the measurement configuration used for this study is described. Furthermore a combined calibration approach in order to increase the spanwise measurement range of the FRAP-HT probe is presented. A discussion of the results from FRAP-HT, steady 4HP (chapter 5.1.1) and the steady high temperature probe F0S-PT100-HT follows (see chapter 5.3). Subsequently the aerodynamic stage efficiency could be calculated from the FRAP-HT measurements and is presented,

together with an efficiency related uncertainty analysis. Finally, the chapter is summarized and some conclusions are drawn.

8.1   Experimental Facility

The test facility is the single stage, centrifugal compressor system, "RIGI", which is located in the Laboratory for Energy Conversion at ETH Zurich. The facility and it's subcomponents are described in detail in Schleer [143]. The layout of the system is shown in Fig. 8-1. It operates in a closed loop with air delivered at a design volume flow rate and pressure ratio of 3.5m^3/s and 2.8, respectively. The parameters of the facility can be adjusted such, that harsh conditions dominate at the outlet of the impeller.
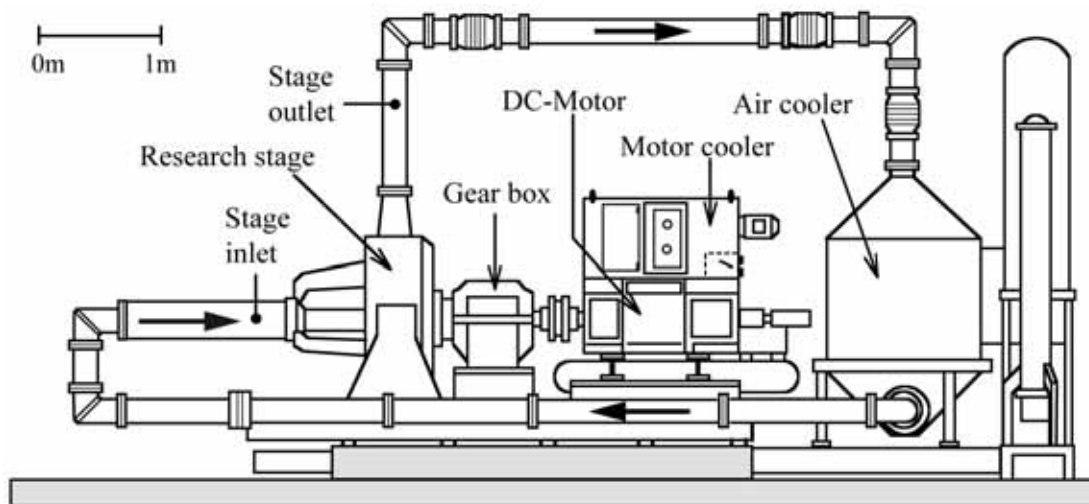
Fig. 8-1   Radial compressor research facility "RIGI".

For the present tests the system is equipped with a centrifugal impeller followed by a vaneless diffuser. The impeller is typical of that found in small-scale distributed power generation and automotive turbocharging applications. This scaled-up model matches the main design criteria and non-dimensional parameters that are typical of the small-scale devices, and also generates flow structures that are representative of those in small-scale compressors, Schleer et al. [144].

The impeller has seven pairs of full and splitter blades as shown in Fig. 8-2. Its outer diameter is 400mm, and at the impeller exit the blade are swept back by an angle of 30° with respect to the radial direction. Immediately downstream of the impeller is a parallel vaneless diffuser with an exit diameter of 580mm; the diffuser height is 15.7mm. The clearance ratio, which is defined as the ratio of the tip gap width 0.7mm, and the diffuser height 15.7mm, is 4.5%. The diffuser is followed by a large toroidal collecting

chamber providing a virtually uniform circumferential pressure distribution at the diffuser outlet [145].
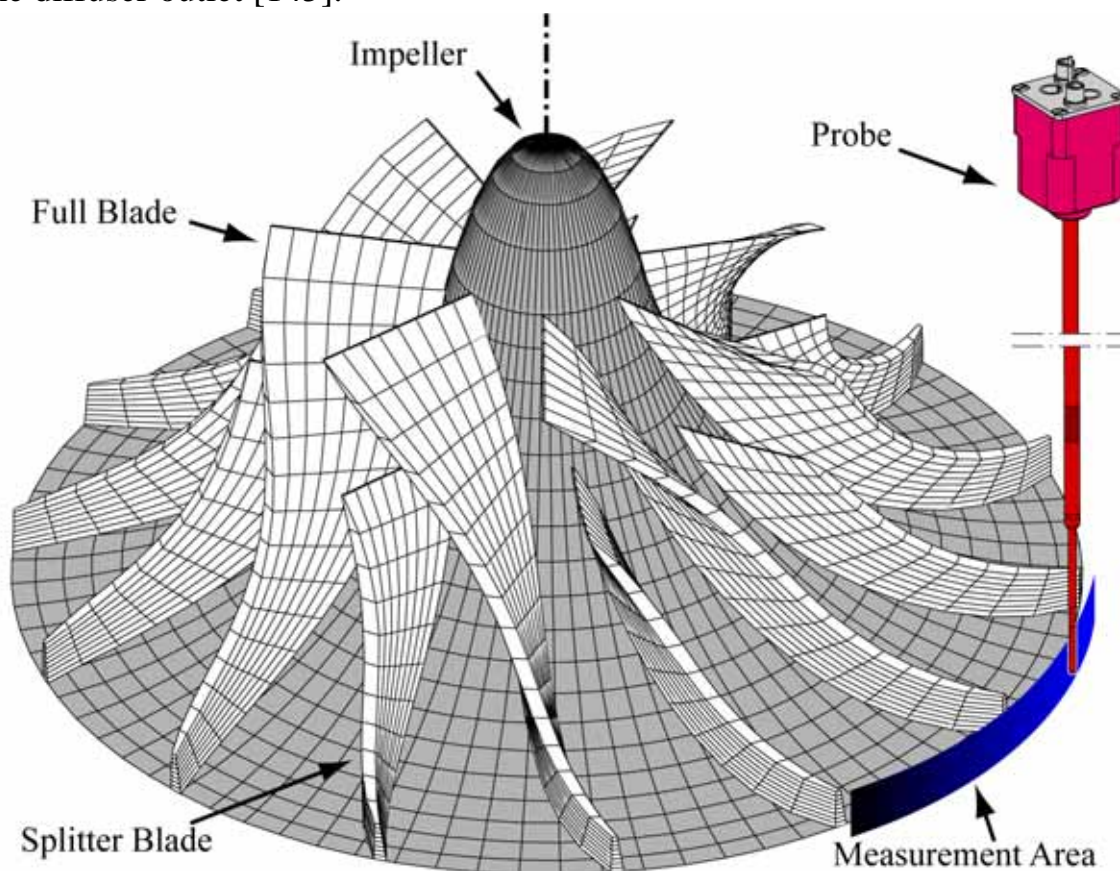
Fig. 8-2   3D rendering of impeller, showing the location of the FRAP-HT probe and the measurement area.

Some of the geometrical design parameters of the used centrifugal compressor configuration as pictured in Fig. 8-2 are tabulated in Table 8-1. The tabulated parameters total pressure ratio Π_O as well as the corrected mass flow rate Q and the stage Mach number Mu are commonly used in radial compressor applications. The reason for their use is related to non-dimensionalizing or dynamic scaling if the scaling group is left with dimensions. The definition of the corrected mass flow rate Q, the total pressure ratio Π_O and the stage Mach number Mu as used in this chapter are provided in the equations 8.1 to 8.3, respectively and base on global parameters. In Eqn. 8.1, $\dot{m}$ equals the mass flow through the compressor. In Eqn. 8.2, U_2 is the blade speed at the impeller exit in *m/s*, κ the specific heat ratio and R the specific gas constant for dry air.

$$Q = \frac{\dot{m} \cdot \sqrt{T_{tot,\,inlet}}}{p_{tot,\,inlet}} \qquad\qquad (8.1)$$

$$Mu = \frac{U_2}{\sqrt{\kappa \cdot R \cdot T_{stat, inlet}}} \qquad (8.2)$$

$$\Pi_0 = \frac{p_{tot, exit}}{p_{tot, inlet}} \qquad (8.3)$$

Geometrical design parameter	Unit	Value
impeller exit diameter d_2	[mm]	400
impeller inlet tip diameter	[mm]	212
impeller inlet hub diameter	[mm]	70
diffuser width	[mm]	15.7
number of blades main/ splitter	[-]	7/ 7
rotational speed	[RPM]	22000
corresponding stage Mach number Mu at $T_{stat,inlet} = 298.65K$	[-]	1.33
tip speed	[m/s]	460
total pressure ratio $\Pi_{o,DP}$ at design point (DP)	[-]	2.8
corrected mass flow rate Q_{DP} at design point (DP)	[$K^{0.5}s^1m^1$]	82.5
design flow rate	[m^3/s]	3.5
inlet pressure	[bar]	0.1 ... 0.5
inlet temperature	[K]	297

Table 8-1   Impeller design properties.

8.2   Measurement Configuration

Due to the increased temperature range of the newly developed FRAP-HT probe, first time ever, resolved measurements at the design point (DP) of our centrifugal compressor facility could be conducted. Fig. 8-3 and Table 8-2 present an overview of all the measurements performed by the newly developed FRAP-HT and pneumatic 4HP. The specific operating conditions at the different measurement points are presented in the performance characteristic of the compressor facility "RIGI" (Fig. 8-3) as well as in Table 8-2 for the used impeller-diffuser configuration.

The x-axis in Fig. 8-3 represents the non-dimensional corrected mass flow Q/Q_{DP}, normalized with respect to the corrected mass flow Q_{DP} at the design point. The y-axis represents the non-dimensional pressure ration $\Pi_o/\Pi_{o,DP}$, normalized with respect to the pressure ratio $\Pi_{o,DP}$ at the design point. The scalar values of the normalized corrected mass flow and the normalized total

pressure ratio is provided in scalar values in Table 8-2 for the respective measurements at a certain compressor operating point. In addition, the total inlet conditions in temperature and pressure as logged during the different measurement cases are provided in Table 8-2. The values for the total pressure vary at most by ±3mbar around the mean values for the different measurement cases (long term repeatability at different days), but are stable within ±1.5mbar during one measurement traverse (short term rig stability). The detected variations during a traverse are therefore within the uncertainty bandwidth of the measurement equipment used to derive the total inlet pressure (see chapter 8.6.2). The same behavior is observed in the total temperature levels. The maximum fluctuation is ±0.35K with respect to the mean value for the different measurement cases. However they are stable within ±0.2K during a certain traverse. This value is within the uncertainty bandwidth of the measurement equipment used to derive the total inlet temperature (see chapter 8.6.2). The repeatability and accuracy of the setting the inlet conditions on a stable manner is therefore provided.

As in chapter 7 the measurements performed with the pneumatic probe have been done to validate the FRAP-HT probe. Furthermore the speed line at *Mu=1* was measured in order to compare to FRAP standard data, since this corresponds to the maximum operating line that could be measured for the previous FRAP probes, due to their limited temperature range.
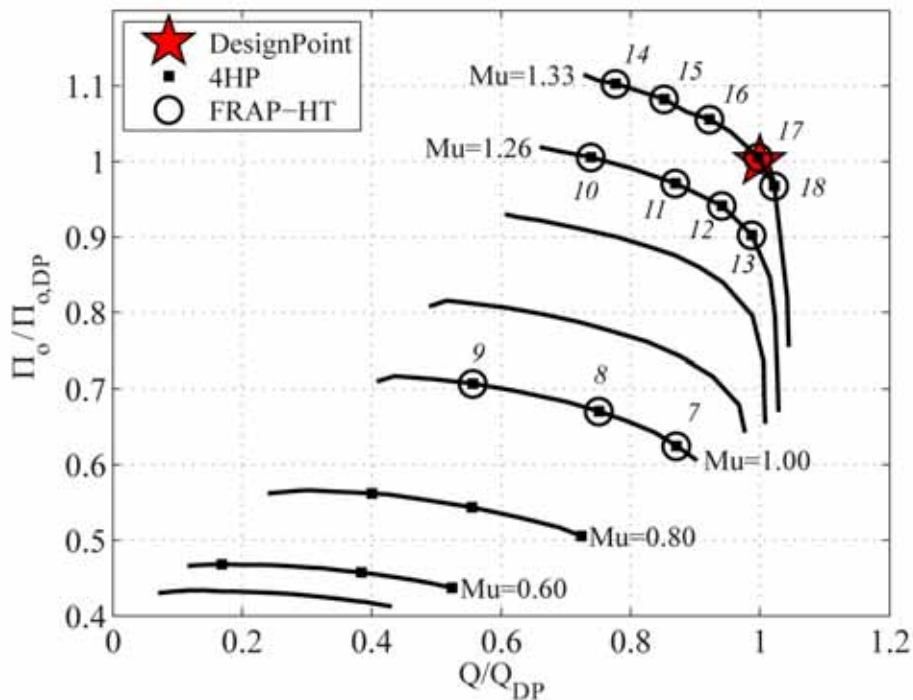
Fig. 8-3   Compressor map/ Performance characteristic of the compressor facility "RIGI" for the used impeller-diffuser configuration.

Measurement point (MP) notation:	Mu [-]	Q/Q_{DP} [-]	$\Pi_o/\Pi_{o,DP}$ [-]	$T_{tot,inlet}$ [K]	$p_{tot,inlet}$ [bar]
7	1.00	0.87	0.62	299.48	0.304
8	1.00	0.75	0.67	298.87	0.303
9	1.00	0.56	0.71	298.98	0.303
10	1.26	0.74	1.01	298.89	0.302
11	1.26	0.87	0.97	299.37	0.303
12	1.26	0.94	0.94	299.13	0.305
13	1.26	0.99	0.90	299.43	0.305
14	1.33	0.78	1.10	298.95	0.308
15	1.33	0.85	1.08	298.91	0.304
16	1.33	0.92	1.06	299.11	0.304
17 (DP)	1.33	1.00	1.00	299.35	0.304
18	1.33	1.02	0.97	299.09	0.305

Table 8-2   Notation and facility operating conditions for the performed FRAP-HT measurement points.

The left hand part of Fig. 8-4 presents the underlying coordinate system used for the measurements at the exit of the radial compressor. The measurement area is located radially 10mm downstream of the impeller exit at a non-dimensional ratio of $R_{meas}/R_{d2}=105\%$.

One measurement case contains multiple measurement positions at different axial locations. At each measurement position during a traverse, a time series of 400'000 data points is acquired at a sampling rate of 200kHz. The measurement grid provides a spatial resolution of the measurements for all measured cases of 0.5mm in the axial direction, and azimuthally depends on the stage Mach number. The circumferential resolution therefore equals 0.50° for *Mu=1.00*, 0.63° for *Mu=1.26 and* 0.66° for *Mu=1.33*, respectively.

The right hand part of Fig. 8-4 shows the angle convention used, to present the measurements. In general, there are two main components existing in any turbomachine. In case of the centrifugal compressor measurements, these are the stationary components as the inlet duct, or the vaneless diffuser and the rotating components such as the impeller. This therefore allows one to define coordinate systems in a frame of reference fixed to the component under consideration and therefore being either stationary if fixed in time and space (absolute), or relative if it moves at the local blade speed of the rotating component. As a convenience in changing the frame of reference, the flow is described by vector triangles. Therefore the right hand part of Fig. 8-4 further presents the two velocity triangles for a stationary measurement position at

two different relative rotor blade positions (time t_1 and t_2). In terms of underlying notation for the velocity components, the local blade speed of the impeller is $\vec{u}(t)$, the velocity component in the relative, or moving frame is $\vec{w}(t)$ and the component in the absolute frame of reference $\vec{c}(t)$. Fig. 8-4 (right) further shows schematically the high temporal fluctuations in the absolute yaw angle due to the strong variations in the relative velocity output along the rotor circumference, which is known to be a common characteristic of centrifugal impellers.
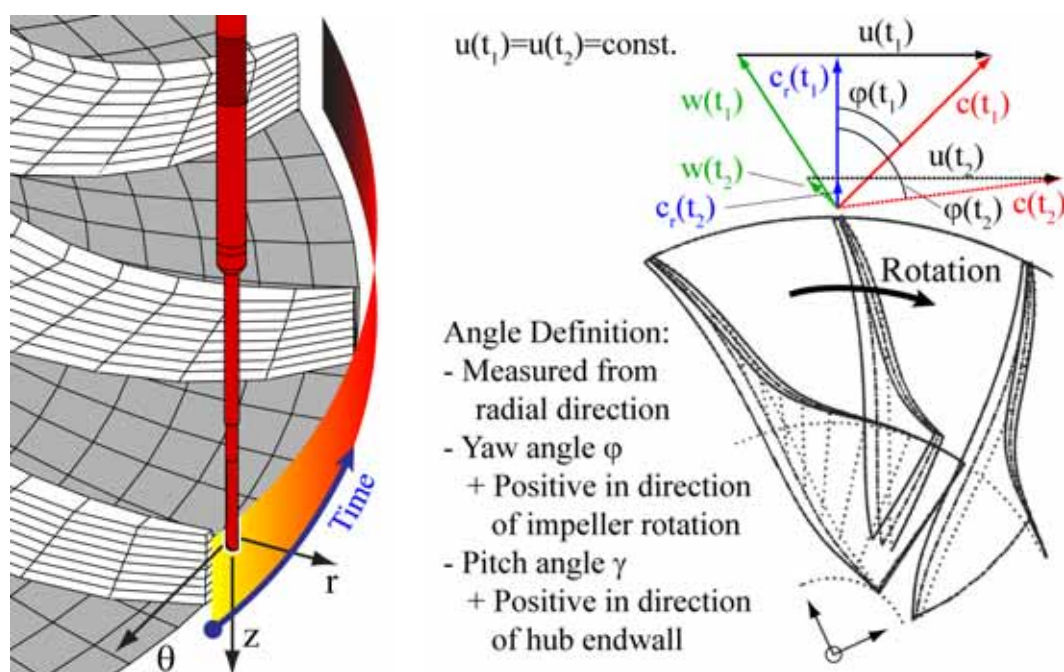
Fig. 8-4   Definition of coordinate system (left) and Angle convention and schematic of velocity triangle variations at on measurement location for two different point of times and impeller blade positions respectively (right).

8.3 Combined Calibration Approach to Increase the spanwise Measurement Range

During operation of the compressor facility, high thermal gradients occur which leads to different thermal expansions due to the different materials involved in the facility. The difference in facility outer casing surface temperatures during operation at *Mu=1.33* as an example is shown in Fig. 8-5. The picture is made with an infrared (IR) camera and clearly shows that high temperature gradients are present. However, the quantitative values must be handled with care due to differences in the emissivities and reflections of the

different components' materials.
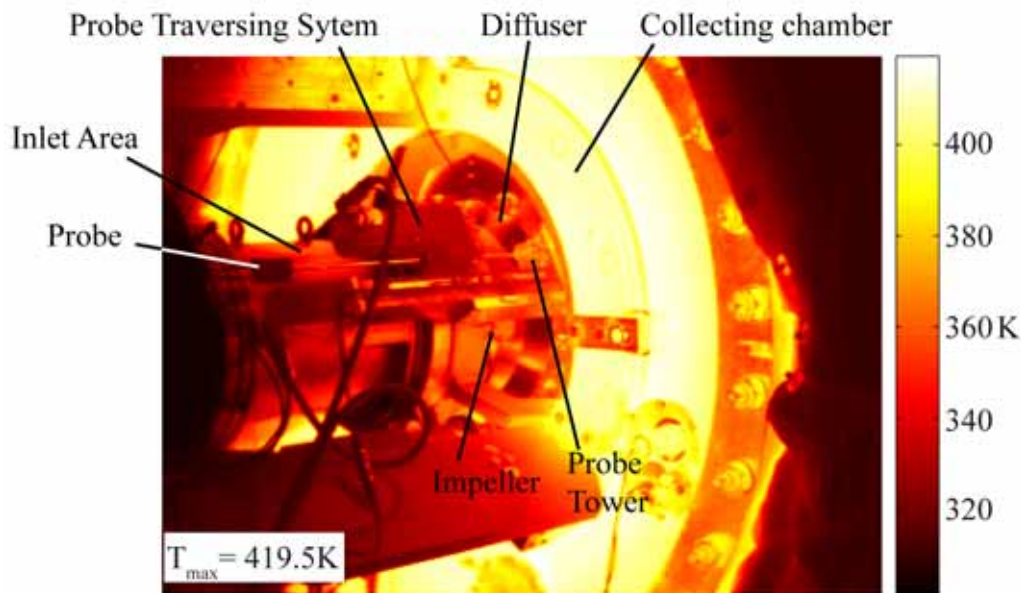
Fig. 8-5   Exemplary temperature distribution of the RIGI facility outer casing surface during operation at Mu=1.33, taken by an IR camera.

Due to these thermal gradients and the different thermal coefficients of expansion, a safety in traversing the probe (0.5mm) to the diffuser endwall (hub) is of major importance in order to avoid that any probe damage results from accidental contact at the hub (Fig. 8-6).
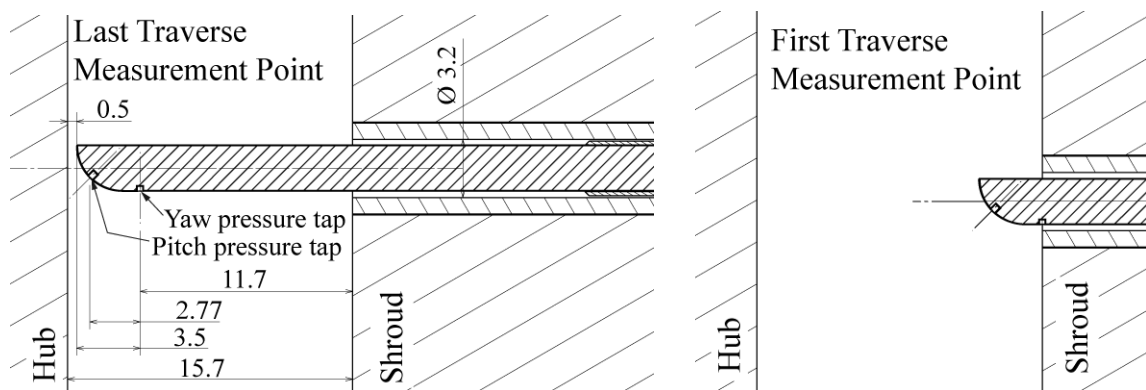
Fig. 8-6   Measurement setup near hub enwall (left) and first measurement point near shroud (right).

Furthermore, the probe pressure sensor tap related to the total pressure coefficient is used to define the measurement position within the flow (yaw pressure tap). This leads to an additional margin in the measurement point location compared to the metal probe tip (3.5mm). Taking into account the diffuser height of 15.7mm and the above-mentioned points, this leads to an overall spanwise measurement range of 75% span in the diffuser.

In order to increase the spanwise measurement range, a combined calibration approach with different aerodynamic calibration coefficient definitions has been developed. The new approach is based on the same set of measurement data, but uses a combination of standard aerodynamic calibration coefficients and newly defined aerodynamic calibration coefficients, subsequently termed "alternative" calibration coefficients.

The standard aerodynamic probe calibration coefficients are as introduced in chapter 3.3 defined as:

$$K_\varphi = \frac{P_2 - P_3}{P_1 - P_m}; \quad K_\gamma = \frac{P_1 - P_4}{P_1 - P_m}; \quad K_t = \frac{P_{tot} - P_1}{P_1 - P_m}; \quad K_s = \frac{P_{tot} - P_{stat}}{P_1 - P_m}; \quad (8.4)$$

, whereas $P_m = (P_2 + P_3)/2$.

The newly defined alternative aerodynamic calibration coefficients which are based on the FRAP-HT pitch hole as the total pressure sensing tap are defined in Eqn. 8.5. The tap numbering convention in this special case of a virtual four sensor measurement is shown in Fig. 8-7.

$$K_\varphi = \frac{P_5 - P_6}{P_4 - P_m}; \quad K_\gamma = \frac{P_1 - P_4}{P_4 - P_m}; \quad K_t = \frac{P_{tot} - P_4}{P_4 - P_m}; \quad K_s = \frac{P_{tot} - P_{stat}}{P_4 - P_m}; \quad (8.5)$$

, whereas $P_m = (P_5 + P_6)/2$.
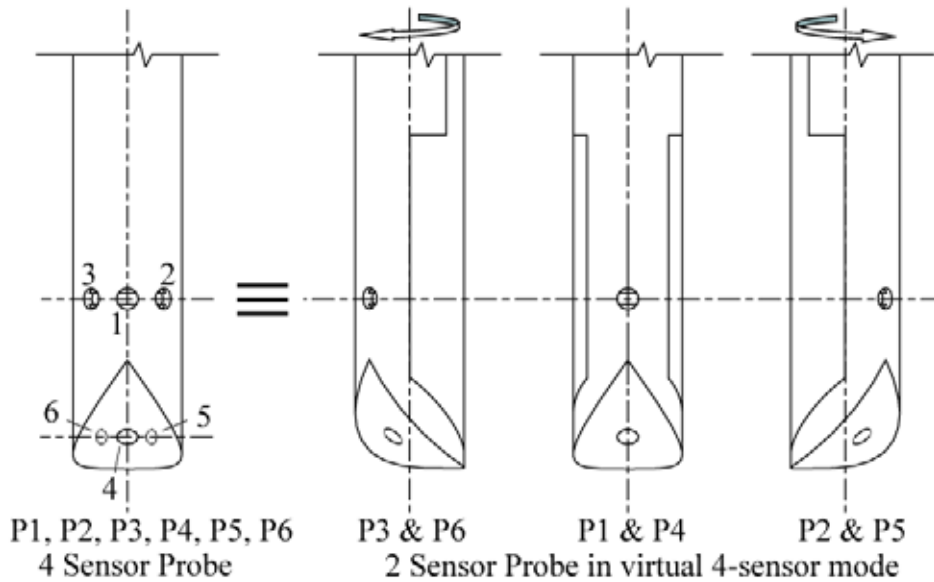
Fig. 8-7   Measurement concept in virtual 4 sensor mode with a two-sensor probe, using the alternative calibration approach.

As mentioned before, the alternative calibration approach is based on use of the pitch hole pressure tap as the central pressure hole. This is of importance,

since the central pressure hole is used to derive the total pressure at a measurement point. Using this approach therefore reduces the additional margin of the measurement point location compared to the metal probe tip down to 0.73mm. Taking into account the diffuser height of 15.7mm versus the traversing safety of 0.5mm and the reduced margin as mentioned above, the new approach allows measurement closer to the hub endwall at maximum spanwise measurement position of 92% span.

However, using the pressure taps *P5* and *P6* will induce some issues in terms of the calibration range, due to flow separations occurring at relatively low angles in both, pitch as well as yaw angle (relative to the zero position in yaw and pitch). This characteristic is related to the probe shape and can be seen in the plots of the sensed pressures by all six pressure taps *P1* to *P6*. The pressure contours for varying yaw and pitch angles are determined from the freejet calibration at *Ma=0.5* and are presented in Fig. 8-8.
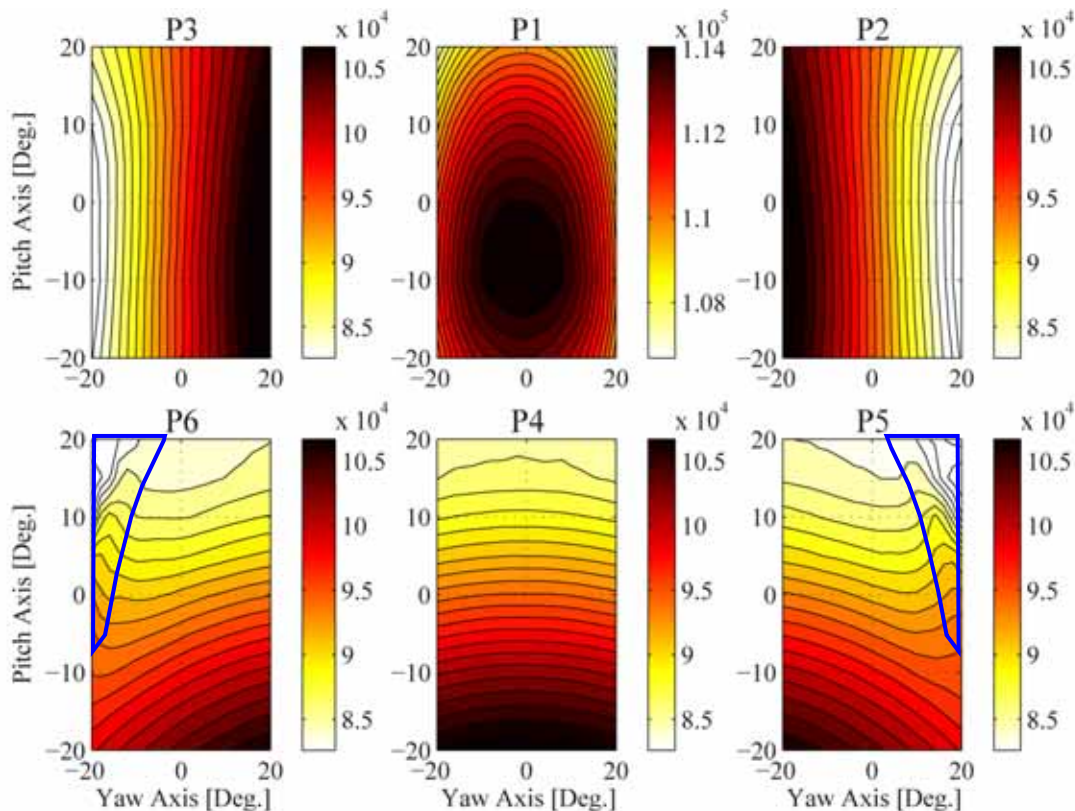
Fig. 8-8   *Sensed pressures at the FRAP-HT probe pressure taps P1 to P6, resulting out of a Freejet calibration at Ma=0.5.*

The flow separation zones at the pressure taps *P5* and *P6* are marked in the respective contours (blue) and show the characteristic of a sudden change in sensed pressures, further noticeable by sudden strong changes in the direction of the isobaric contour lines.

The strong impact of possible pressure tap separation zones on the definition of the different calibration coefficients is presented in Fig. 8-9 on the example of the yaw calibration coefficient K_φ determined at a freejet Mach number of 0.5. (a) presents K_φ for the standard calibration coefficient definition based on Eqn. 8.4 for a calibration range of ±20° in yaw, and ±20° in pitch and (b) presents K_φ for the alternative calibration approach presented over the same range. However, due to the separation effects, the areas for pitch angles higher than 5° and yaw angles lower than -14°, or higher than +14° respectively show strong non-linearities and forming a bivariable polynomial for the complete range would therefore lead to tremendous measurement uncertainties. The range of the alternative calibration approach therefore was reduced to ±14° in yaw and a range of -20° to 5° in pitch, as presented by the blue rectangle in (b) and in an expanded view in the contour (c) of Fig. 8-9.
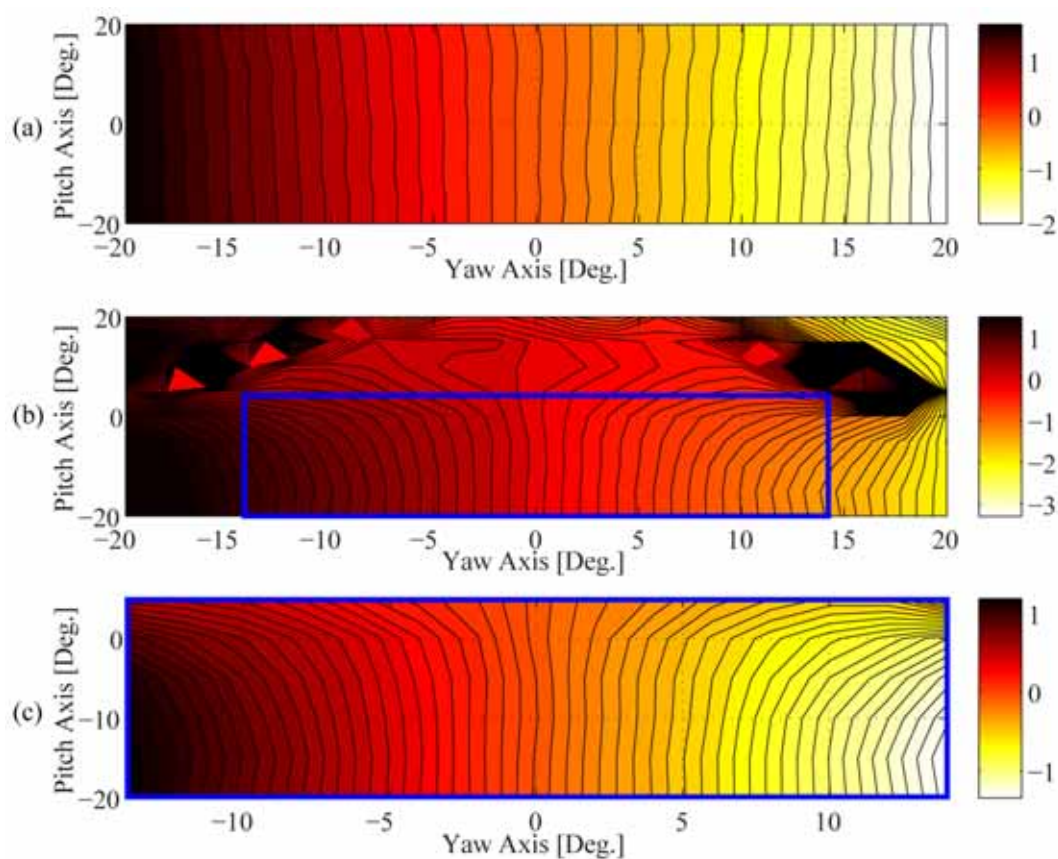
Fig. 8-9 K_φ out of aerodynamic FRAP-HT calibration. (a): for standard method, (b) for alternative approach over the full range and (c) for alternative approach over the reduced range.

Due to its definition, which is based on the pressure taps *P5* and *P6*, it is not surprising that K_φ is not fully decoupled from the pitch angle. However, all the the coefficients using the alternative approach can be formed in the reduced angular range without any singularities, which allows the model to be used.

The final aerodynamic calibration coefficients for the alternative calibration approach are presented in Fig. 8-10 for a Mach number equal to 0.5. The model range is ±14° in yaw angle and a range of -20° to 5° in pitch angle.
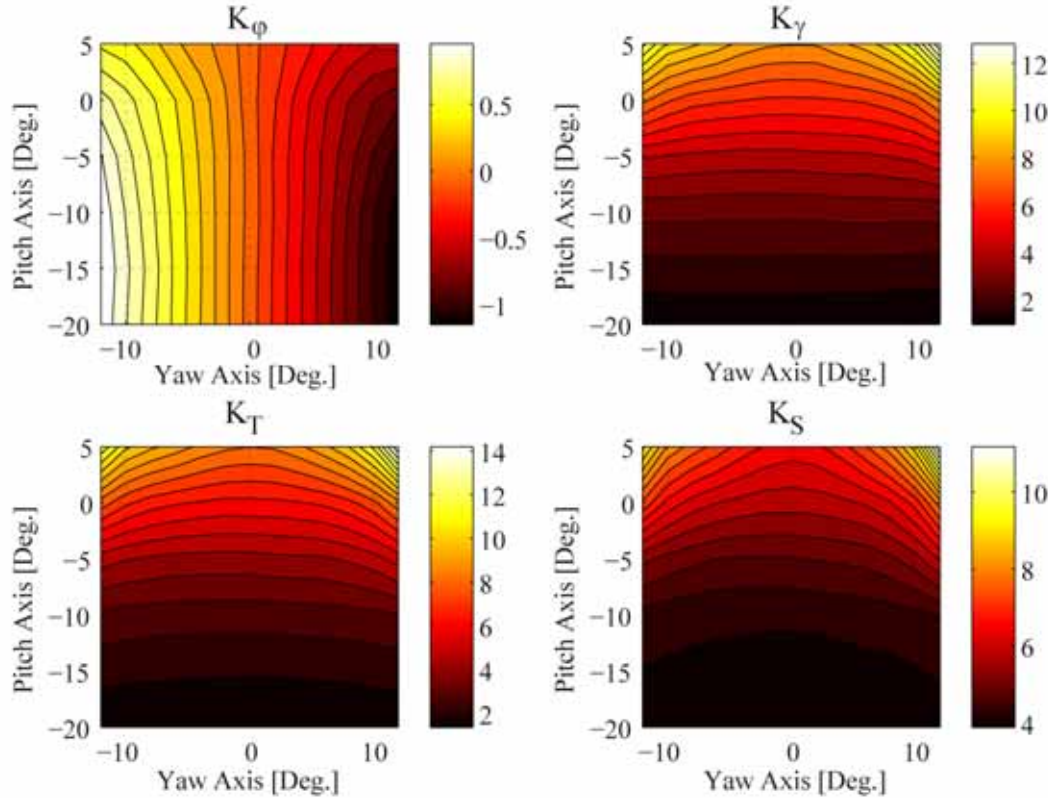
Fig. 8-10   Alternative approach calibration coefficients K_φ, K_γ, K_t and K_s for the FRAP-HT probe as a function of yaw angle ±14° and pitch angle +20° to -5° (Ma=0.5).

The calibration coefficients are modeled by a bivariable polynomial interpolation of 6th degree order. The resulting aerocalibration model accuracy of the new approach are presented in Table 8-3 for the freejet calibration Mach number of *Ma=0.5* and a calibration range of ±14° in yaw and -5° to 20° in pitch.

Parameter	Standard model accuracy	Alternative calibration approach
Model range in Yaw	± 24°	±14°
Model range in Pitch	± 20°	+20° to -5°
φ	± 0.06°	± 0.09°
γ	± 0.13°	± 0.15°
P_{tot}	± 0.25%	± 0.39%
P_{stat}	± 0.25%	± 0.40%
Ma	± 0.18%	± 0.21%

Table 8-3   FRAP-HT model accuracy of alternative calibration approach for Ma=0.5; calibration range yaw: ±14°; pitch +5° to -20°.

The angle uncertainties are given as absolute values, whereas the pressure uncertainties are presented relative to the dynamic head at the freejet Mach number of 0.5 and the Mach number uncertainty is given as a percentage of the freejet calibration Mach number.

The alternative calibration coefficients are applied to the same set of measurement data. In order to increase the spanwise range of the measurements, the data resulting from the standard calibration procedure are combined with the results of the alternative calibration approach. The merging of the two data sets is done such, that the results of the standard calibration procedure are taken into account for 0% to 70% of the span and the data then are completed by the results of the new calibration approach from 70% down to the near hub region.

By combining the data resulting out of the two calibration model techniques, the spanwise measurement range is increased by 17.6%, and now covers approximately 92.2% of the span.

8.3.1   Proof of Concept

The significant and promising increase in the measurement range by applying the combined approach must be validated before using it for the presentation of the measurement results. Therefore two kinds of approach validations are performed, one based on steady, time-averaged results, and a second based on the measured unsteady results.

The time averaged validation of the concept is presented in Fig. 8-11. Fig. 8-11a presents the time-averaged spanwise distribution of the flow angles yaw and pitch resulting out of FRAP-HT measurements at the design point (*MP 17*). The bottom plot, Fig. 8-11b presents the time-averaged spanwise distribution of the total and static pressure coefficients resulting out of FRAP-HT measurements at the design point (*MP 17*). In terms of all measurements presented in this chapter, the total (*Cpt*) and static (*Cps*) pressure coefficients are defined as the respective measured pressure, non-dimensionalized by the total impeller inlet pressure at the respective operating point.

The resulting spanwise range from the standard calibration procedure lasts from the shroud down to 75% span in both plots. The results based on the new calibration approach are presented such, that they at least overlap by 15% with the standard calibration method in order to allow a qualitatively and quantitatively comparison of the methods. The last measurement points in the new calibration method are located at 92% span. Furthermore, in both plots the respective properties measured by the 4HP at the same compressor operating

point are presented. This allows the general results of the FRAP-HT measurements to be evaluated.
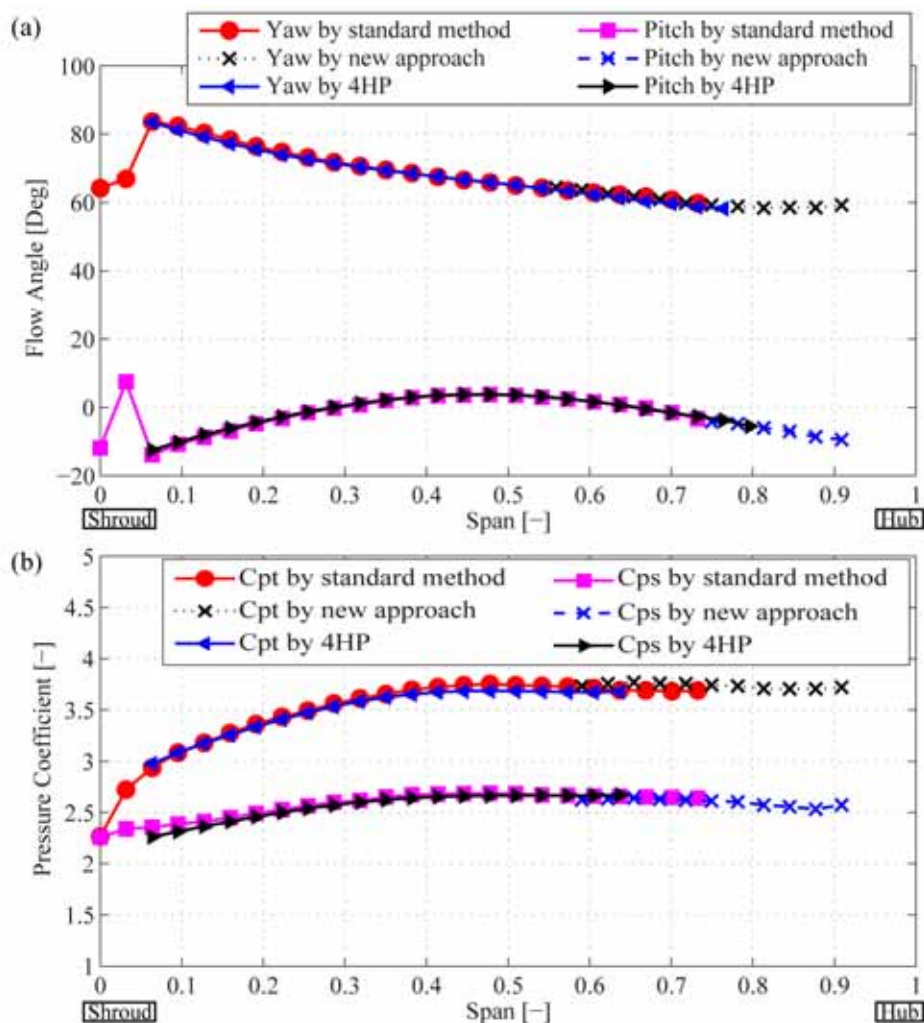
Fig. 8-11   Comparison between FRAP-HT standard aerodynamic calibration method and new approach, as well as 4HP results for the respective properties measured at the design point (MP 17); (a): yaw and pitch angle; (b): C_{pt} and C_{ps}.

Comparing the time-averaged results of the two different calibration approaches with each other as well as to the 4HP measurements, very good agreement both, quantitatively, as well as qualitatively is observed. In terms of the flow angles, strong spatial (as well as temporal) variations in flow angles are measured near the shroud. This is related to boundary layer and wall proximity effects as well as strong secondary flow components due to tip leakage vortices. The variations tend to be more critical in terms of the 4HP measurements. Therefore the first 4HP traverse measurement point is located at 6.4% span.

In this chapter all time-resolved results from FRAP-HT measurements in RIGI are presented as time-span diagrams. In general the *x*-axis of the time-span diagrams represent the time axis. Since the measurements are performed downstream of the impeller exit in a vaneless diffuser configuration, diffuser blade induced potential field effects are non-existent. Therefore the time-axis can be transformed into the geometrical axis around the blade circumference, representing the blade passing of the impeller. The *y*-axis of the time-span diagrams presents the span from shroud (0) to hub (1). Three blade passages are in general presented in the span-time diagrams. The trigger relative position of the impeller full blades (*FB*) and splitter blades (*SB*) are as well schematically adumbrated in the plots. Furthermore the respective pressure side (*PS*) and suction side (*SS*) of the blades are indicated in the plots as well as the sense of rotation of the impeller.

The time-resolved results from the new calibration approach are compared to the time-resolved results of the standard calibration approach in the overlapping spanwise area between 65% and 75% span. They are presented in Fig. 8-12 as non-dimensional time-span diagrams. The operating point used for the comparison is the design point (*MP 17*). The difference between to traverse measurement points is 0.5mm. But by redefining the total pressure sensitive tap being the pitch tap for the new approach versus being the yaw tap for the traditional calibration method shifts the position of the total pressure sensitive tap around 2.77mm to the probe front end. Therefore the actual spanwise measurement positions in the overlapping area of the two methods between 65% and 75% span are not fully identical. In order to allow a comparison between the positions of the two approaches, the span axis for both methods is interpolated to the combined local measurement points and the temporal mean offset in flow property is corrected with respect to the 70% span positions to allow a better qualitative comparison of the two methods.

The upper plot (a) of Fig. 8-12 presents the rms of the difference in yaw angle between the two methods. The results are presented in a normalized manner, whereas the norming is done by the probe calibration range ($\pm 14°$).

Fig. 8-12b shows the same area, but compares the normalized rms of the difference in *Cpt* between the standard calibration approach and the new approach, both resulting from the FRAP-HT measurements. The rms of the difference between the two probe calibration approaches scales the result and allows a better comparison between them. Zones of complete agreement between the two measurements therefore have an rms of zero. The normalization in Fig. 8-12b is made with respect to the global mean *Cpt* at the

design point.
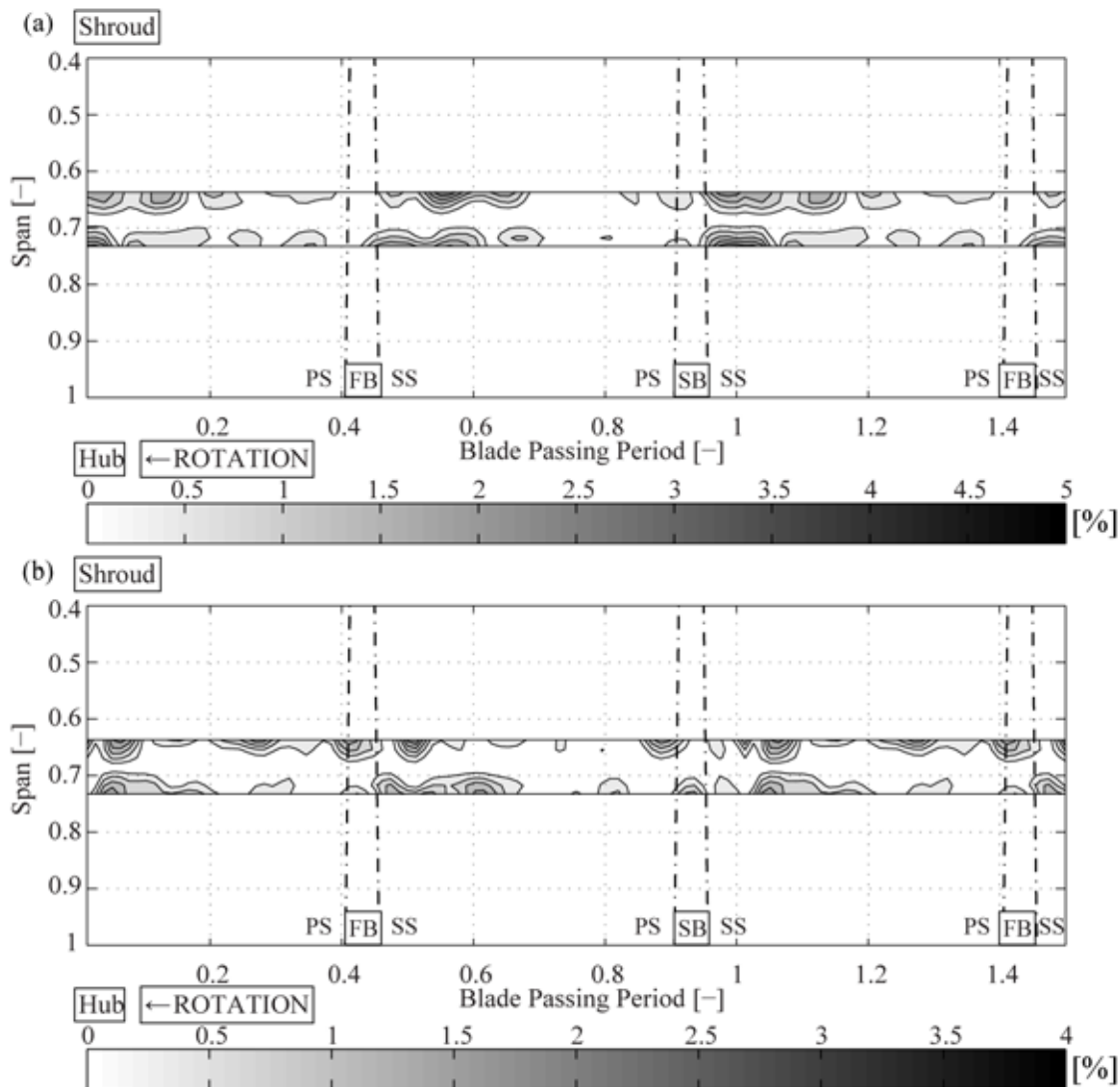
Fig. 8-12 *Non-dimensional time-span diagram of the rms of differences between the standard calibration and the new approach at DP [%]; (a) for yaw angle, normalized by the probe calibration range ±24°; (b) for C_{pt}, normalized by the global mean C_{pt} at the DP.*

Both flow properties, yaw angle as well as *Cpt* agree within less than 2.4% and 2.9% respectively in deviation in the non-dimensional rms difference of the respective flow properties. As expected, a full agreement at 70% span is achieved, whereas some variations occur in the boundary region of the overlapping areas. In terms of the yaw angle comparison (Fig. 8-12a), the maximum deviation between the two methods equals around 0.6°, whereas in the *Cpt* comparison, the respective maximum deviation in *Cpt* equals 0.08.

Reasons for the slight differences in the RSM between two applied coefficient definitions could be related to the spanwise measurement grid

interpolation needed, in order to compare the methods in the overlapping area. Additional reasons are related to differences in polynomial model fit uncertainties between the two methods as presented in Table 8-3, due to variations in flow property dependent measurement sensitivity and due to calibration range limitations of the new method. Furthermore, due to the relatively small diffuser height, even in the overlapping area between 65% and 75% span, some variations due to probe wall proximity effects and blockage effects can not be excluded.

8.3.2   Summary and Concluding Remarks

In order to increase the spanwise measurement range of FRAP-HT measurements in RIGI, a combined calibration approach with varying aerodynamic calibration coefficient definitions has been developed. The new approach is based on the same set of measurement data, but uses a combination of standard aerodynamic calibration coefficients and new defined aerodynamic calibration coefficients.

By combining the data resulting from the two calibration model techniques, the spanwise measurement range is increased for any flow property by around 17.6%, covering now around 92.2% of the span. Fig. 8-13 shows as a representative example the range difference between the traditional method (a) and the new combined calibration method (b) by means of the yaw angle distribution measured at *MP 17*.

The above validation of the new approach shows good agreement in the overlapping areas. The observed slight differences in terms of the time-resolved results are mainly related to interpolation uncertainties, polynomial model fit uncertainties, flow property dependent measurement sensitivities and to calibration range limitations of the new method, as well as are due to probe wall proximity effects and blockage effects.

The new approach therefore allows some fruitful insight to be gained of a significant part of the flow domain without the need of additional measurements with alternate probes and can therefore help to significantly reduce costs related to both rig operation hours, as well as measurement technique development. Due to that, all further presented span-time diagrams out of FRAP-HT measurements in RIGI take into account the new calibration approach and are therefore presented over the increased spanwise measurement range.
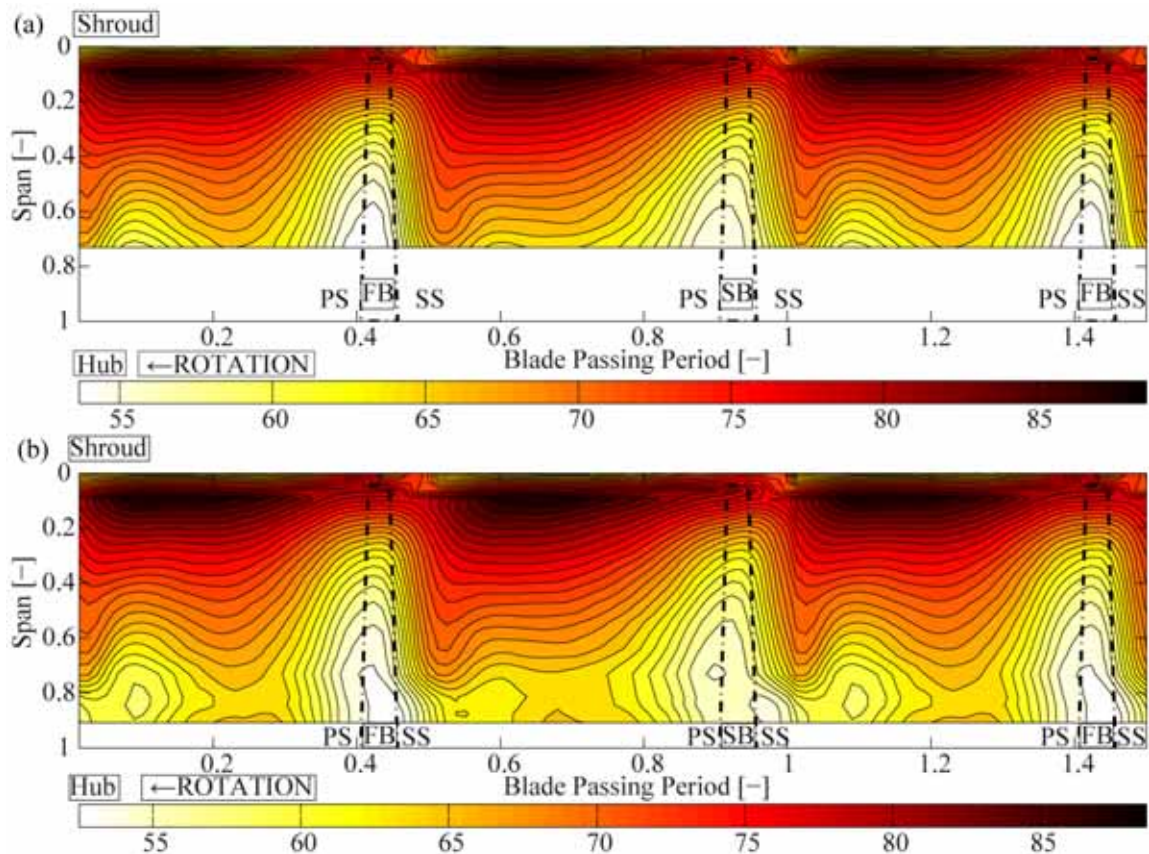
Fig. 8-13   Time-span diagram on yaw angle for both, standard calibration procedure (a), as well as for the combined calibration approach (b), showing an increased spanwise measurement range.

8.4   Validation of Steady Temperature Results

The validation of the steady results from the FRAP-HT measurements has been discussed in chapter 8.3.1 for measurements at the design point (*MP 17*). There, the primary properties, such as the flow angles, as well as the pressure coefficients *Cpt* and *Cps* are presented and compared to pneumatic 4HP measurements (Fig. 8-11). Even though the validation has been performed for measurements at several facility operating points, it will not be discussed further, since all validated *MP's* showed an absolute identical characteristic as for the measurements at *MP 17*.

However, the steady temperature as a secondary property resulting out of FRAP-HT measurements has not yet been validated. Since the temperature is needed in order to derive the aerodynamic stage efficiency (see chapter 8.6.2), a validation of it is of certain importance. By pneumatic 4HP measurements, such a validation is not possible, therefore the steady F0S-PT100-HT probe as

introduced in chapter 5.3 is used to validate the temperature results measured with the FRAP-HT probe.

As discussed in chapter 3.4.2, the direct measurement of total flow temperatures in an accurate manner is always approximated by because of the incomplete recovery of the kinetic energy of the air by the temperature probe. Furthermore, Roduner [87] showed that the recovery factor is not only dependent on the Mach number, but also on the temperature. As discussed in chapter 5.3.1, no further recovery correction is applied to the steady PT100 probe. However, recovery factors have been calibrated for the FRAP-HT probe within the freejet facility. Due to limitations in the temperature range of the facility, the maximum freejet total temperature for which the Mach number dependent calibration factor could be generated, was equal to 343.15K. Additional two sets of recovery factors were generated at freejet total temperatures 303.15K and 323.15K respectively (see chapter 3.4.2).

In Fig. 8-14 the influence of the three different recovery factors on the spanwise distribution of the time averaged FRAP-HT total temperature is presented for the *MP 7*, *8* and *9* respectively, all measured at the compressor speed line equal to *Mu=1.00*. Additionally, the measured temperature distribution by the steady temperature probe (F0S-PT100-HT) at *Mu=1.00* for the different *MP's* is presented. Fig. 8-14a presents the steady FRAP-HT total temperature based on the recovery factor set calibrated at the freejet total temperature 303.15K, Fig. 8-14b for the recovery factor set based on the freejet total temperature 323.15K and Fig. 8-14b for the recovery factor set based on the freejet total temperature 343.15K. The figure shows that the agreement between the FRAP-HT total temperature and the temperature resulting out of the steady PT100 probe measurements improves the higher the freejet temperature is set for determining the recovery factors. This is due to the flow temperatures at *Mu=1.00*, which are clearly above 343.15K. In terms of measurements performed at higher stage Mach operating conditions, due to higher impeller exit temperatures, it's expected to have a stronger deviation between the results of the steady temperature probe and FRAP-HT results, since no calibration at that high freejet temperatures could be achieved.

In Fig. 8-14c, the largest deviation between the steady temperatures out of the two measurements is observed in the shroud region in *MP 7*. The local variation between the two temperatures is in the order of 4K close to the shroud, and no more than 0.9K in the other span locations. The difference in the major part of the span are therefore well within the achievable accuracy in FRAP-HT total temperatures of around ±0.9K at *Ma = 0.5*.
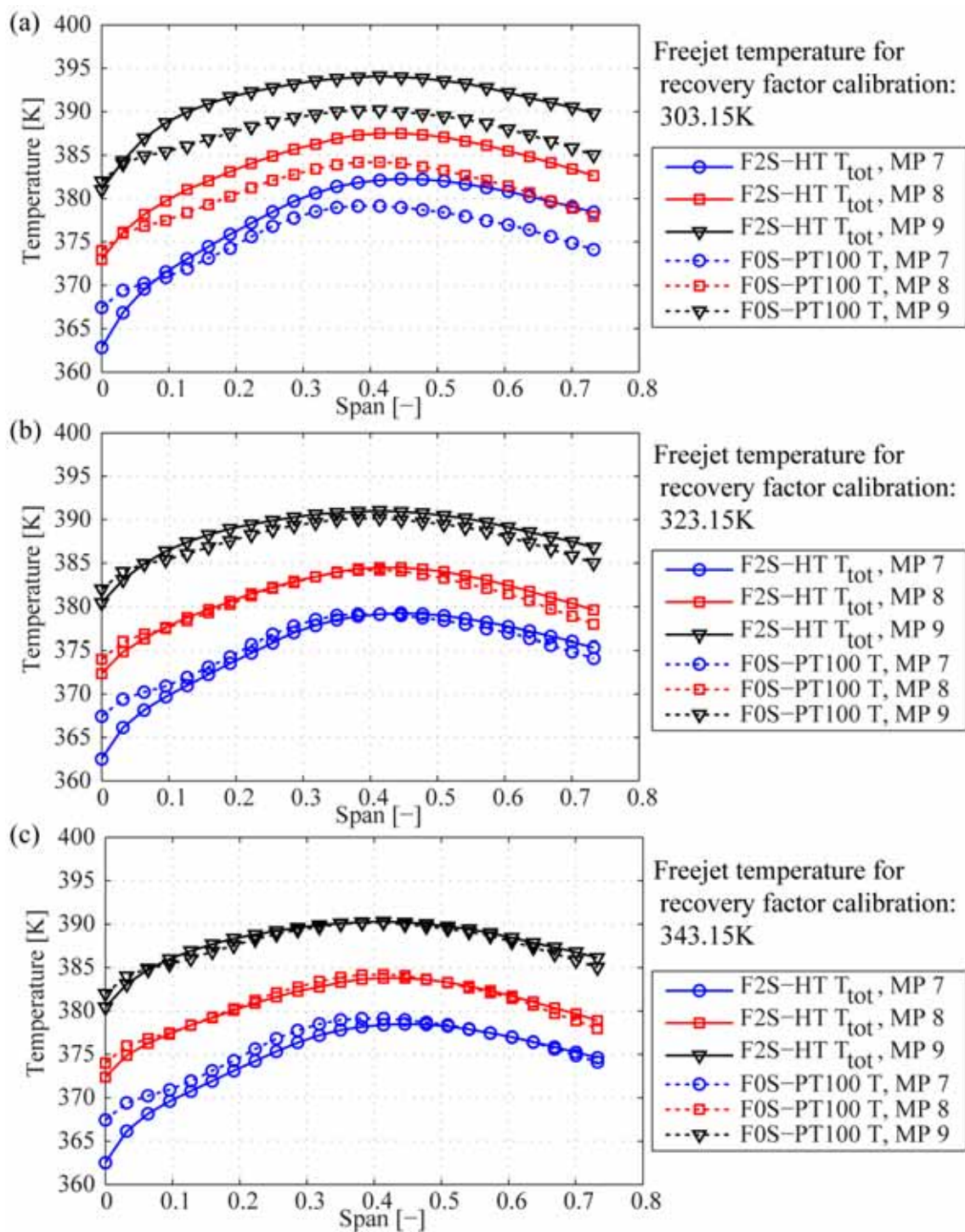
Fig. 8-14 *Spanwise distribution of steady FRAP-HT total temperature vs. resulting temperature distribution by steady temperature probe (F0S-PT100-HT) at Mu=1.00 for recovery factors defined out of various total freejet temperatures (a) to (c).*

A reason for the difference near the shroud could be related to the strength in local gradients of the temperature in the boundary layer. The sensed temperature out of the FRAP-HT measurements is based on a surface integral

over the piezo-resistive transducer. In terms of the PT100 probe, the temperature sensitive part of the sensor is two times longer. The resulting PT100 temperature in the boundary layer could therefore be overestimated since the sensor is influenced by the elevated flow temperature further away from the shroud endwall.

Additional reasons for the differences in-between the two probes close to the channel endwalls are related to the recovery factor definition. For different freejet total temperatures and at low Mach numbers, the recovery factor shows stronger variations (see Fig. 3-25). Since it is not possible to calibrate the recovery factor at freejet temperatures close to the RIGI operating conditions, the uncertainty in deriving the local total flow temperature is expected to be higher for low Mach numbers, which will be the case in the channel boundary region.

As mentioned before, the variation between the FRAP-HT total temperature measurements and the steady PT100 probe measurements are expected to be stronger at higher compressor speed lines due to the elevated flow temperatures. This is shown in Fig. 8-15 for the measurement points 15, 17 and 18, all located on the design speed line *Mu=1.33*. Particularly in the first 40% of the span, some variations are detected. The maximum difference in measured temperature trajectories is around 5K. Nevertheless, the general agreement particularly within the lower 60% of the span is very good and the differences are below 2K. Compared to the elevated absolute temperatures, and the additional sources of uncertainties as discussed below this is a good agreement.

Next to the reasons mentioned above, some probe installation issues as well as the slight differences in geometry as presented in chapter 5.3 could be the reason for the variation in the results. Furthermore, some variation could be related to the facility operating point set-up. Setting the exact same operating conditions in terms of impeller rpm, mass flow and pressure ratio turned out to be more critical for high stage Mach numbers. Both, the difficulty in repeatability of the facility set-up, as well as the slight differences the probe geometry between the two probes are indicated in Fig. 8-16. In this figure, the measured probe shaft temperatures by means of the installed shaft PT100 sensors are presented for the measurements with the two probes at a stage Mach number of *1.33* and for the *MP 15*, *17* and *18* respectively. The temperature within the shaft is increased during the traverse, since the shaft sensor is outside of the probe tower at the beginning of a traverse and then is traversed stepwise toward the hot compressor casing (see corresponding shaft

PT100 temperature position for the first and the last traverse measurement point in Fig. 8-17.
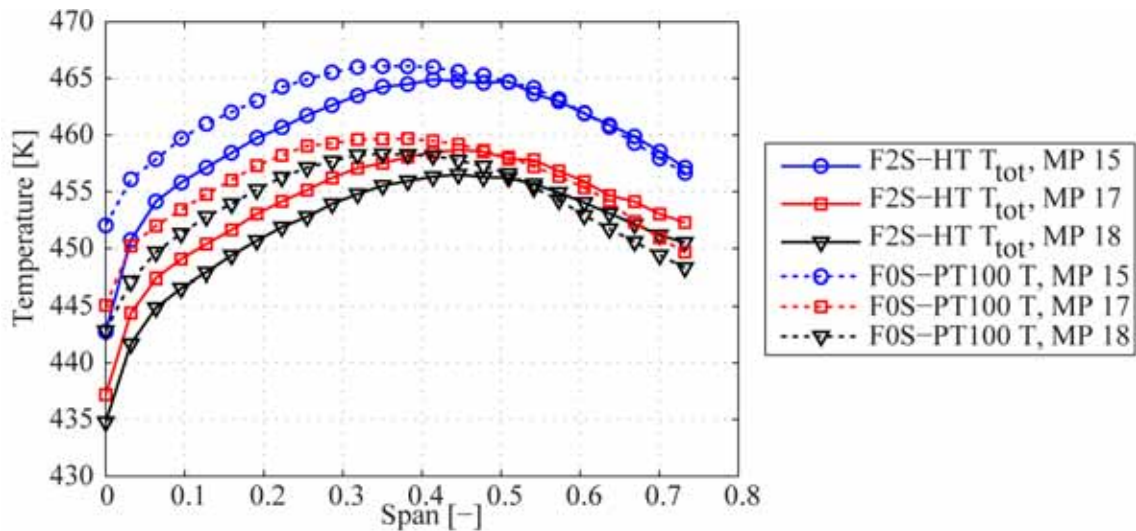
Fig. 8-15 Spanwise distribution of time averaged FRAP-HT total temperature vs. resulting temperature distribution by steady temperature probe (F0S-PT100-HT) at Mu=1.33 (MP 15, 17 and 18) using the recovery factor calibrated at 343.15K.
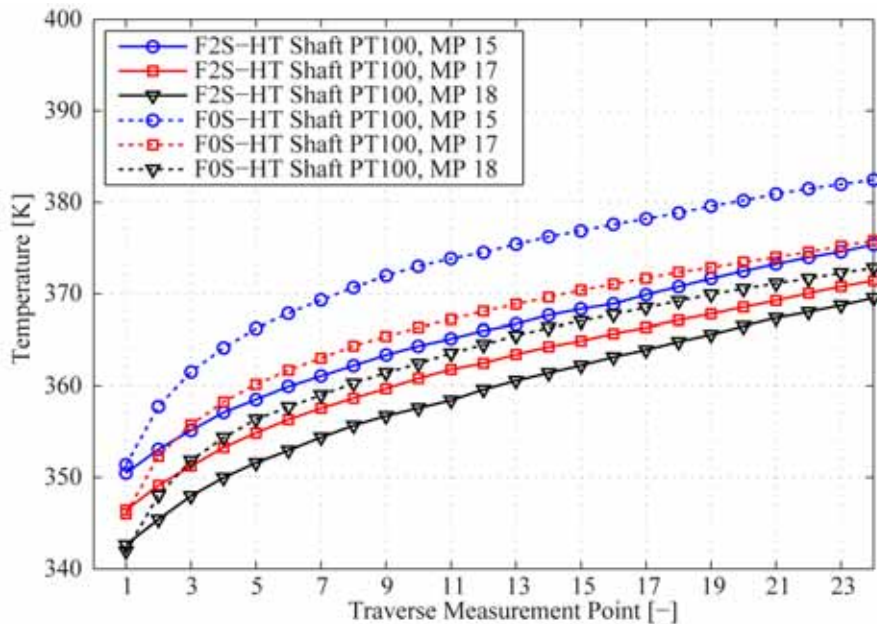
Fig. 8-16 Variation in shaft PT100 temperature during FRAP-HT measurements vs. shaft PT100 temperature during steady temperature probe (F0S-PT100-HT) measurements at MP 15, 17 & 18.
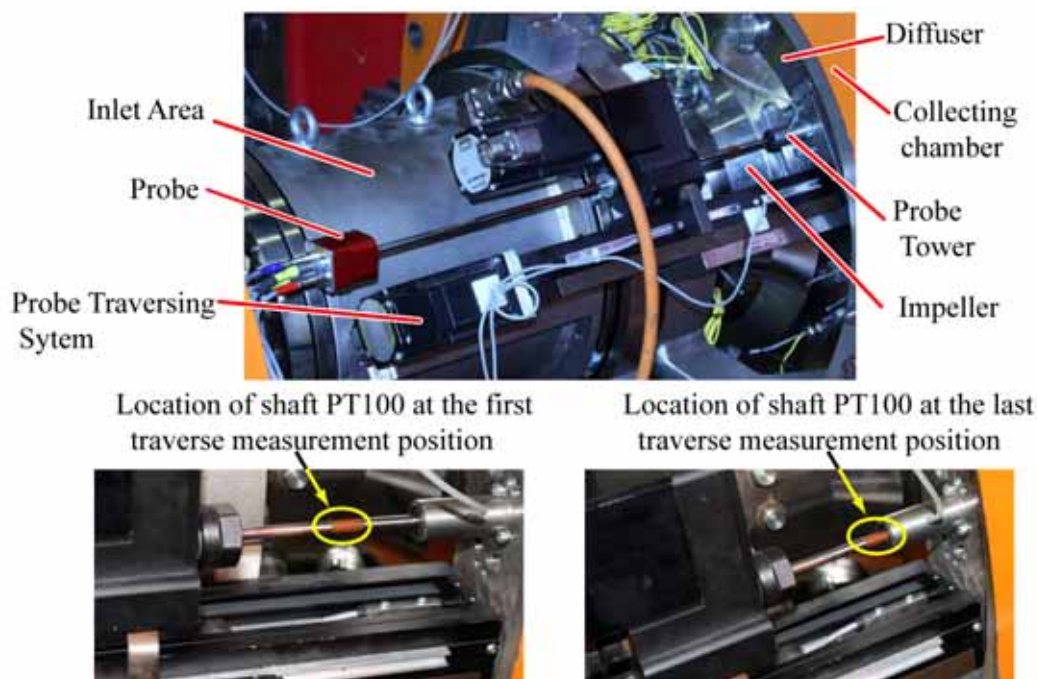
Fig. 8-17 FRAP-HT setup in RIGI (top) and magnified view on the probe to tower interface for the 1st traverse measurement point (bottom left) and the last traverse measurement point (bottom right).

8.5 Time- Resolved Results

The flow at the exit of a centrifugal impeller has been measured by many authors (e.g. [130-131, 146-149]). The flow invariably exhibits a jet-wake flow pattern, although the location and the spreading of the channel wake may vary depending on the impeller geometry and flow rate. The classical jet-wake model has first been introduced by Dean and Senoo [130]. According to their model, a jet is formed on the passage pressure side as a region of high radial velocity and low tangential velocity. On the suction side, the wake region is expected which shows the inverse characteristics compared to the jet region, that is higher absolute tangential velocity and lower radial velocity. Since their model bases on a two-dimensional approach, various extended models have been presented in the last decade by numerous authors (Eckardt [136]). All of them have in common, that they try to consider the highly three dimensional flow occurring in a centrifugal compressor.

In addition to providing a further validation of the newly developed FRAP-HT, the objective of the performed measurements is to get some detailed time-resolved flow structure information of the impeller exit flow operated at the design speed.

Unsteady FRAP-HT measurements have been performed at various operating points and for various speed lines at the described compressor configuration. A detailed flow structure analysis for all the various measurement points showed a principle agreement in trends, but with variations in magnitudes of the different properties. Therefore the focus within this subchapter is the flow structures at the design operating point of the impeller.

All the time-resolved results from FRAP-HT measurements are presented as time-span diagrams in the following subchapter. The measurement area (see Fig. 8-2) is located radially 10mm downstream of the impeller exit at a non-dimensional radius ratio of $R_{meas}/R_{d2}=105\%$. Three blade passages are in presented in the span-time diagrams (x -axis). The y-axis of the time-span diagrams presents the span from shroud (0) to hub (1). The trigger relative position of the impeller full blades (*FB*) and splitter blades (*SB*) are as well schematically adumbrated in the plots. As the contours are plotted 5% impeller radii downstream in the diffuser, the flow features appear with a slight shift relative to the fixed position of the blade.

Fig. 8-18, Fig. 8-19 and Fig. 8-21 respectively, detail directly measured or post- processing derived flow properties at the impeller design point (*MP 17*) on the speed line of *Mu=1.33*.

In order to show at least for a few operating points the principle agreement in trends of the results, Fig. 8-20 details a comparison between three different operating points (*MP 15*, *17* and *18*), all of which are on the design speed line of *Mu=1.33*.

Fig. 8-18a details the time-resolved absolute yaw angle distribution, measured at the design point. The angle is defined as the angle between the flow in the absolute frame of reference and the radial direction. It is positive in the direction of impeller rotation.

The flow direction mapping is bounded by the position of the blade wakes, which are slightly skewed by friction at the diffuser wall (blue lines) and as mentioned before displaced with respect to the impeller channel exit. Most striking are the high angle differences of more than 40° with a steep direction gradient along the diagonal passage direction from the blade pressure side (*PS*) near the hub toward the blade suction side (*SS*) near the shroud.

Furthermore, Fig. 8-18a shows an area of high yaw angle flow close to the shroud and near the *SS* which indicates the occurrence of tip leakage flow. In this area, the flow is not led and turned by the blades and the flow travels from
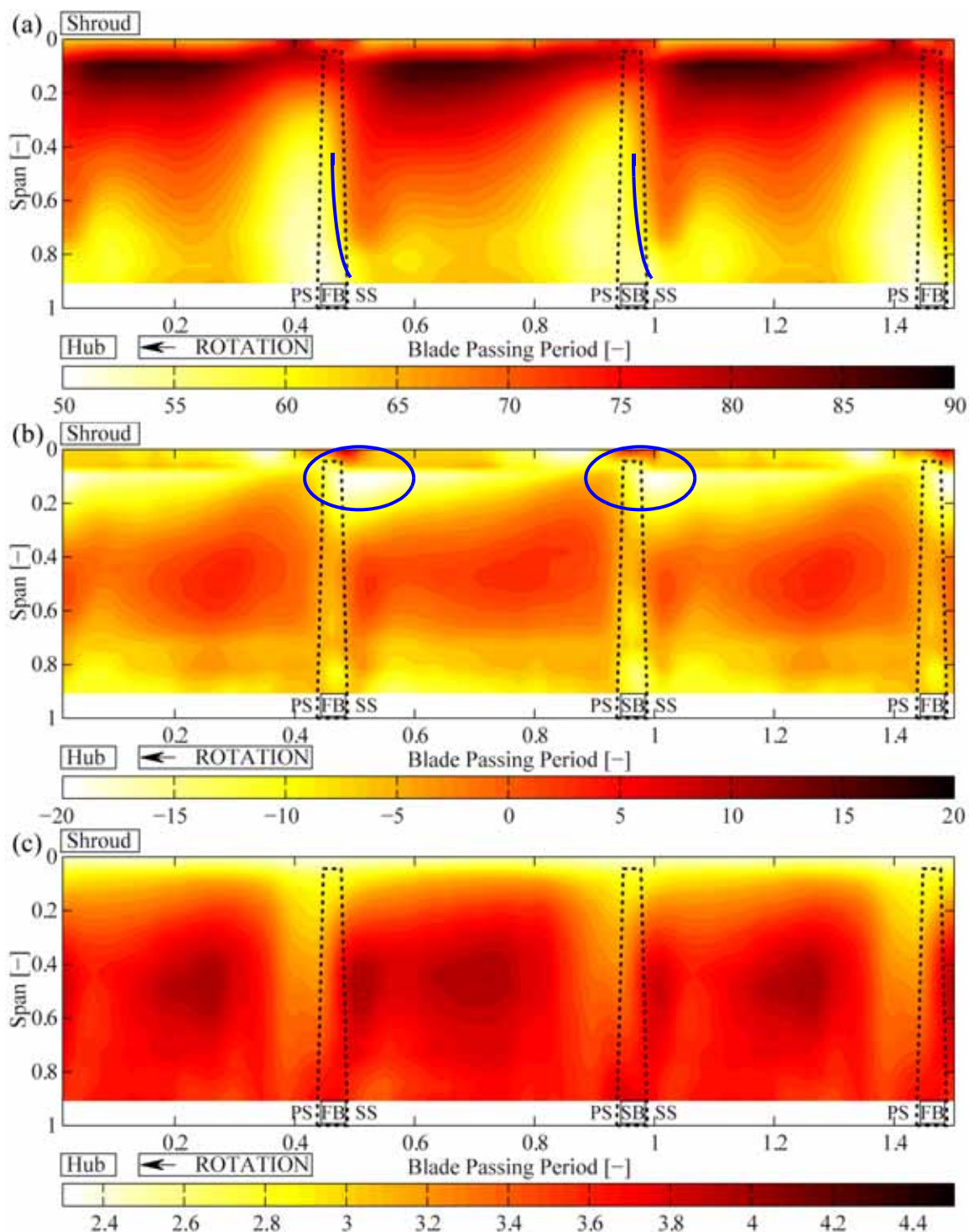
Fig. 8-18 Time-span diagram of various flow properties at the design point
            17 measured by means of FRAP-HT; (a) yaw angle distribution, (b)
            pitch angle distribution and (c) total pressure coefficient C_{pt}.

the suction side over the blade tips. Thus the slip angles in the relative frame as
well as the absolute flow angles are higher than in the bladed area.

   The highly three dimensional nature of the impeller exit flow is seen in Fig.

8-18b, where contours of the pitch angle are plotted. The major part of the passage pitch angles are distributed within ±7°. However, again one zone of highly distorted flows is visible (0% to 15% span) near the blade *SS* (see highlighted area in Fig. 8-18b). As in Fig. 8-18a, this zone is attributed to strong secondary flows due to tip leakage between neighboring passages.

Fig. 8-18c presents the distribution in the time-resolved total pressure coefficient *Cpt*. Although identifiable in all plots of Fig. 8-18, the *Cpt* plot even more clearly shows a certain variation between a passage behind a full blade versus a passage behind a splitter blade. The reason for the difference in the flow property distribution between two neighboring passages can not explicitly be identified by just looking at the flow angles and the total pressure coefficient and will therefore be discussed later. However, in terms of *Cpt* distribution one can clearly identify lower pressure levels in the shroud region between 0% and 20% span. Furthermore a slight periodic reduction in *Cpt* is observed close to the blades near the *PS*. Nevertheless, the circumferential variations in the remaining passage across the diffuser height shows no strong variations in *Cpt*. Due to that, a localization of jet-wake regions identified from the total pressures coefficient as regions of possible losses tends to be difficult. Besides that, as discussed by several authors (e.g. Denton [2]), stagnation pressure is not a useful measure of loss under all conditions and entropy would provide a more appropriate basis for considering departures from the ideal.

Mansour et al. [150] measured the entropy within the same centrifugal compressor facility, but at lower operating speed due to temperature limitation of their measurement probe. They showed, that the jet-wake flow structures and regions of elevated losses are not defined only by areas of reduced total pressure, but additionally requires that the unsteady total temperatures are detailed. The measurement of unsteady total temperature is not possible in case of FRAP-HT. However, the velocity components as presented in Fig. 8-19 can be used to give some indication of the jet-wake structures.

The highly three-dimensional nature of the impeller exit flow is seen in Fig. 8-19, where the radial (a), circumferential (b) and axial (c) components of the absolute velocity are presented.

The tangential velocities are relatively high across the height of the diffuser and are reduced in the near vicinity of the shroud due to effects induced by the boundary layer, as well as by tip gap induced leakage flows. In this region, adjacent to the shroud, the radial velocities are relatively small in magnitude. However, compared to measurements at off design where pronounced areas of

negative radial velocities are seen on the suction side of the blades close to the blade tip and positive velocities are seen on the pressure side, the measurements at the design point as presented here do not indicate any pronounced appearance of reversed flow.
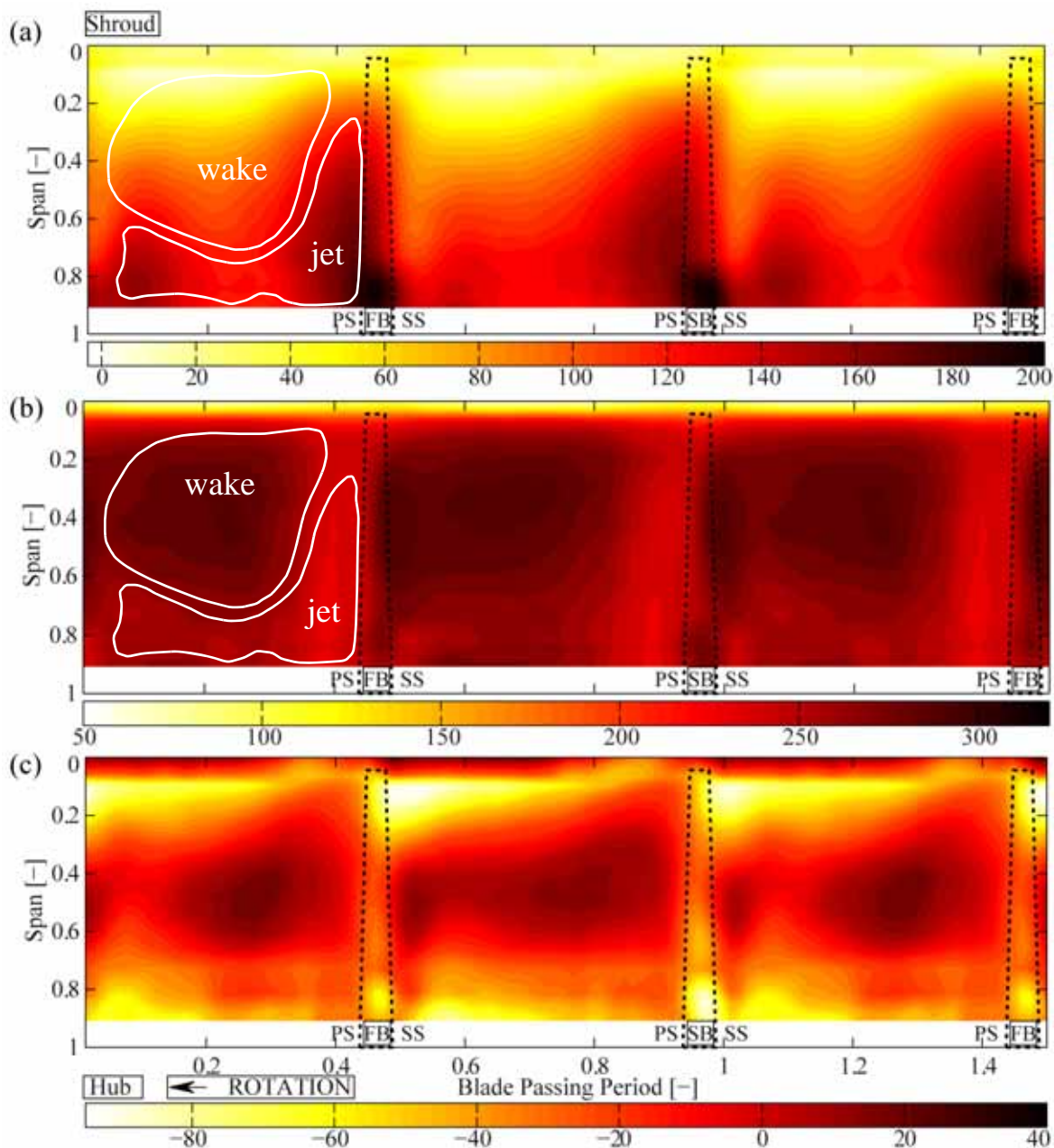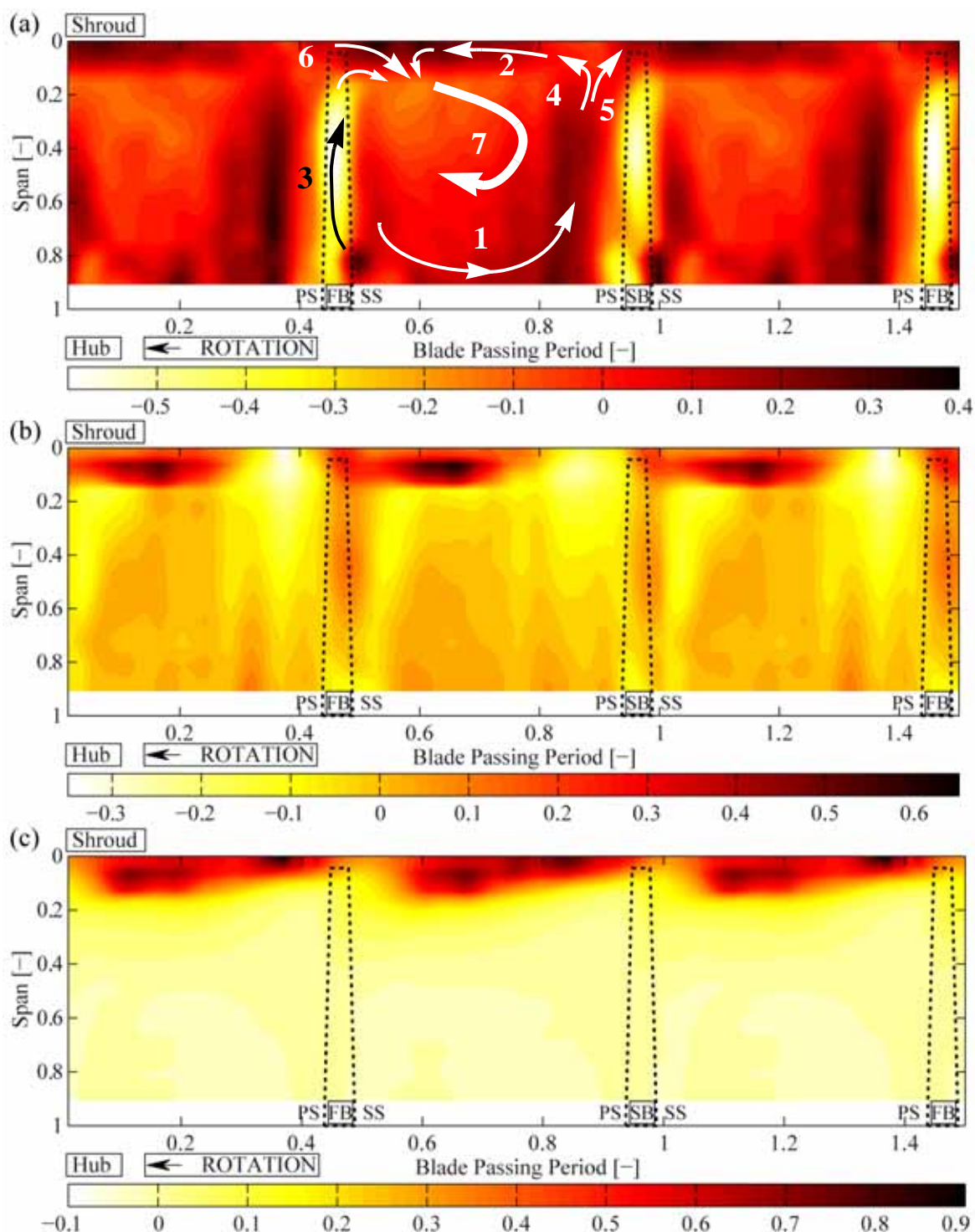

Fig. 8-19   *Time-span diagram of velocity components measured at the design point 17; radial component (a), circumferential component (b) and axial component (c).*

Near the shroud wall, along the blade suction sides, the change in sign of the axial velocities are evidence of secondary flows. These secondary flows are more pronounced adjacent to the full blade compared to the splitter blade

due to the increased meridional blade length of the full blade compared to the splitter blade and therefore due to an increased potential for tip leakage interaction.

Near the hub the circumferential variation differs from that along the shroud, as relatively high radial velocities occur near the pressure side and somewhat smaller radial velocities near the suction side.

The classical jet-wake model, first described by Dean and Senoo [130], can be seen in the pattern of radial and tangential velocities. Near the pressure side of the blades, the region of highest radial velocity covers approximately one third of the passage area and is identified as the jet region. The wake region covers the remaining two-third of the passage width, and shows close to the blade *SS* lower radial velocities and high tangential velocities.

8.5.1   Losses and Secondary Flow Patterns

A further discussion of the loss potential regions is achieved by detailing the random part of the total pressure since regions of high $P'_{tot,rms}$ are indicative of eddy shedding or regions of high turbulence. Even though the unsteady temperature is not measured and therefore not considered in terms of identifying potential regions of losses, it's expected, that contours of $P'_{tot,rms}$ at least indicate some of the regions which are influencing the aerodynamic stage efficiency. The aerodynamic stage efficiency is discussed in chapter 8.6 for various measurement points. A comprehensive view of $P'_{tot,rms}$ for different operating points is therefore of interest for reasons of comparing to the efficiency results in chapter 8.6. Fig. 8-20 therefore details the time-resolved root mean square value of the random part of the total pressure ($P'_{tot,rms}$) at three different operating points (*MP 15*, *17* and *18*). All of the presented measurement points are located on the design speed line of *Mu=1.33*. The contour located at the top of the figure presents the measurements operating point 18 (a), the contour located in the figure center details measurements at the design point 17 (b) and the contour at the bottom of the respective figure presents the measurements at operating point 15 (c).

All three contours show two major areas of elevated $P'_{tot,rms}$. A circularly shaped one at around mid-passage and centered around 30% span associated to the channel wake. This region of high rms levels tends to be circumferentially blurred in the passage adjacent to the *FB*. The second area of elevated $P'_{tot,rms}$ is spread from the hub endwall up to around 30% span located at the schematics of the blade. This region of increased $P'_{tot,rms}$ is associated with the impeller blade wake mixing losses.
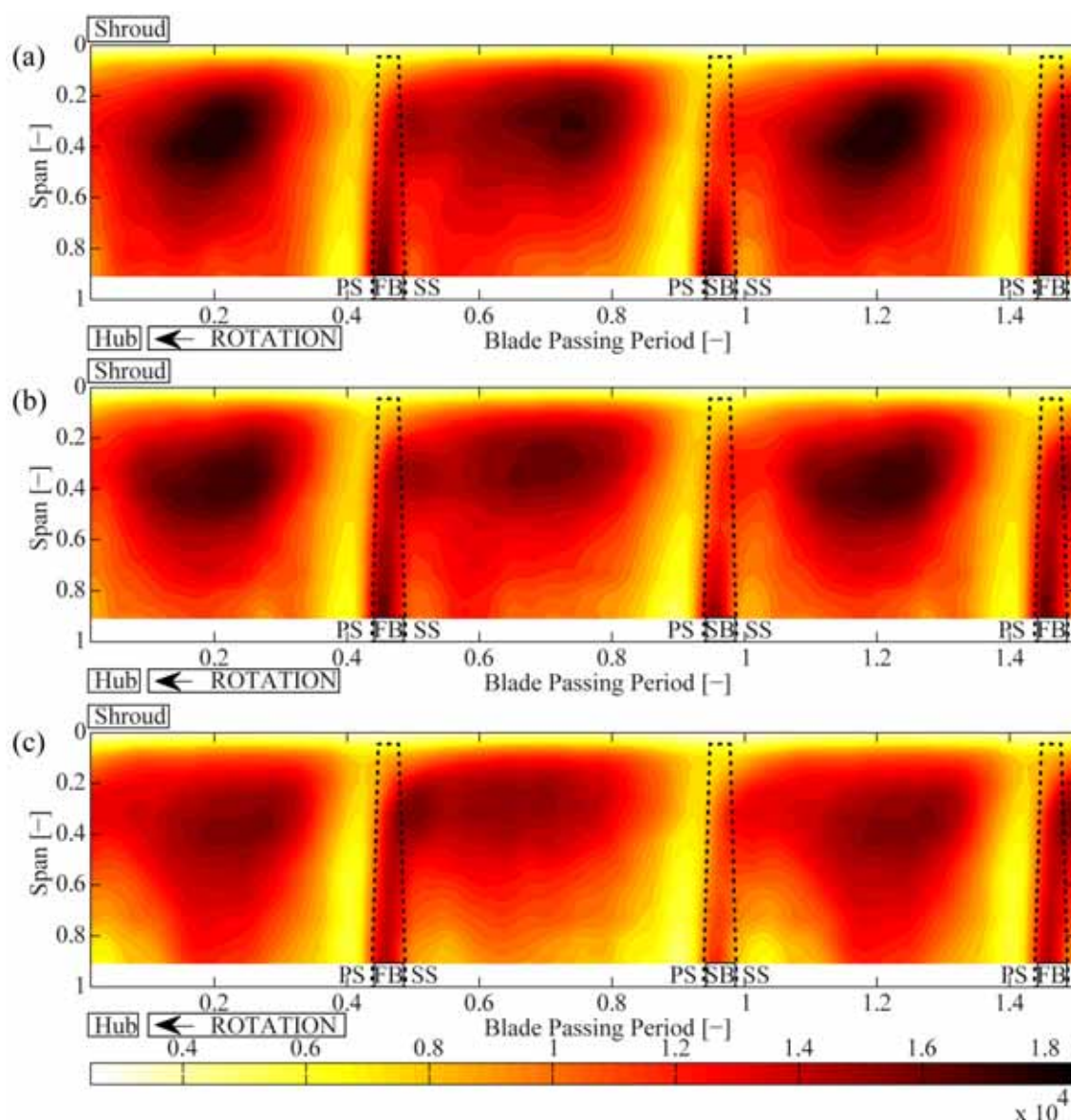
Fig. 8-20   Time-span diagram of P'$_{tot, rms}$ distribution for the operating points 18 (a), the design point 17 (b) and the operating point 15 (c).

As discussed, the results for the three operating points show an analogy in shape and positions of regions of increased $P'_{tot,rms}$. However, they show a significant difference in magnitude of $P'_{tot,rms}$ for the different operating points. Comparing the presented plots to each other shows the highest $P'_{tot,rms}$ levels in Fig. 8-20a, intermediate levels in Fig. 8-20b and the lowest levels in Fig. 8-20c. Since a higher level of $P'_{tot,rms}$ is an indicator of a reduced aerodynamic efficiency, the results are according to the results presented in chapter 8.6. In terms of the compressor map location of the three *MPs'* the results is summarized as follows: Along a constant speed line and for a decreasing corrected mass flux within the stable operating conditions of the compressor, the measured efficiency showed a rise in magnitude.

Another approach to identify areas of possible losses is achieved by highlighting secondary flow patterns. Secondary flows are of significant importance in turbomachinery applications because they produce considerable three-dimensional flow distortions and losses in the endwall regions of blades. Many papers have been published, describing the phenomena associated with secondary flows, as for example by Sieverding [151]. In general, the terminology "secondary flows" turns out to be part of a complex three-dimensional flow field in the endwall regions consisting of a more or less pronounced vortex system caused by different flow phenomena.

Binder et al. [46] provided an approach to identify secondary vortices by means of contour plots of the various flow angles. The same approach has been used in the intelligent aerodynamic probe concept as presented in chapter 4.8. However, in order to simplify the method and identify the secondary flow with a single physical property, we next focus on experimentally determining the vorticity.

The vorticity vector $\vec{\omega}$ is defined as the curl of the velocity field $\vec{c}$:

$$\vec{\omega} = \nabla \times \vec{c} \qquad (8.6)$$

whereas ∇ equals the *Nabla* operator. The components of the vorticity vector in cylindrical coordinates are defined in Eqn. 8.7 to Eqn. 8.9:

$$\omega_r = \frac{1}{r} \cdot \frac{\partial c_z}{\partial \theta} - \frac{\partial c_\theta}{\partial z} \qquad (8.7)$$

$$\omega_\theta = \frac{\partial c_r}{\partial z} - \frac{\partial c_z}{\partial r} \qquad (8.8)$$

$$\omega_z = \frac{1}{r} \cdot \frac{\partial}{\partial r}(r \cdot c_\theta) - \frac{1}{r} \cdot \frac{\partial c_r}{\partial \theta} \qquad (8.9)$$

In terms of the performed measurements at the exit of the centrifugal compressor, one single radial position was measured for all different operating points. The flow field is therefore traversed in the axial z direction and the circumferential direction θ, which allows to derive the related velocity gradients by approximate them by finite differences. However, the gradients in r-direction can not be determined directly out of the measurements (Eqn. 8.8 and Eqn. 8.9). Gregory-Smith et al. [152] first proposed a method for the calculation of the vorticity components in terms of an axial machine type and incompressible flow assumption. Niehuis et al. [153] expanded the approach for compressible flows. This approach is now adapted for a centrifugal

compressor configuration and presented as follows.

The starting equation is the non-dimensional form of the momentum equation for compressible and viscous flows (e.g. Lagerstrom [154]):

$$\rho \cdot \left(\frac{\partial \vec{c}}{\partial t} + (\vec{c} \cdot \nabla)\vec{c} + \frac{1}{\rho}\nabla p \right) = \frac{1}{Re}\left[\nabla \cdot (\mu \ def \ \vec{c}) - \left(\frac{2}{3}\nabla(\mu \nabla \cdot \vec{c}) \right) \right] \quad (8.10)$$

Assuming high Reynolds number flows $(Re \to \infty)$, the right hand side of Eqn. 8.10 is negligibly small, i.e. the viscous terms are small compared to the other terms. Using the general calculation rule:

$$\nabla(\vec{A} \cdot \vec{B}) = (\vec{A} \cdot \nabla)\vec{B} + (\vec{B} \cdot \nabla)\vec{A} + \vec{A} \times (\nabla \times \vec{B}) + \vec{B} \times (\nabla \times \vec{A}) \quad (8.11)$$

and apply it for $\vec{A} = \vec{B}$ equal to the velocity vector $\vec{c}$, it follows after some rearrangements:

$$(\vec{c} \cdot \nabla)\vec{c} = \nabla\frac{c_{abs}^2}{2} - (\vec{c} \times (\nabla \times \vec{c})) \quad (8.12)$$

Substituting the last term of Eqn. 8.12 into Eqn. 8.10 for high Reynolds number flow, it follows:

$$\frac{\partial \vec{c}}{\partial t} - (\vec{c} \times (\nabla \times \vec{c})) + \nabla\frac{c_{abs}^2}{2} = -\frac{1}{\rho}\nabla p \quad (8.13)$$

with $\nabla \times \vec{c} = \vec{\omega}$, the resulting equation is:

$$(\vec{c} \times \vec{\omega}) = \nabla\frac{c_{abs}^2}{2} + \frac{1}{\rho}\nabla p + \frac{\partial \vec{c}}{\partial t} \quad (8.14)$$

Eqn. 8.14 presented in the vector component form for a cylindrical coordinate system yields to:

$$\begin{bmatrix} c_\theta \omega_z - c_z \omega_\theta \\ c_z \omega_r - c_r \omega_z \\ c_r \omega_\theta - c_\theta \omega_r \end{bmatrix} = \begin{bmatrix} \dfrac{1}{2} \cdot \dfrac{\partial c_{abs}^2}{\partial r} + \dfrac{1}{\rho} \cdot \dfrac{\partial P_{stat}}{\partial r} + \dfrac{\partial c_r}{\partial t} \\[3mm] \dfrac{1}{2r} \cdot \dfrac{\partial c_{abs}^2}{\partial \theta} + \dfrac{1}{\rho r} \cdot \dfrac{\partial P_{stat}}{\partial \theta} + \dfrac{\partial c_\theta}{\partial t} \\[3mm] \dfrac{1}{2} \cdot \dfrac{\partial c_{abs}^2}{\partial z} + \dfrac{1}{\rho} \cdot \dfrac{\partial P_{stat}}{\partial z} + \dfrac{\partial c_z}{\partial t} \end{bmatrix} \quad (8.15)$$

Now using the second component line of Eqn. 8.15 instead of the

expression for ω_z from Eqn. 8.8 and the third line of Eqn. 8.15 instead of the expression for ω_θ from Eqn. 8.9, respectively, provides now an expression to derive the complete vorticity vector out of the performed measurements, whereas the gradient with time is not taken into account, since its averaged out due to the ensemble averaging procedure for a fixed impeller relative measurement position. The final equations for the vorticity vector components $(\omega_r, \omega_\theta, \omega_z)$ are therefore:

$$\omega_r = \frac{1}{r} \cdot \frac{\partial c_z}{\partial \theta} - \frac{\partial c_\theta}{\partial z} \tag{8.16}$$

$$\omega_\theta = \frac{1}{c_r} \cdot \left[\frac{1}{2} \cdot \frac{\partial c_{abs}^2}{\partial z} + \frac{1}{\rho} \cdot \frac{\partial P_{stat}}{\partial z} + c_\theta \omega_r \right] \tag{8.17}$$

$$\omega_z = -\frac{1}{c_r} \cdot \left[\frac{1}{2r} \cdot \frac{\partial c_{abs}^2}{\partial \theta} + \frac{1}{\rho r} \cdot \frac{\partial P_{stat}}{\partial \theta} - c_z \omega_r \right] \tag{8.18}$$

The above listed expressions of Eqn. 8.17 to Eqn. 8.18 are now directly derivable from the measurements and are presented in Fig. 8.23.

It should be mentioned, that special care is needed in the derivation of the circumferential and the axial vorticity components, due to the radial velocity component in the denominator. Eqn. 8.17 and Eqn. 8.18 has a singularity if the radial velocity equals zero. In general this occurs in the boundary layer near the end walls. Furthermore the assumption of neglecting viscous terms in case of high Reynolds number flows is not accurate at low absolute velocities c_{abs}, as for instance within the blade wake.

In order to present normalized values of Eqn. 8.16 to Eqn. 8.18, the different components are divided by the absolute value of the difference between the maxima and the minima of the respective vorticity components (see in Fig. 8-21).

An interpretation and allocation of the different secondary flow patterns tends to be more difficult by use of the circumferential and axial components of the vorticity (Fig. 8-21b and c) compared to the radial vorticity component. However, it should be stated, that both components are strongest in the shroud region. This is related to different kind of interactions occurring within the low momentum fluid at the shroud and the tip leakage vortex. These interactions are further supported by the upper passage gradient between *PS* and *SS*, tending to form an upper passage vortex.

Fig. 8-21   Time-span diagram of vorticity components measured at the design point 17; radial component (a), circumferential component (b) and axial component (c).

In principle the above mentioned flow features should also be recognizable within Fig. 8-21a, detailing the radial vorticity component. Our focus is therefore to interpret the radial vorticity component. In terms of sign

convention within Fig. 8-21a, the radial vorticity component is positive when the rotation is oriented counter-clockwise. The numbers, as mentioned in the following discussion are indicators of flow features and are systematically marked within the central passage in Fig. 8-21a.

A typical feature of passage relative flow patterns is the tendency of the core-flow toward the blade pressure side (1). The cross-flow closes to a dominating main vortex (2) in the shroud region and removes low-energy fluid material from the channel surfaces and feeds it into the wake. The same applies for a weaker secondary flow structure in the region of the hub wall and the suction side (3). Part of the fluid influenced by the movements of the dominating main vortex (2) is traveling toward the shroud along the PS of the passage (4) and, in case of low energetic content is redirected and dumped through the tip clearance (5). This pattern then forms the tip leakage vortex (6) and interacts with the channel wake (7). The channel wake itself behaves as a reservoir for low energetic fluid of various sources.

The secondary flow model schematically sketched within Fig. 8-21a agrees in general with the model discussed by Eckardt [136]. This is highlighted in Fig. 8-22 by a bicolored contour of the same results as presented in Fig. 8-21a. Areas of positive radial vorticity are marked black, whereas areas of negative or zero radial vorticity are marked white. The area at the hub enwall between 92% span and 100% span is not measured. No statement can therefore be made about the orientation of the vorticity in that area. To clarify the spanwise measurement range, a dot-an-dashed line is added in Fig. 8-22.
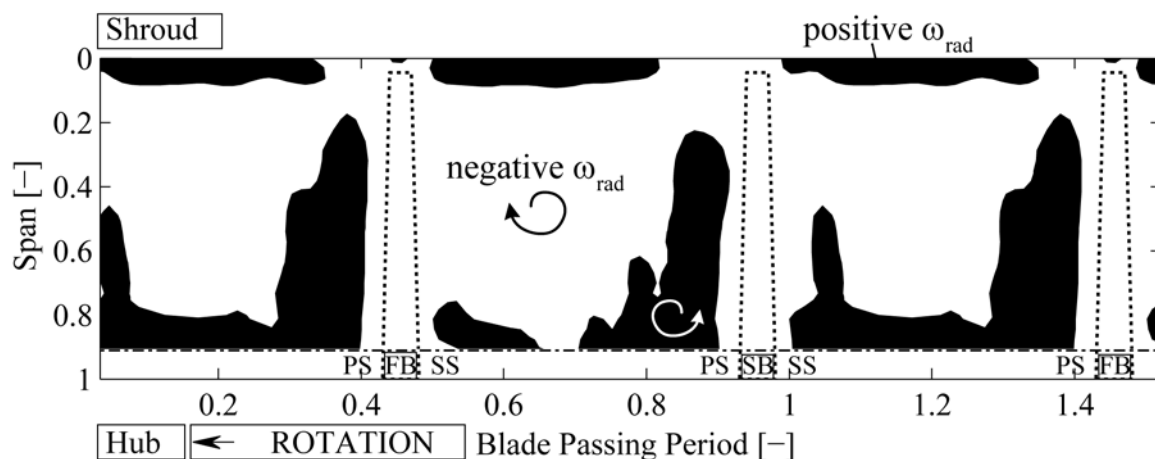
Fig. 8-22   FRAP-HT measured radial vorticity at design point MP 17.

The results of Fig. 8-21a and Fig. 8-22 are schematically summarized on the right hand side of Fig. 8-23 and compared to Eckardt's model [136] (Fig. 8-23, left). Compared to Eckardt's model, the size and location of the channel wake are different. Eckardt performed the Laser-2-Focus-Velocimetry

measurements around 10% upstream of the impeller trailing edge (with respect to the meridional shroud contour length). Since our measurements are performed in the impeller aft area, the channel wake is expected to be more directed toward the pressure side, as well as expected to be wider in spread and intensity due to additional low momentum tip leakage fluid which is fed into the channel wake structure and further intensifies the strength of the secondary flow structures. The growth in size of the channel wake is further supported by the system rotation and stream curvature effects, which counteract and therefore suppress the turbulent mixing between high- and low- energetic fluid material.
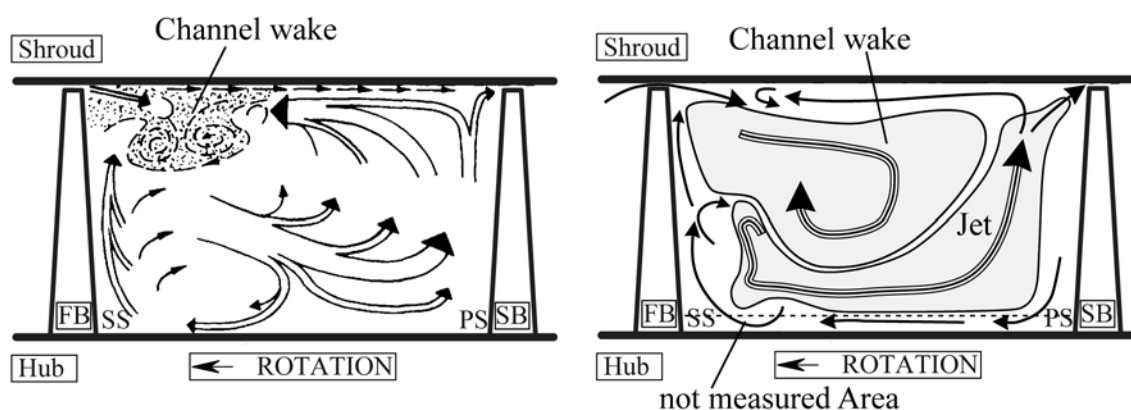
Fig. 8-23   *Schematic of centrifugal impeller secondary flow patterns based on Eckardt (left), vs. secondary flow patterns out of measurements by FRAP-HT at the design point MP 17 (right).*

8.6   Aerodynamic Stage Efficiency

Combining the FRAP-HT results together with operational data of the facility, allowed for first time the derivation of the isentropic total-to-total efficiency. The resulting definition of the efficiency, using the ideal gas assumption with constant specific heat is presented in Eqn. 8.19:

$$\eta_{is,\,tt} \;=\; \frac{\left(\dfrac{\bar{p}_{tot,\,exit}}{p_{tot,\,inlet}}\right)^{(\kappa-1)/\kappa} - 1}{\dfrac{\bar{T}_{tot,\,exit}}{T_{tot,\,inlet}} - 1} \qquad (8.19)$$

Four quantities are required, whereas the inlet quantities are obtained from the operational data of the rig at the specific operation point and the exit quantities are based on mass flow-weighted averages of total pressure and total temperature respectively.

8.6.1   Mass flow-weighted Averaging Procedure for RIGI

Measurements performed by FRAP-HT probes yield time resolved local flow properties. However, for many applications such as the one dimensional theory of centrifugal compressor stages [132], global flow properties are needed. Therefore the applied averaging technique play a major role in order to provide for the validity of the conservation equations for both, local flow properties, as well as for averaged global flow properties.

The basic concept of deriving integral measurement quantities based on mass flow- weighted averaging has been introduced in chapter 4.7.1. However, in terms of measurements in a centrifugal compressor, special care is needed in applying the procedure due to high temporal fluctuations in the absolute yaw angle (Fig. 8-4). The procedure in deriving the global flow properties of measured total pressure and total temperature from time resolved FRAP-HT measurements is described as follows:

The hub-to-shroud distribution of the flow quantities can be obtained from a circumferential averaging. As the speed of the impeller is constant the result is similar to a time-averaging of the flow quantities. Köppel et al. [155] compared the calculation of the circumferential average of FRAP data and pneumatic and therefore time-averaged measured probe data by using the physical approaches by Traupel [132] and Dzung [156] with the simple calculation as an arithmetic average (Eqn. 8.20). They concluded that the usage of the simple formulation of the circumferential or time-average as an arithmetic average lead to a sufficient result.

$$\bar{x}(z) = \frac{1}{n} \cdot \sum_{i=1}^{n} x(t, z) \cdot \Delta z \qquad (8.20)$$

In order to now derive global values of the flow quantities $\bar{x}$ from the hub-to-shroud distribution as shown in Eqn. 8.20, a mass flow-weighted averaging is applied over the span b by using the data of the discrete and time-averaged measurement positions z:

$$\bar{x} = \frac{\sum_{0}^{b} \bar{x}(z) \cdot \bar{c}_r(z) \cdot \bar{\rho}(z) \cdot 2\pi r \cdot \Delta z}{\sum_{0}^{b} \bar{c}_r(z) \cdot \bar{\rho}(z) \cdot 2\pi r \cdot \Delta z} \qquad (8.21)$$

whereas $\bar{c}_r(z)$ equals to the time-averaged radial velocity component at span position z, $\rho(z)$ equals to the time-averaged density at the same position, derived out of the local static temperature $T_{stat}(z)$, the time-averaged static pressure $\bar{p}_{stat}(z)$ and the specific gas constant for dry air

$(R = 287.06 \ J(kg \cdot K)^{-1})$. The parameter r of Eqn. 8.21 represents the radial location of the measurement position (relative to the machine axis) and $\varDelta z$ equals the width resulting out of the differences between the neighboring measurement positions along the span, centered around the measurement point location, as schematically presented in Fig. 8.20.
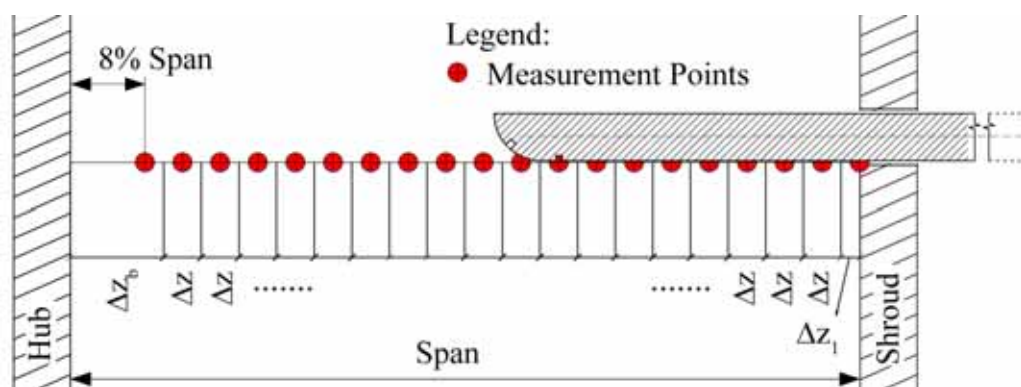
Fig. 8-24   Schematic of definition of $\varDelta z$ used for mass-averaging along one FRAP-HT measurement traverse in RIGI Test.

Even by applying the combined calibration approach to increase the spanwise range in the performed RIGI measurements, the lowest 8% of the span are not measured. This leads to an overestimation of the derived mass-averaged total quantity and will induce an additional uncertainty as discussed in the next subchapter.

8.6.1.1   Uncertainty in Mass flow-weighted Averaging

In order to derive the overall uncertainty information for the efficiency calculations based on Eqn. 8.19, quantitative values of the uncertainties related to the mass-averaging procedures are required. The GUM method ([108]) as introduced in chapter 6, is applied in a first step to derive the uncertainties related to the mass averaging procedure for the total quantities of the temperature and the pressure. In a second step, the influence of the resulting averaging uncertainties, as well as the uncertainty contributions of rig operational data related flow quantities are summarized to derive an expanded uncertainty quantification for the aerodynamic stage efficiency (Eqn. 8.19).

The uncertainty related to the mass flow-weighted averaging procedure basically contains all the induced uncertainties related to the process of deriving a global quantity out of the measured flow quantities at the different measurement positions, as described in the previous subchapter. This means that also uncertainties related to ensemble averaging and time averaging are taken into account in the expanded uncertainty expression of mass flow-

weighting flow quantities. The uncertainty in deriving a mass flow averaged quantity of total pressure, defined as $\Delta \bar{p}_{tot,\,massav}$ in Eqn. 8.22 is therefore a function of the probe measurement induced uncertainties of the ensemble- and time averaged quantities of the measured total pressure $\Delta \bar{p}_{tot,\,probe}$, the radial velocity $\Delta \bar{c}_{r,\,probe}$ and the static pressure $\Delta \bar{p}_{stat,\,probe}$. Furthermore it is functionally dependent on the uncertainties induced by deriving the ensemble averaged static temperature $\Delta T_{stat,\,probe}$ from probe measurements. For the last quantity, time-averaging, does not induce any additional uncertainties, since the measured probe temperature is already acquired in a steady mode. The functional dependency in deriving a mass flow averaged quantity of the total temperature $\Delta \bar{T}_{tot,\,massav}$ is similar to that for total pressure and presented in Eqn. 8.23.

$$\Delta \bar{p}_{tot,\,massav} = f(\Delta \bar{p}_{tot,\,probe}, \Delta \bar{c}_{r,\,probe}, \Delta \bar{p}_{stat,\,probe}, \Delta T_{stat,\,probe}) \qquad (8.22)$$

$$\Delta \bar{T}_{tot,\,massav} = f(\Delta T_{tot,\,probe}, \Delta \bar{c}_{r,\,probe}, \Delta \bar{p}_{stat,\,probe}, \Delta T_{stat,\,probe}) \qquad (8.23)$$

Taking all of these effects into account results in expanded uncertainties (k=2) related to the mass flow-weighted averaging procedure of ±41Pa for $\Delta \bar{p}_{tot,\,massav}$ and ±0.058K for $\Delta \bar{T}_{tot,\,massav}$. These resulting expanded uncertainties are purely related to the procedure in deriving mass-averaged quantities and will further propagate into the efficiency calculation as described in chapter 8.6.2. However, possible errors induced due to the weighting procedure at the hub endwall as described above are not yet considered and must therefore be further discussed.

Considering the physical behavior of the properties their total portion will drop in the boundary region of the hub endwall. However, this region between 90% span and the hub endwall is not measurable as discussed before. The total properties in mass-averaging this region equal to the last traverse measurement point. This procedure therefore overestimates the total pressure, as well as the total temperature of the last cell area and leads to an additional uncertainty in the resulting mass averaged total properties. The crucial impact to the overall uncertainty due to not being able to measure the full span by invasive probe techniques is known and has been discussed for example by Cumpsty et al. [89]. They state that even though inducing a major uncertainty by extrapolating the measurements to the wall, the induced error by not taking into account this zone at all would corrupt the data even more. Due to this, an additional uncertainty related to the overestimation of the total pressure ($\Delta p_{Endwall}$) and the total temperature ($\Delta T_{Endwall}$) near the hub endwall is induced for the definition of the global mass-averaged quantities in Eqn. 8.24

and Eqn. 8.25 respectively.

$$\Delta \bar{p}_{tot, exit} = \Delta \bar{p}_{tot, massav} + \Delta p_{Endwall} \qquad (8.24)$$

$$\Delta \bar{T}_{tot, exit} = \Delta \bar{T}_{tot, massav} + \Delta T_{Endwall} \qquad (8.25)$$

The uncertainties as described in Eqn. 8.24 and Eqn. 8.25 are taken into account in the evaluation of the expanded uncertainty in the calculation of the aerodynamic stage efficiency as follows in chapter 8.6.2.

8.6.2   Uncertainty in Efficiency Calculation

Based on Eqn. 8.19, the uncertainties propagating into the expression of the aerodynamic stage efficiency are related to the FRAP-HT probe measured and subsequently mass-averaged total flow quantities pressure and temperature, as described above. Furthermore the overall uncertainty in efficiency $\Delta \eta_{is, tt}$ depends on uncertainties related to measurements of the total pressure and total temperature facility inlet conditions ($\Delta p_{tot, inlet}$ and $\Delta T_{tot, inlet}$):

$$\Delta \eta_{is, tt} = f(\Delta \bar{p}_{tot, exit} , \Delta \bar{T}_{tot, exit} , \Delta p_{tot, inlet} , \Delta T_{tot, inlet}) \qquad (8.26)$$

The related standard uncertainties ($k=1$), incorporated into the calculation of the total-to-total efficiency are summarized in Table 8-4. The first two input quantities listed in Table 8-4 are the resulting standard uncertainties based on the mass-flow-weighted averaging procedure for total pressure and total temperature out of FRAP-HT measurements as presented in the previous subchapter. As discussed in chapter 8.6.1, the quantification of the uncertainty contributed by not measuring the lowest 9% of the span compared to the deficit in the resulting overall mass flow revealed an additional expanded uncertainty in the order of 0.5% of the resulting mass-averaged exit total pressure, which in terms of standard uncertainty results in ±289Pa. The same approach applied for the exit total temperature uncertainty related to not covering the full span by probe measurements leads to a standard uncertainty of ±0.06K. The last to standard uncertainties listed in Table 8-4 are based on subsystems used to control and operate the RIGI facility. The total pressure at the inlet of the impeller is derived by a static pressure scanner in combination with results from the rig integrated mass-flow measurement device. The resulting standard uncertainty to derive the inlet total pressure was calculated to be in the order of ±86.6Pa. The sensors used to derive the total inlet temperature conditions are based on PT100 sensors and have a standard uncertainty of ±0.12K.

Input Quantity		standard Uncertainty $u(x_i)$	Uncertainty contribution [%]
mass averaged exit total pressure	$\Delta \bar{p}_{tot, massav}$	± 20.4 Pa	0.2
mass averaged exit total temperature	$\Delta \bar{T}_{tot, massav}$	± 0.03 K	0.2
endwall induced error in exit total pressure	$\Delta p_{Endwall}$	± 289 Pa	41.1
endwall induced error in exit total temperature	$\Delta T_{Endwall}$	± 0.06 K	1.0
inlet total pressure	$\Delta p_{tot, inlet}$	± 86.6 Pa	48.6
inlet total temperature	$\Delta T_{tot, inlet}$	± 0.12 K	8.8

Table 8-4   Accuracy related to the total-to-total isentropic efficiency calculation out of FRAP-HT measurements.

The calculated absolute expanded uncertainty (*k=2*) of the isentropic total-to-total efficiency is $\pm 0.65\%$. The uncertainty of the inlet total pressure based on RIGI specific equipment contributes with 48.6% the most to the overall uncertainty, while the endwall induced errors in total pressure measurement are responsible for 41.1%. The facility inlet total temperature measurement contribute 8.8% to the overall uncertainty and the remaining 1.4% are from the other input quantities, representing the mass averaged properties by the FRAP-HT probe. The result of that uncertainty analysis therefore shows, that the uncertainties related to the "real" measured properties by the probe do have a minor influence on the overall uncertainty of the total-to-total efficiency expression. However, a large source of uncertainty is related to the measurement positions traceable during a probe traverse. A reduction of this uncertainty contribution could for instance be obtained by a slot on the hub endwall surface of the diffuser. Any slot induced flow distortion could be reduced by an adapter that includes a spring mechanism, which closes the slot, and is pushed away, when the probe is approaching the endwall. This would allow to intrude the probe tip into the hub endwall and make probe measurements over the full span possible.

8.6.3   Results

The isentropic total-to-total efficiency has been derived for seven measurement points. Three of them are located on the speed line related to the non-dimensional rotational speed *Mu=1.26*. Another four of them are located the *Mu=1.33*, whereas the design point (*DP*) as described in chapter 8.1 has been included in that evaluation procedure. Table 8-5 presents the case respective stage Mach numbers *Mu*, the normalized corrected mass flow rate Q/Q_{DP}, the normalized total pressure ratios $\Pi_0/\Pi_{0,DP}$, as well as resulting

normalized isentropic total-to-total efficiency values in percentage. In general, the normalization procedure is done by dividing the property to be normed by the respective value of the same property at the compressor design point. However, the expression for the total-to-total efficiency is normalized differently. The resulting efficiency at the design point is subtracted for a certain operating point. The resulting expression is then divided by the efficiency at the design point and presented in percentage. The definition of this normalized relative change in efficiency therefore is:

$$\Delta \eta_{is,\, tt,\, rel} = \frac{\eta_{is,\, tt} - \eta_{is,\, tt,DP}}{\eta_{is,\, tt,DP}} \qquad (8.27)$$

Positive values in the relative change in efficiency therefore indicate a higher aerodynamic stage efficiency at the operating point than at the design point and *vice versa*.

Measurement point	Mu [-]	Q/Q_{DP} [-]	$\Pi_o/\Pi_{o,DP}$ [-]	$(\eta_{is,\, tt} - \eta_{is,\, tt,DP})/\eta_{is,\, tt,DP}$ [%]
10	1.26	0.74	1.01	3.80
11	1.26	0.87	0.97	3.23
13	1.26	0.99	0.90	1.72
14	1.33	0.78	1.10	4.80
15	1.33	0.85	1.08	2.98
16	1.33	0.92	1.06	1.74
17 (DP)	1.33	1.00	1.00	0.00
18	1.33	1.02	0.97	-1.38

Table 8-5   Normalized efficiencies (with respect to DP) resulting out of performed FRAP-HT measurements for seven operating points on two speed lines, Mu=1.26 and Mu=1.33.

Furthermore, the efficiency results as presented in Table 8-5 are presented in Fig. 8-25 in order to emphasize the relationship between the respective efficiencies at the different stage Mach numbers.

Both, Table 8-5, as well as Fig. 8-25 show, that the design point does not equal the point of the highest efficiency (best point). However, special care must be taken in drawing conclusions from the results due to the level of the induced uncertainties in deriving the efficiency values. As presented before, the expanded uncertainties stand for a non-normalized value of the efficiency. However, the expanded uncertainties by defining the normalized value of the relative change in efficiency involves measurements at two operating points and therefore the resulting uncertainties have to be considered. Therefore by using the definition of the relative change of efficiency with respect to the

design point as defined in Eqn. 8.27, the expanded uncertainty ($k=2$) based on GUM for the change in relative stage efficiency $\Delta\eta_{is,\,tt,\,rel}$ is in the order of ±1.1%.
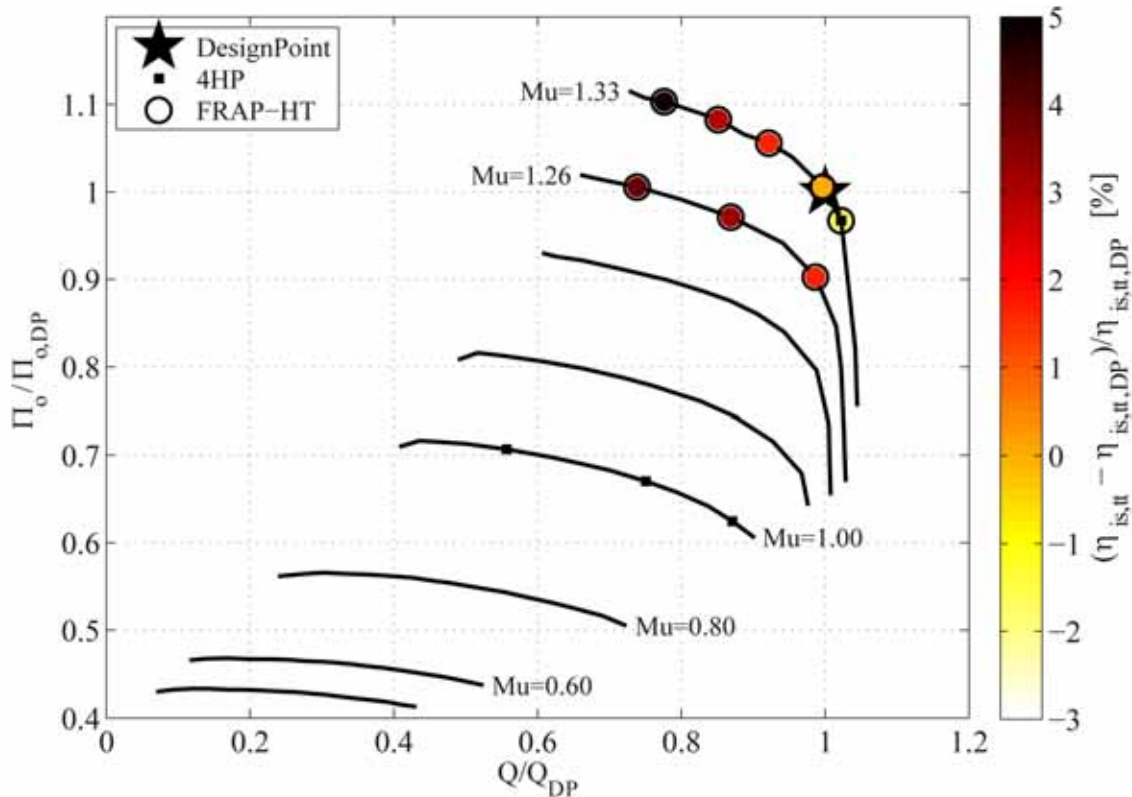
Fig. 8-25 RIGI compressor map, showing the normalized efficiencies result-ing out of performed FRAP-HT measurements for seven operating points on two speed lines, Mu=1.26 and Mu=1.33.

This allows us to now draw the conclusion, that the design point does not equal the best point. Based on the results the best point is expected to be at a lower normalized corrected mass flow rate in-between 0.77 and 0.9. In general, it is not uncommon that the location of the design point does not correspond with the best point, since the manufacturer provides for a certain safety margin between the design point and the compressor stability limit. Furthermore, the calculated aerodynamic stage efficiency could be influenced by the general overestimate resulting out of the performed averaging procedure as discussed before, as well as by the radial measurement location where the FRAP-HT measurements are performed. The calculated efficiency is based on measurements downstream of the impeller but in the leading area of the vaneless diffuser. In terms of possible total pressure losses, even though known to be more pronounced in case of vaned diffusers, the total-to-total efficiency for the complete stage could, depending on the operating point, vary slightly and therefore lead to an offset along the Q/Q_{DP} axis in Fig. 8-25.

8.6.3.1   Isentropic versus polytropic Efficiency

The constant pressure lines on the T-s diagram have a slope proportional to the temperature so that they diverge as the temperature and the entropy increase. In other words the minimum temperature rise to produce a given pressure rise increases both with initial temperature and increased entropy. Thus, the isentropic efficiency of compressors of same aerodynamic performance is therefore lower as the overall pressure ratio is increased, which can be misleading. This misleading observation can be avoided by instead using the so-called polytropic efficiency. This definition of efficiency ensures that compressors of same aerodynamic performance, but significantly different pressure ratios, have the same polytropic efficiency although their isentropic efficiencies are different. The total-to-total polytropic efficiency is defined in Eqn. 8.28:

$$\eta_{poly,\,tt} = \frac{\kappa - 1}{\kappa} \cdot \frac{\ln\left(\dfrac{\bar{p}_{tot,\,exit}}{p_{tot,\,inlet}}\right)}{\ln\left(\dfrac{\bar{T}_{tot,\,exit}}{T_{tot,\,inlet}}\right)} \qquad (8.28)$$

Table 8-6 presents the differences between the polytropic and the isentropic efficiencies for the respective measurement points. As expected all differences are positive, since the polytropic efficiency is generally higher compared to the isentropic stage efficiency. However, the variations between the differences are not that high if compared to the uncertainties involved in expressing the isentropic efficiency (±0.65%).

Measurement point	Mu [-]	Q/Q_{DP} [-]	$\Pi_o/\Pi_{o,DP}$ [-]	$\eta_{poly,\,tt} - \eta_{is,\,tt}$ [%]
10	1.26	0.74	1.01	1.78
11	1.26	0.87	0.97	1.79
13	1.26	0.99	0.90	1.88
14	1.33	0.78	1.10	1.76
15	1.33	0.85	1.08	1.99
16	1.33	0.92	1.06	2.13
17 (DP)	1.33	1.00	1.00	2.30
18	1.33	1.02	0.97	2.45

Table 8-6   Difference between polytropic and isentropic stage efficiency from FRAP-HT measurements at seven operating points on two speed lines, Mu=1.26 and Mu=1.33.

Furthermore, if the measurement points are ranked based on the magnitudes, then both definitions of efficiency show the same relative rankings of the measurement points. The isentropic efficiency related results and the conclusions drawn from the measurements are therefore valid even when an efficiency based on the polytropic efficiency is used.

8.7   Summary and Concluding Remarks

The novel high temperature Fast Response Aerodynamic Probe (FRAP-HT) is applied to the single stage, centrifugal compressor facility equipped with a vaneless diffuser, which is located in our Laboratory at ETH Zurich. The maximum temperature range of the new probe is more than doubled compared to traditional FRAP probes. Therefore first ever time resolved measurements at the design point of our centrifugal compressor facility could be conducted by the novel miniature FRAP-HT probe.

The impeller is typical of that found in small-scale distributed power generation and automotive turbocharging applications. This scaled-up model matches the main design criteria and non-dimensional parameters that are typical of the small-scale devices, and also generates flow structures that are representative of those in small-scale compressors.

In order to increase the spanwise measurement range, a combined calibration approach with varying aerodynamic calibration coefficient definitions has been developed. The new aerodynamic calibration coefficients base on the FRAP-HT pitch hole as total pressure sensing tap and are applied to the same set of measurement data in the near hub area in order to increase the spanwise measurement range. By merging the data resulting from these two techniques, the spanwise measurement range is increased by around 17.6%, covering around 92% of the span.

Comparing the time-averaged results of the two different calibration approaches with each other as well as to the 4HP measurements, a very good agreement both, quantitatively, as well as qualitatively is observed. In terms of the flow angles, strong spatial (as well as temporal) variations in flow angles are measured near the shroud. This is related to boundary layer and wall proximity effects as well as strong secondary flow components due to tip leakage vortices. The rather small differences in terms of the time-resolved results are mainly related to interpolation uncertainties, polynomial model fit uncertainties, flow property dependent measurement sensitivities and to calibration range limitations of the new method, as well as due to probe wall

proximity effects and blockage effects.

The new approach therefore allows us to gain some useful insight in a significant part of the flow domain without the need of additional measurements from other probes and can therefore help to significantly reduce costs related to both rig operation hours, as well as measurement technique development.

The capability to measure the steady temperature by means of the FRAP-HT has been validated by comparing the results to steady temperature measurements obtained with a steady temperature probe (F0S-PT100-HT). Comparing the resulting temperatures for the same operating points showed differences of no more than 4K near the shroud and 0.9K for the rest of the measurement domain. The differences in the major part of the span are therefore well within the achievable accuracy in deriving the total temperatures by FRAP-HT. In terms of measurements at the design operating points, the differences between the two techniques were within 5K. A multiplicity of possible reasons for the variations between the measurement techniques has been discussed. Nevertheless, the general agreement particularly within the lower 50% of the span is very good and the differences are below 2K. Compared to the elevated absolute temperatures this agreement is good.

In addition to providing a further validation of the newly developed FRAP-HT, the objective of the measurements was to get some detailed time-resolved flow structure information of the impeller exit flow operated at the design speed. Some of the primary flow properties such as the flow angles and the total pressure coefficients are detailed. It is shown, that focusing on total pressure coefficient is insufficient to clearly indicate regions of elevated losses when high temperature flows with strong thermal gradients are involved. The focus was therefore to detail the velocity components in order to discuss the classical jet-wake model. Loss potential regions are detailed by the random part of total pressure since regions of high $P'_{tot,rms}$ are indicative of eddy shedding or regions of high turbulence.

In order to investigate the secondary flow patterns, a model is described to get all the three components of the vorticity. Based on the approach, and focusing on radial vorticity, the secondary flow patterns are detailed for FRAP-HT measurements at the design point of the impeller. Based on this, a secondary flow model for the performed measurements has been described, discussed and compared to one of the classical models discussed by Eckardt [136].

The successful measurements within the centrifugal compressor operated at design conditions confirm the highly three-dimensional nature of the impeller's exit flowfield, and the profound effect of the tip gap clearance.

From the measured FRAP-HT data, the aerodynamic stage efficiency for various measured operating points is derived. The discussion of the results involves an uncertainty analysis for the derived efficiencies.

The results show that the design point is not the same as the best point. Based on the results the best point is expected to be at a lower normalized corrected mass flow rate than the actual design point. In general, it is not uncommon that the location of the design point does not correspond with the best point, since the manufacturer provides a safety margin between the design point and the compressor stability limit. Furthermore, the calculated aerodynamic stage efficiency could be influenced by the general overestimate resulting from the performed averaging as well as by the radial measurement location where the FRAP-HT measurements are performed. The calculated efficiency is based on measurements downstream of the impeller but in the leading area of the vaneless diffuser. In terms of possible total pressure losses, though these are known to be more pronounced in case of vaned diffusers, the total-to-total efficiency for the complete stage could, operating point depending, vary slightly and therefore lead to an offset along the axis of corrected mass flow.

9 Conclusions and Outlook

9.1 Concluding Remarks

A novel high temperature fast response aerodynamic probe has been developed, built and tested. The FRAP-HT probe is based on the virtual 4-sensor probe measurement concept. The probe can be applied in flows with temperatures up to 533K (500°F) and can measure three dimensional and unsteady flows up to the cut-off frequency of 25 kHz, covering flow angles of ±24° in yaw and ±20° in pitch direction. Furthermore, the probe is able to measure the steady flow temperature.

The primary measurement elements that are used to derive the unsteady flow properties as well as the steady temperature are two piezoresistive pressure transducers. Additional temperature and strain gauge sensors are embedded in the probe's shaft to allow a much higher degree of robustness in the use of this probe. The additional temperature sensor in the shaft facilitates the thermal management of the probe. The strain gauge sensor is used to monitor probe shaft vibrations.

Entirely new packaging technology had to be developed to make possible the use of this probe at such high temperatures. Furthermore temperature related challenges related to the involved sensor technology, material science as well as signal conditioning and electrical connections have been addressed.

Probe thermal issues have been assessed using a conjugate heat transfer analysis. Moreover, factors influencing the accuracy of the flow temperature measurements, such as overheating and probe temperature recovery factors are detailed for the new developed probe. The results of the analysis show that self-heating effects are of minor impact. However, the overall accuracy of the resulting temperature measurements could be increased if a calibration of the recovery factor is performed at flow temperatures that match the temperatures in the intended application. A further improvement could be achieved by considering the yaw angle dependency of the recovery factor.

Extensive calibration and thermal cycling of the probe are used to quantify the accuracy and the robustness of the probe. The static sensor calibration is performed in a range between 313K and 533K in temperature steps of 5K. For temperatures below 473K, the results of the probe sensor calibration agrees quantitatively with the characteristic tests that are performed on single pressure transducers.

Above around 490K, though repeatable, non-linear effects due to a leakage current flowing from p-type silicon elements into the n-type diaphragm material of the transducers results in highly non-linear output voltages. The sensor calibration is therefore divided into a two temperature range window. Calibration coefficients could be derived for both windows. However, the accuracy of sensor calibration model for the upper window range is reduced due to the strong non-linear effects.

A probabilistic uncertainty evaluation method is applied to quantify the uncertainties related to the FRAP-HT measurement technique. The uncertainties are related to a temperature range up to ~473K. The range chosen for the investigation is in accordance to the range of all performed turbomachinery measurements and showed a satisfying range of expanded uncertainties compared to traditional measurement techniques. For the range between 473K and 533K, the expanded uncertainties have been estimated based on the polynomial uncertainties during sensor calibration. The uncertainties for the temperature measurements are expected to result in expanded uncertainties up to 6 times higher, compared to the lower temperature range area, whereas the uncertainties in the angle and pressure measurements are expected to contribute respectively up to 4 times, and 8 times higher expanded uncertainties compared to the lower temperature range uncertainties.

The probe eigenfrequencies for various probe tip to clamping distances has been determined experimentally and compared to an FEM modal analysis. The results are in good agreement. It is thus concluded, that the installed shaft strain gauge device provides accurate results and could be used in collaboration with an active damping device to counteract on potential probe shaft vibrations.

PROBE DESIGN VALIDATION

The probe's robustness and capability to provide steady temperature and high frequency flow measurements in harsh environments is demonstrated within the flow of a hot streak generator that is installed in the axial 1.5 stage turbine facility, LISA. The combination of this high work aero-engine and hot gas spots leads to sharp temperature gradients within the flow and to interactions with the blade row pressure gradients and secondary flows and therefore presents an ideal scenario to verify the probe's ability to measure under real conditions.

A comparison between measurements using the newly developed high temperature probe against various well-established steady and unsteady measurement techniques is performed in LISA. Agreement between all the techniques has been found and therefore the new probe concept was proven to be applicable. The minor variations between the results for the different probe techniques might be related to combinations of different effects such as, wall proximity effects, blockage effects due to the difference in the probe diameter and relative sensor position, high total pressure gradients near the endwalls and a lower signal-to-noise ratio of the standard FRAP for elevated flow temperatures compared to the new FRAP-HT.

Moreover, the novel high temperature Fast Response Aerodynamic Probe (FRAP-HT) is applied in the single stage, centrifugal compressor facility equipped with a vaneless diffuser, which is located in our Laboratory at ETH Zurich. This allows a further validation of the new probe. Moreover, the maximum temperature range of the new probe is more than doubled compared to traditional FRAP probes. Therefore the first ever time resolved measurements at the design point of our centrifugal compressor facility could be obtained using the novel miniature FRAP-HT probe.

In order to increase the spanwise measurement range of the FRAP-HT probe applied in RIGI, a combined calibration approach with varying aerodynamic calibration coefficient definitions has been developed. The new aerodynamic calibration coefficients are based on the FRAP-HT pitch hole as total pressure sensing tap and are applied to the same set of measurement data in the near hub area in order to increase the spanwise measurement range. By merging the data resulting from these two techniques, the spanwise measurement range is increased by around 17.6%, covering around 92% of the span.

Comparing the time-averaged results of the two different calibration approaches with each other as well as to the 4HP measurements, a very good agreement both, quantitatively, as well as qualitatively is observed. In terms of the flow angles, strong spatial (as well as temporal) variations in flow angles are measured near the shroud. This is related to boundary layer and wall proximity effects as well as related to strong secondary flow components due to tip leakage vortices.

The rather small differences in terms of the time-resolved results are mainly related to interpolation uncertainties, polynomial model fit uncertainties, flow property dependent measurement sensitivities and to calibration range limitations of the new method, as well as due to probe wall proximity effects

and blockage effects.

The new approach therefore allows one to gain some fruitful insight in a significant part of the flow domain without the need of additional measurements from other probes and can therefore help to significantly reduce costs related to both rig operation hours, as well as measurement technique development.

The capability to measure the steady temperature by means of the FRAP-HT has been validated by comparing the results to steady temperature measurements obtained with a steady temperature probe (F0S-PT100-HT). Comparing the resulting temperatures for the same operating points showed differences of no more than 4K near the shroud and 0.9K for the rest of the measurement domain. The differences in the major part of the span are therefore well within the achievable accuracy in deriving the total temperatures by FRAP-HT.

In terms of measurements at the design operating points, the differences between the two techniques were within 5K. Possible reasons for the variations between the measurement techniques are related to the calibration of the probe temperature recovery factor as well as due to differences in the respective sensor surface area involved in the temperature sensing process for the respective probes. Nevertheless, the general agreement particularly within the lower 50% of the span is very good and the differences are below 2K. Compared to the elevated absolute temperatures this is a good agreement.

CONCLUDING REMARKS REGARDING HOT STREAK RELATED TOPICS

The steady hot streak inlet conditions show equal HS core temperatures compared to the temperatures at the injection plane. The trends of the hot jet dissipation and the entrainment of the cold flow by the jet are shown by the reduced gradients at the HS boundary area upstream of the first stator.

In terms of the unsteady flow analysis, the Munk and Prim principle [111], stating that the HS does not affect the secondary flows at the vane exit, is verified for the measurements performed. The flow analysis at the rotor exit further shows the interactions between the HS-related thermally driven effects and the unsteady flow. Kerrebrock and Mikolajc [122] observed the migration of the hot gases toward the rotor pressure side and subsequently toward the endwalls. These effects are identified and visualized in the FRAP-HT measurements by time resolved area plots of the turbulent fluctuating part of the total pressure.

Concluding Remarks related to Measurements in the Centrifugal Compressor Facility

In addition to providing a further validation of the newly developed FRAP-HT, the objective of the measurements in RIGI focused on getting some detailed time-resolved flow structure information of the impeller exit flow operated at the design speed.

The measurements show, that focusing on the total pressure coefficient is insufficient to clearly indicate regions of elevated losses when high temperature flows with strong thermal gradients are involved. The focus was therefore to detail the velocity components in order to discuss the classical jet-wake model. Loss potential regions are detailed by the random part of total pressure since regions of high $P'_{tot,rms}$ are indicative of eddy shedding or regions of high turbulence.

In order to investigate on the secondary flow patterns, a model is described to get all the three components of the vorticity. Based on the approach, and focusing on radial vorticity, the secondary flow patterns are detailed for FRAP-HT measurements at the design point of the impeller. Based on that, a secondary flow model for the performed measurements has been described, discussed and compared to one of the classical models discussed by Eckardt [136].

The successful measurements within the centrifugal compressor operated at design conditions confirm the highly three-dimensional nature of the impeller's exit flowfield, and the profound effect of the tip gap clearance.

From the measured FRAP-HT data, the aerodynamic stage efficiency for various measured operating points has been derived. The discussion of the results involves an uncertainty analysis for the derived efficiencies. The results show that the design point is not the same as the best point. Based on the results the best point is expected to be at a lower normalized corrected mass flow rate than the actual design point. In general, it is not uncommon that the location of the design point does not correspond with the best point, since the manufacturer provides a safety margin between the design point and the compressor stability limit. Furthermore, the calculated aerodynamic stage efficiency could be influenced by the general overestimate resulting from the performed averaging as well as by the radial measurement location where the FRAP-HT measurements are performed. The calculated efficiency is based on measurements downstream of the impeller but in the leading area of the vaneless diffuser. In terms of possible total pressure losses, though these are

known to be more pronounced in case of vaned diffusers, the total-to-total efficiency for the complete stage could, operating point depending, vary slightly and therefore lead to an offset along the axis of the corrected mass flow.

POTENTIAL OF FRAP-HT

The probe's robustness and capability to provide steady temperature and high frequency flow measurements in harsh environments is demonstrated from the measurements in the two turbomachinery facilities. With this probe it is now possible to conduct measurements in real turbomachinery applications, such as at the exit of axial compressors as well as in a wide spectrum of centrifugal compressors. Major challenges related to topics such as sensor technology, signal conditioning, material science, packaging technology as well as electrical connections had to be addressed. Furthermore a much higher degree of robustness in the use of this probe is achieved due to additional temperature and strain gauge sensors that are embedded in the shaft.

The probe therefore is a major contribution both for the turbomachinery community as well as for future developments of unsteady probe technology.

9.2   Future Work

The results of this study have shown the potential of the developed high temperature FRAP probe. Nevertheless some suggestions for future work are given. These suggestions are split into two topics. The first is related to possible developments for the existing FRAP-HT in order to further increase the quality and value of the measurement system. The second topic focuses more on suggestions for alternative approaches in order to possibly perform unsteady flow measurements at even higher temperatures.

The FRAP-HT probe shows good measurement resolution and low uncertainties in measuring the primary flow properties in an unsteady manner. However, the quality of the resulting steady flow temperature measurements could be further improved by calibrating for a temperature recovery factor at elevated flow temperatures. Moreover, the accuracy of the resulting flow temperature could be improved, by calibrating the recovery factor as a function of the angle of attack.

In order to gain more detailed information about the probe internal heat processes, it is suggested to install an additional steady temperature sensing

element (PT100) as close as possible to the piezo-resistive pressure transducers. Though being challenging due to space limitations and signal conditioning issues within the probe tip shaft, it would allow for a simplified heat management of the current probe.

Last but not least, the value and robustness of the detailed FRAP-HT could be even more enhanced, by integrating an active damping device into the probe, such that possible probe vibrations are damped in real time and in an automated manner without requiring any user inputs.

A continual focus for intrusive measurement techniques is further miniaturization in order to reduce the measurement errors that are induced due to blockage effects. A suggestion for future work is therefore related to the size of the current FRAP-HT probe. With the current sensors used for the FRAP-HT probe, a further reduction in probe tip diameter is not possible. Since the MEMS market is still growing and a lot of substantial progress has been achieved in material science for high temperature resistant semiconductors in recent years, the range of available sensors is expected to broaden over the next years. It is therefore possible that silicon-on-insulator, or even silicon-on-sapphire based piezo-resistive transducers of reduced dimensions will be available in near future. This would also reduce the issue of the non-linear sensor characteristic due to leakage current flowing from p-type silicon elements into the n-type diaphragm material.

With the FRAP-HT probe we reached a current manufacturing limit. This is due to the temperature limitations of several subcomponents, such as the components used for signal conditioning the transducers or the materials involved in the transducer assembly procedure. Targeting unsteady flow measurements in turbomachinery applications at even more elevated temperatures than 533K would therefore require completely different methods of approach. One possible workaround is based on the idea of using an optical method to detect vibrations of a membrane encapsulated in a probe tip. In this case, the membrane could for instance be fusion bonded into the tip. Silicone RTV's, shown to be one of the most critical components in terms of high operating temperatures, would not be required in such a case. A light source could be guided onto the membrane surface where it is reflected by the membrane surface. The unsteady flow fluctuations could therefore be monitored by measuring the variation in the light intensity of the reflected source. Such a system would not require any electrical components within the hot probe tip area and would therefore allow the use of the system at even higher flow temperatures.

Appendix

238

A   Bibliography

[1]   Rolls-Royce (Derby), 1996, The Jet Engine, The Technical Publications Department Rolls-Royce, Derby, England.

[2]   Denton, J. D., 1993, "The 1993 IGTI Scholar Lecture - Loss Mechanisms in Turbomachines," Journal of Turbomachinery-Transactions of the ASME, 115(4), pp. 621-656.

[3]   Sharma, O. P., Pickett, G. F., and Ni, R. H., 1992, "Assessment of Unsteady Flows in Turbines," Journal of Turbomachinery-Transactions of the ASME, 114(1), pp. 79-90.

[4]   Doorly, D., 1988, "Modeling the Unsteady Flow in a Turbine Rotor Passage," Journal of Turbomachinery, 110(1), pp. 27-37.

[5]   Lakshminarayana, B., 1996, Fluid Dynamics and Heat Transfer of Turbomachinery, Wiley, New York [etc.].

[6]   Ainsworth, R. W., Miller, R. J., Moss, R. W., and Thorpe, S. J., 2000, "Unsteady Pressure Measurement," Measurement Science and Technology, 11(7), pp. 1055-1076.

[7]   Kupferschmied, P., Koppel, P., Gizzi, W., Roduner, C., and Gyarmathy, G., 2000, "Time-Resolved Flow Measurements with Fast-Response Aerodynamic Probes in Turbomachines," Measurement Science and Technology, 11(7), pp. 1036-1054.

[8]   Sieverding, C. H., Arts, T., Denos, R., and Brouckaert, J. F., 2000, "Measurement Techniques for Unsteady Flows in Turbomachines," Experiments in Fluids, 28(4), pp. 285-321.

[9]   Rohlik, H., 1983, Current and Future Technology in Radial and Axial Gas Turbines, National Aeronautics and Space Administration, [Washington, D.C.].

[10]   Hauser, C., Haas, J., Reid, L., and Stepka, F., 1979, "Turbomachinery Technology," Aeropropulsion (SEE N 80-10205 01-07), pp. 231-272.

[11]   Tanaka, H., 1983, "A Survey on Gas Turbine Technology and Research Work in Japan," Proceedings of the International Gas Turbine Congress, 1, pp. 1-17.

[12]   Swihart, J., 1987, "U. S. Aeronautical R & D Goals- Sst: Bridge to the Next Century," 8th International Symposium on Air Breathing Engines, pp. 55-65.

[13]   Rosen, R., and Facey, J., 1987, "Civil Propulsion Technology for the Next Twenty-Five Years," 8th International Symposium on Air

Breathing Engines pp. 3-13.

[14] Cook, S. C. P., 1989, "The Development of a High Response Aerodynamic Wedge Probe and Use on a High-Speed Research Compressor," 9th International Symposium on Air Breathing Engines.

[15] Epstein, A. H., 1985, "High Frequency Response Measurements in Turbomachines," Measurement Techniques in Turbomachines: Von Karman Institute Lectures Series, Von Karman Institute, Belgium.

[16] Heneka, A., 1983, "Entwicklung und Erprobung einer Keilsonde für Instationäre Dreidimensionale Strömungsmessungen in Turbomaschinen," University of Stuttgart, Stuttgart, Germany.

[17] Kerrebrock, J., Epstein, A., and Thompkins Jr, W., 1980, "A Miniature High Frequency Sphere Probe," In Proceedings of ASME Symposium in Measurement Methods in Rotating Components of Turbomachinery pp. 91-97.

[18] Kupferschmied, P., Koppel, P., Roduner, C., and Gyarmathy, G., 2000, "On the Development and Application of the Fast-Response Aerodynamic Probe System in Turbomachines---Part 1: The Measurement System," Journal of Turbomachinery, 122(3), pp. 505-516.

[19] Larguier, R., 1981, "Experimental-Analysis Methods for Unsteady Flows in Turbomachines," Journal of Engineering for Power-Transactions of the ASME, 103(2), pp. 415-423.

[20] Gossweiler, C. R., Kupferschmied, P., and Gyarmathy, G., 1995, "On Fast-Response Probes. Part 1: Technology, Calibration, and Application to Turbomachinery," Journal of Turbomachinery, 117(4), pp. 611-617.

[21] Humm, H. J., Gossweiler, C. R., and Gyarmathy, G., 1995, "On Fast-Response Probes: Part 2: Aerodynamic Probe Design Studies," Journal of Turbomachinery, 117(4), pp. 618-624.

[22] Lisec, T., Kreutzer, M., and Wagner, B., 1996, "Surface Micromachined Piezoresistive Pressure Sensors with Step-Type Bent and Flat Membrane Structures," IEEE Transactions on Electron Devices, 43(9), pp. 1547-1552.

[23] Takeishi, K., Matsuura, M., Aoki, S., and Sato, T., 1990, "An Experimental-Study of Heat-Transfer and Film Cooling on Low Aspect Ratio Turbine Nozzles," Journal of Turbomachinery-Transactions of the ASME, 112(3), pp. 488-496.

[24] Bruun, H. H., 1996, Hot-Wire Anemometry Principles and Signal Analysis, Oxford University Press, Oxford [etc.].

[25] Pompeo, L. P., 1992, "An Experimental Study of Three-Dimensional Turbulent Boundary Layers," Ph.D. thesis, ETH Zürich, Nr. 9780, Zürich.

[26] Bremhorst, K., and Graham, L. J. W., 1990, "A Fully Compensated Hot Cold Wire Anemometer System for Unsteady-Flow Velocity and Temperature-Measurements," Measurement Science & Technology, 1(5), pp. 425-430.

[27] Ng, W. F., and Epstein, A. H., 1983, "High-Frequency Temperature and Pressure Probe for Unsteady Compressible Flows," Review of Scientific Instruments, 54(12), pp. 1678-1683.

[28] Durst, F., Ernst, F., and Volklein, J., 1987, "Laser-Doppler System for Local Velocity-Measurement in Wind Tunnels - System-Design and Experimental-Verification," Zeitschrift fur Flugwissenschaften und Weltraumforschung, 11(2), pp. 61-70.

[29] Fagan, J. R., and Fleeter, S., 1994, "L2F and LDV Velocimetry Measurement and Analysis of the 3-D Flow-Field in a Centrifugal-Compressor," International Journal of Turbo & Jet-Engines, 11(1), pp. 83-97.

[30] Schodl, R., 1980, "A Laser-2-Focus (L2F) Velocimeter for Automatic Flow Vector Measurements in the Rotating Components of Turbomachines," Journal of Fluids Engineering-Transactions of the ASME, 102(4), pp. 412-419.

[31] Hinsch, K. D., and Herrmann, S. F., 2004, "Holographic Particle Image Velocimetry," Measurement Science & Technology, 15(4).

[32] Schröder, A., 2008, Particle Image Velocimetry New Developments and Recent Applications, Springer, Berlin.

[33] Settles, G. S., 2001, Schlieren and Shadowgraph Techniques Visualizing Phenomena in Transparent Media, Springer, Berlin.

[34] Bryer, D. W., and Pankhurst, R. C., 1971, Pressure-Probe Methods for Determining Wind Speed and Flow Direction, Her Majesty's Stationery Office, London.

[35] Chue, S. H., 1975, "Pressure Probes for Fluid Measurement," Progress in Aerospace Sciences, 16(2), pp. 147-223.

[36] Laguier, R., and Ruyer, C., 1972, "Méthode d'analyse expérimentale de l'ecoulement instationnaire dans un compresseur aéronautique transsonique," La Recherche Aérospatial, 6, pp. 353-356.

[37] Senoo, Y., Kita, Y., and Ookuma, K., 1973, "Measurement of 2-

Dimensional Periodic Flow with a Cobra Probe," Journal of Fluids Engineering-Transactions of the ASME, 95(2), pp. 295-300.

[38] Matsunaga, S., Ishibashi, H., and Nishi, M., 1980, "Measurement of Instantaneous Pressure and Velocity in Nonsteady 3-Dimensional Water-Flow by Means of a Combined 5-Hole Probe," Journal of Fluids Engineering-Transactions of the ASME, 102(2), pp. 196-202.

[39] Gossweiler, C. R., 1993, "Sonden und Messsystem für schnelle aerodynamische Strömungsmessung mit Piezoresistiven Druckgebern," Ph.D. thesis, ETH Zürich, Nr. 10253, Zürich.

[40] Kupferschmied, P., 1998, "Zur Methodik zeitaufgelöster Messungen mit Strömungssonden in Verdichtern und Turbinen," Ph.D. thesis, ETH Zürich, Nr. 12774, Zürich.

[41] Roduner, C., Kupferschmied, P., Köppel, P., and Gyarmathy, G., 2000, "On the Development and Application of the Fast-Response Aerodynamic Probe System in Turbomachines---Part 2: Flow, Surge, and Stall in a Centrifugal Compressor," Journal of Turbomachinery, 122(3), pp. 517-526.

[42] Pfau, A., 2003, "Loss Mechanisms in Labyrinth Seals of Shrouded Axial Turbines," Ph.D. thesis, ETH Zürich, Nr. 15226, Zürich.

[43] Porreca, L., Hollenstein, M., Kalfas, A. I., and Abhari, R. S., 2007, "Turbulence Measurements and Analysis in a Multistage Axial Turbine," Journal of Propulsion and Power, 23(1), pp. 227-234.

[44] Persico, G., Gaetani, P., and Guardone, A., 2005, "Design and Analysis of New Concept Fast-Response Pressure Probes," Measurement Science & Technology, 16(9), pp. 1741-1750.

[45] Ainsworth, R. W., Allen, J. L., and Batt, J. J. M., 1995, "The Development of Fast Response Aerodynamic Probes for Flow Measurements in Turbomachinery," Journal of Turbomachinery, 117(4), pp. 625-634.

[46] Binder, A., and Romey, R., 1983, "Secondary Flow Effects and Mixing of the Wake Behind a Turbine Stator," Journal of Engineering for Power-Transactions of the ASME, 105(1), pp. 40-46.

[47] Schlienger, J., Kalfas, A. I., and Abhari, R. S., 2005, "Vortex-Wake-Blade Interaction in a Shrouded Axial Turbine," Journal of Turbomachinery, 127(4), pp. 699-707.

[48] Smith, C. S., 1954, "Piezoresistance Effect in Germanium and Silicon," Physical Review, 94(1), p. 42.

[49] Pfann, W. G., and Thurston, R. N., 1961, "Semiconducting Stress Transducers Utilizing Transverse and Shear Piezoresistance Effects," Journal of Applied Physics, 32(10), pp. 2008-2019.

[50] Tufte, O. N., Long, D., and Chapman, P. W., 1962, "Silicon Diffused-Element Piezoresistive Diaphragms," Journal of Applied Physics, 33(11), pp. 3322-3327.

[51] Kovacs, G. T. A., 1998, Micromachined Transducers Sourcebook, Wcb, Boston.

[52] Madou, M., 1997, Fundamentals of Microfabrication, CRC Press, Boca Raton, FL [etc.].

[53] Madou, M. J., 2002, Fundamentals of Microfabrication the Science of Miniaturization, CRC Press, Boca Raton, FL.

[54] Maluf, N., and Williams, K., 2004, An Introduction to Microelectromechanical Systems Engineering, Artech House, Boston.

[55] Menz, W., Mohr, J., and Paul, O., 2001, Microsystem Technology, Wiley-VCH, Weinheim.

[56] Chih-Tang, S., Noyce, R. N., and Shockley, W., 1957, "Carrier Generation and Recombination in P-N Junctions and P-N Junction Characteristics," Proceedings of the IRE, 45(9), pp. 1228-1243.

[57] Codreanu, C., Avram, M., Obreja, V., Voitincu, C., and Codreanu, I., 2003, "Interface States and Related Surface Currents in Sic Junctions," 2003 International Semiconductor Conference, Vols 1 and 2, Proceedings, pp. 297-300, 410.

[58] Josan, I., Boianceanu, C., Brezeanu, G., Obreja, V., Avram, M., Puscasu, D., and Ioncea, A., 2009, "Extreme Environment Temperature Sensor Based on Silicon Carbide Schottky Diode," Cas: 2009 International Semiconductor Conference, Vols 1 and 2, Proceedings, pp. 525-528, 564.

[59] Obreja, V., Manea, E., Codreanu, C., Avram, M., and Podaru, C., 2005, "The Junction Edge Leakage Current and the Blocking I-V Characteristics of Commercial Glass Passivated Thyristor Devices," Cas 2005: International Semiconductor Conference Vol 1 and 2, pp. 447-450, 478.

[60] Obreja, V. V. N., and Obreja, A. C., 2010, "Activation Energy Values from the Temperature Dependence of Silicon Pn Junction Reverse Current and Its Origin," Physica Status Solidi (a), 207(5), pp. 1252-1256.

[61]   Mehregany, M., and Zorman, C. A., 1999, "Sic Mems: Opportunities and Challenges for Applications in Harsh Environments," Thin Solid Films, 356, pp. 518-524.

[62]   Mehregany, M., Zorman, C. A., Rajan, N., and Wu, C. H., 1998, "Silicon Carbide MEMS for Harsh Environments," Proceedings of the IEEE, 86(8), pp. 1594-1610.

[63]   Ned, A. A., Kurtz, A. D., Beheim, G., Masheeb, F., and Stefanescu, S., 2004, "Improved Sic Leadless Pressure Sensors for High Temperature, Low and High Pressure Applications," I. Kulite Semiconductor Products, eds., Lexington, Maryland.

[64]   Okojie, R. S., Ned, A. A., and Kurtz, A. D., 1997, "Operation of Alpha(6h)-Sic Pressure Sensor at 500 Degrees C," Transducers 97 - 1997 International Conference on Solid-State Sensors and Actuators, Digest of Technical Papers, Vols 1 and 2, pp. 1407-1409.

[65]   Okojie, R. S., Ned, A. A., and Kurtz, A. D., 1998, "Operation of Alpha(Gh)-Sic Pressure Sensor at 500 Degrees C," Sensors and Actuators a-Physical, 66(1-3), pp. 200-204.

[66]   Cristoloveanu, S., 1987, "Silicon Films on Sapphire," Reports on Progress in Physics, 50(3), pp. 327-371.

[67]   Cristoloveanu, S., and Li, S. S., 1995, Electrical Characterization of Silicon-on-Insulator Materials and Devices, Kluwer Academic Publ., Boston [etc.].

[68]   Hefyene, N., Cristoloveanu, S., Ghibaudo, G., Gentil, P., Moriyasu, Y., Morishita, T., Matsui, M., and Yasujima, A., 2000, "Adaptation of the Pseudo-Mos Transistor for the Characterization of Silicon-on-Sapphire Films," Solid-State Electronics, 44(10), pp. 1711-1715.

[69]   Pretet, J., Cristoloveanu, S., Hefyene, N., Matsui, M., Moriyasu, Y., and Kawakami, Y., 2001, "Electrical Evaluation of Innovating Processes for Improving Sos Materials," Microelectronic Engineering, 59(1-4), pp. 443-448.

[70]   Drack, H., and Ainouz, L., 1996, "Gold Bonding Wire Properties and Their Influence on Ball Bonding," Microelectronics Journal, 27(8), pp. R19-R22.

[71]   Krzanowski, J. E., and Murdeshwar, N., 1990, "Deformation and Bonding Processes in Aluminum Ultrasonic Wire Wedge Bonding," Journal of Electronic Materials, 19(9), pp. 919-928.

[72]   Chen, G. K. C., 1967, "On Physics of Purple-Plague Formation and

Observation of Purple Plague in Ultrasonically-Joined Gold-Aluminum Bonds," IEEE Transactions on Parts Materials and Packaging, Pmp 3(4), pp. 149-153.

[73] Footner, P. K., Richards, B. P., and Yates, R. B., 1986, "Purple Plague - Eliminated or Just Forgotten," Gec Journal of Research, 4(3), pp. 174-180.

[74] Horsting, C. W., 1972, "Purple Plague and Gold Purity," eds., pp. 155-158.

[75] Selikson, B., and Longo, T. A., 1964, "Study of Purple Plague + Its Role in Integrated Circuits," Proceedings of the IEEE, 52(12), pp. 1638-1641.

[76] Wilson, J., 1987, "Purple Plague Is Back," Electronics & Wireless World, 93(1613), pp. 308-308.

[77] Philofsky, E., 1970, "Intermetallic Formation in Gold-Aluminum Systems," Solid State Electronics, 13, pp. 1391-1394.

[78] Philofsky, E., 1971, "Design Limits When Using Gold-Aluminum Bonds," eds., pp. 114-119.

[79] Philofsky, E., 1970, "Purple Plague Revisited," eds., pp. 177-185.

[80] Bolger, J. C., and Mooney, C. T., 1984, "Die Attach in Hi-Rel P-Dips: Polyimides or Low Chloride Epoxies?," IEEE transactions on components, hybrids, and manufacturing technology, 7(4), pp. 394-398.

[81] Pfau, A., Schlienger, J., Kalfas, A. I., and Abhari, R. S., 2003, "Unsteady, 3-Dimensional Flow Measurement Using a Miniature Virtual 4 Sensor Fast Response Aerodynamic Probe (FRAP)," eds., Atlanta, Georgia, Paper No. GT2003-38128.

[82] Köppel, P. D., 2000, "Instationäre Strömung in Turbomaschinen Analyse Zeitabhängiger Sondenmessungen," Ph.D. thesis, ETH Zürich, Nr.13500, Zürich.

[83] Johansen, E. S., and Rediniotis, O. K., 2002, "Development of Unsteady Calibration Facilities and Techniques for Fast-Response Pressure Probes," AIAA, eds., Reno, NV, AIAA-2002-689.

[84] Bohn, D., and Simon, H., 1975, "Mehrparametrige Approximation der Eichraeume und Eichflaechen von Unterschall- und Ueberschall-5-Loch-Sonden," ATM Messtechnische Praxis, Germany.

[85] Harris, C. M., 2002, Harris' Shock and Vibration Handbook, McGraw-Hill, New York.

[86] Incropera, F. P., 2007, Fundamentals of Heat and Mass Transfer, Wiley,

Hoboken, N.J.

[87] Roduner, C. H., 1999, "Strömungsstrukturen in Radialverdichtern, Untersucht mit schnellen Sonden," Ph.D. thesis, ETH Zürich, Nr. 13428, Zürich.

[88] Nag, P. K., 2005, Engineering Thermodynamics, Tata McGraw-Hill, Dedicated Website: http://mhhe.com/nae/et.

[89] Cumpsty, N. A., and Horlock, J. H., 2006, "Averaging Nonuniform Flow for a Purpose," Journal of Turbomachinery-Transactions of the ASME, 128(1), pp. 120-129.

[90] Bendat, J. S., and Piersol, A. G., 1986, Random Data Analysis and Measurement Procedures, Wiley, New York. USA.

[91] Schlienger, J. P., 2003, "Evolution of Unsteady Secondary Flows in a Multistage Shrouded Axial Turbine," Ph.D. thesis, ETH Zürich, Nr. 15230, Zürich.

[92] Franken, A. R. C., and Ivey, P., 2002, "Reducing Aero-Engine Development Time and Costs by Using Artificial Intelligence," eds., St. Louis, Missouri, AIAA-2002-3251.

[93] Lenherr, C., Oschwald, M., Kalfas, A. I., and Abhari, R. S., 2004, "Flow Adaptive Aerodynamic Probe for Turbomachinery Flows," eds., Stockholm, Sweden.

[94] Behr, T., Porreca, L., Mokulys, T., Kalfas, A. I., and Abhari, R. S., 2006, "Multistage Aspects and Unsteady Effects of Stator and Rotor Clocking in an Axial Turbine with Low Aspect Ratio Blading," Journal of Turbomachinery-Transactions of the ASME, 128(1), pp. 11-22.

[95] Thompson, J., Soni, B., and Weatherill, N., 1999, Handbook of Grid Generation, CRC.

[96] Kalfas, A. I., and Elder, R. L., 1995, "Determination of the Intermittency Distribution in the Boundary Layer of a Flat Plate with C4 Leading Edge," ERCOFTAC Bulletin No 24 on Transition, 24, pp. 65-67.

[97] Treiber, M., Kupferschmied, P., and Gyarmathy, G., 1998, "Analysis of the Error Propagation Arising from Measurements with a Miniature Pneumatic 5-Hole Probe," eds., Limerick, Ireland.

[98] Schlienger, J., Pfau, A., Kalfas, A. I., and Abhari, R. S., 2002, "Single Pressure Transducer Probe for 3D Flow Measurements," eds., Cambridge, UK.

[99] Treaster, A. L., and Yocum, A. M., 1979, "Calibration and Application of 5-Hole Probes," ISA Transactions, 18(3), pp. 23-34.

[100] Pisasale, A. J., and Ahmed, N. A., 2002, "Theoretical Calibration for Highly Three-Dimensional Low-Speed Flows of a Five-Hole Probe," Measurement Science & Technology, 13(7), pp. 1100-1107.

[101] Tanaka, K., Kalfas, A. I., and Hodson, H. P., 2000, "Development of Single Sensor Fast Response Pressure Probes," eds., Florence, Italy.

[102] Arts, T., Boerrigter, H., Carbonaro, M., Charbonnier, J., Degrez, G., Olivari, D., Riethmuller, M., and Van Den Braembussche, R., 2001, "Measurement Techniques in Fluid Dynamics," Von Karman Institute for Fluid Dynamics, Brussels, Belgium.

[103] Dudzinski, T., and Krause, L., 1969, "Flow-Direction Measurement with Fixed-Position Probes," NASA TM X-1904.

[104] Behr, T., Kalfas, A. I., and Abhari, R. S., 2007, "Unsteady Flow Physics and Performance of a One-and-1/2-Stage Unshrouded High Work Turbine," Journal of Turbomachinery, 129(2), pp. 348-359.

[105] Schuepbach, P., Abhari, R. S., Rose, M. G., Germain, T., Raab, I., and Gier, J., 2008, "Improving Efficiency of a High Work Turbine Using Non-Axisymmetric Endwalls. Part II: Time-Resolved Flow Physics," Proceedings of the ASME Turbo Expo 2008, Vol 6, Pt A, pp. 1121-1133.

[106] Schuepbach, P., Abhari, R. S., Rose, M. G., Germain, T., Raab, I., and Gier, J., 2008, "Effects of Suction and Injection Purge-Flow on the Secondary Flow Structures of a High-Work Turbine," Proceedings of the ASME Turbo Expo 2008, Vol 6, Pt A, pp. 1135-1145.

[107] ANSI/ASME PTC 19.1-1985, Supplement to Performance Test Coded, Instruments and Apparatus. Part 1-Measurement Uncertainty, The American Society of Mechanical Engineers, New York.

[108] 1995, ISO: Guide to the Expression of Uncertainty in Measurement (Gum), 1st edition, 1993, corrected and reprinted 1995, International Organisation for Standardisation Geneva, Switzerland.

[109] Behr, T., 2007, "Control of Rotor Tip Leakage and Secondary Flow by Casing Air Injection in Unshrouded Axial Turbines," Ph.D. thesis, ETH Zürich, Nr. 17283, Zurich.

[110] Winternitz, F., and Ing, D., 1952, "Probe Measurements in Three-Dimensional Flow," Trans. Amer. Soc. Mech. Engrs, 74, pp. 1327-1336.

[111] Munk, M., and Prim, R., 1947, "On the Multiplicity of Steady Gas Flows Having the Same Streamline Pattern," Proceedings of the National Academy of Sciences of the United States of America, 33(5), pp. 137-141.

[112] Hermanson, K. S., and Thole, K. A., 2000, "Effect of Inlet Conditions on Endwall Secondary Flows," Journal of Propulsion and Power, 16(2), pp. 286-296.

[113] Barringer, M. D., Thole, K. A., Polanka, M. D., Clark, J. P., and Koch, P. J., 2009, "Migration of Combustor Exit Profiles through High Pressure Turbine Vanes," Journal of Turbomachinery-Transactions of the ASME, 131(2), p. 021010-10.

[114] Povey, T., Chana, K. S., Jones, T. V., and Hurrion, J., 2007, "The Effect of Hot-Streaks on Hp Vane Surface and Endwall Heat Transfer: An Experimental and Numerical Study," Journal of Turbomachinery-Transactions of the ASME, 129(1), pp. 32-43.

[115] Barringer, M. D., Thole, K. A., and Polanka, M. D., 2009, "An Experimental Study of Combustor Exit Profile Shapes on Endwall Heat Transfer in High Pressure Turbine Vanes," Journal of Turbomachinery-Transactions of the ASME, 131(2), p. 021009-10.

[116] Jenkins, S., Varadarajan, K., and Bogard, D. G., 2004, "The Effects of High Mainstream Turbulence and Turbine Vane Film Cooling on the Dispersion of a Simulated Hot Streak," Journal of Turbomachinery-Transactions of the ASME, 126(1), pp. 203-211.

[117] Butler, T. L., Sharma, O. P., Joslyn, H. D., and Dring, R. P., 1989, "Redistribution of an Inlet Temperature Distortion in an Axial-Flow Turbine Stage," Journal of Propulsion and Power, 5(1), pp. 64-71.

[118] Roback, R. J., and Dring, R. P., 1993, "Hot Streaks and Phantom Cooling in a Turbine Rotor Passage. 1. Separate Effects," Journal of Turbomachinery-Transactions of the ASME, 115(4), pp. 657-666.

[119] Roback, R. J., and Dring, R. P., 1993, "Hot Streaks and Phantom Cooling in a Turbine Rotor Passage. 2. Combined Effects and Analytical Modeling," Journal of Turbomachinery-Transactions of the ASME, 115(4), pp. 667-674.

[120] Dorney, D. J., Davis, R. L., Edwards, D. E., and Madavan, N. K., 1992, "Unsteady Analysis of Hot Streak Migration in a Turbine Stage," Journal of Propulsion and Power, 8(2), pp. 520-529.

[121] Rai, M. M., and Dring, R. P., 1990, "Navier-Stokes Analyses of the Redistribution of Inlet Temperature Distortions in a Turbine," Journal of Propulsion and Power, 6(3), pp. 276-282.

[122] Kerrebrock, J., and Mikolajc, A., 1970, "Intra-Stator Transport of Rotor Wakes and Its Effect on Compressor Performance," Journal of

Engineering for Power, 92(4), pp. 359-368.

[123] Dunn, M. G., 2001, "Convective Heat Transfer and Aerodynamics in Axial Flow Turbines," Journal of Turbomachinery-Transactions of the ASME, 123(4), pp. 637-686.

[124] Ong, J., and Miller, R., 2008, "Hot Streak and Vane Coolant Migration in a Downstream Rotor," Proceedings of the ASME Turbo Expo 2008, GT2008-50971, Berlin, Germany.

[125] An, B.-T., Liu, J.-J., and Jiang, H.-D., 2009, "Combined Unsteady Effects of Hot Streak and Trailing Edge Coolant Ejection in a Turbine Stage," Proceedings of the ASME Turbo Expo 2009, GT2009-59473, Orlando, Florida, USA pp. 433-444.

[126] Jenny, P., Lenherr, C., Kalfas, A. I., and Abhari, R. S., 2010, "Effect of Unsteady Blade Row Interaction on Hot Streak Migration in an Axial Turbine," Proceedings of the ASME Turbo Expo 2010, GT2010-23034, Glasgow, UK.

[127] Basol, A. M., Jenny, P., Ibrahim, M., Kalfas, A. I., and Abhari, R. S., 2010, "Hot Streak Migration in a Turbine Stage: Integrated Design to Improve Aero-Thermal Performance," Proceedings of the ASME Turbo Expo 2010, GT2010-23556, Glasgow, UK.

[128] Sell, M., Schlienger, J., Pfau, A., Treiber, M., and Abhari, R., 2001, "The 2-Stage Axial Turbine Test Facility Lisa," Proceedings of the ASME Turbo Expo 2001, 2001-GT-0492, New Orleans, USA.

[129] Came, P. M., and Robinson, C. J., 1999, "Centrifugal Compressor Design," Proceedings of the Institution of Mechanical Engineers Part C-Journal of Mechanical Engineering Science, 213(2), pp. 139-155.

[130] Dean, R., and Senoo, Y., 1960, "Rotating Wakes in Vaneless Diffusers," ASME Journal of Basic Engineering, 82(3), pp. 563-574.

[131] Eckardt, D., 1975, "Instantaneous Measurements in the Jet-Wake Discharge Flow of a Centrifugal Compressor Impeller," Journal of Engineerring for Power, 97, pp. 37-46.

[132] Traupel, W., 1988, Thermische Turbomaschinen, Springer, Berlin [etc.].

[133] Bammert, K., and Rautenberg, M., 1974, "On the Energy Transfer of Centrifugal Compressors," Proceedings of ASME Turbo Expo, 74-GT-121.

[134] Inoue, M., and Cumpsty, N. A., 1984, "Experimental-Study of Centrifugal Impeller Discharge Flow in Vaneless and Vaned Diffusers," Journal of Engineering for Gas Turbines and Power-Transactions of the

ASME, 106(2), pp. 455-467.

[135] Jansen, W., 1964, "Rotating Stall in a Radial Vaneless Diffuser," ASME Journal of Basic Engineering, 86(3), pp. 750-758.

[136] Eckardt, D., 1976, "Detailed Flow Investigations within a High-Speed Centrifugal Compressor Impeller," Journal of Fluids Engineering, 88, pp. 390-402.

[137] Krain, H., 1981, "A Study on Centrifugal Impeller and Diffuser Flow," Journal of Engineering for Power-Transactions of the ASME, 103(4), pp. 688-697.

[138] Runstadler Jr, P., and Dolan, F., 1975, "Design, Development, and Test of a Laser Velocimeter for High Speed Turbomachinery," Proceedings of the LDA Symposium, Copenhagen 1975, pp. 523-552.

[139] Schleer, M., Song, S. J., and Abhari, R. S., 2008, "Clearance Effects on the Onset of Instability in a Centrifugal Compressor," Journal of Turbomachinery-Transactions of the ASME, 130(3).

[140] Stahlecker, D., and Gyarmathy, G., 1998, "Investigations of Turbulent Flow in a Centrifugal Compressor Vaned Diffuser by 3-Component Laser Velocimetry," ASME Turbo Expo, 98-GT-300.

[141] Kämmer, N., and Rautenberg, M., 1982, "An Experimental Investigation of Rotating Stall Flow in a Centrifugal Compressor," ASME Turbo Expo, 82-GT-82.

[142] Roduner, C., Koeppel, P., Kupferschmied, P., and Gyarmathy, G., 1999, "Comparison of Measurement Data at the Impeller Exit of a Centrifugal Compressor Measured with Both Pneumatic and Fast-Response Probes," Journal of Turbomachinery, 121(3), pp. 609-618.

[143] Schleer, M., 2006, "Flow Structure and Stability of a Turbocharger Centrifugal Compressor," Ph.D. thesis, ETH Zürich, Nr. 16605, Zürich.

[144] Schleer, M., Mokulys, T., and Abhari, R. S., 2003, "Design of a High Pressure-Ratio Centrifugal Compressor for Studying Reynolds Number Effects," Compressors and Their Systems, (4), pp. 391-404.

[145] Hunziker, R., 1993, "Einfluss der Diffusorgeometrie auf die Instabilitätsgrenze des Radialverdichters," Ph.D. thesis, ETH Zürich, Nr. 10252, Zürich.

[146] Johnson, M. W., and Moore, J., 1980, "The Development of Wake Flow in a Centrifugal Impeller," Journal of Engineering for Power, 102(2), pp. 382-389.

[147] Johnson, M. W., and Moore, J., 1983, "The Influence of Flow Rate on

the Wake in a Centrifugal Impeller," Journal of Engineering for Power, 105(1), pp. 33-39.

[148] Johnson, M. W., and Moore, J., 1983, "Secondary Flow Mixing Losses in a Centrifugal Impeller," Journal of Engineering for Power, 105(1), pp. 24-32.

[149] Krain, H., 1988, "Swirling Impeller Flow," Journal of Turbomachinery-Transactions of the ASME, 110(1), pp. 122-128.

[150] Mansour, M., Chokani, N., Kalfas, A. I., and Abhari, R. S., 2008, "Unsteady Entropy Measurements in a High-Speed Radial Compressor," Journal of Engineering for Gas Turbines and Power, 130(2), pp. 021603-9.

[151] Sieverding, C. H., 1984, "Recent Progress in the Understanding of Basic Aspects of Secondary Flows in Turbine Blade Passages," Mechanical Engineering, 106(7), pp. 86-86.

[152] Gregory-Smith, D., Graves, C., and Walsh, J., 1988, "Growth of Secondary Losses and Vorticity in an Axial Turbine Cascade," Journal of Turbomachinery -Transactions of the ASME, 110(1), pp. 1-8.

[153] Niehuis, R., Lücking, P., and Stubert, B., 1989, "Experimental and Numerical Study on Basic Phenomena of Secondary Flows in Turbines," AGARD-CP-469.

[154] Lagerstrom, P. A., 1996, Laminar Flow Theory, Princeton University Press, Princeton, New Jersey.

[155] Köppel, P. D., Roduner, C., Kupferschmied, P., and Gyarmathy, G., 2000, "On the Development and Application of the Fast-Response Aerodynamic Probe System in Turbomachines---Part 3: Comparison of Averaging Methods Applied to Centrifugal Compressor Measurements," Journal of Turbomachinery, 122(3), pp. 527-535.

[156] Dzung, L., 1967, "Mittelungsverfahren in der Theorie der Schaufelgitter," Brown Boveri Mitteilungen.

B   Nomenclature

Symbols

$(r/\theta/z)$	Global facility coordinate system	[-]
$(X/Y/Z)$	Local probe coordinate system	[-]
A	Sensor surface	[m^2]
b	Diffuser span	[m]
c	Absolute flow velocity	[m/s]
$\vec{c}, \vec{c}$	Flow velocity vector	[m/s]
cp, c_p	Sensor specific heat capacity	[J/(kg K)]
Cp	Non-dimensional pressure coefficients	[-]
Cps, Cp_s	Non-dimensional static pressure coefficients:	[-]

LISA: $Cp_s = (p_{stat} - p_{stat,exit})/(p_{tot,inlet} - p_{stat,exit})$;
RIGI: $Cp_s = p_{stat}/p_{tot,inlet}$;

Cpt, Cp_t	Non-dimensional total pressure coefficients:	[-]

LISA: $Cp_t = (p_{tot} - p_{stat,exit})/(p_{tot,inlet} - p_{stat,exit})$;
RIGI: $Cp_t = p_{tot}/p_{tot,inlet}$;

c_θ	Circumferential flow velocity component	[m/s]
c_r	Radial flow velocity component	[m/s]
c_x, c_z	Axial flow velocity component	[m/s]
d	Distance	[m]
D, d	Probe tip diameter	[mm]
d_2	Impeller exit diameter	[m]
f	Frequency	[Hz]
g	Uncertainty sensitivity coefficient	[-]
h	Heat transfer coefficient	[W/(m^2 K)]
I_E	Excitation current, Feeding Current	[mA]
J_o	Sensor calibration offset adjustment coefficient out of Offset/Gain procedure	[-]
J_I	Sensor calibration gain adjustment coefficient out of Offset/Gain procedure	[-]
k	Thermal conductivity	[W/(m K)]
k	Uncertainty coverage factor	
K_φ	Calibration coefficient of flow yaw angle	[-]
K_γ	Calibration coefficient of flow pitch angle	[-]

K_t	Calibration coefficient of total pressure	[-]
K_s	Calibration coefficient of static pressure	[-]
$k_{ij\varphi}$	Polynomial aero-calibration coeff. of yaw angle	[-]
$k_{ij\gamma}$	Polynomial aero-cal. coeff. of pitch angle	[-]
k_{ijt}	Polynomial aero-cal. coeff. of total pressure	[-]
k_{ijs}	Polynomial aero-cal. coeff. for static pressure	[-]
k_p	Polynomial sensor-cal. coeff. of pressure	[-]
k_T	Polynomial sensor-cal. coeff. of temperature	[-]
m	Sensor mass	[kg]
$\dot{m}$	Mass flow	[kg/s]
Ma	Mach number	[-]
Mu	Stage Mach number	[-]
p, P	Pressure	[mbar]
$P1, P2,...P5$	Probe tap pressures	[Pa]
P_{atm}	Atmospheric pressure	[Pa]
P_{ref}	Reference pressure	[Pa]
P_{stat}	Static pressure	[Pa]
P_{tot}	Total pressure	[Pa]
Q	Corrected mass flow rate	[K$^{0.5}$ s m]
R	Resistance	[Ohm]
R	Specific gas constant	[J/(kg K)]
r	Temperature recovery factor	[-]
Re_d	Reynolds Number with respect to probe tip	[-]
R_{meas}/R_{d2}	Non-dimensional radius ratio:	[-]
	(R_{meas}: measurement radius; R_{d2}: impeller exit radius)	
S, S_I	Pressure sensitivity	[mV/(mA bar)]
S_{5mW}	Standardized pressure sensitivity	[mV/bar]
T	Temperature	[K]
t	Time	[s]
t/T	Time over blade period	[-]
TCO_I	Temperature coefficient of offset voltage	[mV/(mA K)]
TCR_E	Temperature coefficient of resistivity	[1/K]
T_{HS}	Hot streak core temperature	[K]
T_{tot}/T_{MF}	Stagnation to main flow temperature ratio	[-]
U	Sensor output voltage	[V]

U	Expanded uncertainty	
u	Standard uncertainty	
$\vec{u}$, $\vec{u}$	Blade velocity vector	[m/s]
U_2	Blade speed at impeller exit	[m/s]
Ue, U_E	Sensor excitation voltage	[V]
$\vec{w}$, $\vec{w}$	Relative velocity vector	[m/s]
x	Input parameter	
y	Result parameter	

Greek Symbols

α	Temperature coefficient	[1/K]
Δ	Difference value, relative to reference value	[-]
φ	Flow yaw angle	[Deg]
γ	Flow pitch angle	[Deg]
ρ	Density	[kg/m^3]
μ	Dynamic Viscosity	[Pa s]
υ	Kinematic viscosity	[m^2/s]
κ	Isentropic coefficient (specific heat ratio): $(\kappa = c_p/c_v)$	[-]
τ	Time constant	[s]
Π_o	Total pressure ratio	[-]
$\eta_{is,tt}$	Isentropic total-to-total efficiency	[-]
$\Delta\eta_{is,tt,rel}$	Normalized relative change in isentropic total-to-total efficiency	[-]
Δz	Incremental step between measurement points	[m]
$\vec{\omega}$, $\vec{\omega}$	Vorticity vector	[1/s]

Subscripts

0	Turbine inlet
3	Turbine exit
abs	Absolute
atm	Atmospheric
av	Average
c	Based on calibration
cal	Calibrated
$diff$	differential

DP	Design point
exit	Corresponding value at the exit
HS	Hot streak
hyst	Hysteresis
i,j,m,n	Index, counter
in, inlet	Corresponding value at the inlet
m	Measured
mav, massav	Mass-averaged
MF	Main flow
mod, model	Calibration model
OG	Offset-Gain
probe	Measured value by probe
θ	Circumferential direction
r	Radial direction
Ref, ref	Reference
rel	Relative
rep	Repeatability
rms	Root mean square
S	Piezoresistive pressure transducer
sensed	Sensed value by the piezoresistive pressure transducer
SH	Self heating
stat	Static
tot	Total
z, x	Axial direction

Superscripts

~	Ensemble Average
-	Mean value, time- or mass-average value
´	Turbulent fluctuation

Abbreviations

2D	2-dimensional
3D	3-dimensional
4HP	Pneumatic 4-hole probe
5HP	Pneumatic 5-hole probe

CAD	Computer aided design
CFD	Computational Fluid Dynamic
conf	Configuration
D	Dimensional
DAQ	Data acquisition system
def	Deformation tensor: $def\ \vec{c} = grad\ \vec{c} + (grad\ \vec{c})'$
DF	Detection function
DP	Design point
DRUCK DPI520	Pressure source
ETH Zurich	Eidgenössisch Technische Hochschule Zürich; ETH Zurich
F0S-PT100-HT	Steady high temperature probe
FB	Full blade
FEM	Finite Element Method
flexprint	Flexible printed circuit board
FP	Flow property value
FRAP	Fast Response Aerodynamic Probe
FRAP-HT	High Temperature Fast Response Aerodynamic Probe
GF	Gauge factor
grad	Gradient
GUM	Guide to the Expression of Uncertainty in Measurement
HERKULES	Name of data reduction and post-processing software
HS	Hot streak
HSG	Hot streak generator
IC	Integrated circuit
IR	Infrared
LabView Vi's	LabView Virtual instrument
LE	Leading edge
LEC	Laboratory for Energy Conversion at ETH Zurich
LED	Light-emitting diode
LISA	Name of axial research turbine at LEC, ETH Zurich
MEMS	Micro-Electro-Mechanical-Systems
MP	Measurement plane
MP	Measurement point
MUI	Master User Interface

N_A	Actual number of measurement points
NGV	Nozzle guide vane
N_L	Number of loops
N_P	Number of points/loop
N_T	Total number of possible measurement points
P788	Piezoresistive pressure transducer used for 1st generation FRAP
PCB	Printed circuit board
PG	Pressure gradient section
PM	Minimum pressure section
PPU	Power- Pressure- Unit
PRPT-HT	Piezo-Resistive Pressure Transducer used for FRAP-HT
PS	Blade pressure side
PSD	Power-Spectral-Density
PSI	Pressure unit: pounds per square inch
PT100	Type of thermocouple temperature sensor
RIGI	Name of centrifugal research compressor at LEC
rms	Root mean square
RPM	Rounds per minute
RTV	Room-temperature-cross-linking
SB	Splitter blade
SOI	Silicon-on-insulator
SOS	Silicon-on-sapphire
SS	Blade suction side
TC	Test case
TCx	Test case no. x
TE	Trailing edge
TET	Turbine entry temperature
TO	Transistor outliner
YA	Yaw angle section

C   List of Figures

D   List of Tables

E   List of Publications

First author publications

Lenherr, C., Oschwald, M., Kalfas, A. I. and Abhari, R.S., (2004). "Flow Adaptive Aerodynamic Probe for Turbomachinery Flows." 17th Symp. on Measuring Techniques in Transonic and Supersonic Flow in Cascades and Turbomachines, Stockholm, Sweden.

Lenherr, C., Oschwald, M., Kalfas, A. I. and Abhari, R.S., (2004). "Towards an Intelligent Aerodynamic Probe Concept for Turboachinery Flows." 1st International Conference on Gas Turbine Instrumentation, EVI-GTI, Barcelona, Spain, Paper Presentation.

Lenherr, C., Kalfas, A. I. and Abhari, R. S. (2006). "Application of Fast Response Aerodynamic Probes in Low Dynamic Head Automotive Truck AC Systems." 18th Symp. on Measuring Techniques in Transonic and Supersonic Flow in Cascades and Turbomachines, Thessaloniki, Greece.

Lenherr, C., Kalfas, A. I. and Abhari, R. S. (2007). "A flow adaptive aerodynamic probe concept for turbomachinery." Measurement Science and Technology 18(8): 2599-2608.

Lenherr, C., Jenny, P., Kalfas, A. I. and Abhari, R. S. (2009). "Time-Resolved Measurements of Hot Streaks in an Unshrouded Turbine Using a Novel High Temperature FRAP Probe." In: XIXth International Symposium on Air-Breathing Engines, Montréal, Canada, ISABE Paper Presentation.

Lenherr, C., Kalfas, A. I. and Abhari, R. S. (2010). "High Temperature Fast Response Aerodynamic Probe." Proceedings of the ASME Turbo Expo 2010, GT2010-23010, Glasgow, UK.

Lenherr, C., Kalfas, A. I. and Abhari, R. S. (2011). " High Temperature Fast Response Aerodynamic Probe." J. Eng. Gas Turbines Power 133(1), GTP-10-1064.

Publications as co-author

Jenny, P., Lenherr, C., Kalfas, A. I. and Abhari, R. S. (2010). "Effect of Unsteady Blade Row Interaction on Hot Streak Migration in an Axial Turbine." Proc. of the ASME Turbo Expo, GT2010-23034, Glasgow, UK.

Mansour, M., Kocer, G., Lenherr, C., Chokani, N., Abhari, R. S. (2010). "Full Scale Wind Turbine Flowfield Measurements using a 7-Sensor Fast Response Probe." Proc. of the ASME Turbo Expo, GT2010-23425, Glasgow, UK.

F   Curriculum Vitae

Christian Lenherr

Born on February 25, 1978 in St.Gallen, Switzerland, citizen of Gams (SG)

Education

1985 - 1991	Primarschule Boppartshof, St.Gallen, Switzerland
1991 - 1993	Katholische Kantonssekundarschule, St.Gallen, Switzerland
1993 - 1998	Gymnasium, Kantonsschule am Burggraben, St.Gallen, Switzerland, Federal Maturity.

Studies

1999 - 2004	Study of Mechanical Engineering, at Swiss Federal Institute of Technology (ETH Zurich), Switzerland
2003	Exchange studies at Department of Energy Technology, KTH Stockholm, Sweden; Semester Thesis „Modelling of Aerodynamic Low Engine Order Excitation in a High- Pressure Turbine Stage".
2004	Master Thesis at Laboratory for Energy Conversion (LEC), ETH Zurich, „Experimental Investigation of Smart Probe Concept for Unsteady Flows in Axial Turbines".
2004	Diploma degree in Mechanical Engineering, ETH Zurich.
2004 - 2010	Doctoral student at LEC, ETH Zurich.

Working Experience

2002	Internship at ALCAN MASS TRANSPORTATION SYSTEMS, Switzerland
2005 - 2010	LIMMAT SCIENTIFIC AG, Zurich, Switzerland. Development engineer & Project Manager.
2004 - 2010	LABORATORY FOR ENERGY CONVERSION (LEC), ETH Zurich Research and teaching assistant.

Miscellaneous

1998 - 1999	Ski instructor at Swiss Ski school in Davos, Switzerland.
2001 - 2008	Member executive committee of the Open Air Music Festival St.Gallen, Switzerland
2007 - 2008	Swiss Military Airforce Company Commander as a First Lieutenant (Mobile Airforce Radar Company 21).